The Dissertation Committee for William Kenneth Bell III Certifies that this is the approved version of the following dissertation:

Photocrosslinkable Nonlinear Optical Polymers and Directly-Patternable Polyimide Dielectrics

Committee:

C. Grant Willson, Supervisor

Christopher Ellison

Eric Anslyn

Adrian Keatinge-Clay

Paul Ho

Michael Rose

Photocrosslinkable Nonlinear Optical Polymers and Directly-Patternable Polyimide Dielectrics

by

William Kenneth Bell III, B.S.

Dissertation

Presented to the Faculty of the Graduate School of

The University of Texas at Austin

in Partial Fulfillment

of the Requirements

for the Degree of

Doctor of Philosophy

The University of Texas at Austin

August 2014

Dedication

For Mom

Acknowledgements

Many have contributed to my studies over the past few years and for that I am eternally grateful. Of course my advisor is at the very top of this long list. Prof. Willson has cultivated an environment of unique research opportunities and outstanding people, both of which made for a tremendously rewarding graduate school experience. I owe a great deal to Prof. Willson for welcoming me into his group and supporting in my time here. I also thank Donna Martin and Kathleen Sparks for fighting the university bureaucracy and keeping the group running smoothly.

I would like to thank the many Willson group alumni who have aided me throughout this journey. I am indebted to Prof. Brian Long for furthering my training as a synthetic chemist, especially in the dark art of column chromatography. Dr. Jeff Strahan provided an interesting counterpoint to Prof. Long's chemical approach, teaching me to value simplicity and scalability over synthetic elegance. But despite their best efforts, neither convinced me to cut my hair. Dr. Michael Jacobsson was a particularly good mentor and friend—I always looked forward to that afternoon coffee break and the interesting discussions we would share. Dr. Brandon Rawlings taught me a great deal in his time at UT and worked tirelessly, even during the dog days of NLO. I am glad our collaboration continues, if only remotely. Finally, I would like to thank Dr. Chris Bates for his insight and encouragement in pursuits both scientific and musical.

I am grateful to have such wonderful colleagues in the Willson group. Team Packaging has been a particularly fun crowd to work with. I cannot thank Colin "Chase" Hayes enough for his friendship, encouragement and unending energy. I only wish that we could share a lab bench for a few more years. Andrew Dick and Philip Liu have been

invaluable members of the project and I have learned a great deal from both. I was also fortunate to work with two very talented undergraduates: Chad Webb and Brendan Luke. Each made significant research contributions and I wish them the best of luck in their future endeavors. I also thank Ryan Mesch, Will Durand, Michael Maher, Greg Blachut and Austin Lane for making this group so enjoyable.

My summer term at Seagate Technology was a tremendous experience, in no small part due to Gene Gauzner. An outstanding boss, Gene taught me to enjoy process development, but also supported me in pursuing some of my crazier (*to an electrical engineer*) ideas. I thank him for trusting a chemist with multi-million dollar nanoimprint tools. The fact that I did not break anything is certainly due to Hieu Tran, who aided me with many experiments. I would also like to thank the entire nanofabrication team at Seagate Media Research for their support and advice. Outside of Seagate, in that time I was fortunate to get to know Brennen Mueller, who has become a close friend and valued collaborator.

In my transition from Welch Hall to the dark catacombs of CPE, I am very glad to have worked with the Ellison group. Prof. Chris Ellison and his students have been invaluable in helping me adapt to a very different environment. In particular, I would like to thank Paola Gonzalez for her advice in dealing with problematic casting solvents and Reika Katsumata for her help with my ellipsometry endeavors. Despite having to fight Dr. Dustin Janes for use of the Novacure, I am grateful to have worked with him. Our frequent discussions of industrial R&D and the future of optical lithography have been both fun and intellectually stimulating.

I am fortunate to have forged several close friendships in my time here. Eric Silver was the first person I met at UT and has been a good friend ever since. I will fondly remember the many Friday evenings spent at the Crown, alternately discussing

research troubles and 90s action films. My bandmates, past and present, will remain an important part of my life long after we part ways. I am forever thankful that Dr. David Walker approached me during our first semester and asked me to join his band. This led to several friendships I cannot imagine being without: David, Chris Fage, Logan Duplant and Barrett Worley. Ultimately it is these bonds which have made the past few years unforgettable.

Photocrosslinkable Nonlinear Optical Polymers and Directly-Patternable Polyimide Dielectrics

William Kenneth Bell III, Ph.D.

The University of Texas at Austin, 2014

Supervisor: C. Grant Willson

The development of high-efficiency nonlinear optical (NLO) polymers has opened up many opportunities in the field of electro-optics. However, current NLO polymers do not meet stability requirements for semiconductor integration. In an effort to improve this, we examined the effects of crosslinking following electric field poling. A series of photocrosslinkable polymers bearing side chain chromophores was synthesized, poled and evaluated on the basis of the thermal stability of Second Harmonic Generation. Photoinitiation allowed for control of the onset of curing. Crosslinking was monitored by FTIR and optimal conversion was achieved by applying a slow temperature ramp during exposure. The ultimate stability of the poled polymers was directly related to the number of crosslinking substituents attached to the chromophore pendant group. With two reactive groups per chromophore significant SHG was retained at temperatures beyond the polymer T_g.

In integrated circuit packaging there is a need for directly-patternable polymers of low dielectric constant. Bridging the gap between the high-value silicon chip and circuit board is a substrate comprising alternating layers of metal conductor and polymer dielectric. PMDA-ODA, an aromatic polyimide, meets many of the requirements for integration and can be patterned using a photobase generator (PBG). Due to absorbance

by the PMDA-ODA precursor, this PBG must have activity at visible wavelengths. Several oxime urethanes were synthesized and evaluated as candidate long wavelength PBG. These compounds exhibit clean photochemistry and high visible light sensitivity. Unfortunately, carbamate thermal stability is insufficient for patterning PMDA-ODA.

For improved material properties, PMDA-TFMB, a fluorinated polyimide, was also evaluated. Importantly, the polymer precursor is sufficiently transparent to employ thermally-stable near-UV photobases. With photobase, 2.5 micron features were resolved in PMDA-TFMB. An ancillary benefit of this methodology is reduced cure temperature (~200 °C), a traditional drawback of polyimides. This material demonstrates a dielectric constant near 3 and a thermal expansion coefficient (CTE) of approximately 6 ppm/°C in-plane. Through-plane thermal expansion is somewhat problematic, with a CTE of approximately 160 ppm/°C, and will likely require a nanoparticle composite strategy. However, this combination of material and lithographic properties make PMDA-TFMB a promising candidate for this application.

Table of Contents

List of Tables

List of Figures

Chapter 1: Introduction to Photolithography

GENESIS

The modern computer was born of a device known as the Electronic Numerical Integrator And Computer (ENIAC), which became operational in 1945. It was developed during World War Two as an alternative to the mechanical computers then used to perform ballistic calculations.[1] While costly and maintenance-intensive, the improvements afforded by ENIAC were undeniable. Previously, solving a 60 second trajectory might take a day or more with a desktop calculator or 15 minutes using a state-of-the-art differential analyzer.[2] ENIAC required a mere 30 seconds. However, it was this device's versatility which had the greatest impact. Owing to its programmability, ENIAC was readily adapted for use in areas outside of ballistics. Famously, the first problem assigned to ENIAC was a portion of Edward Teller's "Super" thermonuclear weapon model.[3] Through nearly two decades of operation, ENIAC would find use in areas as diverse as atomic energy, weather prediction, reservoir simulation, and aerodynamics.[4]

While powerful, ENIAC was incredibly unwieldy, weighing nearly 30 tons and occupying 1800 square feet. Critical to its operation were nearly 18,000 vacuum tubes, 70,000 resistors, 10,000 capacitors and many thousands of other components, all interconnected by hand-soldering.[5] The vacuum tubes were especially problematic, with failures occurring on a daily basis. Even with modernization in the early 1950s, ENIAC was rarely operational for more the 100 hours per week.[2]
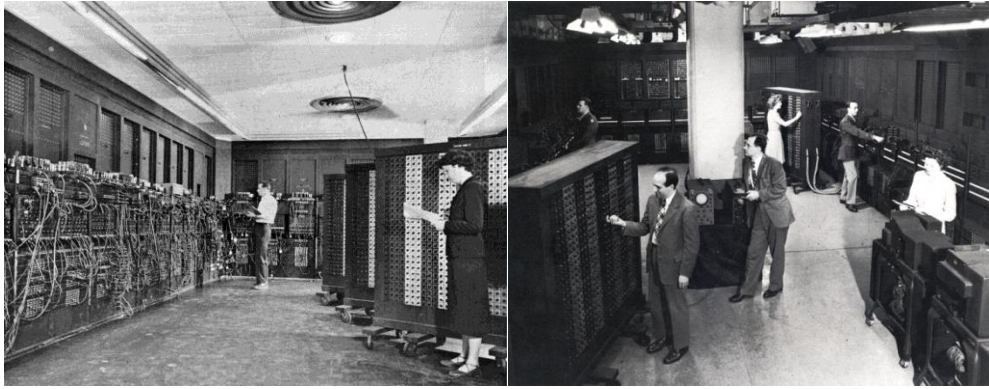
Figure 1.1: Photos of ENIAC[6, 7]

The journey from large tube-based devices to the modern computer is a story of continuous improvement and innovation. The fundamental discovery which enabled this process took place only a few years after ENIAC began operation. In 1947, scientists at Bell Labs were researching alternatives to vacuum tubes for use in signal amplification. A group consisting of William Shockley, Walter Brattain and John Bardeen looked to older crystal-based amplifiers for inspiration. Rather than relying on galena or pyrite, the common semiconductors of the time, the group opted to instead study exotic materials like single-crystal silicon. When silicon devices demonstrated disappointing results, the decision was made to switch to germanium, which at the time was available in much higher purity.

Their germanium device was a handmade point-contact transistor, consisting of three electrical connections.[8-10] The semiconducting material rested atop a conducting base (Figure 1.2). The other two contacts, the emitter and collector, were created by spreading a strip of gold over a triangular piece of plastic. The gold was wired at both ends and then sliced through the tip to create a discontinuity. This was mounted on a spring which held it in contact with the base. With this design, slight changes in emitter current resulted in much larger changes at the collector—the amplification effect the

researchers were looking for. In 1956, Shockley, Brattain and Bardeen received the Nobel Prize in Physics for this breakthrough finding.[11]
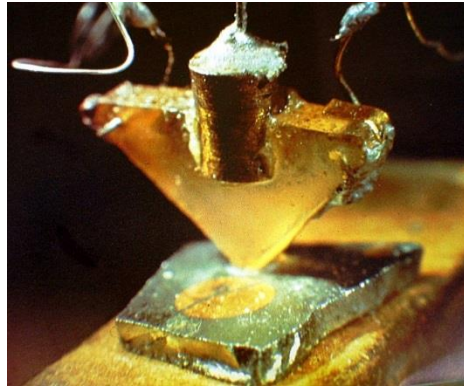
Figure 1.2: The Bell Labs point-contact transistor[12]

The Bell Labs transistor and the designs which followed were to prove adequate in replacing vacuum tubes. However, they remained relatively large. Moreover, circuit fabrication still involved manual connection of discrete components such as transistors, resistors and capacitors to form a complete device. This process did not lend itself to mass production or miniaturization. The next step was the transition from the discrete to integrated circuit.

There is some debate regarding the invention of the integrated circuit, but Jack Kilby was the first to demonstrate a functioning device. In 1958 while at working at Texas Instruments, he constructed a circuit consisting of transistor, capacitor and resistor elements, all on a single piece of germanium. Impetus for this design came largely as a result of the shortcomings of Kilby's primary project, the more conventional Micro-Module program.[13] He would later recall:

> *In my discouraged mood, I began to feel that the only thing a semiconductor house could make in a cost-effective way was a semiconductor. Further thought led me to the conclusion that semiconductors were all that were really required—*

that resistors and capacitors, in particular, could be made from the same material as active devices. I also realized that, since all of the components could be made of a single material, they could also be made in situ, interconnected to form a complete circuit.

It is important to note that the issue of interconnection was a major limitation of Kilby's otherwise revolutionary design. Though Texas Instruments was quick to commercialize the invention, introducing the Type 502 IC in 1960, components were still connected manually with fragile gold wires. Though not an adequate manufacturing solution, Kilby's scientific breakthrough would be recognized with the 2000 Nobel Prize in Physics.[14] Ultimately it would fall to Robert Noyce at Fairchild Semiconductor to develop an integrated circuit amenable to mass-market applications. Noyce independently conceived of the monolithic integrated circuit less than six months after Kilby. Building on a planar fabrication process developed by Jean Hoerni, he designed an IC with interconnects formed from vapor-deposited aluminum.[15] Rather than isolating these connections by the flying-wire technique of TI, Noyce proposed using silicon dioxide to produce a system that was mechanically robust. Fairchild produced the first circuit via this methodology in 1960 and its impact was profound.[16] This combination of aluminum conductor and silicon dioxide insulator would sustain the microelectronics industry for the next forty years.
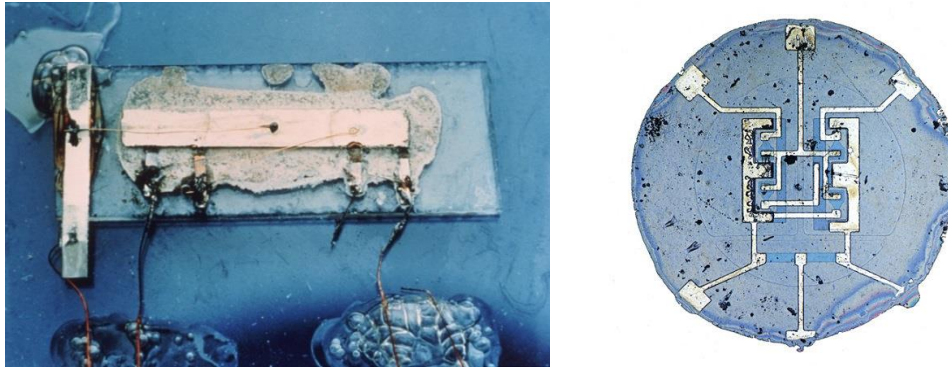
Figure 1.3: Kilby's germanium integrated circuit (left)[17] and Fairchild's planar device (right)[18]

With advent of the Fairchild process, miniaturization would continue with increasing fervor. In 1965, Fairchild employee Gordon Moore observed that the number of transistors on an integrated circuit doubled annually.[19] Foreseeing no fundamental limits in the near term, Moore anticipated continuation of this trend on economic grounds. As the minimum manufacturing cost of a chip was essentially fixed, the cost per component could be decreased simply by increasing component density. This would prove to be a strong driving force in increasing circuit complexity. While the initial estimate proved somewhat optimistic and was revised in 1975 to doubling every two years, Moore's Law has effectively driven the microelectronics industry to the present day.[20]
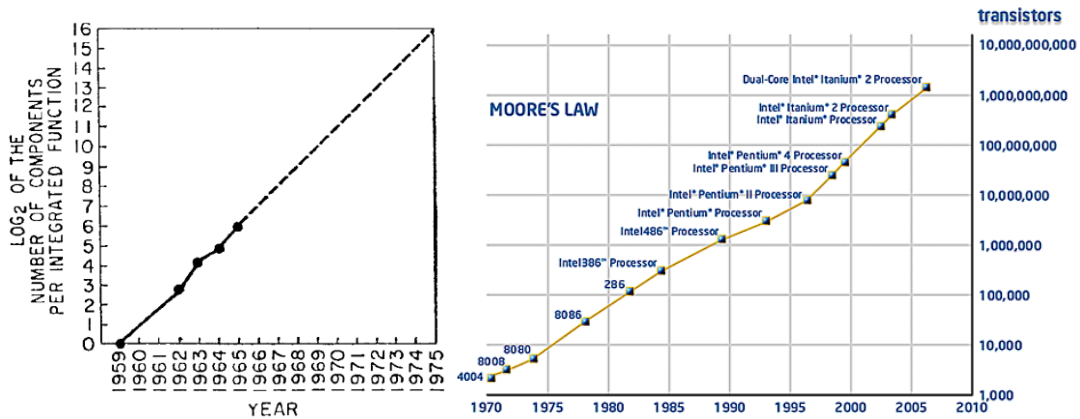
Figure 1.4: Moore's initial observation (left)[19] and Intel microprocessors from 1971 to 2006 (right).[21] *Copyright 1998, IEEE.*

PHOTOLITHOGRAPHY

Key to maintaining Moore's Law, photolithography is the process which first defines circuit components on the device. Continued advances in this field have allowed for fabrication of ever-smaller structures, thereby sustaining the constant increase in device density. Fundamentally, photolithography is very similar to traditional photography. Both techniques rely on a photochemical reaction in a film, followed by a series of processing steps to convert the initial image into a useful structure. An overview of the photolithographic process is shown in Figure 1.5.
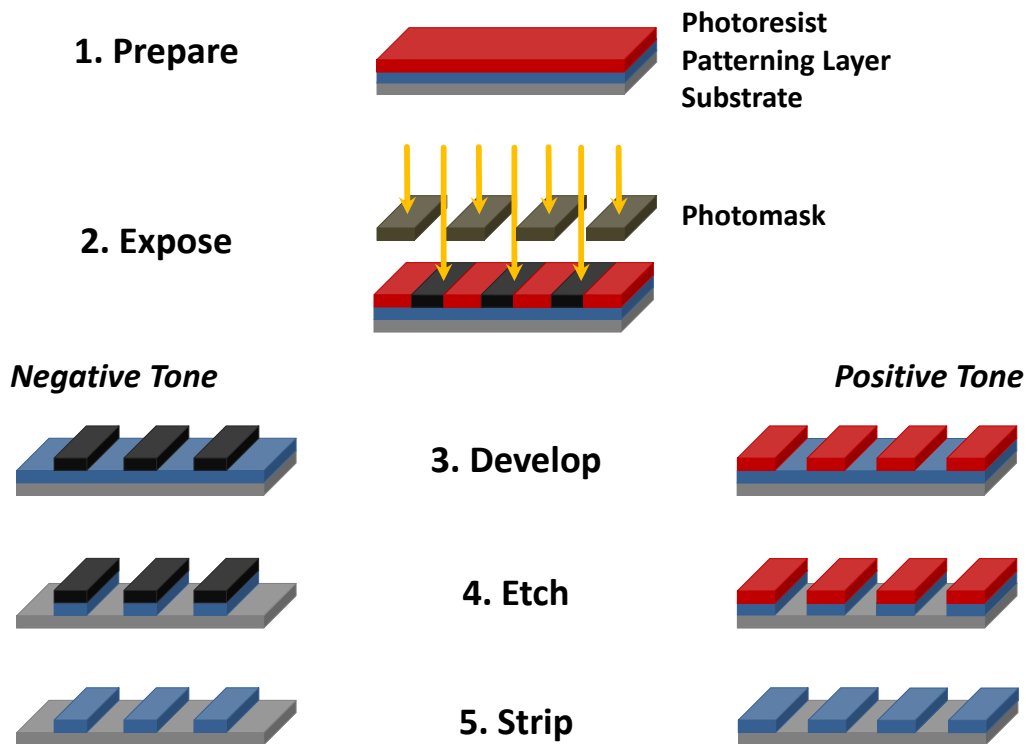
Figure 1.5: Depiction of the photolithographic process. Photoresist (red) is coated onto a patterning layer (blue) supported by a substrate (light gray). The film is exposed through a photomask (dark gray). Subsequent steps are depicted for both negative tone (left) and positive tone resists (right).

This process begins with deposition of a photoresist onto the surface to be patterned. In microelectronics manufacturing this surface is typically a semiconductor (generally silicon), a metal, or an insulator such as silicon dioxide. The photoresist is a solution which contains a polymer, a photoactive compound, and other additives which serve to optimize pattern formation and transfer. The chemistry of photoresist materials will be discussed in greater detail subsequently. To improve photoresist performance, the patterning surface may first be treated with an adhesion promoter or an anti-reflective coating. The resist is deposited via spin-coating, where the solution is dispensed onto the substrate and rotated at high speed, yielding a uniform polymer film. Resist thickness is

controlled by the spin speed, solution concentration, and dispense volume. Following spin-coating, the substrate is heated to drive off residual solvent and stabilize the film (Post Apply Bake, PAB).

Areas of the photoresist are then selectively exposed to an intense source of light using a photomask. This step converts the pattern in the photomask into a latent image in the resist film. In regions exposed to light, a photochemical reaction occurs. Depending on the chemistry, this may increase or decrease the solubility of exposed regions, giving rise to two classes of photoresist: positive tone and negative tone, respectively.

Once exposed, the latent image must be converted into a usable structure. This is accomplished by leveraging the aforementioned solubility switch. Exposed films are treated with a developer solvent, which selectively dissolves one of the two regions. As an example, many negative tone resists rely on photocrosslinking to drastically decrease solubility in exposed areas. When immersed in an appropriate solvent, the unexposed regions are completely dissolved to reveal the underlying layer. Exposed areas are left intact. The opposite is true of positive tone resists, though the chemistry differs.

Development forms the desired relief structure in the photoresist, which is transferred into the underlying material in a subsequent step. Pattern transfer may be subtractive (etching) or additive (deposition, implantation). Etching removes regions of underlayer not protected by photoresist film, exploiting chemical differences between the two materials. For example, hydrofluoric acid solution is a common etchant for silicon dioxide. While HF readily dissolves SiO_2, it has minimal effect on organic materials such as photoresist. Such an etchant is said to be selective, readily attacking the underlayer without significantly eroding the resist. Etch selectivity is an important consideration in the design and application of photoresists. Following pattern transfer, the remaining resist is removed and the substrate proceeds to the next manufacturing step.

8

Modern integrated circuits are built up by repeating this process dozens of times, adding and removing layers of insulator, metal, and other materials.

LITHOGRAPHIC RESOLUTION

In the context of photolithography, resolution describes the smallest grating feature which can be patterned with adequate quality and control.[22] The minimum resolution R is given using the Rayleigh resolution criterion (Equation 1.1):

$$R = k_1 \frac{\lambda}{NA} \tag{1.1}$$

Where k_1 is a process-dependent scaling factor, λ is the wavelength of light (note that sources are typically monochromatic), and NA is the numerical aperture of the optical element. As can be seen from equation 1.1, to improve resolution it is desirable to reduce k_1 and exposure wavelength, while simultaneously increasing numerical aperture. k_1 is affected by several variables and is generally believed have a fundamental limit of 0.25, though current methods operate closer to 0.4. Significant effort has been devoted to improving optics in photolithography, and numerical apertures have increased from around 0.28 in the late 1970s, to 1.3 or more in modern systems (Figure 1.6).[23] For current methods, the theoretical limit is 1.44 as dictated by the refractive index of the immersion fluid, water. High index immersion fluids are one area of continued development in optical lithography.[24]

Figure 1.6: Illustration of a modern optical lithography tool. The lens stack is visible at center.[23] *Copyright 2014, ASML.*

The final term, λ, will be of particular interest to chemists as it dictates the photochemistry of resist materials. Exposure wavelength has been steadily reduced since the adoption of photolithography, and is chosen largely for economic reasons. More specifically, it has been selected for the availability of intense, efficient sources of light. Historically, this was the mercury arc lamp, which emits strongly in the visible and near ultraviolet (Figure 1.7). For the purposes of patterning, the two most prominent peaks are centered at 436 nm (g-line) and 365 nm (i-line). These two wavelengths sustained the industry for many years, and mercury lamps are still used in many low resolution applications. The need for intense light sources in the deep ultraviolet culminated in the development of excimer lasers at 248 nm (KrF), followed by 193 nm (ArF). Great effort has been devoted to adoption of shorter wavelengths (157 nm, EUV, X-ray). However,

none have demonstrated feasibility in manufacturing; 193 nm will likely remain state-of-the-art for the foreseeable future.
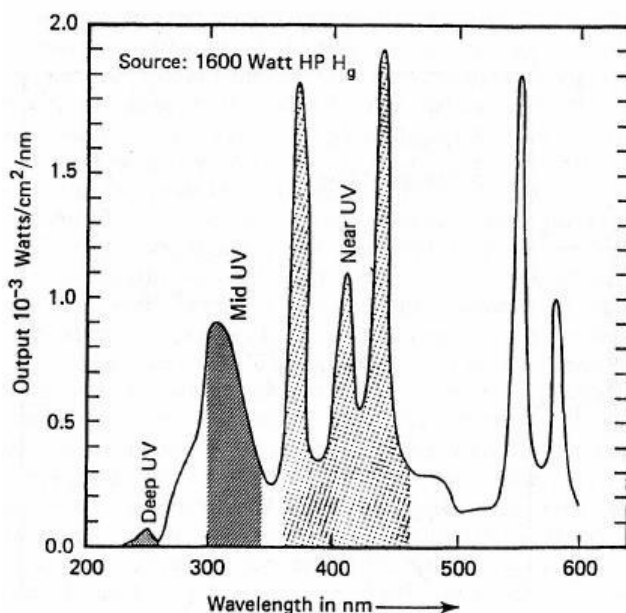
Figure 1.7: Output of a mercury arc lamp from 200-600 nm. Reprinted with permission from Willson, *et al.*[25] *Copyright 1983, American Chemical Society.*

EARLY PHOTORESISTS

As mentioned previously, exposure wavelength determines the fundamental resist chemistry, and changes in wavelength have necessitated modification of resist design. The first commercially successful photoresist was developed by Kodak in 1954.[26] This material, marketed as Kodak Thin Film Resist (KTFR) consisted of cyclized polyisoprene and a bis(aryl azide) photoactive compound. Upon exposure, typically to a g-line source, the aryl azide functional groups decompose to form highly reactive nitrene species (Figure 1.8). In a matrix of unsaturated material like cyclized polyisoprene, these nitrenes insert into C=C and C-H bonds. As the aryl azides are bifunctional, the

11

polyisoprene is rapidly crosslinked, decreasing its solubility in exposed regions—a negative tone resist.
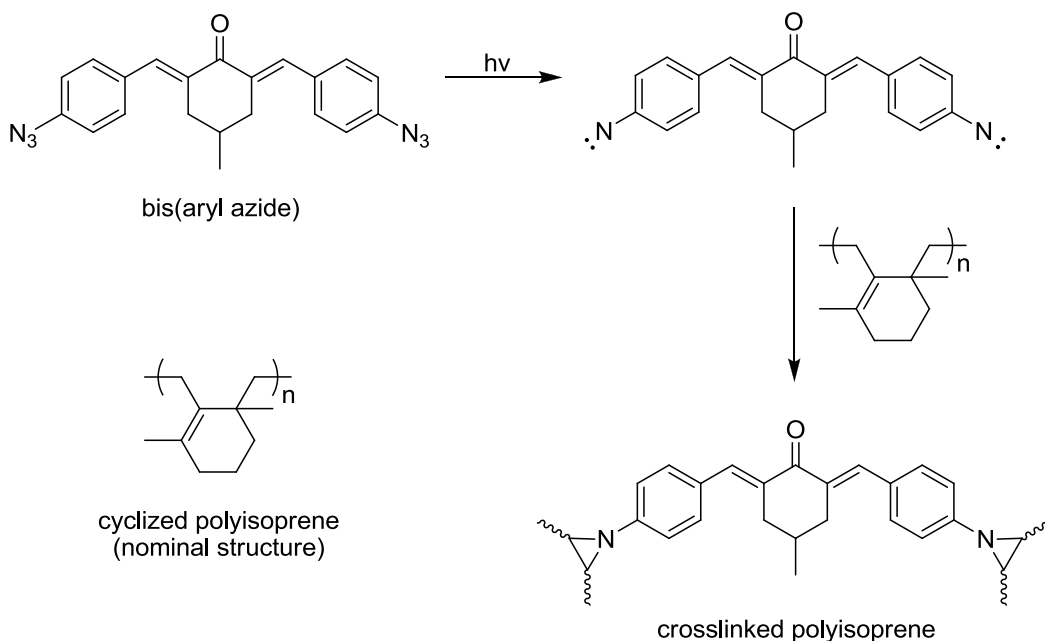
Figure 1.8: Representative crosslinking reaction in KTFR.

KTFR was the mainstay of photolithography until the early 1970s, when resolution requirements approached 2 microns. A limitation of KTFR was its reliance on crosslinking, an increase in the effective molecular weight of the polymer, as the solubility switch. While the increased molecular weight prevents complete dissolution of exposed areas during development, it does not entirely exclude developer from these regions. Indeed, patterns in KTFR tend to swell in the organic solvents used for development. At micron length scales, this effect is catastrophic (Figure 1.9).
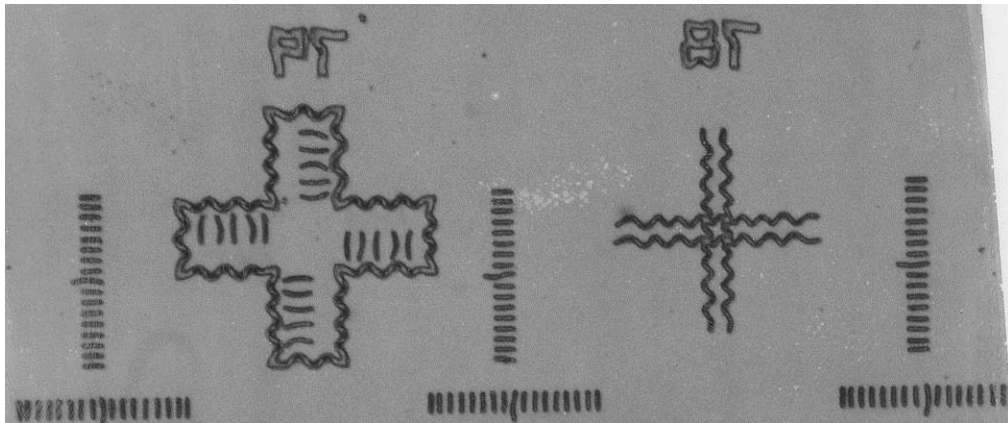
Figure 1.9: Swelling in KTFR. Reprinted with permission from Willson, *et al.*[25] *Copyright 1983, American Chemical Society.*

To overcome these limitations, a very different photoresist was needed. The solution came from a material developed at the same time as KTFR. Around 1950, Kalle AG in Weisbaden, Germany began marketing a material known as Ozatec® for use in photographic plates. Instead of relying on changes in molecular weight, patterns in this material are delineated by significant chemical differences between the exposed and unexposed regions. Ozatec® consisted of a mixture of novolac—a phenol formaldehyde resin and a diazonaphthoquinone (DNQ) photosensitizer. Novolac is a phenolic material that dissolves readily in aqueous base. However, addition of sufficient quantities of DNQ prevents dissolution of the novolac matrix. Exposure of the DNQ to light effects a photochemical Wolff rearrangement, to produce a ketene which is then rapidly hydrolyzed to form a carboxylic acid (Figure 1.10). As a result, the dissolution rate in exposed films of DNQ-novolac increases by several orders of magnitude: ideal positive tone behavior.

13
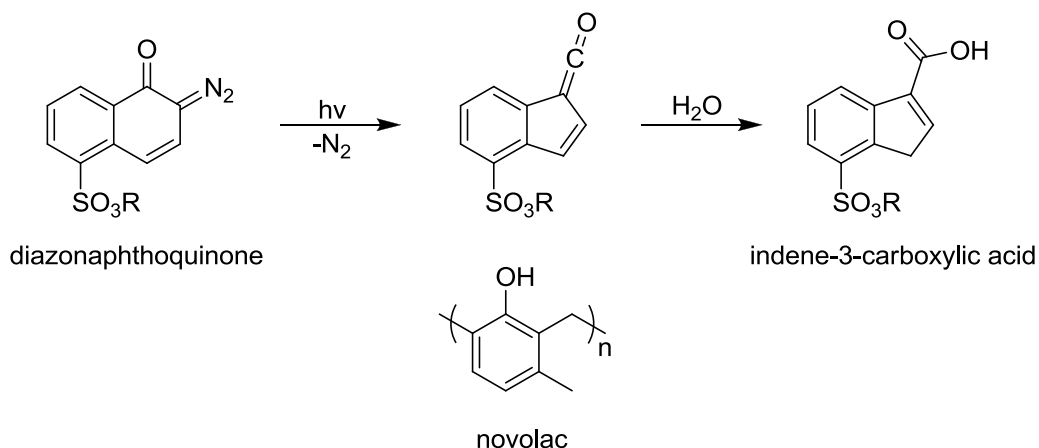
Figure 1.10: Photochemical Wolff rearrangement of diazonaphthoquinone in novolac.

DNQ-novolac resists were adopted by the microelectronics industry in 1972, and quickly supplanted KTFR in areas demanding high resolution. Sources were initially broadband or mercury g-line, but this was eventually shortened to i-line as features continued to shrink. Though minor modifications were required to ensure adequate transparency in the near-UV, DNQ-novolac proved to be a supremely effective i-line resist, sustaining the industry until the late 1980s. Its combination of pattern fidelity, etch resistance, and benign aqueous developer have led to its continued use in many lower-resolution applications.

DUV AND CHEMICAL AMPLIFICATION

Eventually miniaturization required another wavelength reduction, in this case to the deep ultraviolet (DUV, typically 254 nm). At this wavelength, DNQ and its photoproducts are too strongly absorbing to be of any practical use. Moreover, the DUV output of mercury vapor lamps is approximately ten percent of that in the near ultraviolet. This drop in source intensity required a departure from traditional photoresist design. While KTFR and DNQ-novolac relied on a single photon to initiate one reaction in the

resist, economic patterning at 254 nm would only be realized if many chemical reactions were to occur for every photon absorbed—chemical amplification. While several negative-tone examples already existed, leveraging radical crosslinking, the industry was generally averse to negative resists following experience with KTFR.

The first positive-tone chemically amplified photoresist was described by G. H. Smith of 3M in 1973.[27]   This system also used novolac resin, replacing the DNQ dissolution inhibitor with a tetrahydropyranyl ether protecting group. Exposure of the THP ether to a catalytic amount of acid liberates the phenol, converting the material from a hydrophobic to hydrophilic form (Figure 1.11). In this case acid is formed using an onium salt photoacid generator (PAG).[28]   Since this acid is not consumed by the deprotection chemistry, a single photon is able to cause multiple chemical events within the resin. The end result is an extremely sensitive photoresist. As with DNQ-novolac resists, exposed regions are dissolved with aqueous base. Strangely, this revolutionary design was not exploited by 3M and was lost in the patent literature.
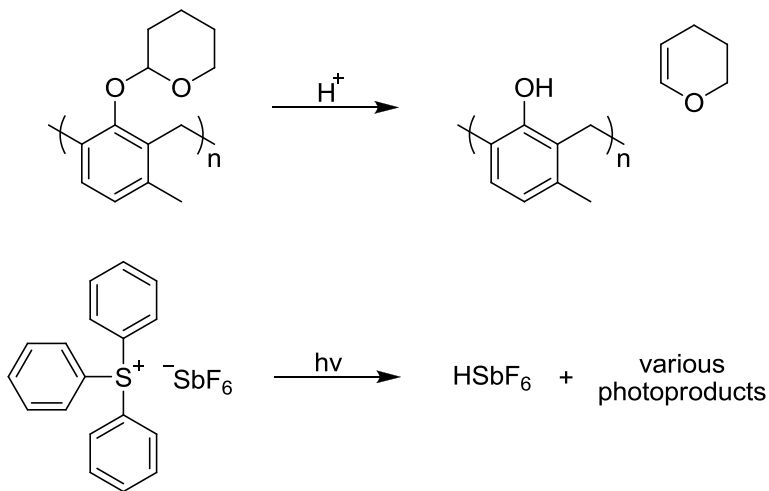
Figure 1.11: Smith's chemically amplified resist system (top) and an example onium salt photoacid (bottom).

Chemically amplified resists were not implemented until much later, following extensive work at IBM in the early 1980s. While initial efforts were directed at photoinduced depolymerization of polyacetals, the research team of Willson, Fréchet, and Ito eventually settled on a design similar to Smith's long-forgotten THP-novolac system.[29] Rather than using novolac resin, the IBM group opted for a polymer with greater transparency in the deep-UV. Poly(p-hydroxystyrene) (PHOST) had previously been studied as a replacement for novolac in DNQ-based resists, meeting most of the material requirements.[30] However, DNQ could not effectively inhibit dissolution of PHOST and its contrast ultimately proved too low for this application.[25] The IBM chemically amplified resist employed a t-butoxycarbonyl (t-BOC) ester to block the phenolic site and prevent dissolution in aqueous base. This protecting group is readily cleaved in the presence of catalytic acid at elevated temperatures, forming carbon dioxide and isobutylene (Figure 1.12). As with Smith's resist, this catalyst is formed using a photoacid generator, typically a sulfonium or iodonium salt.
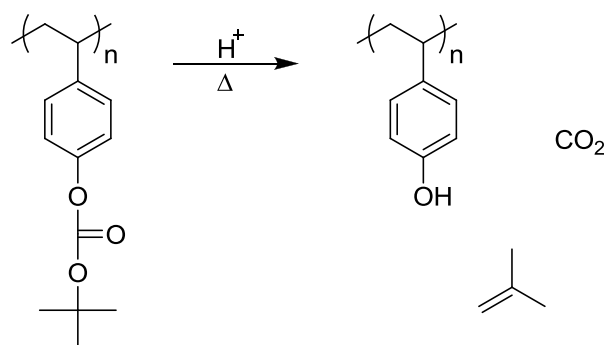
Figure 1.12: Acid catalyzed deprotection of poly(t-BOC styrene).

The IBM material demonstrated sensitivity approaching 1 mJ/cm^2, improving on diazonaphthoquinone by two orders of magnitude.[25] Interestingly, it could serve as either

a positive or negative tone resist. While development in aqueous base resulted in the typical positive tone behavior, organic developers like anisole allowed for high-resolution negative tone images. Concerns about blurring of the image from acid diffusion were allayed by electron beam lithography experiments demonstrating 20 nanometer resolution.[31] The only apparent drawback of this resist was its extreme sensitivity to basic contaminants, notably volatile amines used in other steps of the photolithography process.[32] Alternative polymers were studied, but ultimately this problem was eliminated through the use of carbon-filtered air in manufacturing facilities.[33] This resist was introduced to manufacturing in 1990, patterning 1 micron isolation masks for 1 Mbit DRAM.[34]

As with i-line, DUV lithography eventually reached its resolution limit. Again the industry moved to a shorter wavelength, selecting the 193 nm ArF excimer laser as the source. This posed a significant challenge to resist chemists, as aromatic compounds are opaque at such a short wavelength. Up to that point, photoresists relied on aromatic constituents for etch resistance. In order to achieve both adequate transparency and etch resistance, new design principles were needed. The breakthrough came with the observation that certain alicyclic polymers exhibit etch rates comparable to novolac.[35] This was later formalized as the "ring parameter," an empirical model relating the etch rate to the relative amount of carbon contained in ring structures.[36] By combining alicyclic pendant groups with a transparent poly(methacrylate) backbone, 193 nm resists with sufficient imaging quality and etch resistance were ultimately realized.[37] Additional effort was directed at systems which incorporate rings directly into the polymer backbone.[38] Examples of both approaches are given in Figure 1.13.

17
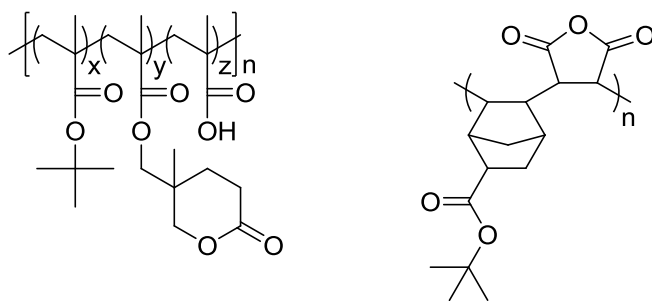
Figure 1.13: Representative 193 nm resists - methacrylate terpolymer (left) and norbornene-alt-maleic anhydride copolymer (right).

193 nm photolithography was adopted for manufacturing in 2001.[39] Through incorporation of techniques such as immersion and multiple patterning, it continues to sustain the industry to this day.[40] While there is again a push to develop higher-resolution patterning techniques, continued wavelength reductions seem increasingly unlikely. The F_2 excimer laser (157 nm) was for a time considered, and great effort was devoted to finding materials suitable for that wavelength.[41, 42] However, it was ultimately shelved by Intel and the rest of the industry quickly followed suit. Similarly, the challenge of extreme-ultraviolet lithography (EUV) increasingly drives researchers to look beyond photolithography in order to sustain Moore's Law. Alternative technologies, particularly directed self-assembly and nanoimprint lithography are enjoying increasing interest. For discussions of next-generation lithography, the reader is directed to several dissertations from this group.[43-45]

INTERCONNECT DELAY

Lithographic challenges aside, there exists another obstacle to improving computing power. While constant decreases in feature size have reduced semiconductor gate delay, complications arise when trying to efficiently interconnect the many billions of gates in a modern microprocessor. Increasing the density of transistors necessarily

18

requires increasing the density of the many wiring levels joining them; individual wires must be made smaller and packed closer together. This has two negative effects. First, the electrical resistance of a given pathway increases with decreasing cross-sectional area. Second, capacitance between adjacent lines increases as their spacing is reduced. These problems are manifest as interconnect delay, which is directly proportional to the resistance and capacitance. In older architectures (features >1 micron), this is negligible relative to intrinsic gate delay (Figure 1.14).[46] However, for smaller features the effect of interconnect delay becomes pronounced, eventually dominating device performance.
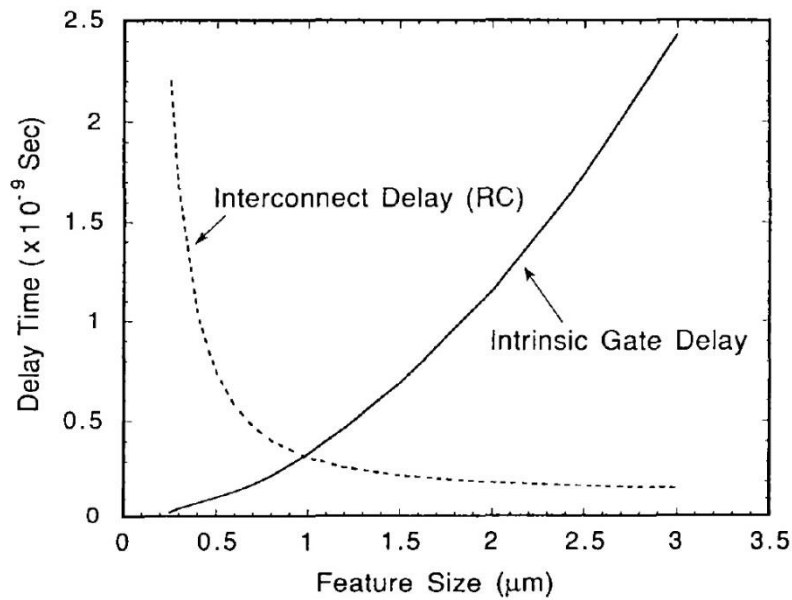
Figure 1.14: Scaling of gate delay and interconnect delay with device dimensions. Reproduced with permission from Jeng, *et al.*[46]

There are several ways to combat this problem. Designs which reduce interconnect length through use of hierarchical wiring levels have proven particularly effective.[47] But to the chemist, this challenge presents great opportunity for materials development and innovation. One of the first (and arguably most disruptive) material

changes took place in 1997. Until that point, aluminum served as the primary metal in microelectronics. Among its advantages were low resistivity (28 nΩ·m), compatibility with plasma etching and low cost. Due to the growing problem of interconnect delay, IBM opted to switch to a metal of significantly lower resistivity: copper (17 nΩ·m). However, this change was only realized with great difficulty, as copper cannot be patterned in the same manner as aluminum. Rather than depositing blanket metal and selectively etching to form an isolated line (as in Figure 1.5), copper must be electroplated into a preformed trench to obtain an equivalent structure. This is known as the Damascene process and is the basis for modern interconnects.

To reduce capacitance and its contribution to interconnect delay, researchers focused on new insulating materials. Silicon dioxide had been the standard insulator since planar fabrication was introduced at Fairchild. As with aluminum, silica is well suited to the many processes in semiconductor manufacturing; there exist numerous methods to form and etch SiO_2 films with great control. Furthermore, its thermal and mechanical properties are outstanding. These attributes, along with its low dielectric constant (k=3.9-4.5), contributed to its longevity as the primary insulating material in microelectronics. However, as capacitance became increasingly problematic with scaling, insulators of lower dielectric constant ("low-k dielectrics") were required.[48] Low-k dielectrics were introduced into manufacturing in 2000 with the adoption of fluorine-doped silicon dioxide (F-SiO_2, k=3.8). Continued improvements in doping and the introduction of porosity have reduced dielectric constants in modern insulators to around 2.2.[49] As with feature size, there exists a concerted effort to steadily reduce this value. However, it is unclear what the practical limit will be.

DISSERTATION STRUCTURE

This chapter provides the historical background and concepts upon which this dissertation is founded. The remainder of the document focuses on materials intended for use in lesser known areas of microelectronics. Unlike photoresists, the polymeric materials described herein are intended to serve as functional components of a complete device. Therefore, emphasis will be placed on issues pertaining to device compatibility, in addition to photopatternability. Chapter 2 discusses efforts at improving the stability of nonlinear optical polymers, materials which are critical for the adoption of chip-scale optical interconnects. Chapter 3 details the synthesis of photobase generators intended for the direct patterning of polyimide dielectric materials. Finally, chapter 4 describes the evaluation of directly patternable low-k polyimides for use in integrated circuit packaging.

Chapter 2: Photocrosslinkable Nonlinear Optical Polymers[1]

INTRODUCTION TO NONLINEAR OPTICS

Nonlinear optics concerns the study of optical phenomena unique to dielectric media which are nonlinear. Specifically, "nonlinear" refers to the polarization of the medium in response to an applied electromagnetic field. For linear behavior, the molecular polarization response p is described according to equation 2.1:

$$p = p_0 + \alpha E \qquad (2.1)$$

Where p_0 is the molecular dipole moment, α is the microscopic linear polarizability and E is the electric field vector.[50] This can be extended to bulk materials as:

$$P = P_0 + \chi^{(1)} E \qquad (2.2)$$

Here P_0 is the static dipole moment and $\chi^{(1)}$ is the macroscopic linear polarizability, which relates to a material's index of refraction and absorption. However in the presence of an extremely intense optical field, behavior may begin to deviate significantly from that shown above. The molecular polarization of must instead be described by:

$$p = p_0 + \alpha E + \beta EE + \gamma EEE + \cdots \qquad (2.3)$$

Where β and γ are the chromophore first and second order hyperpolarizabilities, respectively.[50] As with linear polarization, nonlinear behavior can be applied bulk media according to equation 2.4:

---

[1]Brandon Rawlings performed the SHG measurements. Brian Long developed the polymer synthesis. Chad Webb and Keith Keitz assisted with the polymer synthesis. C. Grant Willson supervised the work.

$$P = P_0 + \chi^{(1)}E + \chi^{(2)}EE + \chi^{(3)}EEE + \cdots \qquad\qquad (2.4)$$

$\chi^{(2)}$ and $\chi^{(3)}$ are the first and second order nonlinear susceptibilities, which give rise to second and third order nonlinear optical phenomena, respectively.[50] The field of nonlinear optics traces its roots to the development of the laser in 1960. This invention allowed for the generation of optical fields of sufficient intensity that the contribution of the higher order terms becomes measureable. There are many interesting effects in nonlinear optics, but for the purposes of this chapter, discussion will be limited to two second-order processes: second harmonic generation (SHG) and the electro-optic (EO) effect.

Second harmonic generation was first observed in 1961.[51] Researchers found that irradiation of quartz with 694 nm light from a ruby laser produced an emission at twice the laser frequency (347 nm). Famously, the faint second harmonic, which was recorded on photographic paper using a spectrometer, was mistaken for a speck of dirt and removed from the published figure.[52] Initially a scientific curiosity, SHG eventually found widespread practical use in the form of diode-pumped solid-state frequency doubled lasers. In this application, an infrared laser diode is used to pump a lasing crystal (commonly Nd:YAG) which emits light at 1064 nm.[53] This light is then passed through a crystalline nonlinear optical material such as potassium titanyl phosphate (KTP) to produce light with a wavelength of 532 nm. This is employed in green laser pointers, where direct generation of green light is generally impractical.

Of greater interest for electronics applications is the electro-optic effect, which is the variation of a material's refractive index proportionally with an applied electric field. This effect allows for design of devices which modulate optical signals in phase, polarization, or amplitude. A common example of such a modulator is a built around a Mach-Zehnder interferometer, in this case fabricated from an electro-optic material

(Figure 2.1). In the illustration, light is coupled into the waveguide at left and is split between the two pathways. The top arm is surrounded by an electrode which allows a voltage to be applied across the beam path. The applied voltage increases the refractive index of the material, thereby slowing the propagating wave. At a specific voltage (V_π), half-wave phase delay is achieved and the two waves will recombine destructively, suppressing the output at the right. In this way, rapid amplitude modulation of a continuous wave (CW) optical source is achieved.
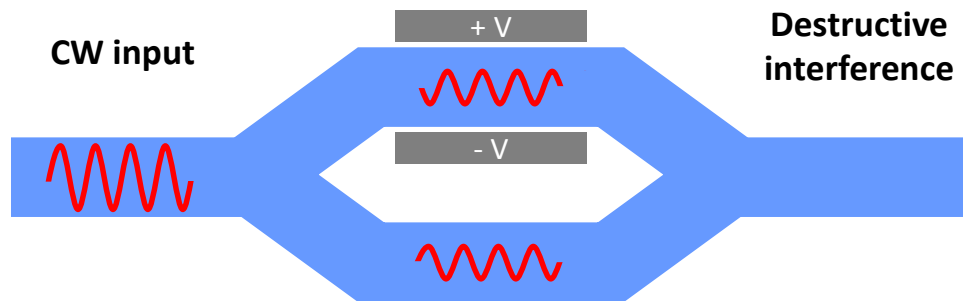
Figure 2.1: Illustration of a Mach-Zehnder EO modulator for the case of a half-wave phase delay in the top arm.

This effect is currently employed at the interface of electronic and optical communications (i.e. fiber-optic signal transduction). As fiber-optic communication continues to expand, this interface is being pushed closer to the end user, with the fiber-to-the-home (FTTH) model taking this trend to its logical conclusion. In this situation, affordable and efficient electro-optic modulators must be widely available. Furthermore, the realization of chip-scale optical interconnects and the promise of reduced interconnect delay first requires improvements in modulator size and efficiency.[6, 54] This, in turn, requires materials with improved electro-optic coefficients. However, designing for large

EO coefficients is no small task, as it involves considerable optimization at both the microscopic and macroscopic levels.

In order for a material to exhibit second-order nonlinear optical effects (e.g. SHG, EO effect) it must be noncentrosymmetric—that is, it must lack an inversion center. A symmetric molecule such as benzene exhibits a linear polarization in the presence of an oscillating electric field (Figure 2.2). However if the molecule possesses a net dipole moment, the polarization response is affected by its electronic structure. Such a material is exemplified by p-nitroaniline, which contains an electron-rich donor opposite an electron withdrawing acceptor. For the case illustrated below, its nonlinear response is the sum of the fundamental (linear) polarization, the second harmonic, and a DC field component.[50]
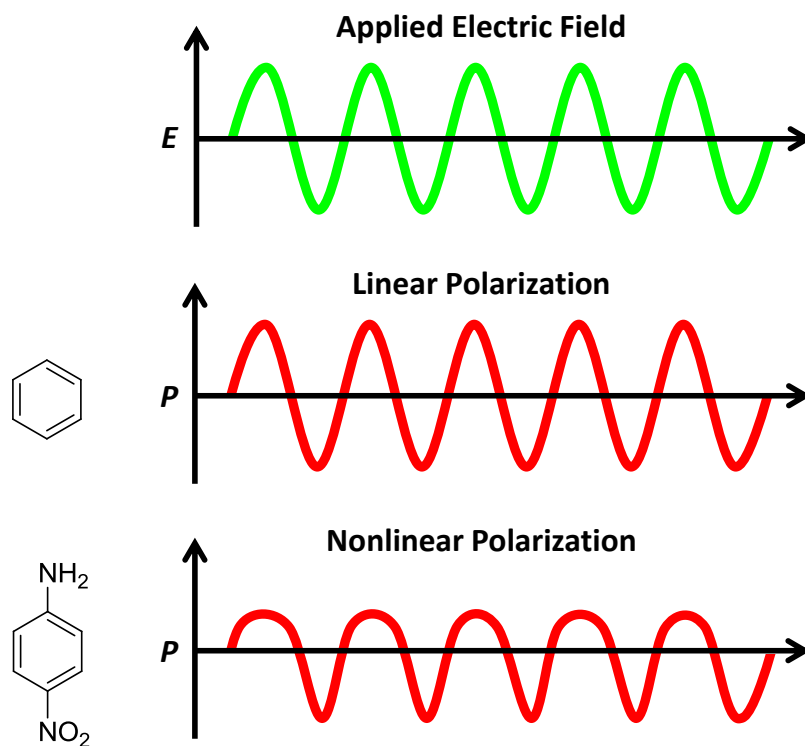
Figure 2.2: The polarization *P* of benzene and p-nitroaniline in response to an electric field *E*.

Noncentrosymmetry is needed only for even-order terms. Third-order (χ^3) phenomena such as the Kerr effect do not share this requirement. The primary difficulty is *not* finding a material with a large dipole moment, as the synthetic chemist will be quick to envision many such molecules. Rather, the challenge lies in converting an ensemble of the molecular dipoles into a material with bulk noncentrosymmetry.

This need is met by certain crystalline materials that possess noncentrosymmetric unit cells. While quartz was already named as a material which exhibits second-harmonic generation (and is therefore noncentrosymmetric), a clearer example is lithium niobate (Figure 2.3). Here, the lithium atoms are displaced slightly in the vertical direction relative to niobium and oxygen.[55] Lithium niobate is among the most common nonlinear optical materials and is the basis of most commercial EO modulators.[56] Its excellent thermal stability, transparency at telecommunications wavelengths (near IR) and intermediate electro-optic coefficient (~30 pm/V) all contribute to its continued popularity.
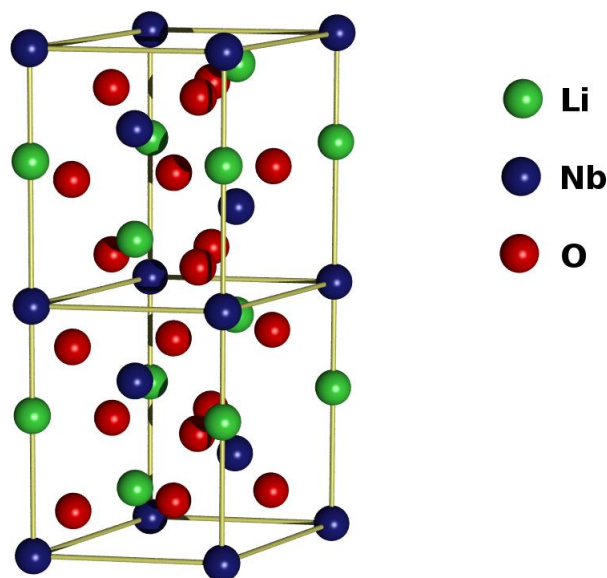
Figure 2.3: Hexagonal Lithium Niobate (LiNbO$_3$) unit cell. Reprinted from Hellwig.[57]

NONLINEAR OPTICAL POLYMERS

While there are many classes of nonlinear optical materials, polymers are of particular interest due to their compatibility with thin-film fabrication methods. Numerous devices have been demonstrated using such materials.[6, 7, 58-61] Additionally, NLO polymers promise superior electro-optic (EO) coefficients and thus greater modulation efficiencies than their crystalline counterparts.[62] However, while crystalline NLO materials benefit from intrinsic noncentrosymmetry, polymers must be processed in a manner which imparts long-range order to individual dipole moments. The most common approach to this is electric field poling, where dipoles are oriented using a strong electric field. This is generally performed by contact poling, where a polymer film is sandwiched between two electrodes to form a capacitor (Figure 2.4). To allow individual dipoles sufficient mobility to orient in the field, the polymer must be near or above its glass transition temperature.

A typical process flow involves deposition of a polymer film on a transparent conductor (e.g. ITO), which serves as the bottom electrode. A second electrode is then deposited on the film surface. The electrodes are connected to a voltage source and the film is heated to near the glass transition temperature. Once near T_g, a voltage is applied and the dipoles are gradually aligned as depicted in Figure 2.4. After poling is complete, the field is maintained while the film is cooled to room temperature. Once the film is cooled, the field is then removed. As segmental motion is significantly restricted below T_g, the resulting dipolar order is relatively stable. The thermal stability of this poled order is a key consideration in NLO polymers and will be discussed in greater detail shortly.
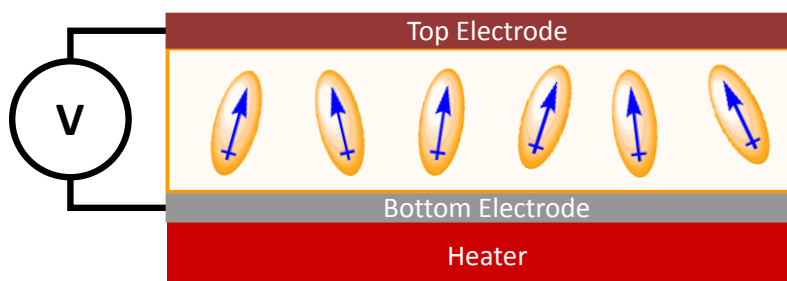
Figure 2.4: Contact poling of an NLO polymer film.

Though contact poling allows application of a uniform field over a wide area, dielectric breakdown can occur at higher voltages. For most polymers this takes place at field strengths above 100 V/μm, but the presence of film defects can dramatically reduce the damage threshold.[63] As such, contact poling requires very high quality films. A second technique, which is generally more forgiving of defects, is corona poling (Figure 2.5). In this scheme, the top electrode is replaced with a thin needle suspended several centimeters above the film. A very high voltage (~4-5 kV) is applied, producing a corona discharge at the needle tip. The resulting ions settle on the film surface and behave analogously to the top electrode in Figure 2.4. The key advantage of corona poling is its tolerance of film defects; it is not susceptible to shorting in the same manner as contact poling.[64] However, the field strength is more difficult to control, leading to some variability between corona poled samples.
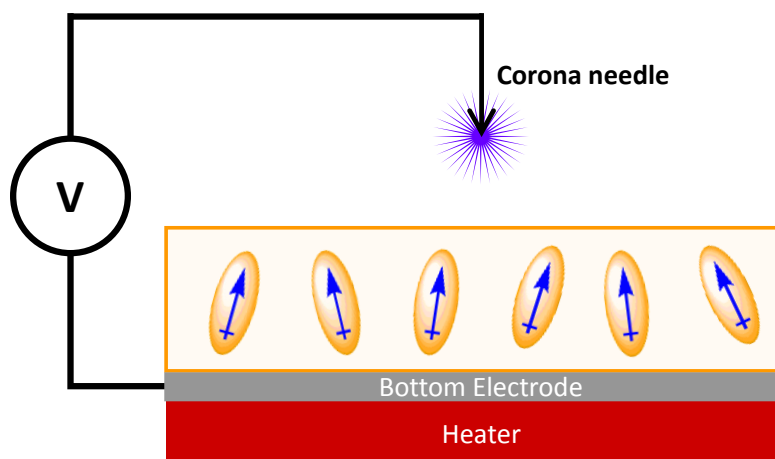
Figure 2.5: Corona poling of an NLO polymer film. The corona discharge is indicated in purple.

MOLECULAR NONLINEARITY

Historically, the study of organic nonlinear optical materials focused on maximizing molecular hyperpolarizability (β). This is unsurprising, as the long-held advantage of organics, especially poled polymers, is the potential for very high NLO coefficients ($r_{33} > 100$ pm/V).[62] For most organic NLO materials, the dipoles comprise extended pi systems, which are broken down into three design elements. In the case of p-nitroaniline these are: an electron-rich donor (amino), an electron-deficient acceptor (nitro), and a conjugated system linking the two (phenyl). The design of more advanced NLO chromophores will be discussed, examining each of these components in greater detail. Note that the figure of merit for microscopic nonlinearity is the product of a molecule's first hyperpolarizability and dipole moment—$\mu\beta$.

Donors

The most common donors are substituted amines, typically aniline derivatives. Dialkyl anilines (Figure 2.6a) are particularly popular, both for their electron donating ability and their widespread commercial availability. Additionally, the alkyl chains may

serve as a site for further functionalization of the chromophore. Diaryl anilines (Figure 2.6b) offer greatly improved thermal stability. However, due to further delocalization of the nitrogen lone pair, this stability is realized only at the expense of hyperpolarizability.[65] Solubility is also generally reduced. Alkoxy-substituted derivatives (Figure 2.6c) provide an effective balance of stability and hyperpolarizability, but are significantly more difficult to synthesize.[66] Other modifications include attachment of bulky substituents to restrict molecular motion (Figure 2.6d), as well as use of heteroaromatic substituents in place of phenyl groups (not shown).[66, 67]
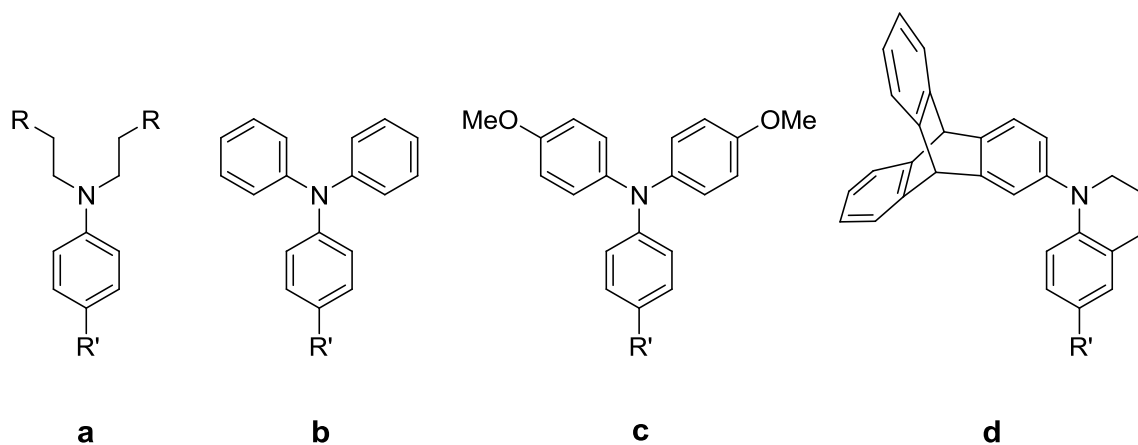
Figure 2.6: Selected aniline donors.

Bridges

Electronic communication between the donor and acceptor is facilitated by a pi bridge. As β is related to both the molecular dipole and the energy of HOMO-LUMO gap, it is generally desirable to maximize effective bridge length.[68] By shifting the HOMO-LUMO transition closer to the wavelength of interest, polarizability can be dramatically enhanced.[69] Unfortunately, there are several drawbacks which limit this approach. Due to optical loss, a λ_{max} at the device wavelength is obviously unacceptable.

Standard communication wavelengths are 1.3 and 1.55 microns, so the material must be transparent in this region. A related issue is chromophore stability. While driving the electronic transitions of a material to lower energies will result in enhanced nonlinearity, it will also dramatically increase its reactivity. The result is a stability/hyperpolarizability tradeoff similar to that encountered in donor optimization, but with much greater effect on both $\mu\beta$ and chromophore decomposition.[70]
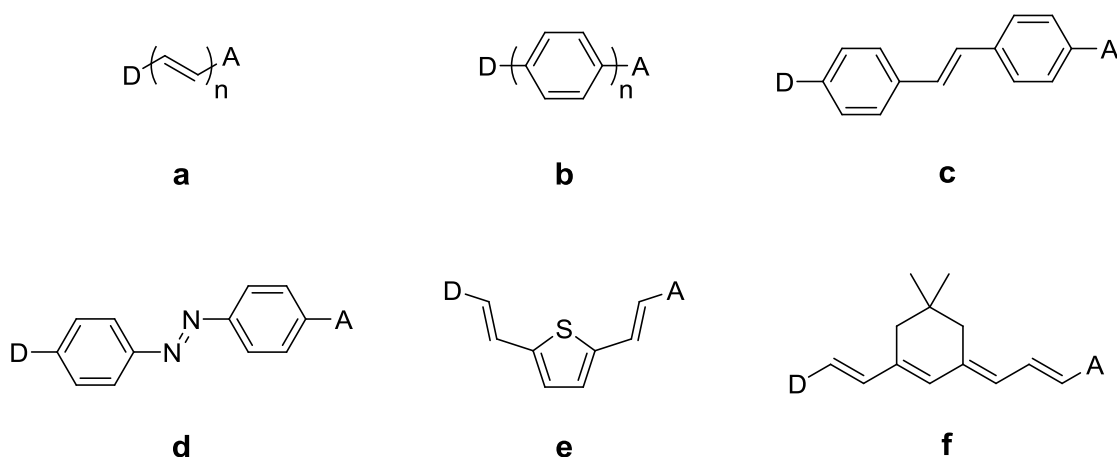
Figure 2.7: Selected bridges: polyene (a), polyphenylene (b), stilbene (c), azobenzene (d), thienylvinylene (e), and ring-locked tetraene (f).

Early research focused on simple polyene systems (Figure 2.7a), in some cases demonstrating a quadratic scaling of β with bridge length.[71-74] Practical application of these proved impossible, as they are prone to rapid degradation. Polyphenylene bridges (Figure 2.7b) alleviate this to a degree, but invariably result in diminished NLO activity.[73] Polarization requires disruption of aromaticity in these systems and is thus significantly more difficult. Additionally, the effective conjugation length is no more than n=2, limiting bridge length. Hybrid approaches such as stilbenes (2.7c), azobenzenes (2.7d) and tolanes (not shown) have also been studied, generally offering intermediate values of

stability and nonlinearity.[50] The thienylvinylene bridge (2.7e) takes this concept a step further by reducing the aromaticity of the intervening rings.[75] This is one of the most popular chromophores, as it combines high nonlinearity with adequate thermal and photochemical stability.[59, 60, 76]

To date, the most potent NLO materials are based on the ring-locked tetraene bridge (Figure 2.7f).[62] For a given donor/acceptor combination this yields values of $\mu\beta$ nearly twice that of the thienylvinylene bridge.[77] Because of this, significant effort has been devoted to improve the thermal and photochemical stability of these species. Specifically, by substituting the 2-position of the isophorone ring, the reactivity of the bridge towards dienophiles can be reduced.[78, 79] This is particularly important when considering photodegradation, where singlet oxygen is the primary reactive species.[80]

Acceptors

Of the three structural components, acceptors have undergone the most refinement since the advent of organic NLO materials. Early acceptors were simple electron-withdrawing substituents such as the nitro, nitrile, or sulfone functional groups. While synthetically accessible, it was quickly recognized that the overall efficacy of these was quite limited. More potent systems were realized in the form of the dicyanovinyl (Figure 2.8c) and tricyanovinyl chromophores, but these suffer from limited thermal stability.[81] Isoxazolones (Figure 2.8d) eventually addressed this issue, though $\mu\beta$ values remained fairly modest.[82] However, this indicated a general move away from unprotected multi-cyanovinyl acceptors.
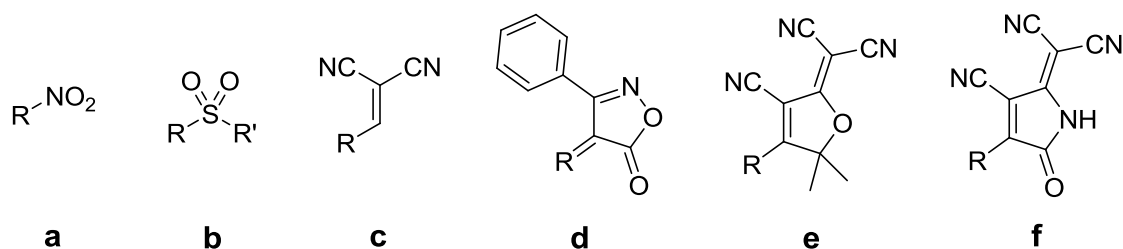
Figure 2.8: Selected acceptors: nitro (a), sulfone (b), dicyanovinyl (c), isoxazolone (d), tricyanofuran (e), and tricyanopyrroline (f).

The tricyanofuran (TCF, Figure 2.8e) and tricyanopyrroline (TCP, Figure 2.8f) acceptors exemplify this trend, combining thermal stability with unparalleled electron-withdrawing ability.[62, 83] The TCF has enjoyed particular success, quickly becoming the standard acceptor following its adaptation to the field.[60, 75] Materials employing this acceptor have demonstrated $\mu\beta$ values exceeding 10,000 x 10^{-48} esu and excellent thermal stability (T_d > 300 °C).[81] Surprisingly, synthesis of this structure is somewhat trivial, as it involves a one-pot reaction of an alpha-hydroxyketone with two equivalents of malononitrile.[84] Because of this, many TCF derivatives have been studied.[76, 85-87] The most notable modification has been the incorporation of a trifluoromethyl group in the 5-position of the furan (CF$_3$-TCF), which has further increased β.[69] However, significant deviation from the original TCF structure has led to dramatic decreases in synthetic yield (e.g. <25% for CF$_3$-TCF).[85, 88] Figure 2.9 shows a complete NLO chromophore employing a modified TCF acceptor, as well as several design elements discussed in the preceeding sections.

33
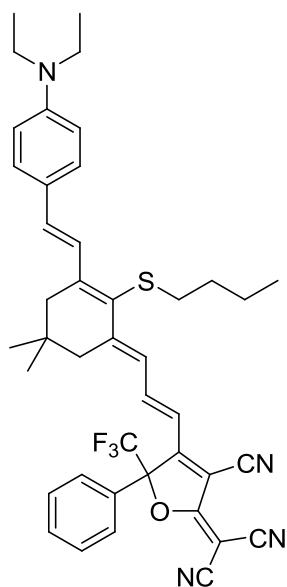
Figure 2.9: A high-β tetraene chromophore with enhanced photostability.[79]

MACROSCOPIC NONLINEARITY

Conversion of molecular nonlinearity into a useful bulk material property requires an appropriate host matrix. Early materials consisted of small molecule chromophores doped into a transparent host polymer. Due to its simplicity, this so-called guest-host approach remains popular for studying new chromophores. However for NLO devices, where processability and thermal stability are key considerations, this approach is being replaced with other methods. Note that in this specific context "thermal stability" refers not to chemical decomposition, but the loss of bulk noncentrosymmetry through chromophore reorientation. This typically occurs at temperatures well below the chromophore T_d. Efforts to stabilize noncentrosymmetric order have focused on restricting chromophore motion post-poling. Unfortunately most of these techniques also restrict chromophore mobility during poling, thereby limiting attainable bulk nonlinearity. This "nonlinearity-stability tradeoff" significantly limits the use of poled polymers in high temperature applications.[81]
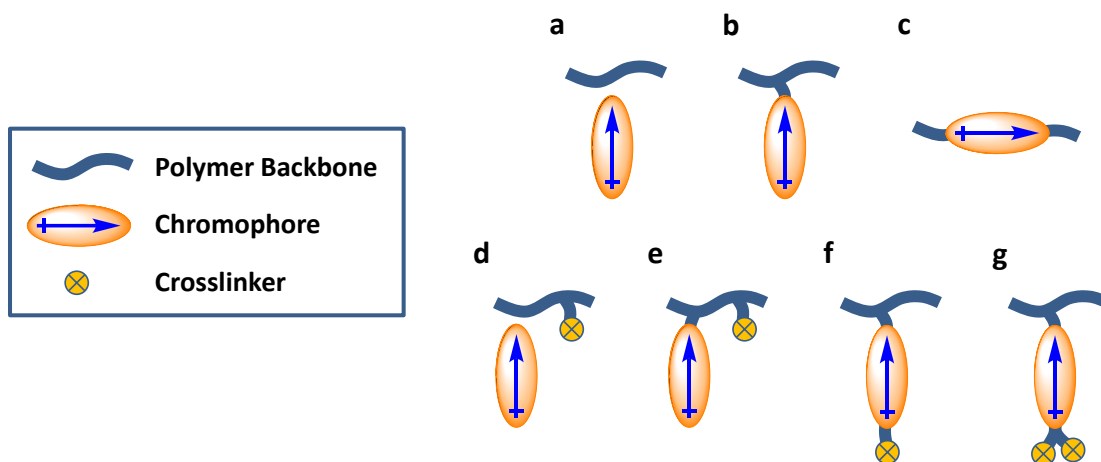
Figure 2.10: Common NLO polymer designs: guest-host (a), pendant chromophore (b), main-chain chromophore (c), guest-host in a crosslinkable matrix (d), pendant chromophore in a crosslinkable matrix (e), crosslinkable pendant chromophore (f), doubly-crosslinkable pendant chromophore (g).

Guest-host

One of the first poled polymers consisted of 2 weight percent 4-dimethylamino-4'-nitrostilbene (DANS) doped into a liquid crystalline poly(methacrylate).[89] Thermal stability is dictated by the host polymer T_g, though relaxation can be significant below this temperature. This is problematic as much higher chromophore loadings (often >20 wt%) are required, resulting in plasticization and a decreased in T_g.[90] Further complications include aggregation and phase separation of chromophores from the host matrix.[91] Despite these difficulties, this approach is commonly employed both in basic research and device construction. Improved stability is realized by using host materials with much higher glass transition temperatures (<150 °C), such as polycarbonates and polyimides.[62, 70, 92] For electro-optic modulators used in telecommunications, thermal requirements are relatively mild (<10% loss at 85 °C for 25 years).[93] This is readily met using high-T_g polycarbonate hosts. However, the thermal requirements for microelectronics applications are more stringent, with operating temperatures

approaching 100 °C.[14, 94] Additionally, excursions to even higher temperatures (200-300 °C) will take place during device fabrication, making guest-host polymers impractical for these applications.

Covalent Incorporation

Chromophore motion can be further reduced by direct attachment to the polymer backbone (Figure 2.10b), which largely eliminates relaxation below T_g. A comparison of side-chain and guest host stability is shown in Figure 2.11. Singer *et al.* monitored the relative intensity of second harmonic generation in both systems over a span of several weeks.[95]   The guest-host material consisted of 4-(dicyanovinyl)-4'-(dialkylamino)azobenzene blended with PMMA (DCV/PMMA), while the side-chain material employed the same chromophore as a pendant group on a methacrylate backbone (DCV-MMA). In this study, the pendant chromophore demonstrated excellent long-term stability at room temperature. Covalent attachment also avoids the phase separation issues endemic to guest-host materials.[96] Main-chain systems (Figure 2.10c) take this approach to the extreme, further restricting chromophore motion by incorporating it directly into the polymer backbone.[97-99]
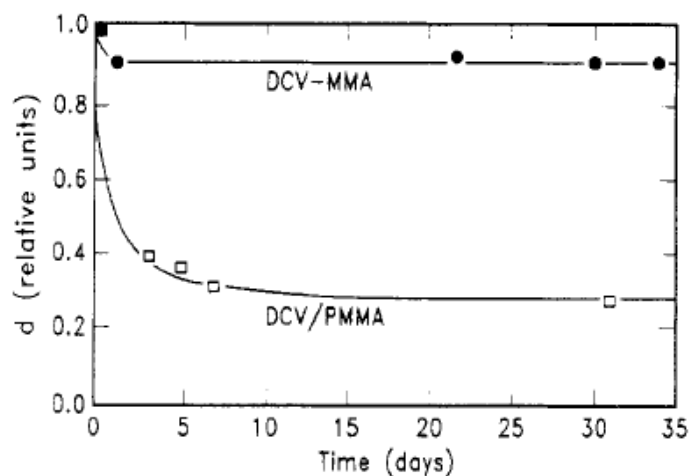
Figure 2.11: Comparison of guest-host and pendant NLO polymer thermal stabilities. Reprinted with permission from Singer *et al.*[95] Copyright 1988, American Institute of Physics.

As with guest-host materials, higher temperatures will lead to rapid decay if the polymer undergoes a glass transition. Using very high T_g materials (e.g. polyimides), very impressive long term stability has been demonstrated above 200 °C.[100, 101] While meeting thermal requirements, such polymers are extremely difficult to pole. By limiting chromophore motion, alignment is restricted, as well as relaxation. In the absence of a lattice-hardening step, little can be done to avoid the nonlinearity-stability tradeoff.

Crosslinking

The introduction of crosslinkable groups offers the possibility of avoiding this dilemma by first poling at a low temperature, then crosslinking to greatly increase thermal stability.[69, 70, 81] There are many variations on this approach (Figure 2.10d-g), with crosslinkable pendant chromophores (Figure 2.10f, g) enjoying the most success. These double-end crosslinkable (DEC) systems are particularly popular, as they offer the same advantages as main-chain chromophores without the associated poling difficulties. A key challenge of crosslinking in NLO polymers is maintaining control over the onset of

37

crosslinking, so as not to interfere with the poling process. Additional considerations include crosslinking conversion, as well as the stability of the chromophores to the crosslinking chemistry.

There exists a large body of literature describing NLO materials which employ traditional thermoset chemistry (e.g. epoxides, urethanes).[102-109] Due to the highly reactive nature of these materials, significant crosslinking can occur at lower temperatures, even prior to poling. This greatly limits control over the process and these have been replaced by other functional groups. More effective thermal crosslinkers have been demonstrated, employing azide-alkyne and fluorovinyl ether cycloaddition reactions.[58, 77, 110-112]

Recent efforts have focused on Diels-Alder crosslinking reactions, which, combined with careful chromophore design, offer surprising compatibility with high-β chromophores.[69] A particularly interesting approach leverages the thermal reversibility of the Diels-Alder reaction (Figure 2.12).[113, 114] Using furan-protection of the maleimide dienophile, the crosslinking reaction with anthracene is inhibited. The material can be cast and poled, then heated to its cycloreversion temperature to remove the protecting group. This allows for improved control, but requires a cycloreversion temperature slightly above the poling temperature. Additional work has focused on tuning these reactions in order to optimize the curing temperature.[14] Using DA crosslinking in a maleimide-α-methylstyrene copolymer (T_g: 215 °C), excellent long-term stability was demonstrated at 150 °C.[94]
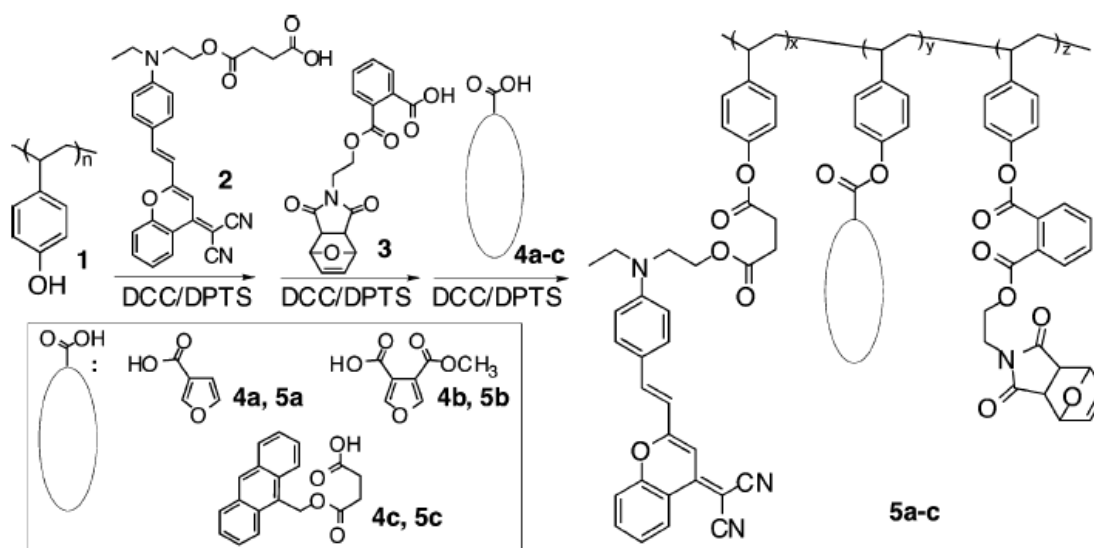
Figure 2.12: Use of furan protecting group to control Diels-Alder crosslinking. Reprinted with permission from Haller *et al.*[114] *Copyright 2004, American Chemical Society.*

Photocrosslinking offers the possibility of completely separating the poling and crosslinking processes, and is the subject of the remainder of this chapter. Comparatively few instances of photocrosslinkable NLO polymers are found in the literature.[49, 115-119] Fewer still have demonstrated significant stability gains in the crosslinked state.[119] A major challenge for photocrosslinking is effective photoinitiation, as NLO materials are strongly absorbing and generally photosensitive. The objective of this work is to apply photocrosslinking to a series of side-chain polymers (Figure 2.10b, f, g), and further demonstrate stability at temperatures *above* the initial T_g.

POLYMER DESIGN

In an ideal NLO polymer, poling would take place at a relatively low temperature. This would be followed by a distinct crosslinking step which would raise the thermal stability beyond the initial T_g. Unfortunately, crosslinking has resulted in modest stability gains relative to polymer T_g, and the most successful approaches still employ

39

high T_g backbones[94, 107, 119-121]   It has been proposed that this results from limited interchain crosslinking and that a second crosslinker will further improve thermal stability.[122] In the case of intrachain crosslinking, the material may still be capable of the cooperative motion required for relaxation, as this merely requires rotating segments of the polymer backbone (Figure 2.13). However, if the chromophore can be incorporated at both ends into an interpenetrating network of multiple polymer chains, relaxation should be greatly hindered.
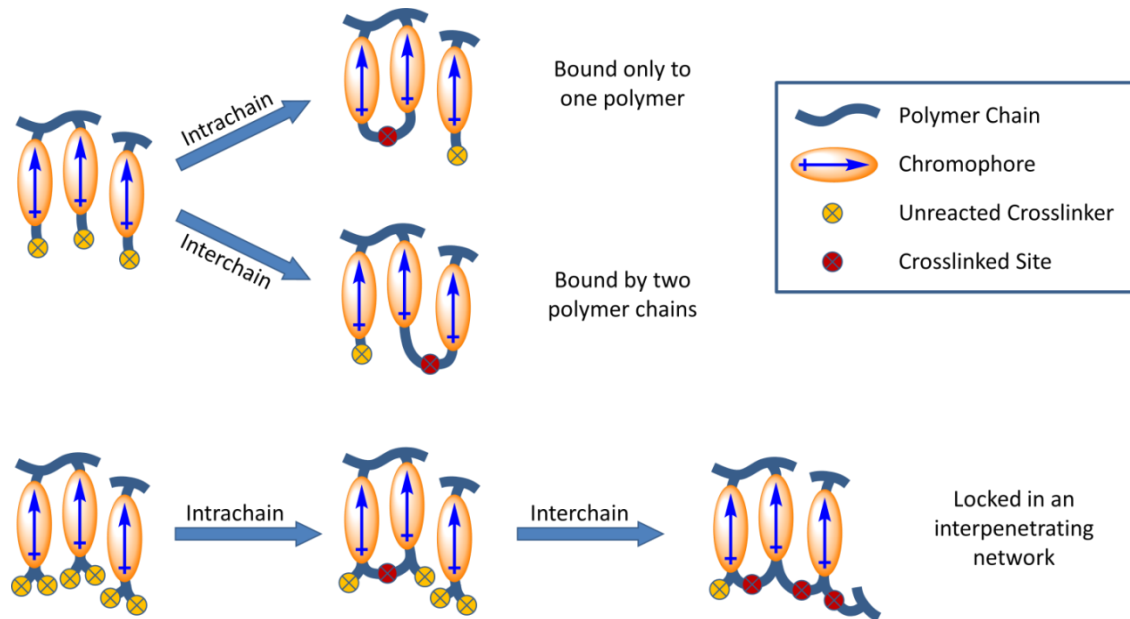
Figure 2.13: Illustration of several possible outcomes when crosslinking pendant NLO polymers.

To evaluate this, side-chain NLO polymers with varying crosslinker substitution were designed according to Figure 2.13. The methacrylate crosslinker was selected due to the availability of radical photoinitiators over a wide spectral range, ideally allowing for initiation at a wavelength the NLO chromophore does not absorb. The design further calls for a material which does not require post-polymerization modification, and

40

therefore the polymerization reaction cannot affect the crosslinker groups. Ring-opening metathesis polymerization (ROMP) has demonstrated excellent functional group tolerance, and is therefore well-suited to this approach.

As this study is concerned only with testing the design concept, synthetic accessibility was emphasized over molecular hyperpolarizability when selecting a chromophore. While dialkylanilines remain the most common donors, the sulfone acceptor has been largely replaced by the more potent acceptors discussed previously. For our purposes, the sulfone was chose due to its ease of attachment to the polymer backbone; advanced acceptors such as the TCF and TCP are generally difficult to functionalize.[119, 123] Likewise, the tolane bridge was selected because it is readily prepared using Sonogashira coupling chemistry, and is anticipated to be more resistant to photodegradation than polyenes.
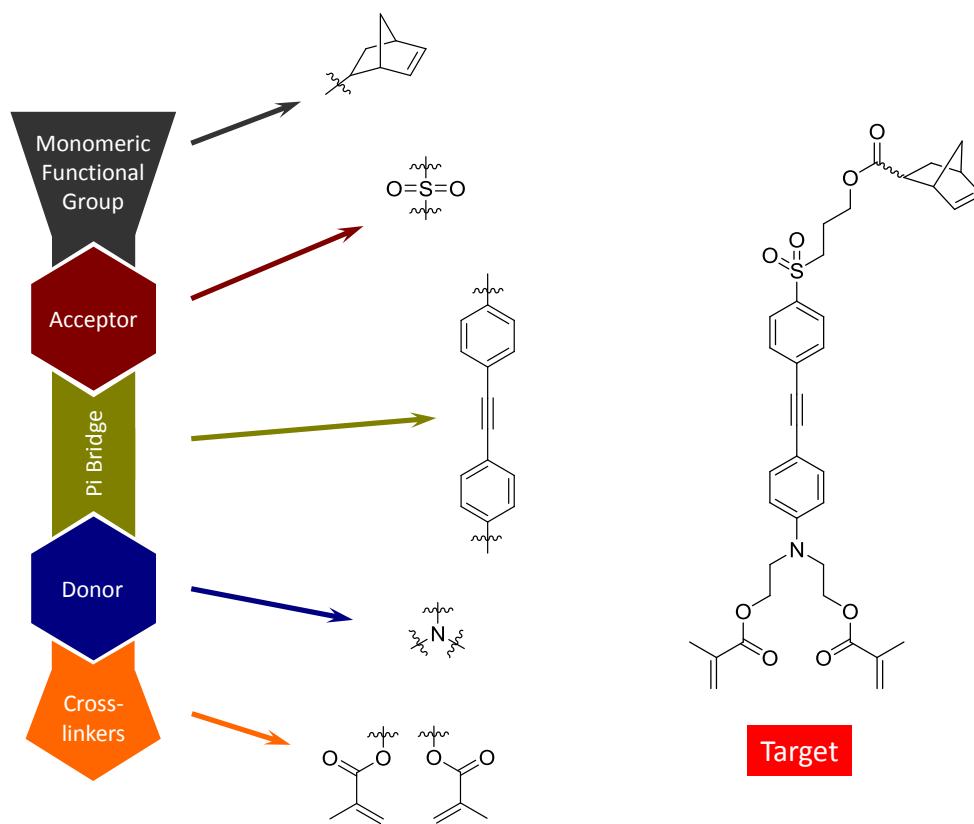
Figure 2.14: Illustration depicting key monomer components, with the completed doubly-crosslinkable monomer as an example.

This monomer can be approached retrosynthetically as two fragments, dividing in the middle of the pi bridge. Synthesis of the acceptor fragment **2.4** is shown in Figure 2.15, beginning with the alkylation of p-bromothiophenol. Oxidation forms sulfone **2.3**, which is subsequently esterified with 5-norbornene-2-carboxylic acid to complete **2.4**
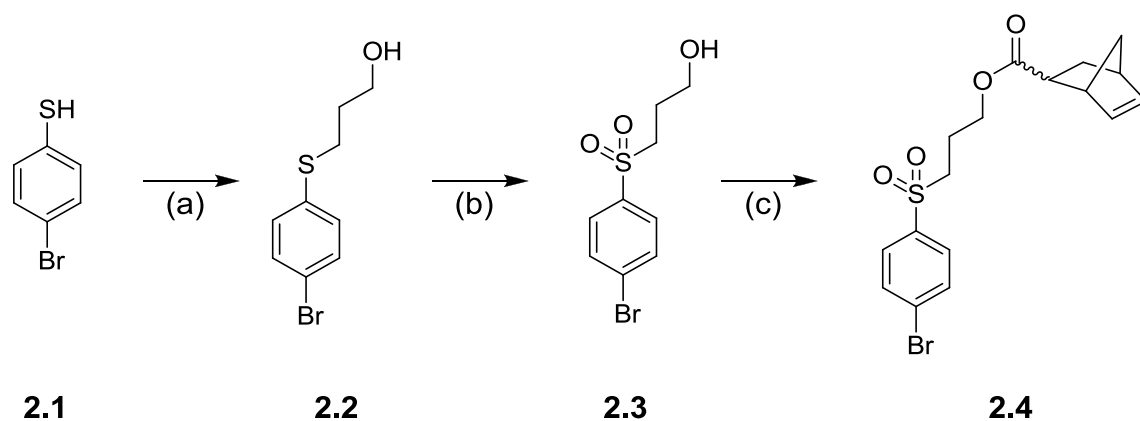
Figure 2.15: Synthesis of 2.4. Reagents and conditions: (a) (i) NaH, THF; (ii) 3-bromopropanol, THF. (b) (i) 30% H_2O_2, HOAc, reflux; (ii) NaOH, MeOH, 90 °C. (c) 5-norbornene-2-carboxylic acid, DCC, DMAP, TEA, DCM.

Three distinct donor fragments were employed, with functionality varying according to the desired number of crosslinkers. All were prepared using the same general route, but optimal conditions varied slightly with functionality. For brevity, **2.8c** is given as a representative example (Figure 2.16). Detail on the synthesis of the remaining two fragments can be found in the experimental section, as well as the original report.[124] Synthesis of **2.8c** began with the iodination of N-phenyldiethanolamine, thereby installing the requisite functionality for the subsequent Sonogashira coupling with trimethylsilylacetylene. Compound **2.7c** was then deprotected to obtain the free alkyne **2.8c**.
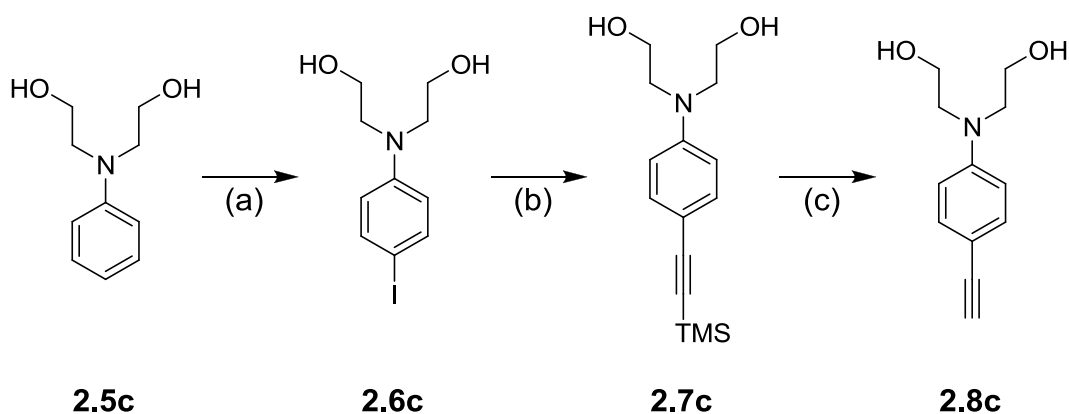
Figure 2.16: Synthesis of 2.8c. Reagents and conditions: (a) ICl, HCl (b) trimethylsilylacetylene, Pd(PPh$_3$)$_2$Cl$_2$, CuI, TEA, THF, 60 °C. (c) K$_2$CO$_3$, MeOH.

The donor and acceptor fragments were then cross-coupled in a second Sonogashira reaction, yielding tolanes **2.9a-c** (Figure 2.17).   This was followed by methacrylation to complete the series of monomers **2.9a, 2.10b, 2.10c**. Ring-opening metathesis polymerization (Figure 2.18) yielded polymers **2.11-2.13**, low T$_g$ materials of intermediate molecular weight (Table 2.1).   In the case of both crosslinkable polymers, NMR analysis confirmed that the methacrylates were unaffected during polymerization.
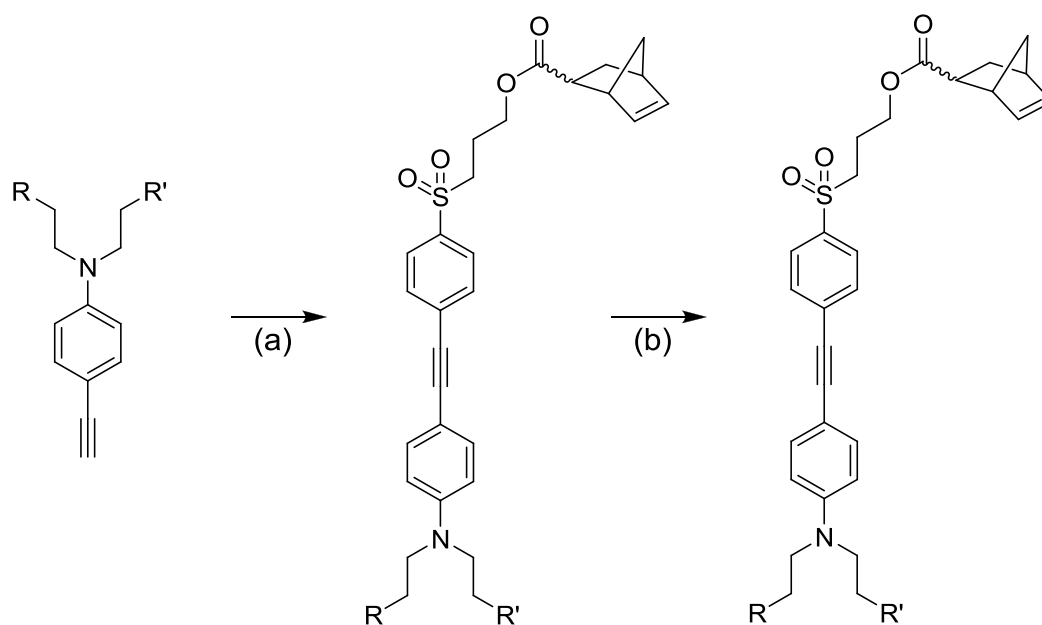
2.8a, R = R' = OAc   **2.9a**, R = R' = OAc
2.8b, R = OH, R' = H   **2.9b**, R = OH, R' = H   **2.10b**, R = OMac, R' = H
2.8c, R = R' = OH   **2.9c**, R = R' = OH   **2.10c**, R = R' = OMac

Figure 2.17: Synthesis of monomers 2.9a, 2.10b, and 2.10c. Reagents and conditions: (a) 2.4, Pd(PPh₃)₂Cl₂, CuI, TEA, THF, 60 °C. (b) methacryloyl chloride, TEA, DCM. (c) (i) Grubbs II, DCM; (ii) ethyl vinyl ether.

2.9a, R = R' = OAc   **2.11**, R = R' = OAc
2.10b, R = OMac, R' = H   **2.12**, R = OMac, R' = H
2.10c, R = R' = OMac   **2.13**, R = R' = OMac
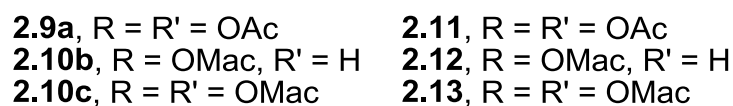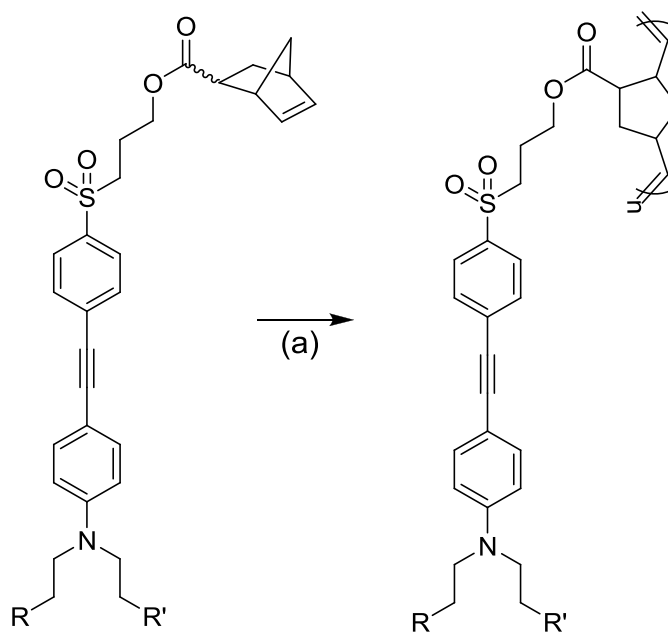
Figure 2.18: Polymerization of monomers 2.9a, 2.10b, and 2.10c. Reagents and conditions: (a) (i) Grubbs II, DCM; (ii) ethyl vinyl ether.

Polymer	M_n (kDa)[a]	PDI[a]	T_g (°C)[b]
2.11	33	1.59	76
2.12	52	1.62	71
2.13	59	1.90	60

Table 2.1: Selected polymer properties. [a]By GPC with polystyrene standards. [b]By DSC.

PHOTOCROSSLINKING

Previous work demonstrated that **2.12** and **2.13** crosslink upon exposure with ultraviolet light, even in the absence of photoinitiator. While crosslinked films were rendered insoluble, there was no appreciable change in thermal stability of SHG in poled

materials.[124] It was reasoned that the extent of crosslinking was very limited, and that greater attention should be paid to methacrylate conversion. Therefore, crosslinking was examined by FTIR. Useful peaks for the methacrylate functional group are the vinyl C-H bend near 815 cm^{-1} and the C=C stretch at 1635 cm^{-1}.[21, 23] The C-H bend is obscured in **2.12** and **2.13**, so conversion was determined from the 1635 cm^{-1} stretch exclusively (Figure 2.19).
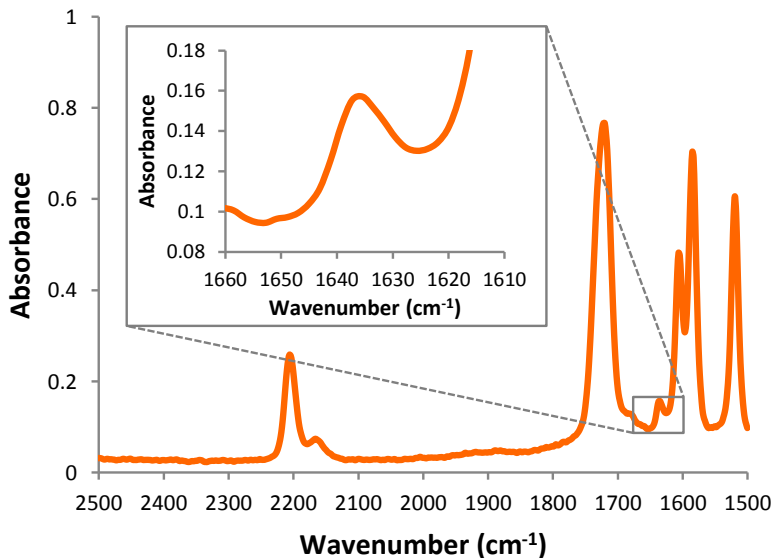
Figure 2.19: IR spectrum of a film of 2.12 with the methacrylate peak expanded.

As anticipated, without photoinitiator the methacrylate peak is largely unchanged by broadband irradiation, even at doses exceeding 5 J/cm^2 (Figure 2.20). Irgacure 819, a commercial near-UV initiator (BASF), was then evaluated. Though obscured by the NLO chromophore absorbance, addition of this compound improved conversion dramatically under the same exposure conditions.

No initiator   **5% Irgacure 819**
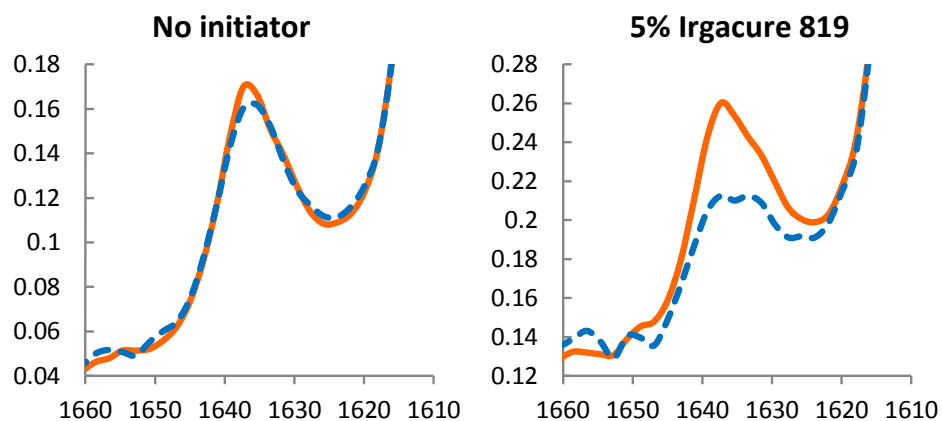
Figure 2.20: Comparison of 1635 cm^{-1} peak in 2.12 films before (solid) and after (dashed) exposure.

As can be seen from Figure 2.20, conversion remains limited even with a relatively high loading of photoinitiator (5 wt%). It was presumed that below T$_g$ the lack of chain mobility limits the extent of crosslinking that can be achieved. To test this, films of **2.13** and Irgacure 819 were irradiated at elevated temperatures (Figure 2.21). As anticipated, conversion increased significantly with heating. Importantly, there was no evidence of reaction in the absence of light, indicating that initiation is purely photochemical.
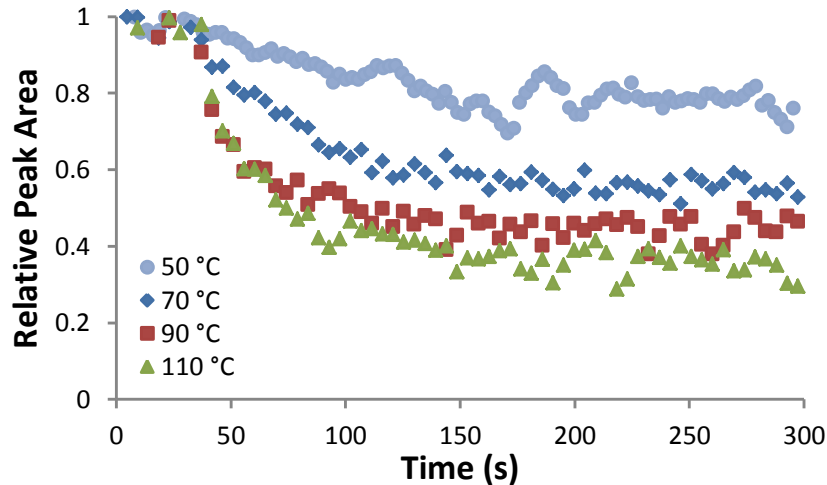
Figure 2.21: Effect of temperature on methacrylate conversion in 2.13 with 5 wt% Irgacure 819 under broadband UV irradiation (intensity $= 25$ mW/cm^2). Exposure begins at 30 seconds.

Initially, we hoped to demonstrate the complete separation of the poling and curing processes through photocrosslinking. However, the improvements afforded at higher temperatures were very significant and could not be ignored. Application of these findings to poled polymers was complicated by our use of corona poling to orient the chromophores. A drawback of corona poling is that catastrophic film damage will result if the polymer film is heated beyond T_g while under the corona field. To circumvent this, samples were first poled for 10 minutes at a temperature below T_g, then crosslinking was initiated with UV exposure. During the exposure step, the temperature was slowly increased to 100 °C. The crosslinking stabilizes the film, allowing for this steady increase in temperature, while avoiding film damage. In this way the methacrylate conversion in both **2.12** and **2.13**, reached or exceeded 60%, while the film integrity was maintained (Figure 2.22).
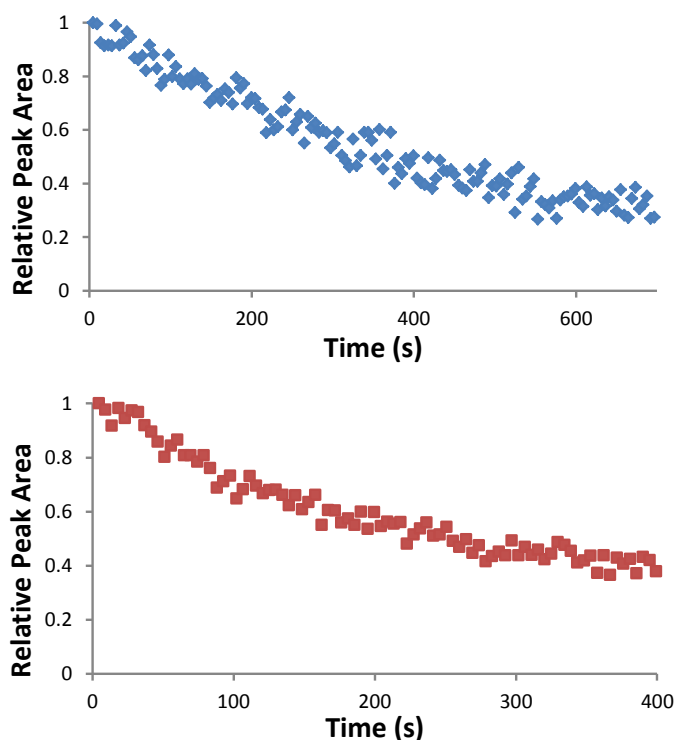
Figure 2.22: Conversion of 2.12 (top) and 2.13 (bottom) upon irradiation while ramping the temperature from 55 to 100 °C. Note the different time scales. Temperature ramp rates are 4.6 °C/min (2.12) and 6.7 °C/min (2.13).

PHOTOSTABILITY

As discussed earlier, many NLO chromophores are photosensitive. This is especially true of the high-β tetraene materials, which are degraded appreciably even with low energy wavelengths (near IR).[80] As bridges containing aromatic or heteroaromatic substituents are generally more robust, our system was expected to be reasonable stable.[69] However, these polymers were exposed to very high doses (> 5 J/cm^2) of broadband ultraviolet light, so photodegradation was a concern.

To examine this, films of **2.12** were cast on quartz and crosslinked in the same manner as the poled samples. UV/Vis absorbance was measured before and after irradiation. As indicated in Figure 2.23, this polymer exhibits significant photobleaching,

50

evidenced by the decrease in absorbance of the 370 nm peak. This is consistent with the measureable decrease in second-harmonic intensity observed in poled samples following irradiation at room temperature. While purging with nitrogen reduces the extent of photodegradation, these results highlight the challenges associated with photocrosslinkable NLO materials.
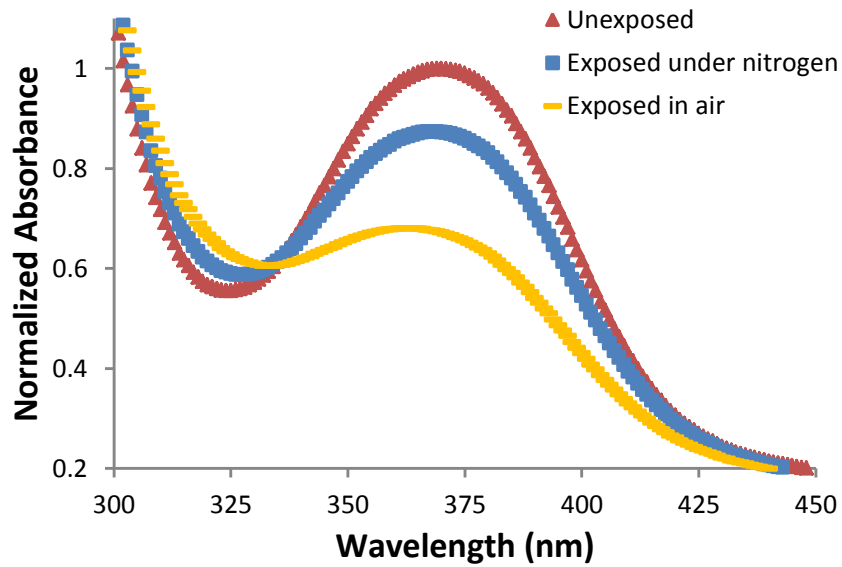
Figure 2.23: UV/Vis spectra of 2.12 films prior to exposure (triangles), exposed under nitrogen (squares) and exposed in air (bars).

THERMAL STABILITY

The thermal stability of poled order was evaluated by measuring second-harmonic generation as a function of time (isothermal decay) or temperature (dynamic decay). SHG coefficients were normalized according to equation 2.5.

$$\frac{d}{d_0} \cong \frac{\sqrt{I_{2\omega}/I_{2\omega}^{(0)}}}{I_\omega/I_\omega^{(0)}} \tag{2.5}$$

Where $I_{2\omega}$ is the intensity of frequency-doubled light and I_ω is the fundamental intensity. $I_{2\omega}^{(0)}$ and $I_\omega^{(0)}$ are the initial SHG and fundamental intensities, respectively. Polymer films were cast on ITO and corona poled under an atmosphere of nitrogen for 10 minutes. In the case of **2.11**, the film was then cooled to room temperature and the electric field was then removed. For the crosslinkable polymers **2.12** and **2.13**, which were cast with 5% Irgacure 819, samples were then cured. The cure step consisted of a broadband UV exposure ($I = 25$ mW/cm^2) while ramping the temperature to 100 °C at 5 °C per minute. At this point, the crosslinked samples were cooled to room temperature and the field was removed. SHG coefficients were measured immediately thereafter.

Polymers were first compared based on their isothermal stability over an extended period. 50 °C was chosen as it is near initial T_g and uncrosslinked samples should exhibit very rapid decay. However, if appreciable crosslinking is achieved in the exposed materials, their relaxation behavior should be dramatically altered. As seen in Figure 2.24, this is in fact the case. While uncrosslinked films exhibit very little second-harmonic generation after the first hour, exposed materials retain significant activity after 12 hours. Further, the benefit of a second crosslinkable group is visible, as **2.13** demonstrates improved stability relative to **2.12**.
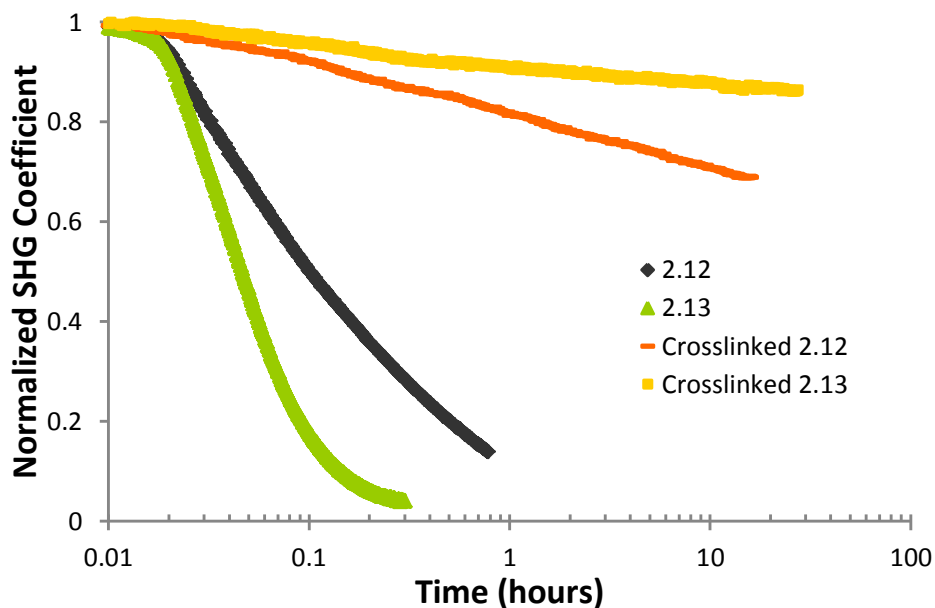
Figure 2.24: Isothermal decay of second harmonic generation in films of 2.12 and 2.13 at 50 °C.

A second method of characterizing NLO stability involves heating samples at a constant rate while monitoring SHG (dynamic decay). In this case materials will undergo very little change up to a certain temperature, above which relaxation is extremely rapid. In uncrosslinked polymers this is near T_g, as can be seen for **2.11**, as well as unexposed samples of **2.12** and **2.13** (Figure 2.25). However once crosslinked, **2.12** and **2.13** exhibit very different behavior. Rather than a sharp onset, both exhibit a gradual increase in the rate of decay with increasing temperature. Above 100 °C, the advantage of the second crosslinker in **2.13** is apparent.
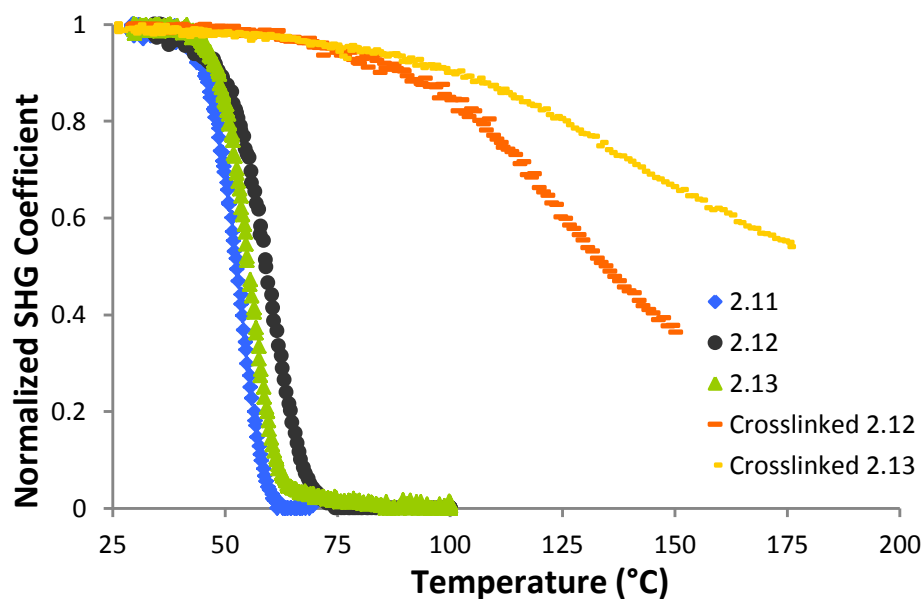
Figure 2.25: Dynamic decay of second harmonic generation in 2.11, 2.12 and 2.13. Temperature ramp rate is 10 °C/min.

The addition of reactive diluents is known to improve conversion in acrylate photopolymerizations.[125] Thus, it was anticipated that a polyfunctional co-crosslinker such as pentaerythritol triacrylate (PETA) would further promote interchain crosslinking and improve thermal stability. PETA was added to **2.13** at 10 wt% loading, along with the 5 wt% of photoinitiator. This additive has a dramatic plasticization effect on the polymer, depressing the T_g significantly—clearly visible when examining the dynamic relaxation of the uncrosslinked material (Figure 2.26). As a result, films containing PETA were poled at a lower temperature (40 °C) to avoid damage, then heated to 100 °C while crosslinking in the usual manner. As can be seen in Figure 2.22, the dynamic decay behavior of **2.13** is further improved with the addition of pentaerythritol triacrylate. A subtle but important difference is apparent below 100 °C, where the co-crosslinked material exhibits almost no measureable decay.
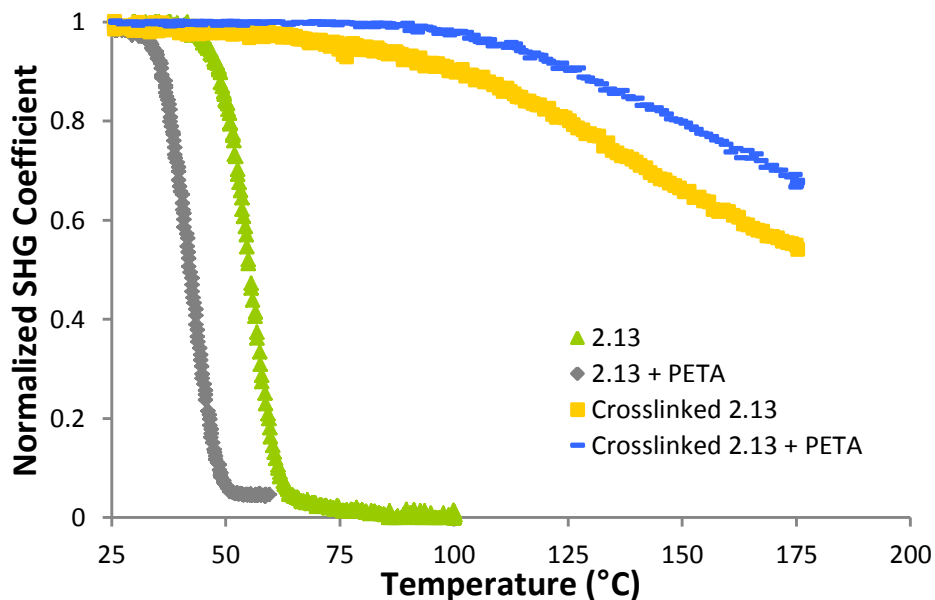
Figure 2.26: Dynamic decay of second harmonic generation in films of 2.13 with and without pentaerythritol triacrylate (PETA). Temperature ramp rate is 10 °C/min.

A high temperature isotherm (100 °C) further differentiates these two materials (Figure 2.27). While the SHG coefficient of crosslinked **2.13** fell to 52% of the initial value after 8 hours, **2.13** with PETA was much higher—77%. After 60 hours, the coefficient of this co-crosslinked sample was still over 70% of the initial value. This is quite remarkable considering this material was poled at 40 °C.
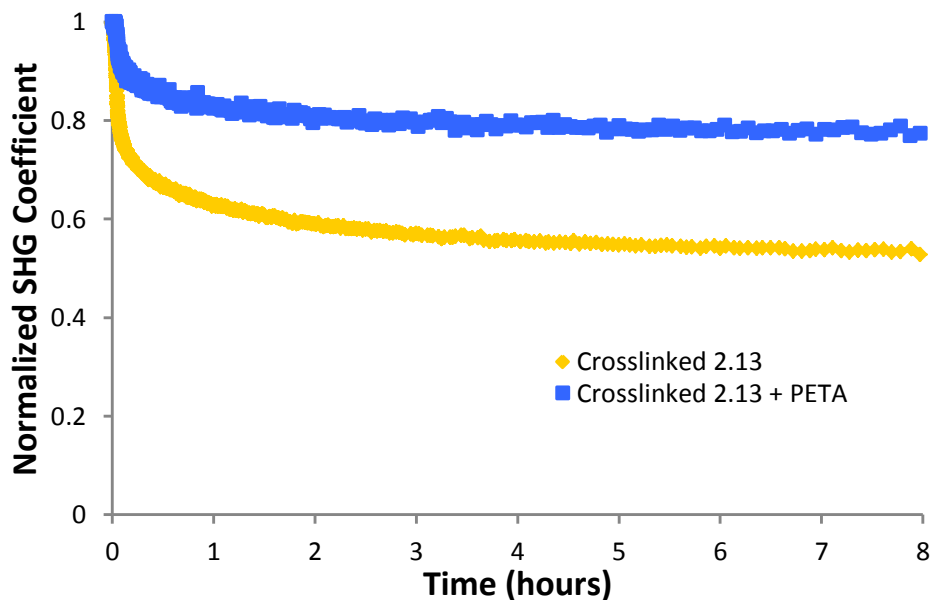
Figure 2.27: Isothermal decay of second harmonic generation in 2.13 with and without pentaerythritol triacrylate (PETA) at 100 °C.

CONCLUSIONS

A series of pendant nonlinear optical polymers was prepared via ring opening metathesis polymerization. To study the effect of photocrosslinking at the chromophore end, the number of methacrylate crosslinkers was varied from zero to two. Methacrylate conversion was examined by FTIR, and improved significantly with the use of photoinitiator at elevated temperatures. A process was developed to allow application of these findings to corona-poled materials while avoiding film damage. Polymers are first poled in the conventional manner and then crosslinking is initiated by irradiation of the film. During the crosslinking step, the film is slowly heated in order to promote conversion. In this manner effective control over the curing process is maintained, limiting interference with the poling.

Stability of poling-induced noncentrosymmetry was evaluated by monitoring second harmonic generation in polymer films. Thermal stability was found to increase

56

significantly with crosslinker substitution. While uncrosslinked materials relax rapidly near T_g, crosslinked materials retain significant SHG, even at temperatures above initial T_g. The improved stability of **2.13** relative to **2.12** is believed to result from the increased likelihood of interchain crosslinking. Combining **2.13** with pentaerythritol triacrylate co-crosslinker appears to further enhance this effect, yielded a material which exhibits excellent stability at twice the poling temperature. This constitutes a successful demonstration of the design concept using a relatively simple model system. Further extension of this approach to high T_g systems and more efficient chromophores is believed to hold promise for obtaining device quality NLO materials.

EXPERIMENTAL

General Methods and Materials

All solvents and reagents were obtained from Sigma-Aldrich and were used without further purification except where noted. DCM, pyridine, and TEA were distilled from CaH_2 while THF was distilled from sodium/benzophenone. Methacryloyl chloride was fractionally distilled prior to use. Reactions were run in flame-dried glassware and under an atmosphere of nitrogen unless otherwise noted. ^1H and ^{13}C NMR spectra were recorded on a Varian Unity Plus 400 MHz instrument. Chemical shifts are reported in ppm downfield from TMS using residual protonated solvent as an internal standard (DMSO-d_6, ^1H 2.49 ppm and ^{13}C 39.5 ppm or CDCl$_3$, ^1H 7.26 ppm and ^{13}C 77.0 ppm). Coupling constants are expressed in Hz. HRMS (CI) was obtained on a VG analytical ZAB2-E instrument while HRMS (ESI) was obtained on an Ion Spec FT-ICR (7 Tesla) instrument. IR data was recorded on a Nicolet Avatar 360 FT-IR using either a KBr

pellet or thin film on a NaCl disc. Melting points were recorded using a Mel-Temp II and are uncorrected. Polymer molecular weights were determined using an Agilent 1100 series GPC relative to polystyrene standards. Thermogravimetry and differential scanning calorimetry were performed using a TA Instrument Q500 TGA and TA Q100 DSC, respectively.
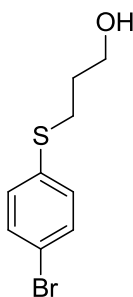
Synthesis of 3-[(4-bromophenyl)thio]propan-1-ol (2.2). A 100 mL round bottom flask with reflux condenser and magnetic stir bar was loaded with NaH (1.70 g, 60% in mineral oil, 42.5 mmol) and THF (30 mL). *p*-Bromothiophenol (**2.1**) (8.03 g, 42.5 mmol) was added to a separate 50 mL round bottom flask and was dissolved in THF (15 mL). The thiol solution was added to the suspension of NaH dropwise over a period of 20 minutes and stirred for an additional 30 minutes at room temperature. 3-bromopropanol (3.71 mL, 42.5 mmol) was placed into a separate 25 mL round bottom flask followed by THF (5 mL). The 3-bromopropanol solution was added to the 100 mL flask dropwise, after which the reaction mixture was heated to reflux for 1 hour. The mixture was then cooled to room temperature and quenched with water. The aqueous layer was extracted three times with ether, and the organic layers were combined, washed with 1 M KOH,

water, brine, then dried over MgSO$_4$, filtered, and concentrated to give **2.2** as colorless

viscous oil (10.3 g, 94%). ^{1}H NMR (DMSO-d_6): δ 1.69 (p, J = 6.6 Hz, 2H), 2.99 (t, J =

7.5 Hz, 2H), 3.48 (q, J = 5.4 Hz, 2H), 4.57 (t, J = 5.4 Hz, 1H), 7.23 (d, J = 6.3 Hz, 2H),

7.46 (d, J = 8.7 Hz, 2H); ^{13}C NMR (DMSO-d_6): δ 136.29, 131.73, 129.53, 118.16, 59.15,

31.71, 28.60; HRMS [M+H]$^+$ calcd. = 246.9792 found = 246.9797; FTIR ν = 3340 (br),

2920, 2869, 1467, 1382, 1091, 1071, 1001, 811 cm^{-1}.
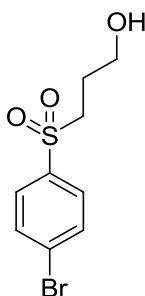
Synthesis of 3-[(4-bromophenyl)sulfonyl]propan-1-ol (2.3). Compound **2.2** (10.36 g,

41.9 mmol) was placed in a 250 mL round bottom flask equipped with reflux condenser

and magnetic stir bar. Hydrogen peroxide (50 mL, 30 wt% in water) was added followed

by glacial acetic acid (100 mL). The reaction mixture was stirred at room temperature for

1 hour and then heated to 90 °C for 10 hours. The reaction was cooled and extracted with

three portions of diethyl ether. The organic fractions were combined and washed with 1

M KOH until basic, then washed with brine, dried over MgSO$_4$, filtered, and

concentrated to yield a mixture of the free alcohol and acetylated product (8.85 g). The

mixture was placed in a 250 mL flask with condenser, along with MeOH (75 mL) and

NaOH (2.6 g, 65 mmol). The reaction mixture was heated to 70 °C for 4 hours and then

cooled to room temperature. The reaction was then quenched with 1 M HCl and extracted with diethyl ether. The organic layers were combined and washed with saturated NaHCO$_3$, water, and brine, then dried over MgSO$_4$, filtered, and concentrated to give **2.3** as a white solid (5.6 g, 65%). mp 64-66 °C; ^{1}H NMR (DMSO-d_6): δ 1.65 (m, 2H), 3.1 (m, 2H), 3.39 (q, J = 5.4-6.3 Hz, 2H), 4.63 (t, J = 5.4 Hz, 1H), 7.85 (m, 4H); ^{13}C NMR (DMSO-d_6): δ 25.89, 52.01, 58.60, 127.94, 129.76, 132.56, 138.20; HRMS [M+H]$^+$ calcd. = 277.9613 found = 277.9612; FTIR ν = 3514 (br), 3083, 2951, 2920, 2869, 1572, 1394, 1312, 1273, 1137, 1067, 1005 cm^{-1}.
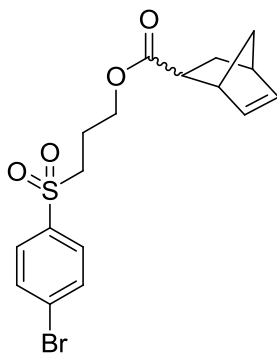
Synthesis of 3-[(4-bromophenyl)sulfonyl]propylbicyclo[2.2.1]hept-5-ene-2-carboxylate (2.4). A 250 mL round bottom flask was loaded with alcohol **2.3** (6.790 g, 24.33 mmol), 5-norbornene-2-carboxylic acid (3.360 g, 24.33 mmol), DMAP (0.297 g, 2.433 mmol), and DCM (100 mL). The flask was then immersed an ice bath and a solution of DCC (29.2 mmol, 1 M in DCM) was added dropwise. Following addition, the reaction was warmed to room temperature and stirred overnight. The solution was filtered to remove precipitated urea, then concentrated. The resulting residue was washed

with saturated NaHCO$_3$ and extracted three times with diethyl ether. The extracts were combined and washed with water and brine, then dried over MgSO$_4$, filtered and concentrated to give a brown solid. Flash chromatography using 20% ethyl acetate in hexanes as eluent yielded a mixture of *endo* and *exo* **2.4** as white solid (84%). mp 64-67 °C; ^{1}H NMR (DMSO-d_6): δ 1.27 (m, 2H), 1.82 (m, 4H), 2.92 (m, 3H), 3.39 (m, 2H), 3.99 (m, 2H), 5.80 (m, 1H), 6.15 (m, 1H), 7.88 (m, 4H); ^{13}C NMR (CDCl$_3$): δ 175.8, 174.3, 138.0, 137.9, 137.7, 132.7, 131.9, 129.6, 129.2, 61.8, 61.5, 53.2, 49.6, 46.5, 46.2, 45.6, 43.1, 42.9, 42.4, 41.5, 30.3, 29.1, 22.5; HRMS [M+H]$^+$ calcd. = 399.0266   found =399.027; FTIR ν = 3084, 3060, 2975, 2870, 1728, 1577, 1394, 1313, 1274, 1169, 1150 cm^{-1}.
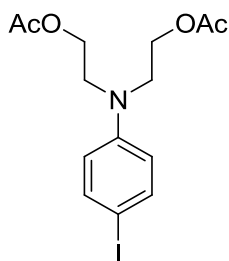
Synthesis of [(4-iodophenyl)imino]diethane-2,1-diyl diacetate (2.6a). Compound **2.6c** (1.03 g, 3.3 mmol) was added to a dry 250 mL round bottom flask under a nitrogen atmosphere. A catalytic amount of DMAP was then added followed by pyridine (66 mL) and acetic anhydride (15 mL, 163 mmol). The reaction mixture was stirred for 12 hours at room temperature and then concentrated *in vacuo*. The product was isolated by silica gel chromatography using 25% Ethyl acetate in Hexanes as eluent yielding **2.6a** as a viscous clear liquid. (82%) ^{1}H NMR (DMSO-d_6): δ 1.97 (s, 6H,CH$_3$), 3.55 (t, *J* = 6.0 Hz,

4H), 4.11 (t, J = 5.9 Hz, 4H), 6.61 (d, J = 9.3 Hz, 2H), 7.41 (d, J = 8.7 Hz, 2H); ^{13}C NMR (DMSO-d_6): δ 170.37, 146.96, 137.32, 114.46, 77.11, 60.82, 48.82, 20.65; HRMS ([M+H]$^+$ calcd. = 392.0355 found = 392.0359) FTIR ν = 3071, 2959, 2893, 1871, 1735, 1584, 1499, 1378, 1234, 1048, 803 cm^{-1}.
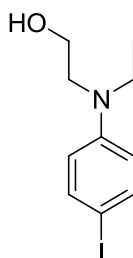
Synthesis of 2-[ethyl(4-iodophenyl)amino]ethanol (2.6b). 2-(N-ethylanilino)ethanol (4.00 g, 24.2 mmol) were added to dioxane (180 mL) and pyridine (180mL) in a 500 mL round bottom flask with magnetic stir bar. The reaction mixture was cooled to 0 °C and I$_2$ (9.23 g, 36.2 mmol) was added in one portion. The reaction was maintained at 0 °C for one hour then warmed to room temperature for a further hour. I$_2$ (3.07 g, 12 mmol) was added and stirred for an additional hour. The reaction mixture was washed with 1 M Na$_2$S$_2$O$_3$ until the brown color dissipated and was then extracted with DCM. The crude product was purified via column chromatography using DCM as eluent to afford pure **2.6b** as a white solid (5.527 g, 78%). mp 50-52 °C; ^{1}H NMR (DMSO-d_6): δ 1.03 (t, J = 6.9 Hz, 3H), 3.30 (m, 4H), 3.50 (q, J = 6Hz, 2H), 4.70 (t, J = 5.4Hz, 1H), 6.49 (d, J = 8.7Hz, 2H), 7.36 (d, J = 9Hz, 2H); ^{13}C NMR (DMSO-d_6): δ 147.3, 137.2, 114.0, 75.3, 58.2, 51.9, 44.5, 11.7; HRMS ([M+H]$^+$ calcd. = 291.0120 found = 291.0120) FTIR ν = 3304, 3215, 2920, 2866, 1499, 1588, 1355, 1266, 1184, 1064, 796 cm^{-1}.

Synthesis of 2,2'-[(4-iodophenyl)imino]diethanol (2.6c). N-Phenyldiethanolamine (10.00 g, 55.18 mmol) and dilute HCl (1 M, 55 mL) were added to a 250 mL round bottom flask with magnetic stir bar. ICl (8.96 g, 55.18 mmol) was added to HCl (90 mL, 6 N), cooled in an ice bath and then added to the reaction flask in one portion with stirring. The reaction mixture turned dark red immediately and after 2 hours, 1 M $Na_2S_2O_3$ was added slowly until the solution became colorless. The reaction mixture was added dropwise to a saturated solution of $NaHCO_3$ and the product precipitated out as an off white solid. The solid was filtered off, washed with cold water, and dried *in vacuo* to obtain **2.6c** as a white solid (83%). mp 82-84 °C; ^{1}H NMR (DMSO-d_6): δ 3.36 (t, J = 6 Hz, 4H), 3.49 (t, J = 6 Hz, 4H), 4.74 (bs, 2H), 6.51 (d, J = 9 Hz, 2H), 7.36 (d, J = 9 Hz, 2H); ^{13}C NMR (DMSO-d_6): δ 147.6, 137.1, 114.1, 75.5, 57.9, 53.1; HRMS [M+H]$^+$ calcd. = 308.0142 found = 308.0143; FTIR ν = 3254 (br), 2944, 2862, 1580, 1491, 1351, 1192, 1060, 812 cm^{-1}.
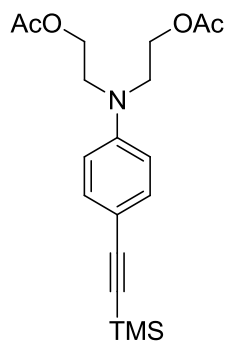
Synthesis of [(4-(trimethylsilyl)ethynylphenyl)imino]diethane-2,1-diyl diacetate (2.7a). A 100 mL round bottom flask was loaded with PdCl$_2$(PPh$_3$)$_2$ (170 mg, 0.237 mmol) and copper (I) iodide (34 mg, 0.119 mmol). THF (30 mL) was added, followed by **2.6a** (0.929 g, 2.37 mmol) dissolved in THF (10 mL) and ethynyltrimethylsilane (0.822 mL, 5.94 mmol). Diisopropylamine (3.3 mL, 2.37 mmol) was added in one portion and the mixture was degassed by three freeze-pump-thaw cycles and was stirred at room temperature for 30 minutes. The reaction was then heated to 60 °C for 12 hours, after which it was concentrated *in vacuo* and passed through a plug of silica gel and celite using 5% acetone in DCM as eluent. The mixture was concentrated and purified by flash chromatography using DCM as the eluent yielding **2.7a** as a viscous yellow liquid (98%). ^{1}H NMR (DMSO-d_6): δ .018 (s, 9H), 1.97 (s, 6H), 3.61 (t, J = 5.6 Hz, 4H), 4.13 (t, J = 5.9 Hz, 4H), 6.72 (d, J = 10.8 Hz, 2H), 7.22 (d, J = 9 Hz, 2H) ; ^{13}C NMR (DMSO-d_6): δ 170.34, 147.61, 132.84, 111.48, 108.88, 106.65, 91.02, 660.91, 48.67, 20.61, 0.15; HRMS ([M+H]$^+$ calcd. = 362.1782 found = 362.1788) FTIR ν = 3048, 2959, 2897, 2147, 1743, 1600, 1514, 1382, 1238, 1048, 850, 757 cm^{-1}.
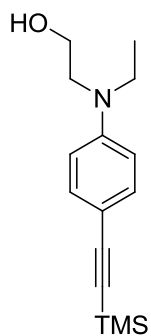
Synthesis of 2-[ethyl(4-(trimethylsilyl)ethynylphenyl)amino]ethanol (2.7b). A 100 mL round bottom flask was loaded with compound **2.6b** (0.521 g, 1.79 mmol), PdCl$_2$(PPh$_3$)$_2$ (125.6 mg, 0.179 mmol), and copper (I) iodide (17 mg, 0.0894 mmol). THF (25 mL) was then added, followed by ethynyltrimethylsilane (0.623 mL, 4.49 mmol) and diisopropylamine (2.5 mL, 1.79 mmol) in one portion. The reaction was degassed by three freeze-pump-thaw cycles and stirred at room temperature for 30 minutes, then heated to 70 °C for 14 hours. After cooling to room temperature, the reaction mixture was concentrated *in vacuo* and passed through a short silica gel/celite plug with 2% acetone in DCM to obtain **2.7b** as a yellow liquid (97%). ^{1}H NMR (CDCl$_3$): δ 0.23 (s, 9H), 1.15 (t, *J* = 5.4 Hz, 3H), 3.41 (t, *J* = 5.1 Hz, 2H), 3.46 (t, *J* = 4.8 Hz, 2H), 3.78 (t, *J* = 4.5 Hz, 2H), 6.63 (d, *J* = 6.6 Hz, 2H), 7.31 (d, *J* = 6.6 Hz, 2H); ^{13}C NMR (CDCl$_3$): δ 148.05, 133.31, 111.71, 109.98, 106.29, 91.26, 60.16, 52.23, 45.47, 21.03, 11.82, 0.17; HRMS ([M+H]$^+$ calcd. = 261.1549 found = 261.1547) FTIR ν = 3386, 3040, 2959, 2893, 2147, 1603, 1514, 1401, 1359, 1242, 1188, 1044, 862 cm^{-1}.
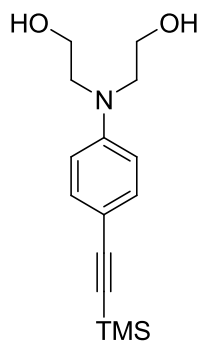
Synthesis of 2,2'-[(4-(trimethylsilyl)ethynylphenyl)imino]diethanol (2.7c). Compound **2.6c** (1.00 g, 3.256mmol) was added to a round bottom flask containing PdCl$_2$(PPh$_3$)$_2$ (0.230 g, 0.325 mmol) and CuI (31 mg, 0.166 mmol). THF (30 mL) was added, followed by ethynyltrimethylsilane (1.12 mL, 8.14 mmol) and TEA (4.54 mL, 32.56 mmol). The reaction mixture was degassed by three freeze-pump-thaw cycles and was stirred for 30 minutes before heating to 60 °C for 15 hours. The crude mixture was reduced *in vacuo* and passed through a plug of celite and silica gel before purification via flash column chromatography with 15% acetone in DCM as eluent. **2.7c** was obtained as a faint yellow solid (97%). mp 98-100 °C; ^{1}H NMR (DMSO-d_6): δ 0.18 (s, 9H), 3.41 (t, J = 5.7 Hz, 4H), 3.50 (t, J = 5.4 Hz, 4H), 4.76 (t, J = 5.4 Hz, 2H), 6.62 (d, J = 8.7 Hz, 2H), 7.20 (d, J = 9 Hz, 2H); ^{13}C NMR (DMSO-d_6): δ 148.23, 132.80, 111.07, 107.66, 107.09, 90.65, 57.97, 53.04, 0.23; HRMS [M+H]$^{+}$ calcd. = 278.1576 found = 278.1579; FTIR ν = 3243 (br), 3138, 2955, 2874, 2140, 1604, 1518, 1355, 1184, 1068, 1002, 847 cm^{-1}.
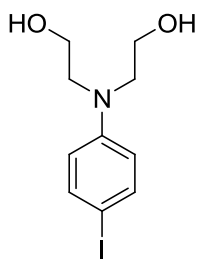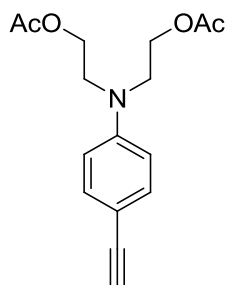
Synthesis of [(4-ethynylphenyl)imino]diethane-2,1-diyl diacetate (2.8a). Compound

2.7a (0.44 g, 1.3 mmol) was added to a 50 mL round bottom flask followed by THF (20

mL) and 3 drops of water. TBAF (2 mL, 1 M in THF; 2 mmol) was added in one portion

and the reaction mixture was stirred at room temperature for 10 hours. The reaction

diluted with 1:1 ethyl acetate/diethyl ether and washed with water and brine. The extract

was dried over $MgSO_4$, filtered, concentrated, and then chromatographed on silica gel

using 25% ethyl acetate in hexanes to yield **2.8a** as a viscous yellow oil (60%). ^{1}H NMR

(DMSO-d_6): δ 1.97 (s, 6H, CH_3), 3.60 (t, J = 6 Hz, 4H), 3.86 (s, 1H, CH), 4.13 (t, J =

6.15 Hz, 4H), 6.74 (d, J = 9 Hz, 2H), 7.25 (d, J = 8.7 Hz, 2H); ^{13}C NMR (CDCl$_3$): δ

170.89, 147.36, 133.50, 111.47, 109.69, 84.30, 75.10, 61.14, 49.45, 20.82; HRMS

([M+H]$^+$ calcd. = 290.1396 found = 290.1392) FTIR ν = 3281, 3048, 2955, 2892, 2096,

1739, 1603, 1517, 1378, 1234, 1043, 822 cm^{-1}.
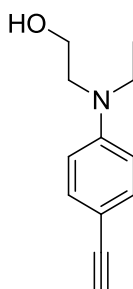
Synthesis of 2-[ethyl(4-ethynylphenyl)amino]ethanol (2.8b). Compound **2.7b** (0.102 g, 0.39 mmol) was added to a 25 mL round bottom flask, followed with THF (5 mL) and one drop of water. TBAF (0.6 mL, 1 M in THF; 0.6 mmol) was added and stirred at room temperature overnight. The reaction mixture was diluted with 1:1 hexanes/ethyl acetate and washed with water, brine and dried with $MgSO_4$. The solvent was removed *in vacuo* and the crude material was purified with a silica gel plug using DCM as eluent to produce compound **2.8b** as a faint yellow solid (95%). mp 50-53 °C; ^1H NMR (DMSO-d_6): δ 1.05 (t, *J* = 6.9 Hz, 3H), 3.36 (m, 4H), 3.51 (q, *J* = 5.7 Hz, 2H), 3.81 (s, 1H), 4.72 (t, *J* = 5.4 Hz, 1H), 6.61 (d, *J* = 6.9 Hz, 2H), 7.22 (d, *J* = 6.9, 2H); ^{13}C NMR (DMSO-d_6): δ 147.84, 132.83, 111.03, 107.01, 84.88, 77.68, 58.21, 51.88, 44.56, 11.83; HRMS ([M+H]$^+$ calcd. = 190.1232 found = 190.1236) FTIR ν = 3254, 2963, 2897, 2093, 1883, 1611, 1510, 1401, 1172, 1009, 819, 536 cm^{-1}.
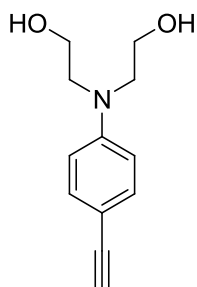
Synthesis of 2,2'-[(4-ethynylphenyl)imino]diethanol (2.8c). Compound **2.7c** (0.936 g, 3.37 mmol) was added to a 50 mL round bottom flask. MeOH (20 mL) and K_2CO_3 (1.502 g, 10.12 mmol) were added and the reaction mixture was stirred at room temperature for 2 hours. The reaction mixture was reduced *in vacuo* and purified using a plug of silica gel (1:5 acetone/DCM), yielding **2.8c** as a faint yellow solid (97%). mp 119-121 °C; ^{1}H NMR (DMSO-d_6): δ 3.41 (t, J = 6 Hz, 4H), 3.50 (t, J = 5.7 Hz, 4H), 3.82 (s, 1H), 4.76 (t, J = 5.4 Hz, 2H), 6.63 (d, J = 9 Hz, 2H), 7.21 (d, J = 9 Hz, 2H); ^{13}C NMR (DMSO-d_6): δ 148.15, 132.76, 111.11, 107.16, 84.84, 77.79, 57.97, 53.03; HRMS [M+H]$^+$ calcd. = 206.1181 found = 206.1186; FTIR ν = 3285 (br), 2928, 2882, 2093, 1612, 1511, 1355, 1060, 1041, 823 cm^{-1}.
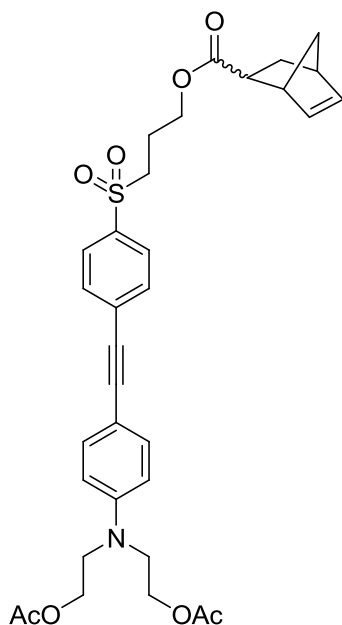
Synthesis of 2.9a. Alkyne **2.8a** (0.458 g, 1.58 mmol), PdCl$_2$(PPh$_3$)$_2$ (121 mg, 0.170 mmol), and CuI (16 mg, 0.086 mmol) were added to an oven dried 100 mL round bottom flask. The flask was maintained under N$_2$ atmosphere and compound **2.4** (0.691 g, 1.73 mmol) dissolved in THF (20 mL) was added. Diisopropylamine (2.43 mL, 17.3 mmol) was added and the reaction was degassed by three freeze-pump-thaw cycles, and then stirred at room temperature for 40 minutes before heating to 50 °C for 15 hours. The crude reaction mixture was reduced in vacuo and passed through a plug of celite and silica prior to purification by column chromatography (2% acetone in DCM) to obtain **2.9a** as a viscous yellow oil (52%). ^{1}H NMR (DMSO-d_6): δ 1.18-1.32 (m, 3H), 1.77-1.86 (m, 3H), 1.97 (s, 6H) 2.83 (s, 1H), 2.97 (dt, J = 4.2, 9 Hz, 1H), 3.08 (s, 1H), 3.34-3.420 (m, 2H), 3.65 (t, J = 5.1 Hz, 5H), 3.98 (t, J = 6 Hz, 2H), 4.16 (q, J = 5.4 Hz, 5H), 5.81 (dd, J = 2.7, 5.4 Hz, 1H), 6.13 (dd, J = 3, 5.7 Hz, 1H), 6.82 (d, J = 6 Hz, 2H), 7.37 (d, J = 8.7 Hz, 2H), 7.72 (d, J = 8.7 Hz, 2H), 7.88 (d, J = 8.4 Hz, 2H); ^{13}C NMR (DMSO-d_6): δ

173.56, 170.37, 148.11, 137.64, 137.16, 133.05, 132.27, 131.56, 128.88, 128.06, 111.74, 107.79, 94.92, 86.30, 61.52, 60.91, 51.63, 49.08, 48.74, 45.12, 42.45, 41.92, 41.03, 28.65, 22.21, 20.63; HRMS ([M+H]$^+$ calcd. = 608.2325 found = 608.2313) FTIR ν = 3056, 2966, 2209, 1735, 1603, 1588, 1522, 1363, 1234, 1126, 1052, 819, 733, 710 cm^{-1}.
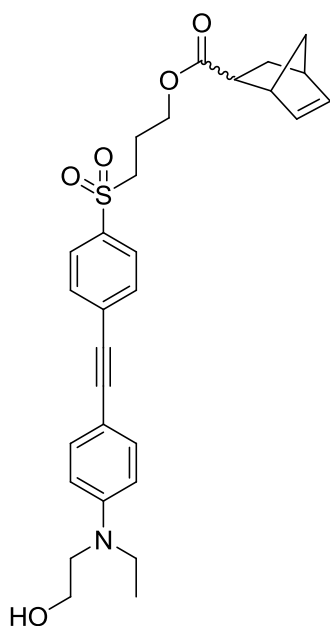
Synthesis of 9b. Alkyne **2.8b** (1.392 g, 7.355 mmol), PdCl$_2$(PPh$_3$)$_2$ (516 mg, 0.736 mmol), and CuI (70 mg, 0.368 mmol) were added to an oven dried 250 mL round bottom flask. The flask was maintained under N$_2$ atmosphere and compound **2.4**(2.878 g, 7.21 mmol) dissolved in THF (150 mL) was added. Diisopropylamine (10.31 mL, 73.552 mmol) was added and the reaction was degassed by three freeze-pump-thaw cycles, and then stirred at room temperature for 40 minutes before heating to 50 °C for 15 hours. The reaction mixture was reduced in vacuo and passed through a plug of celite and silica gel prior to purification by column chromatography (2% acetone in DCM) to obtain **2.9b**

71

as a viscous yellow oil (52%). ^{1}H NMR (DMSO-d_6): δ 1.180 (t, J = 5.4 Hz, 3H), 1.262 (d, J = 6 Hz, 1H), 1.335-1.381 (m, 1H), 1.416-1.462 (m, 1H), 1.835-1.914 (m, 1H), 1.988-2.204 (m, 3H), 2.888-2.931 (m, 2H), 3.156 (p, J = 6 Hz, 2H), 3.458 (q, J = 5.1 Hz, 2H), 3.506 (t, J = 5.1 Hz, 2H), 3.806 (t, J = 5.1 Hz, 1H), 4.054-4.174 (m, 1H), 5.839-5.860 (m, 1H), 6.099-6.187 (m, 1H), 6.693 (d, J = 6.6 Hz, 2H), 7.385 (d, J = 6.6 Hz, 2H), 7.638 (d, J = 9 Hz, 2H), 7.825 (d, J = 9 Hz, 2H); ^{13}C NMR (DMSO-d_6): δ 174.4, 170.8, 148.5, 137.9, 136.4, 133.3, 132.0, 131.7, 130.4, 127.9, 111.6, 108.3, 86.1, 61.6, 59.9, 53.2, 52.1, 49.6, 46.5, 45.7, 45.4, 43.1, 42.4, 29.1, 22.5, 11.8; HRMS ([M+H]$^+$ calcd. = 508.2155 found = 508.2158) FTIR ν = 3514 (br), 3060, 2970, 2873, 2205, 1728, 1584, 1522, 1401, 1312, 1188, 912, 734 cm^{-1}.
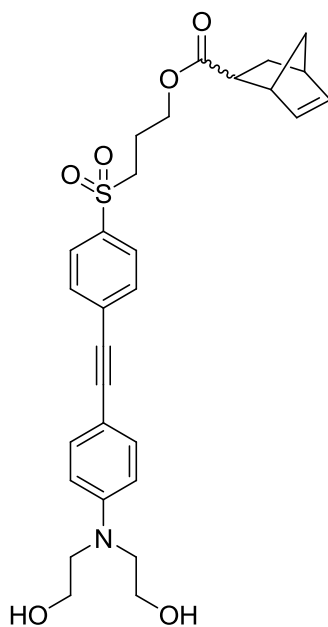
Synthesis of 9c. Alkyne **2.8c** (0.137 g, 0.662 mmol), PdCl$_2$(PPh$_3$)$_2$ (47 mg, 0.066 mmol), and CuI (7 mg, 0.033 mmol) were added to a 25 mL round bottom flask with magnetic

stir bar. The flask was maintained under N_2 atmosphere and compound **2.4** (0.238 g, 0.596 mmol) dissolved in THF (10 mL) was added. Diisopropylamine (1 mL) was added and the reaction was degassed by three freeze-pump-thaw cycles, and then stirred at room temperature for 40 minutes before heating to 60 °C for 15 hours. The crude reaction mixture was reduced in *vacuo* and passed through a plug of celite and silica gel before purification by column chromatography (15% acetone in DCM) to yield **2.9c** as a yellow solid (82%). mp 56-59 °C; *endo*-norbornyl isomer: ^{1}H NMR (DMSO-d_6): δ 1.18-1.30 (m, 3H), 1.77-1.86 (m, 3H), 2.83 (s, 1H), 2.97 (dt, J = 4.2, 9.3 Hz, 1H), 3.09 (s, 1H), 3.34-3.420 (m, 2H), 3.46 (t, J = 5.1 Hz, 4H), 3.534 (t, J = 5.7 Hz, 4H), 3.97 (t, J = 6.3 Hz, 2H), 4.79 (t, J = 5.4 Hz, 2H), 5.80 (dd, J = 2.7, 5.4 Hz, 1H), 6.13 (dd, J = 2.7, 5.4 Hz, 1H), 6.72 (d, J = 9 Hz, 2H), 7.36 (d, J = 8.7 Hz, 2H), 7.71 (d, J = 8.7 Hz, 2H), 7.87 (d, J = 8.4 Hz, 2H); ^{13}C NMR (DMSO-d_6): δ 173.57, 148.74, 137.65, 136.97, 132.99, 132.28, 131.44, 129.05, 128.06, 111.34, 106.51, 95.46, 86.16, 61.53, 57.99, 53.04, 51.63, 49.09, 45.13, 42.45, 41.92, 28.66, 22.22; HRMS [M+H]$^+$ calcd. = 523.2029 found = 523.2023; FTIR ν = 3379 (br), 3052, 2963, 2866, 2198, 1720, 1603, 1584, 1522, 1130 cm^{-1}.
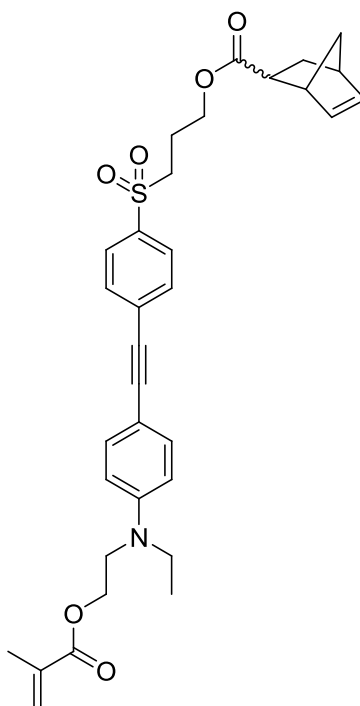
Synthesis of 2.10b. Compound **2.9b** (4.261 g, 8.4 mmol) and DMAP (0.0137 g, 0.096 mmol) were placed in a 250 mL round bottom flask. DCM (200 mL) and TEA (4.7 mL, 33.55 mmol) were added, followed by methacryloyl chloride (1.60 mL, 16.78 mmol). The reaction mixture was stirred at 0 °C for 1 hour, then at room temperature for a further 10 hours. The reaction was diluted with DCM, washed with water and brine, then dried over MgSO$_4$, filtered, and concentrated. The crude material was purified by column chromatography (1% acetone in DCM) to yield **2.10b** as a viscous yellow oil (72%). ^{1}H NMR (CDCl$_3$): δ 7.797 (d, J = 8.4 Hz, 2H), 7.595 (d, J = 8.4 Hz, 2H), 7.352 (d, J = 8.7 Hz, 2H), 6.655 (d, J = 8.7 Hz, 2H), 6.111 (m, 1H), 6.046 (s, 1H), 5.804 (m, 1H), 5.534 (s, 1H), 4.265 (t, J = 6 Hz, 2H), 4.059 (m, 2H), 3.592 (t, J = 6.6 Hz, 2H), 3.406 (q, J = 6.6 Hz, 2H), 3.120 (m, 3H), 2.847 (m, 2H), 2.042-1.790 (m, 3H), 1.883 (s, 3H), 1.447-1.198 (m, 3H), 1.144 (t, J = 6.9 Hz, 3H); ^{13}C NMR (CDCl$_3$): δ 175.7, 174.1, 167.1, 147.9,

137.9, 137.7, 136.5, 135.8, 135.4, 133.2, 131.9, 131.5, 130.2, 127.8, 125.8, 111.3, 108.3, 95.4, 85.9, 61.7, 61.6, 61.5, 53.3, 53.1, 49.4, 48.3, 46.4, 46.1, 45.5, 44.9, 42.9, 42.7, 42.3, 41.4, 30.7, 30.2, 28.9, 22.4, 18.1, 11.9; HRMS [M+H]$^+$ calcd. = 576.2420 found = 576.2405. FTIR ν = 3060, 2974, 2873, 2205, 2166, 1716, 1607, 1588, 1512, 1448, 1161, 1083, 819, 733 cm^{-1}.
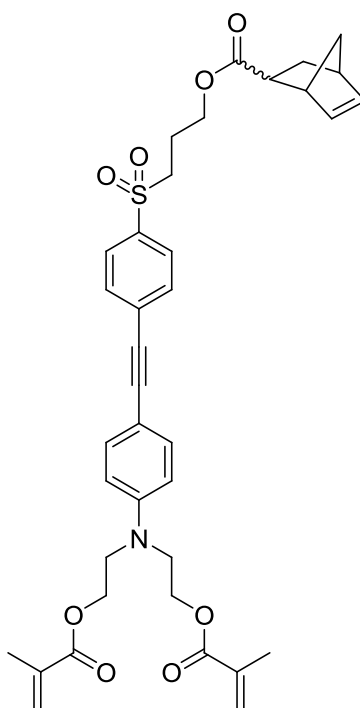
Synthesis of 2.10c. Compound **2.9c** (0.503 g, 0.96 mmol) and DMAP (0.0137g, 0.096 mmol) were placed in a 100 mL round bottom flask. DCM (5 mL) and TEA (0.54 mL, 3.84 mmol) were added, followed by methacryloyl chloride (0.281 mL, 2.90 mmoles). The reaction mixture was stirred at 0 °C for 1 hour, then room temperature for an additional 10 hours. The reaction was diluted with DCM, washed with water and brine, then dried over MgSO$_4$, filtered, and concentrated. The crude mixture was purified by

column chromatography (1% acetone in DCM) to yield **2.10c** as a viscous yellow oil (46%). ^{1}H NMR (DMSO-d_6): δ δ 1.18-1.30 (m, 3H), 1.77-1.86 (m, 3H), 2.1 (s, 3H), 2.83 (s, 1H), 2.97 (dt, J = 4.2, 9.3 Hz, 1H), 3.09 (s, 1H), 3.30-3.41 (m, 2H), 3.738 (t, J = 5.4 Hz, 4H), 3.97 (t, J = 5.4 Hz, 2H), 4.263 (t, J = 5.4 Hz, 4H), 5.66 (t, J = 1.8 Hz, 1H), 5.98 (bs, 1H), 6.87 (d, J = 8.7 Hz, 2H), 7.38 (d, J = 9 Hz, 2H), 7.72 (d, J = 8.4 Hz, 2H), 7.88 (d, J = 8.7 Hz, 2H); HRMS [M+H]$^+$ calcd. = 660.2631 found = 660.2631.
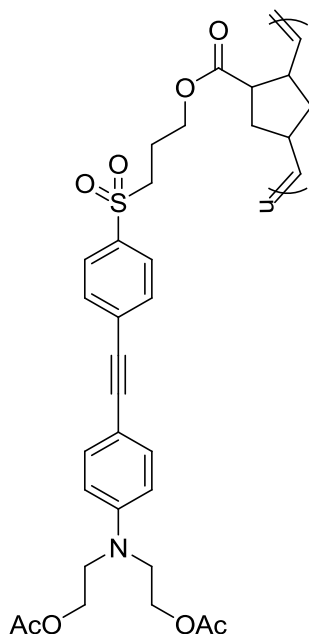
Synthesis of 2.11. To a 500 mL round bottom flask was added Grubbs II catalyst (53 mg, 0.062 mmoles), which was then cooled in an ice bath. To a separate 500 mL flask was added **2.9a** (3.788 g, 6.539 mmoles) and DCM (400 mL). The monomer solution was degassed via three freeze-pump-thaw cycles and then transferred via canula to the flask containing catalyst. The reaction was warmed to room temperature and stirred for 12 hours before quenching with ethyl vinyl ether and concentrating. The resulting solid

was redissolved in THF and precipitated in cold hexanes, yielding **2.11** as a light yellow powder (85%). M_n = 33 kDa; PDI = 1.59.
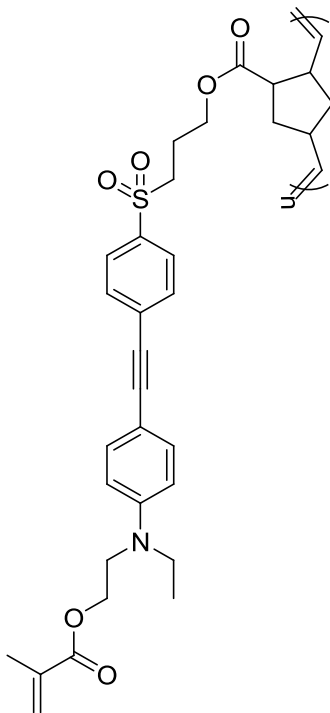
Synthesis of 2.12. To a 500 mL round bottom flask was added Grubbs II catalyst (78 mg, 0.0920 mmoles), which was then cooled in an ice bath. To a separate 500 mL flask was added **2.10b** (5.30 g, 9.20 mmoles) and DCM (400 mL). The monomer solution was degassed via three freeze-pump-thaw cycles and then transferred via canula to the flask containing catalyst. The reaction was warmed to room temperature and stirred for 12 hours before quenching with ethyl vinyl ether and concentrating. The resulting solid was redissolved in THF and precipitated in cold hexanes, yielding **2.12** as a light yellow powder (85%). M_n = 52 kDa; PDI = 1.62
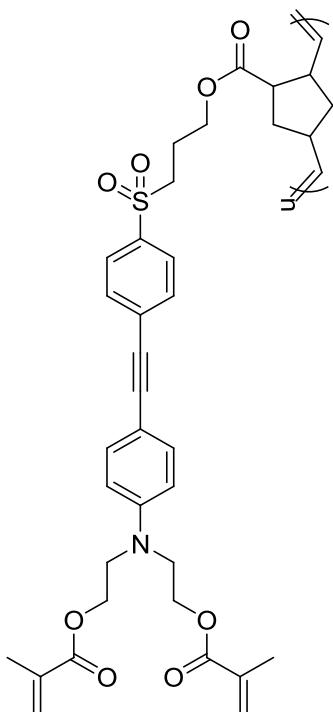
Synthesis of 2.13. To a 500 mL round bottom flask was added Grubbs II catalyst (34 mg, 0.0397 mmoles), which was then cooled in an ice bath. To a separate 500 mL flask was added **2.10c** (2.509 g, 3.974 mmoles) and DCM (250 mL). The monomer solution was degassed via three freeze-pump-thaw cycles and then transferred via canula to the flask containing catalyst. The reaction was warmed to room temperature and stirred for 12 hours before quenching with ethyl vinyl ether and concentrating. The resulting solid was redissolved in THF and precipitated in cold hexanes, yielding **2.13** as a light yellow powder (85%). M_n = 59 kDa; PDI = 1.9; ^{1}H NMR (DMSO-d_6): δ 1.78 (bs), 3.33 (bs), 3.69 (bs), 3.95 (bs), 4.22 (bs), 5.32 (bt), 5.59 (bs), 5.94 (bs), 6.81 (bs), 7.32 (bs), 7.64 (bs), 7.81 (bs).

Crosslinking Conversion

IR spectra were collected with a Magna 550 spectrometer (Thermo Scientific, Inc.). Samples were spin coated onto aluminum-backed silicon wafers and IR absorbance was measured in a normal specular reflectance configuration using a reflectance accessory (Axiom Analytical, Inc.) with nitrogen purging. Exposures were performed using a Novacure 2100 spot curing system (Lumen Dynamics) at a 5 inch distance, with a broadband intensity of 25 mW/cm^2. Conversion was determined from the C=C stretch at 1635 cm^{-1}, normalized to the aromatic stretch at 1585 cm^{-1}, which was unchanging.

Photobleaching

UV/visible spectra were collected using an Evolution 220 spectrophotometer (Thermo Scientific, Inc.). Samples were spin-coated onto quartz and exposed using a Novacure 2100 spot curing system (Lumen Dynamics) at a 5 inch distance, either under air or with a nitrogen purge. Exposure time was 10 minutes at 25 mW/cm^2 broadband intensity. Absorbance was normalized to the $\pi \rightarrow \pi^*$ peak at 370 nm.

Poling and Nonlinear Optical Characterization

Polymer solutions were formulated in cyclopentanone and stored in the dark. Solutions were spin coated onto ITO-coated glass substrates (Sigma-Aldrich, 70 Ω/sq sheet resistance) at 1500 rpm and baked at 85 °C overnight in a vacuum oven. Samples were corona poled in a nitrogen atmosphere with a stainless steel needle at 4.5 kV with the tip 1 cm above the sample. Films were heated to 70 °C (40 °C in the case of samples containing PETA) for ten minutes. Samples for photocrosslinking were irradiated at 25 mW/cm^2 while the temperature was raised at a rate of 5 °C/min to 100 °C. Poling current was monitored with a picoammeter to detect shorting. Following poling, the temperature was reduced to 25 °C and the poling field subsequently removed. In uncrosslinked films

that were heated to 100°C, film damage caused by the corona field prevented SHG measurement.

SHG measurements were completed immediately following poling. Samples were enclosed in a heater with a 6 mm hole to allow for beam clearance and placed in the beam path. Light from the source, a 500 mW Nd:YLF 1053 nm laser Q-switched at 200 kHz, is polarized perpendicular to the sample normal, which is oriented at a 45° angle to the propagation direction. Second harmonic output from the sample passed through a 523 nm bandpass filter (Andover) and a polarizer (*p*-transmission) and was focused on a PMT detector (Hamamatsu). The fundamental frequency was collected by a beam splitter and directed to a Si photodiode (UDT Instruments). Following measurement of initial fundamental and SHG signals, heating commenced and the signals were measured at regular intervals. For constant temperature experiments, the sample reached thermal equilibrium within one minute, while for temperature ramp experiments, a ramp rate of 10 °C/min was used.

Chapter 3: Long Wavelength Photobases for Photosensitive Polyimide

INTRODUCTION

From Chapter 1, the reader will recall the importance of photoactive compounds in microelectronics fabrication. Foremost among these are the photoacid generators (PAGs) employed by chemically amplified photoresists. Similarly, the previous chapter described photocrosslinking in a nonlinear-optical polymer, which was achieved using a commercial photoinitiator. Both PAGs and radical photoinitiators are incredibly useful, allowing for generation of reactive species with excellent spatial and temporal control. They have been heavily studied and are widely employed in industrial applications, and as such, there exist many commercial examples.[126, 127] Conversely, photochemical generation of basic species has received relatively limited attention (Figure 3.1). Despite frequently-cited advantages such as insensitivity to oxygen and reduced corrosion of metal substrates, photobase generators (PBGs) have found fewer practical applications.[11] Though many PBGs have been developed, they remain largely an academic curiosity.
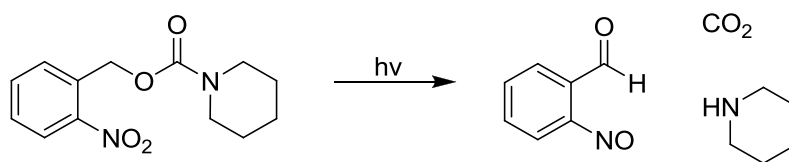
Figure 3.1: Representative PBG. In this example the photogenerated base is piperidine.

A unique opportunity for the application of photobases emerged from several findings at IBM in the early 1990s. At the time, researchers were studying the curing behavior of a class of polyimide precursors known as poly(amic alkyl esters). It was noted that amines exhibit a strong catalytic effect on the imidization of these polymers, dramatically reducing the temperature at which the reaction occurs.[128] By using a

photobase generator, spatial control over the cure reaction could be achieved; that is, with photobase, this material behaves as a photoresist.[129, 130] Given the widespread use of polyimide as an insulating material, this was a very valuable discovery.

POLYIMIDE

For the purposes of this chapter, discussions of polyimide will focus primarily on poly(pyromellitic dianhydride-co-4,4'-oxydianiline) (PMDA-ODA). Marketed by DuPont as Kapton, PMDA-ODA is by far the most common polyimide, and it is frequently used as a dielectric material in microelectronics packaging and as a substrate for flexible circuits. Greater detail regarding the application and structure-property relationships of polyimide will be discussed in Chapter 4.

Aromatic polyimides like PMDA-ODA are completely intractable, infusible materials. Therefore, they are prepared by a two-step process (Figure 3.2). First, the parent diamine and dianhydride are reacted in a polar aprotic solvent such as N-methylpyrrolidone (NMP) to form a polyamide precursor. This solution is then coated onto a surface and heated to high temperature (300-400 °C) to drive off excess solvent and completely cure the polymer. Alternatively, the polyamide precursor can be treated with a dehydrating agent to effect the curing at a lower temperature.
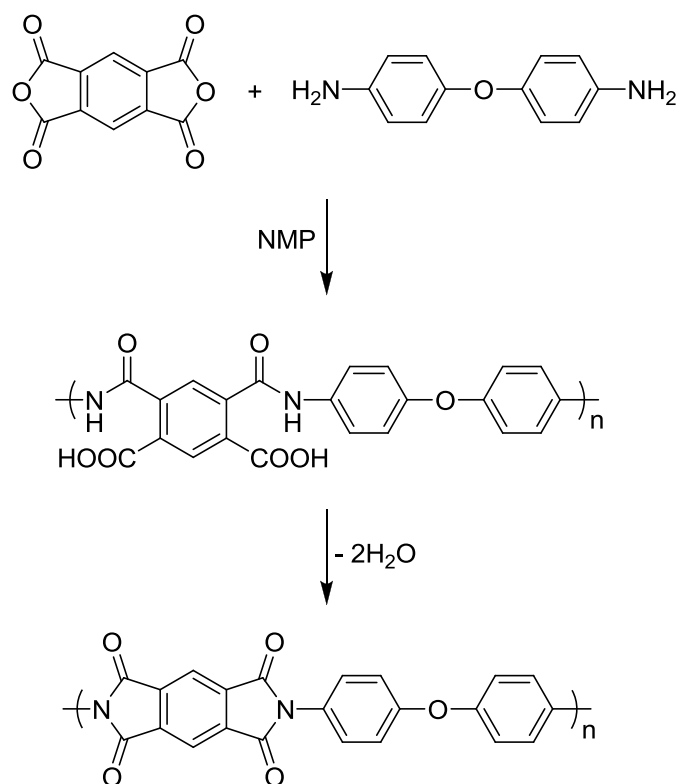
Figure 3.2: Synthesis of PMDA-ODA. The intermediate poly(amic acid) is a mixture of both meta (shown) and para isomers.

Traditionally, polyimides are patterned in the same manner as interlayer dielectrics like SiO_2. First, a blanket film of polymide precursor is deposited and cured. A photoresist is then deposited and patterned to form the target structure. This pattern is transferred into the underlying polyimide through a separate etch step (recall Figure 1.5). However, a more efficient approach is to render the polyimide or its precursor directly photopatternable, as in IBM's system. Indeed, within the field of microelectronics photosensitive polyimide is an area of significant research and commercialization.[131] Several common schemes exist, yielding materials of both negative and positive tone.

The earliest examples were based on crosslinkable precursors such as the poly(amic ester) shown in Figure 3.3.[132, 133] These polymers are patterned by photocrosslinking of the pendant methacrylates to produce a negative tone image.

Following development, the crosslinked material is cured at high temperature to convert the precursor into polyimide. During this step the methacrylates are volatilized, resulting in significant outgassing and film shrinkage, a major drawback for this approach. Additionally, these crosslinkers were found to negatively impact performance of the final material.[134] In spite of this, these polymers were investigated for implementation in IC packaging and the lithographic quality was found to be adequate.[135, 136] However, due to the high optical density of these polymers, the dose required to pattern thick films is extremely high (>2 J/cm^2), dramatically reducing throughput.
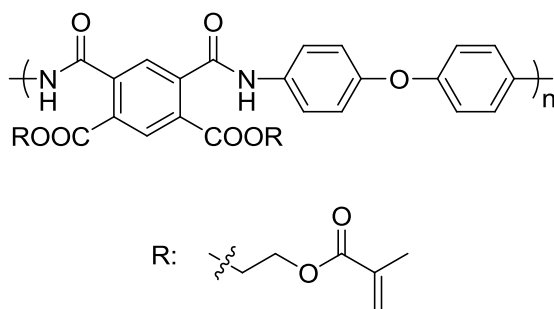
Figure 3.3: Methacrylate-based negative-tone photosensitive polyimide.

Following a similar trend as photoresists, focus gradually shifted from organic-developable negative-tone systems towards positive-tone and aqueous development. By leveraging the same photochemical Wolff rearrangement as classical i-line resists, researchers have demonstrated a range of positive-tone systems.[137-141] Resolution is generally comparable to methacrylate systems. Using DNQ-based dissolution inhibitors,

which are active to the red of most polyimide precursors, dose requirements are reduced significantly (<250 mJ/cm^2 in most cases). The main shortcoming of this approach is the tendency of unexposed areas to partially dissolve during development—dark erosion. This is not a problem unique to photosensitive polyimide, but rather is a general consideration for all positive photoresists. However, dissolution of poly(amic acids) is considerably more difficult to inhibit than the novolac resin discussed in Chapter 1. Very high loading of dissolution inhibitor is often required, degrading the material properties of the final polyimide.[138, 139]
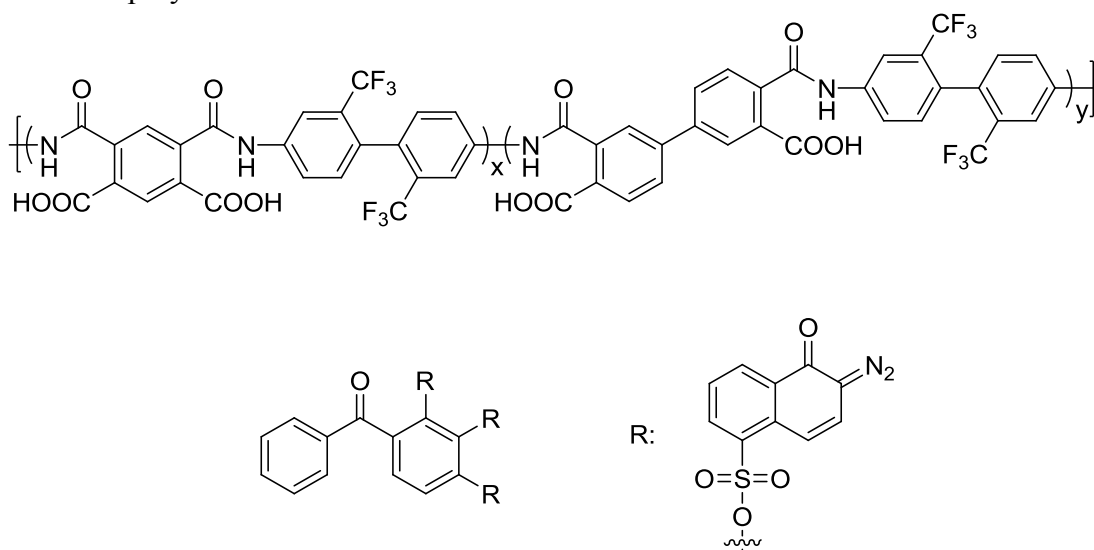
Figure 3.4: Positive-tone photosensitive polyimide based on a fluorinated poly(amic acid) copolymer (top) and a DNQ dissolution inhibitor (bottom).

There are many additional examples of both positive and negative tone photosensitive polyimides. However, rather than discussing every approach herein, the interested reader is instead directed to a comprehensive review.[131] The remainder of this section will instead focus on the methodology pioneered by IBM.

As discussed earlier, it was discovered that amine bases catalyze the imidization of polyimide precursors at relatively low temperature.[128] This effect was uncovered

85

largely by chance, as researchers noted differences in cure behavior of the poly(amic esters) depending on the purity of the NMP casting solvent. Interestingly, solutions of poly(amic ester) in relatively impure NMP were observed to gel during prolonged storage, indicative of significant imidization. As methylamine is a common impurity in NMP, amines were immediately suspected, and further purification of the solvent eliminated this behavior. Further studies demonstrated a direct relation to amine basicity, with stronger bases like DBU being particularly effective catalysts.[128, 142] A mechanism was proposed according to Figure 3.5.
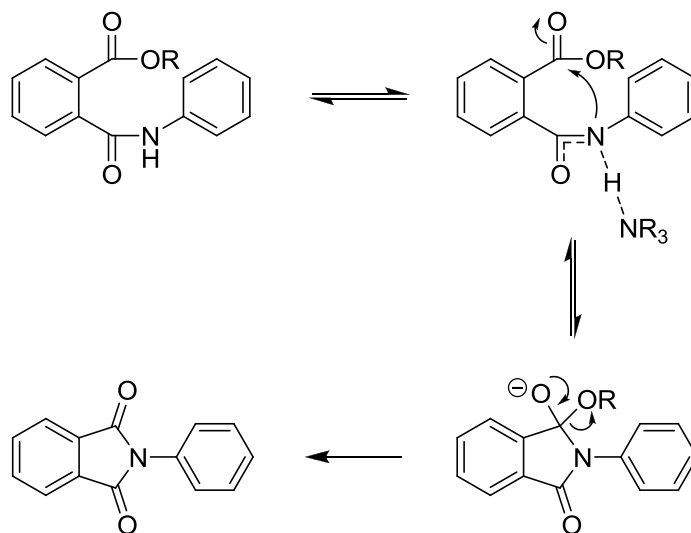
Figure 3.5: Proposed mechanism for amine-catalyzed imidization.[142]

Owing to the catalytic nature of this reaction and the significant decrease in solubility when converting the precursor into polyimide, the utility of this chemistry was immediately recognized. By formulating the poly(amic ester) with a photolatent amine (PBG), the IBM group produced a chemically-amplified negative-tone resist.[129, 130, 143] Upon irradiation, a small amount of amine is released in the poly(amic ester) film. This is followed by a post-exposure bake at a temperature where imidization occurs only in the

presence of amine (ca. 150 °C). This partial imidization reduces polymer solubility, allowing selective removal of unexposed regions. The key advantage of this approach is that the imaging and cure chemistry are the same. Rather than employing a sacrificial crosslinker which causes excessive shrinkage, or dissolution inhibitor which degrades material performance, this system simply requires addition of a small amount of PBG to a conventional polyimide precursor.

The main shortcoming of this imaging method results from the high optical density of most polyimide precursors. This results in extremely high dose requirements (> 1 J/cm^2) and limits patterning in thick films. In the case of the PMDA-ODA precursor, the maximum thickness was approximately 5 microns.[143] While thick by advanced lithography standards, this is nowhere near the 20+ microns commonly required of packaging materials.

Because few photobases are active at longer wavelengths (e.g. visible), emphasis was placed largely on reducing the optical density of the polyimide precursor. While improving transparency, these modifications also tend to degrade lithographic performance. Flexibility was introduced along the polymer backbone in order to break up conjugation and limit charge transfer. However, as the flexible backbone more readily dissolves, this decreases contrast between exposed and unexposed regions during development. Many recent demonstrations of photosensitive polyimide have employed this technique.[144-148] However, all have relied on near-UV photobases with transparent precursor backbones. Additionally, few of these demonstrate patterning in extremely thick films.[149] As PMDA-ODA (Kapton) will likely remain the preeminent polyimide, an efficient method of patterning is desirable. As such, it is the goal of this project to prepare a photobase generator which is active to the red of the PMDA-ODA precursor.

Of the many classes of photobase generators, ortho-nitrobenzyl carbamates (Figure 3.1) are the most popular. These compounds have been employed in a number of schemes where controlled release of amine is required.[11] The photolysis mechanism consists of an intramolecular redox reaction, forming ortho-nitrosobenzaldehyde, carbon dioxide, and free amine (Figure 3.6). In this example, the chromophore absorbs only at very short wavelengths (<300 nm). Further substitution can extend this to lower energies (Figure 3.7). However, the photolysis quantum efficiency tends to decrease dramatically when approaching visible wavelengths.
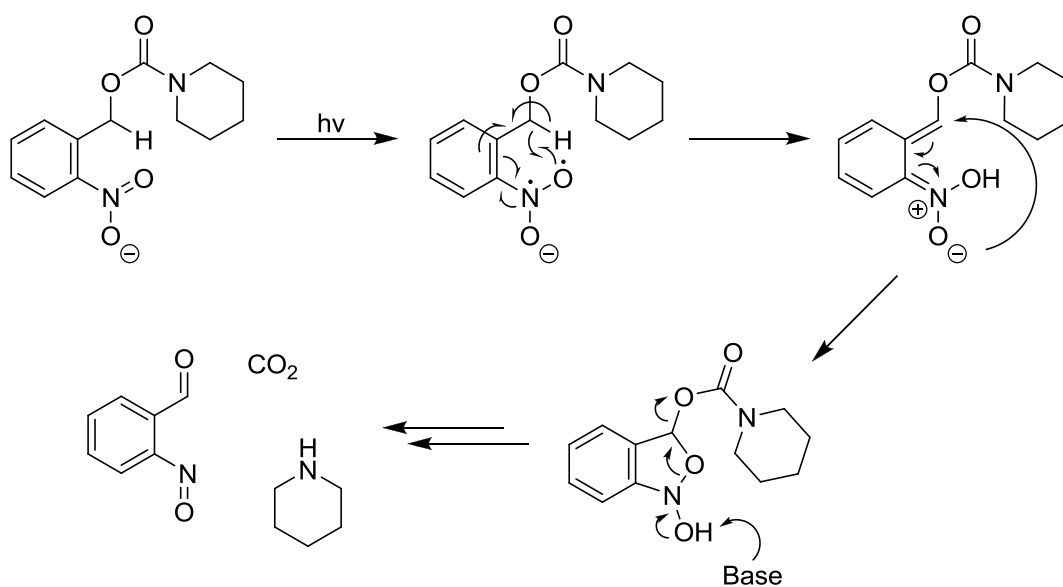
Figure 3.6: o-nitrobenzyl carbamate photolysis mechanism.

Rather than attempting to redshift the absorbance of an existing photobase via chromophore modification, it was decided to instead repurpose an existing visible light photoactive compound. There is some precedent for this strategy, as o-nitrobenzyl

sulfonate esters were evaluated as covalent PAGs well before the development of o-nitrobenzyl carbamate photobases (Figure 3.7).[150]
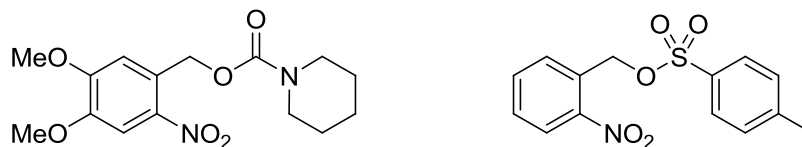
Figure 3.7: Near-UV o-nitrobenzyl carbamate PBG (left) and o-nitrobenzyl sulfonate ester PAG (right).

This approach could be further extended to oxime sulfonates, such as the visible light photoacid generator manufactured by BASF (Figure 3.8).[126, 151] This unusual thiophene-derived chromophore (*vide infra*) gives rise to very strong absorbance up to 450 nm (Figure 3.9). Irradiation forms the sulfonic acid with reasonable quantum efficiency (>0.1) using 436 nm light (g-line).[151] Importantly for patterning, the chromophore bleaches readily at the exposure wavelength, allowing adequate light transmission through thick films.
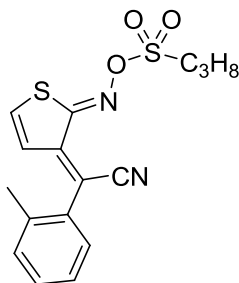
Figure 3.8: Irgacure PAG 103 (BASF).
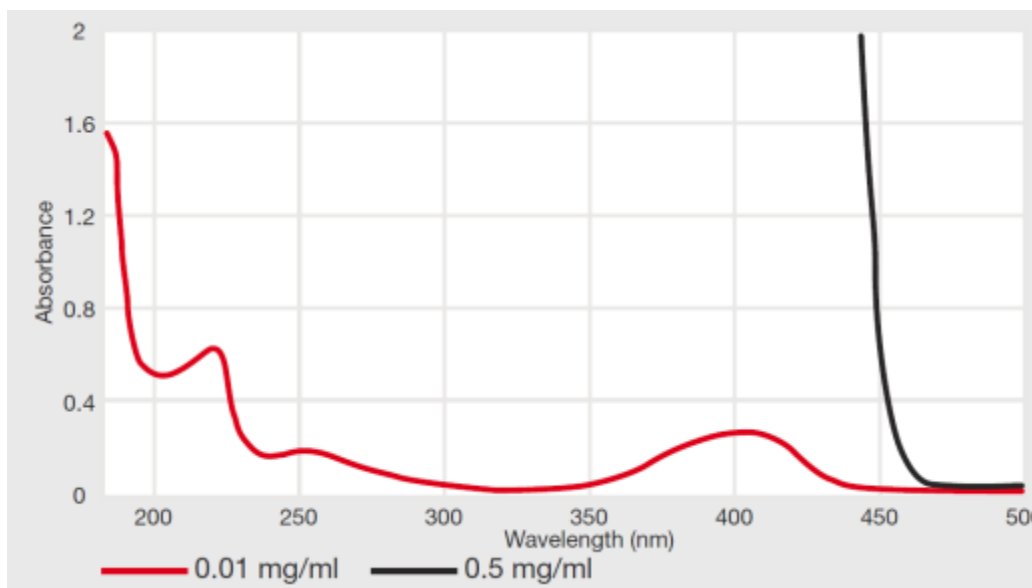
Figure 3.9: Irgacure PAG 103 absorbance spectrum.[126]

As with the o-nitrobenzyl compounds, the sulfonate ester can be replaced with a carbamate to produce a compound which releases amine upon irradiation, and there exist several deep-ultraviolet photobase generators derived from aromatic oxime-urethanes.[152-155] The core structure of the proposed PBG is shown Figure 3.10.
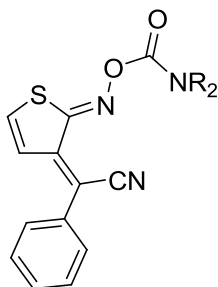
Figure 3.10: General design of the visible-light photobase generator.

OXIME-URETHANE PHOTOBASE

The precursor oxime is produced in a single step from 2-nitrothiophene and phenylacetonitrile in basic methanol (Figure 3.11).[156] This reaction is general to nitro-

aromatics, and was first observed with nitrobenzene.[157, 158] In nitrobenzene, addition is preferential to the 4-position, though 4-substituted nitrobenzene derivatives will undergo similar addition at the 2-position.[159] However in 2-nitrothiophene, addition is preferential to the 3-position. In the original report, the structure was incorrectly assigned as the 5-addition product, which was later refuted by x-ray crystallography.[156, 160, 161]
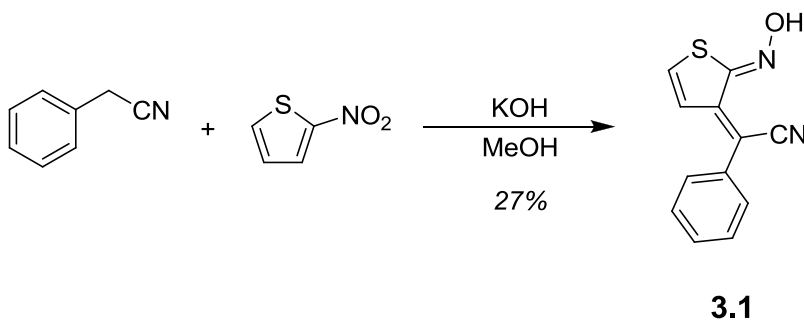
Figure 3.11: Synthesis of oxime **3.1**.

Unlike nitrobenzene, addition of phenylacetonitrile anion to 2-nitrothiophene results in side-reactions, yielding a very complex mixture of products. In addition to formation of both E and Z-isomers about the new double bond, significant degradation occurs with extended reaction times. Optimal results were obtained by stopping the reaction after 5 hours. As the Z-isomer is the major product and the basis of the BASF photoacid generator, it was used exclusively.[160]

The crude material obtained from this reaction was a black tar which required several purification steps. Column chromatography eliminated most byproducts. However, complete separation of the E and Z-isomers by chromatography was impractical. One or more crystallizations were generally required following chromatography in order to completely eliminate the E-isomer. The carbamate was prepared in the conventional manner, by reacting the parent oxime with the appropriate

carbamyl chloride (Figure 3.12). Base generation in **3.2** was confirmed by ^{1}H NMR (Figure 3.13). In acetonitrile, the carbamate N-methylene protons resonate at 4.56 ppm; exposure to 405 nm light results in a steady decrease in this peak. Dibenzylamine release is evidenced by the appearance of a peak at 3.75 ppm.

3.1   **3.2**
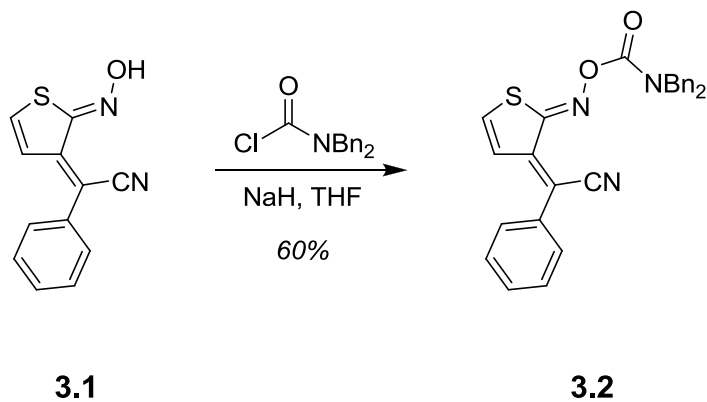
Figure 3.12: Synthesis of dibenzyl carbamate **3.2**.
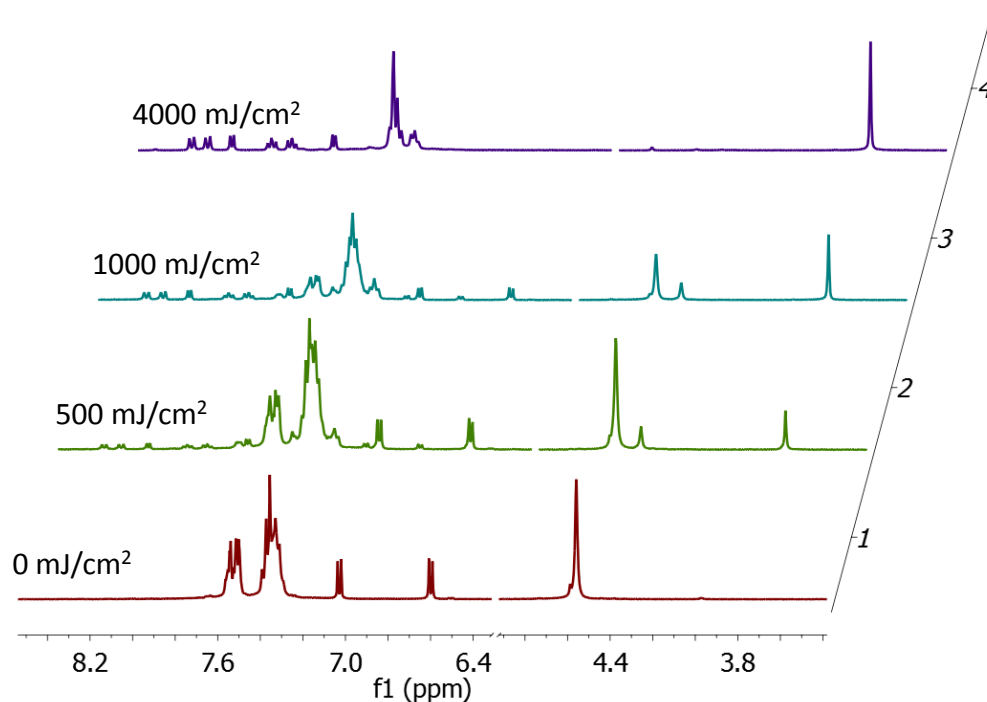
Figure 3.13: Partial ^{1}H NMR spectra of **3.2** during exposure (7 mM in CD$_3$CN, 405 nm irradiation). Note the 15° offset.

Carbamate **3.2** was previously studied by our group as a photobase generator.[160] While exhibiting promising photochemistry, the thermal stability was found to be inadequate for this application (T$_d$: 145 °C), and we sought to modify the core structure of **3.2** in an attempt to improve this. In reviewing the original Ciba patent, it was noted that oxime sulfonates derived from the 1-nitronaphthalene adduct exhibited particularly high thermal stability (ca. 200 °C).[156] However, the patent results also suggested that these derivatives are photochemically inactive. As such, the thianaphthene analog was proposed as a possible compromise between thermal stability and photochemical efficiency (Figure 3.14).
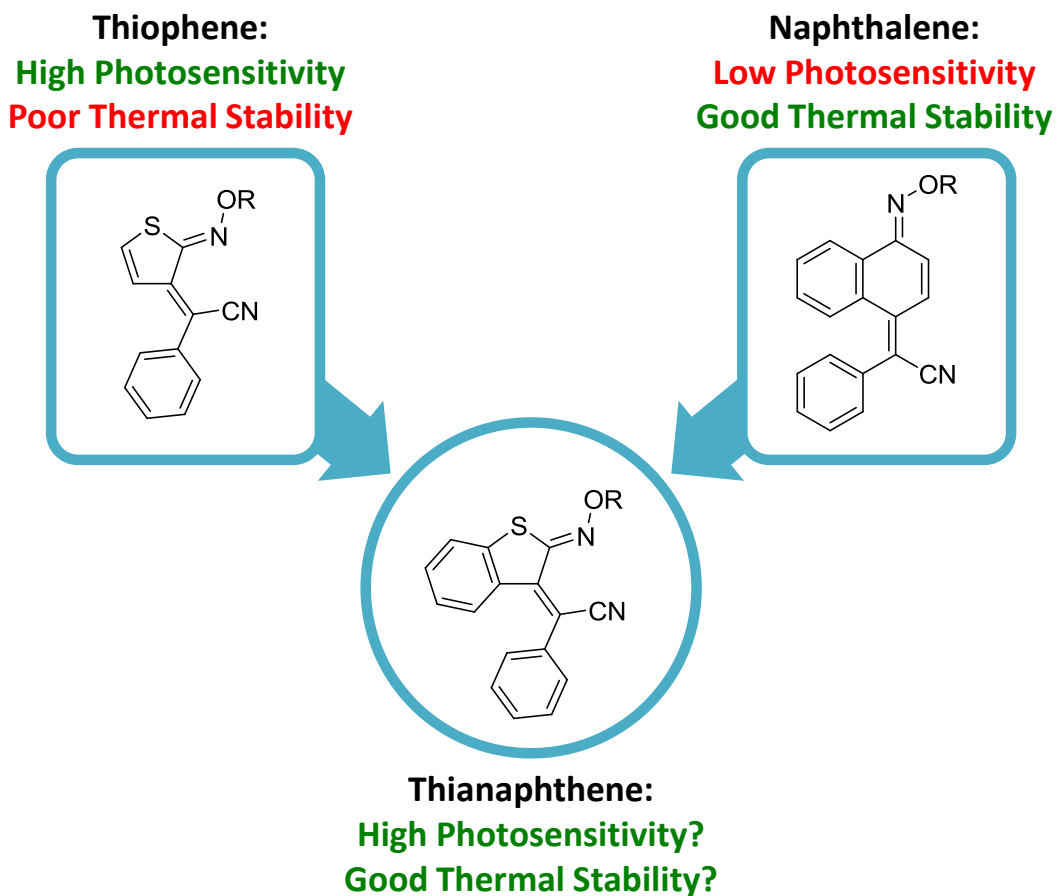
Figure 3.14: Proposed thianaphthene oxime chromophore.

THIANAPHTHENE

The thianaphthene analog was prepared as shown in Figure 3.15. As direct nitration of thianaphthene yields a large amount of the 3-isomer, it is advantageous to first block this position.[162] Bromination of commercial thianaphthene yielded **3.3**, which was subsequently nitrated.[163] Even with the blocking group, this reaction produces a complex mixture of nitration products. Fortuitously, the desired material can be isolated by crystallization from ethanol. Removal of the blocking group from **3.4** by common methods such as copper/quinoline led to rapid degradation and poor isolated yield

(<20%).[162] An alternative procedure using copper/benzoic acid resulted in much higher yields and required minimal purification.[164-166]
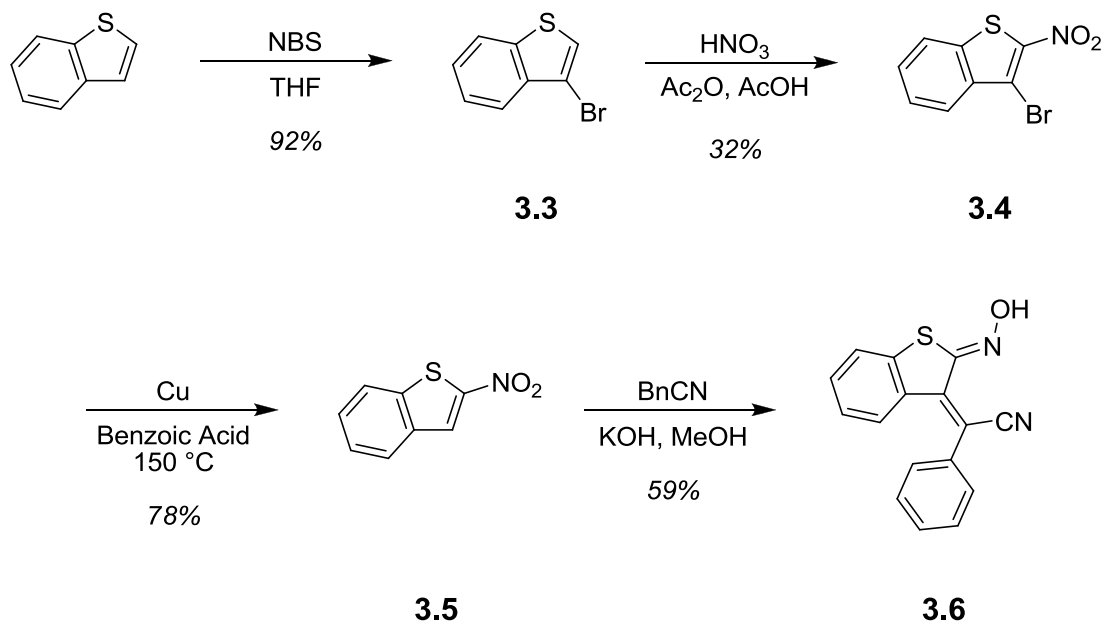
Figure 3.15: Synthesis of 2-nitrothianaphthene oxime (**3.6**).

With **3.5** in hand, the reaction with phenylacetonitrile was performed. This substrate resulted in a much cleaner reaction, as evidenced by thin-layer chromatography. Furthermore, a dramatic difference was noted in the color of the reaction. Using 2-nitrothiophene, the solution quickly darkens from reddish-orange to a brown/black. Conversely, the reaction of **3.5** forms a brilliant yellow color, which does not change appreciably with extended reaction times. As long as the solution is protected adequately from light, no product decomposition occurs and **3.6** is obtained in reasonable yield. Carbamate **3.7** was then prepared in manner analogous to **3.2** (Figure 3.16).
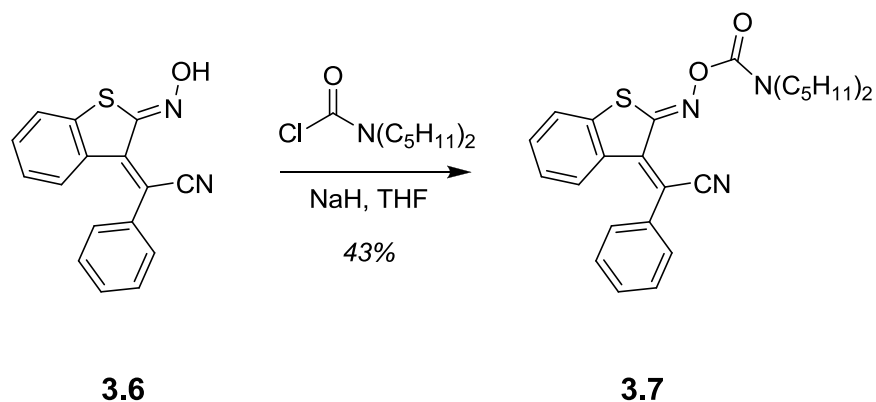
Figure 3.16: Synthesis of carbamate **3.7**.

PHOTOPHYSICAL EVALUATION

Absorbance of **3.7** was measured by ultraviolet-visible spectroscopy (Figure 3.17). The carbamate absorbs out to 450 nm, allowing for initiation with either mercury h (405 nm) or g-line (436 nm) radiation. As the polyimide precursor is transparent at these wavelengths, this material is extremely promising for use in thick films. Photobleaching experiments were conducted in acetonitrile using 405 nm light (Figure 3.18). This material bleaches cleanly and efficiently, as evidenced by the many isosbestic points—suggesting stoichiometric conversion of **3.7** to photoproducts. An important observation is the presence of an isosbestic point at 400 nm (Figure 3.18 inset), indicating a photoproduct which absorbs significantly at this wavelength. This absorbance persists even at very high doses (>1 J/cm^2), precluding the use of an h-line source for thick film patterning. However, bleaching at 436 nm is significant. Therefore, a g-line source would be more appropriate for patterning. As this a more common wavelength in photolithography, this photobase is compatible with existing infrastructure.
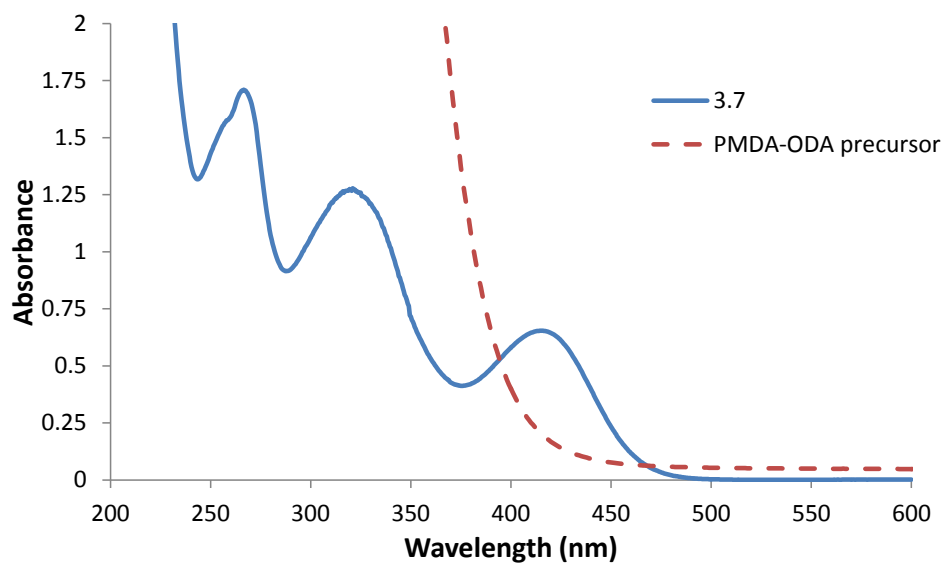
Figure 3.17: UV-Vis spectrum of carbamate **3.7** in acetonitrile (9E-5 M). A 7.5 micron film of polyimide precursor is shown for comparison.
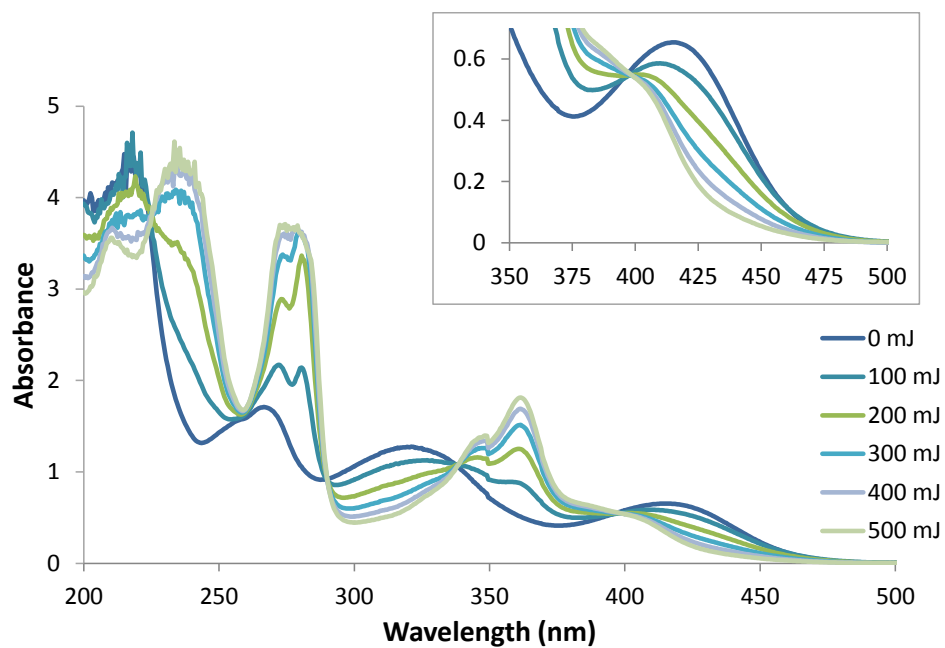
Figure 3.18: Photobleaching of carbamate **3.7** upon h-line irradiation (9E-5 M in acetonitrile).

To determine whether amine is formed, NMR was used to monitor photolysis of carbamate **3.7** (Figure 3.19). In acetonitrile, the carbamate N-methylene protons are observed at 3.35 ppm. Upon h-line exposure, this peak steadily decreases, disappearing completely at doses above 3.5 J/cm^2. The desired photoproduct, dipentylamine, appears at 2.5 ppm as confirmed by standard addition. An unexpected observation is the formation of a new peak at 3.2 ppm at intermediate doses. This resonance is consistent with the E-isomer of **3.7** (Figure 3.20).
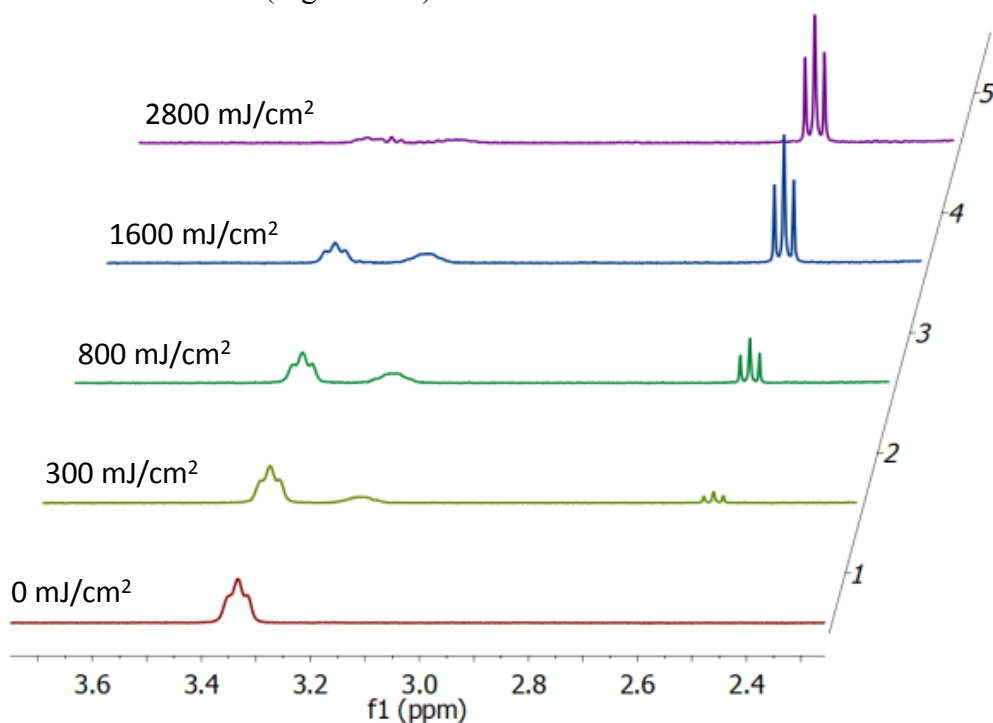
Figure 3.19: Selected NMR spectra of **3.7** during exposure (7 mM in CD$_3$CN, 405 nm irradiation). Note the 15° offset.
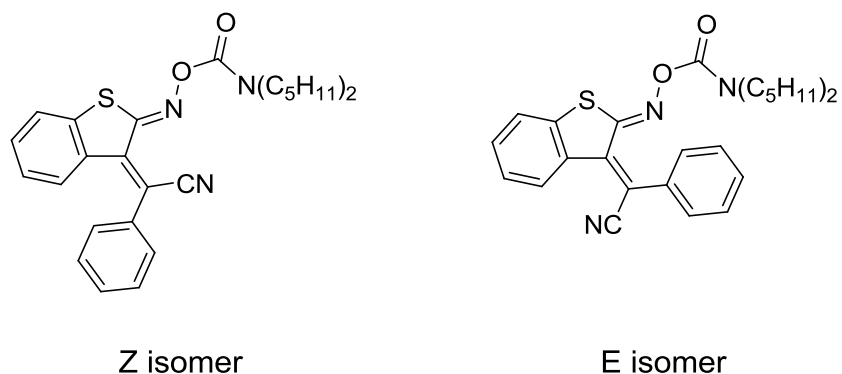
Z isomer   E isomer

Figure 3.20: Z and E isomers of **3.7**.

As the photolysis spectra were extremely clean, these three peaks could be tracked over the course of the entire experiment. Figure 3.21 shows the relative conversion of the starting PBG into the E-isomer and dipentylamine. Initially, amine formation is somewhat delayed; the primary photoproduct at lower doses is the E-isomer of **3.7**, as confirmed by preparative photolysis. This photoisomerization hints at a two-stage photolysis mechanism, and the apparent nonlinear amine generation is consistent with previous work with **3.2**.[160] However, further study is needed to confirm this. Ultimately, **3.7** is photolyzed quantitatively to dipentylamine using h-line radiation (3.6 J/cm^2). An important note is that doses given for solution-phase experiments do not directly translate to lithographic dose. These results are in fact comparable to several sensitive i-line photobases.[147, 149]
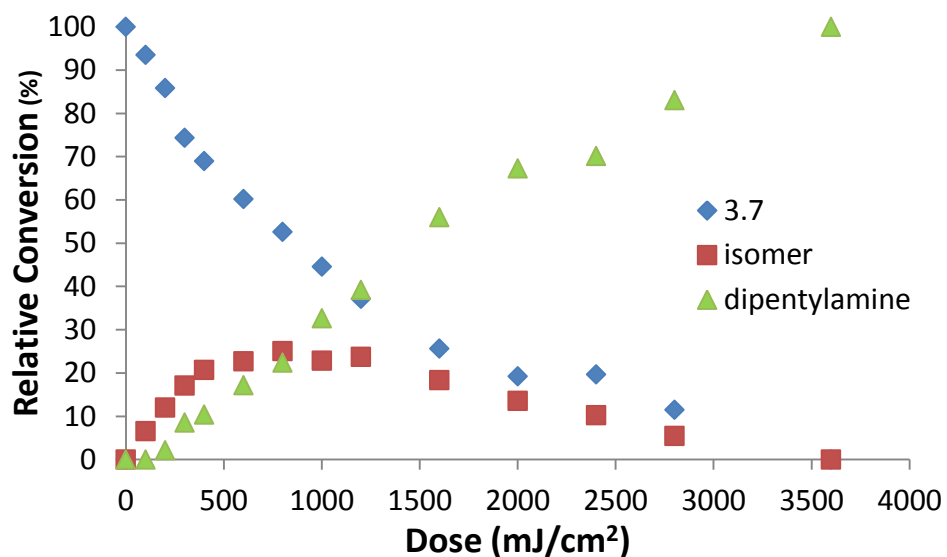
Figure 3.21: Conversion of **3.7** to free amine as determined by NMR (7 mM in CD$_3$CN, 405 nm radiation).

THERMAL STABILITY

As described in the introduction, amine-catalyzed imidization requires elevated temperatures (typically 150 °C) to occur in the solid phase. This requires that the photobase generator is stable at this temperature, or at the very least, does not decompose thermally to form amine. As can be seen in Figure 3.22, degradation of **3.7** begins at 100 °C. Examining the TGA trace, there are two distinct decomposition events. The first occurs between 100 and 135 °C and corresponds to a 43.5% mass loss. This observation is in good agreement with mass loss expected with the elimination of dipentylamine and carbon dioxide (43.6%). Given these results, **3.7** must be ruled out as a candidate photobase generator for this application.
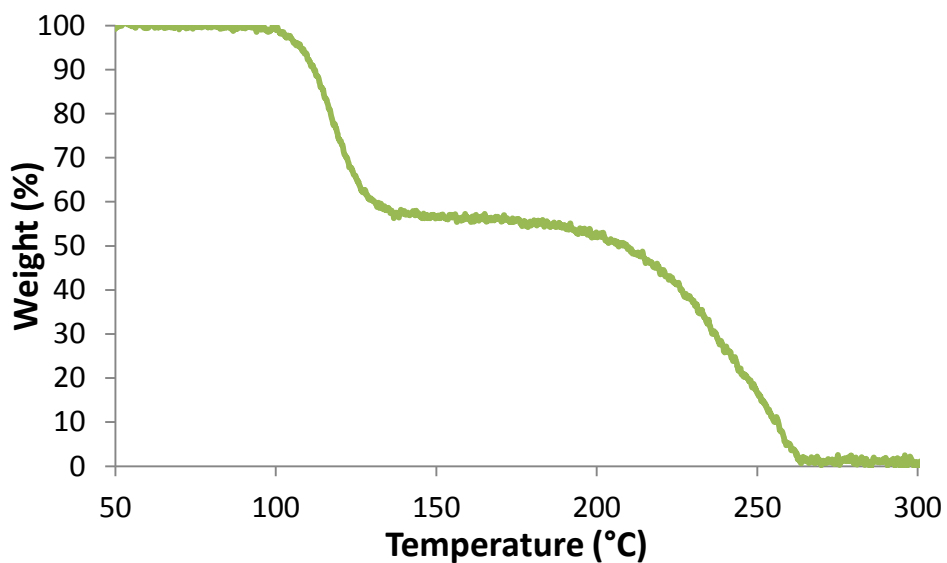
Figure 3.22: Thermogravimetric analysis of carbamate **3.7**.

As the second decomposition event does not occur until much higher temperatures, it was reasoned that the chromophore itself is relatively stable. Indeed, the parent oxime **3.6** exhibits no mass loss below 175 °C and the methanesulfonate ester of **3.6** is stable to 170 °C. Interestingly, this methanesulfonate ester is significantly more stable than Irgacure PAG 103 (T_d: 140 °C).[126] More importantly, it was anticipated that modification of the carbamate would improve stability.
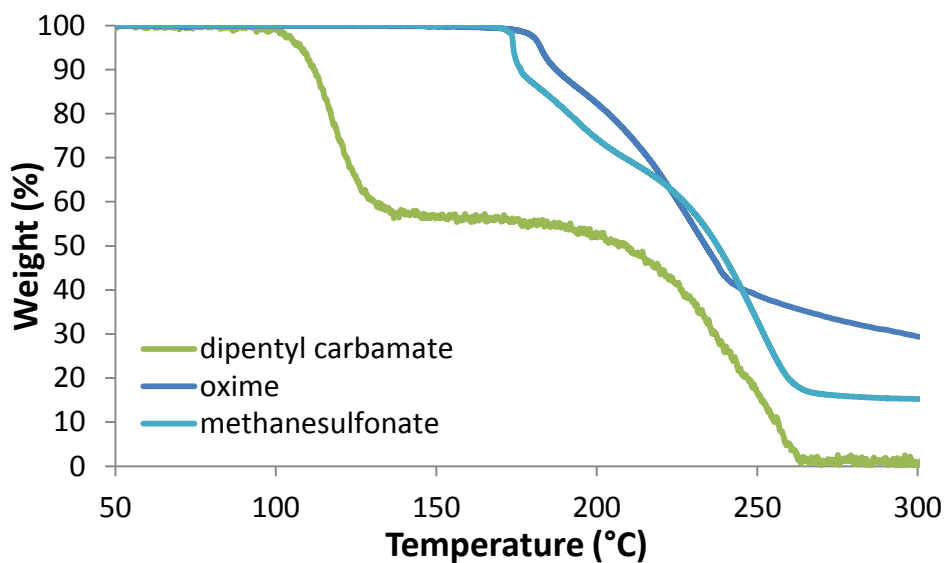
Figure 3.23: Comparison of **3.7** with oxime **3.6** and the methanesulfonate ester.

Dipentylamine was chosen for its high boiling point (202-203 °C) in order to minimize catalyst evaporation during the post-exposure bake step. However, these bulky pentyl substituents were suspected to contribute to the extremely low thermal stability of **3.7**. Several modified carbamates were thus prepared, using both shorter alkyl chains, as well as aromatic substituents. Both approaches resulted in higher decomposition temperatures (Figure 3.24). While both the phenyl carbamate (T_d: 183 °C) and diphenyl carbamate (T_d: 155 °C) exceed the target of 150 °C, the concomitant decrease in basicity of the free amines limits their effectiveness as imidization catalysts. Additionally, the phenyl carbamate has poor solution stability due to the reverse reaction to form phenyl isocyanate and **3.6**.
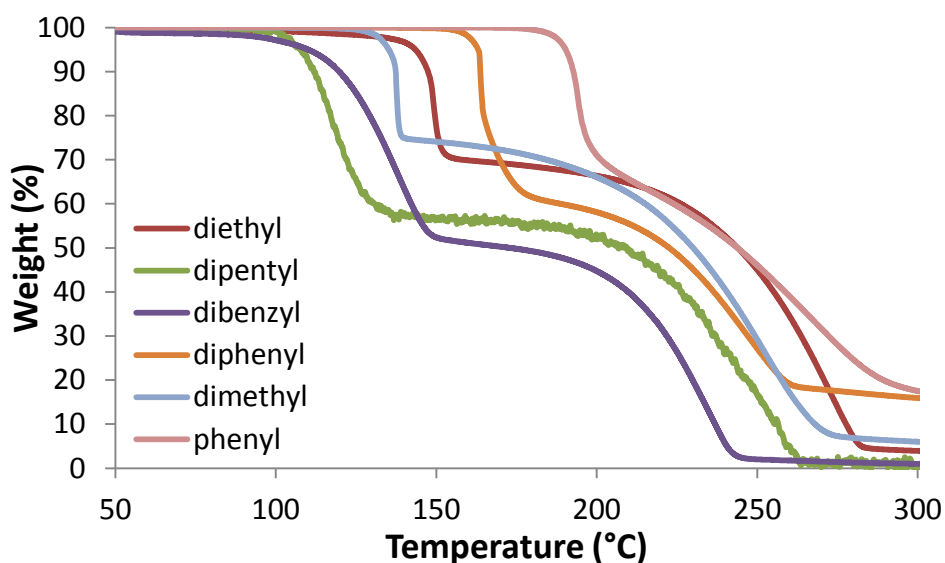
Figure 3.24: Effect of carbamate substitution on thermal stability.

CONCLUSIONS

A thiophene-derived oxime urethane was evaluated as a candidate visible-light photobase generator for the direct patterning of polyimide. The chromophore was synthesized by the condensation of phenylacetonitrile with 2-nitrothianaphthene to produce a structure with significant absorbance up to 450 nm. Carbamate **3.7** was shown to photobleach rapidly upon h-line (405 nm) irradiation. NMR photolysis experiments confirmed the generation of amine with exposure to this wavelength. As the absorbance extends to 450 nm, this PBG is presumably also effective at g-line (436 nm). In keeping with previous observations, photogeneration of amine appears to be nonlinear and may occur in a two-stage process.

As the thermal stability of **3.7** was inadequate, several derivatives were prepared. Aromatic substituents provided thermal stabilities in excess of the target 150 °C, though at the expense of amine basicity. Unfortunately, the effectiveness of amines as imidization catalysts scales with their basicity, and little is gained through this approach.

Though this photobase generator does not meet the requirements for the direct patterning of polyimide, it may find use in applications which do not require high thermal stability. Currently there exist few, if any, visible-light sensitive photobase generators with appreciable efficiency. Moreover, **3.7** is a potential starting point for many long-wavelength photoactive compounds, and further chromophore modification might yield compounds with even longer wavelength activity.

EXPERIMENTAL

General Methods and Materials

All solvents and reagents were obtained from Sigma-Aldrich and were used without further purification except where noted. TEA was distilled from CaH_2 while THF was distilled from sodium/benzophenone. Reactions were run in flame-dried glassware and under an atmosphere of nitrogen unless otherwise noted. Photosensitive reactions were protected from ambient light by wrapping reaction flasks with aluminum foil. ^1H and ^{13}C NMR spectra were recorded on a Varian Unity Plus 400 MHz instrument. Chemical shifts are reported in ppm downfield from TMS using residual protonated solvent as an internal standard (DMSO-d_6, ^1H 2.49 ppm and ^{13}C 39.5 ppm or CDCl$_3$, ^1H 7.26 ppm and ^{13}C 77.0 ppm). Coupling constants are expressed in Hz. HRMS (CI) was obtained on a VG analytical ZAB2-E instrument while HRMS (ESI) was obtained on an Ion Spec FT-ICR (7 Tesla) instrument. IR data was recorded on a Nicolet Avatar 360 FT-IR using either a KBr pellet or thin film on a NaCl disc. Melting points were recorded using a Mel-Temp II and are uncorrected. Thermogravimetry was performed using a TA Instruments Q500 TGA.
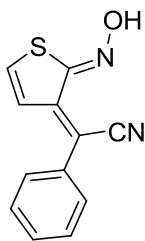
Synthesis of (Z)-2-((Z)-2-(hydroxyimino)thiophen-3(2H)-ylidene)-2-phenylacetonitrile (3.1). Potassium hydroxide (10.844 g, 193.26 mmol) was dissolved in 50 mL of methanol and added to a 250 mL round-bottom flask. This solution was cooled to 0 °C and benzyl cyanide (5.711 g, 48.75 mmol) was added dropwise. 2-nitrothiophene (6.214 g, 48.12 mmol) was then dissolved in 50 mL of methanol and added to the reaction over a 25 minute period. The solution rapidly became dark orange, and then gradually faded to deep brown/black. After 20 minutes, the reaction was quenched with 50% acetic acid/water at 0 °C and diluted with ethyl acetate. This solution was washed with water and brine, dried with $MgSO_4$, filtered and concentrated to obtain approximately 11 grams of a black, tarry substance. This material was purified by column chromatography (20% ethyl acetate in hexanes) and crystallization from toluene to yield a deep brown solid (2.983 g, 27% yield). MP: 168-170 °C (dec); ^{1}H NMR (400 MHz, DMSO-d6): δ 6.56 (d, J = 6.6 Hz, 1H), 7.38 (d, J = 6.6 Hz, 1H), 7.53 − 7.41 (m, 5H), 13.24 (s, 1H); ^{13}C NMR ($CDCl_3$): δ 104.29, 119.28, 122.58, 129.10, 129.12, 129.41, 134.55, 136.25, 145.63, 151.92; HRMS [M+H]$^+$ calcd. = 229.0436, found = 229.0435; FTIR ν = 3220 (br), 3008, 2955, 2835, 2215, 1525, 1492, 1428, 1334, 1285, 1258, 1230, 1112, 989, 839 cm^{-1}.
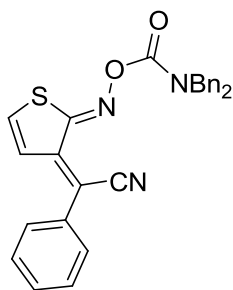
Synthesis of (Z)-2-((Z)-2-(dibenzylcarbamoyloxyimino)thiophen-3(2H)-ylidene)-2-phenylacetonitrile (3.2). To a 25 mL round-bottom flask added **3.1** (0.337 g, 1.48 mmol), dry THF (10 mL) and dibenzylcarbamyl chloride (1.299 g, 5.00 mmol). This solution was cooled to -78 °C and NaH (0.028 g, 60% mineral oil dispersion—0.694 mmol) was added in one portion. The reaction was then shielded from light and warmed to room temperature. Stirring was continued for 4 hours, after which the reaction was quenched with water and diluted with ethyl acetate (50 mL). This extract was washed three times with water and once with brine, dried over MgSO$_4$, filtered and concentrated. The crude material was purified by column chromatography (30% ethyl acetate in hexanes), followed by crystallization from toluene to yield **3.2** as a yellow solid (0.401 g, 60%). MP: 140-142 °C; ^{1}H NMR (400 MHz, CDCl$_3$): δ 7.24-7.52(m, 15H), 6.816(d, J=6.4, 1H), 6.626(d, J=7.6, 1H), 4.55(s, 2H), 4.45(s, 2H); ^{13}C-NMR (100 MHz, CDCl3): δ 153.07, 144.26, 136.43, 134.43, 132.68, 130.06, 129.43, 129.02, 127.77, 123.15, 118.01, 111.2, 50.31, 49.27; HRMS [M+H]$^+$ calcd. = 452.1433 found = 452.1432; FTIR ν = 3109, 2207, 1740, 1521, 1494, 1453, 1410, 1323, 1263, 1198, 1086, 1010, 943, 866, 778 cm^{-1}.
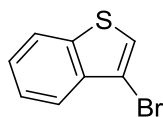
Synthesis of 3-bromobenzo[b]thiophene (3.3). Benzo[b]thiophene (5.051 g, 37.64 mmol) was dissolved in 120 mL THF and added to a 250 mL round-bottom flask. The solution was cooled to 0 °C and NBS (10.147 g, 57.01 mmol) was added portionwise. The mixture was stirred for 30 minutes at 0 °C, then warmed to room temperature and stirred for an additional 48 hours. The reaction was quenched with aqueous $Na_2S_2O_3$ and extracted with ether. The extracts were combined and washed, dried with $MgSO_4$, filtered and concentrated to obtain approximately 10 grams of crude material. This was purified by column chromatography (hexanes), yielding a clear oil (7.373 g, 92%). ^{1}H NMR (400 MHz, CDCl$_3$): δ 7.91 – 7.79 (m, 2H), 7.56 – 7.35 (m, 3H); ^{13}C NMR (101 MHz, CDCl$_3$): δ 138.40, 137.33, 125.14, 124.88, 123.36, 122.89, 122.57, 107.57; HRMS [M]$^+$ calcd. = 211.9295 found = 211.9294; FTIR ν = 3104, 3058, 1492, 1453, 1429, 1316, 1253, 1145, 1060, 1017, 929, 820 cm^{-1}.
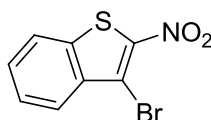
Synthesis of 3-bromo-2-nitrobenzo[b]thiophene (3.4). To a 500 mL round bottom flask was added 3-bromobenzo[b]thiophene (12.795 g, 60.045 mmol) and 200 mL of acetic anhydride. The solution was cooled to 0 °C and a mixture of 25 mL of nitric acid and 20 mL of acetic acid was added dropwise with vigorous stirring. A yellow precipitate began to form after several minutes. Once the addition was complete, the ice bath was removed and the reaction stirred for two hours at room temperature. The mixture was then poured into ice water and the resulting precipitate collected by filtration. The solid was washed with water and crystallized from ethanol, yielding a

107

fluffy golden solid (4.926 g, 32%). Only the first crop of material contains the desired product. MP: 160-162 °C; ^{1}H NMR (400 MHz, DMSO-d6) δ 7.65 (ddd, J = 8.2, 7.2, 1.1 Hz, 1H), 7.73 (ddd, J = 8.4, 7.2, 1.3 Hz, 1H), 7.99 (ddd, J = 8.2, 1.2, 0.7 Hz, 1H), 8.16 (ddd, J = 8.2, 1.4, 0.9 Hz, 1H); ^{13}C NMR (101 MHz, DMSO-d6): δ 111.89, 123.79, 126.29, 127.26, 130.72, 136.45, 136.60, 145.96; HRMS [M+H]$^+$ calcd. = 257.9224, found = 257.9220; FTIR ν = 3074, 1591, 1552, 1520, 1484, 1334, 1303, 1243, 917, 867, 803, 761, 740, 727, 710 cm^{-1}.
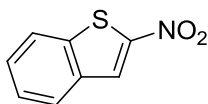
Synthesis of 2-nitrobenzo[b]thiophene (3.5). 3-bromo-2-nitrobenzo[b]thiophene (4.313 g, 16.71 mmol) and benzoic acid (7.555 g, 61.87 mmol) were added to a 3-neck 100 mL round bottom flask. The solids were mixed thoroughly with a magnetic stir bar and the reaction was purged 3 times before heating to 150 °C. Under a cone of nitrogen, copper powder (5.159 g, 81.19 mmol) was then added to the melt. The reaction was stirred for an additional 30 minutes at 150 °C, then slowly cooled to room temperature. The resulting solid was suspended in dichloromethane and the residual copper was removed by gravity filtration. The DCM solution was washed three times with saturated NaHCO$_3$, once with water and once with brine.   This was then dried over MgSO$_4$, filtered and concentrated to obtain a golden power (2.326 g, 78%). MP: 109-112 °C; ^{1}H NMR (400 MHz, CDCl$_3$): δ 8.20 (d, J = 3.3 Hz, 1H), 7.88 (ddd, J = 38.1, 8.1, 2.6 Hz, 2H), 7.53 (dtd, J = 15.0, 7.2, 2.9 Hz, 2H); ^{13}C NMR (101 MHz, CDCl$_3$): δ 151.32, 140.33, 136.08, 129.13, 127.00, 126.11, 125.61, 122.89; HRMS [M]$^+$ calcd. = 179.0041 found = 179.0044; FTIR ν = 3098, 1594, 1558, 1516, 1496, 1451, 1424, 1346, 1315, 1250, 1190, 1160, 1126, 1081, 1052, 872, 849, 802, 757 cm^{-1}.
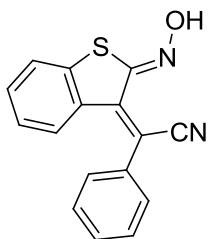
Synthesis of (Z)-2-((Z)-2-(hydroxyimino)benzo[b]thiophen-3(2H)-ylidene)-2-phenylacetonitrile (3.6). Potassium hydroxide (0.530 g, 9.44 mmol) was dissolved in 10 mL of methanol and added to a 50 mL round-bottom flask. The solution was then cooled to 0 °C and benzyl cyanide (0.276 g, 2.36 mmol) was added dropwise. 2-nitrobenzo[b]thiophene (0.422 g, 2.36 mmol) was dissolved in 25 mL of methanol and added dropwise to the reaction vessel. The solution immediately became brilliant yellow and gradually darkened to a vibrant orange color. The reaction was then protected from light by covering the flask with aluminum foil and stirred overnight at room temperature. Upon completion as determined by TLC, the reaction was poured into 200 mL of water, then acidified with 50% acetic acid/water. The resulting suspension was extracted 3 times with ethyl acetate. The extracts were combined, washed with water and brine, dried with MgSO$_4$, filtered and concentrated to obtain 0.62 grams of crude material. Purification by column chromatography (20% ethyl acetate in hexanes) yielded **3.6** as a yellow powder (0.389 g, 59%). MP: 184-185 °C (dec; sample darkened at 175 °C without melting); ^{1}H NMR (400 MHz, DMSO-d6): δ 13.15 (s, 1H), 7.70 – 7.48 (m, 6H), 7.39 – 7.30 (m, 1H), 6.89 (ddd, J = 8.4, 7.4, 1.2 Hz, 1H), 6.38 (dd, J = 8.2, 0.5 Hz, 1H); ^{13}C NMR (101 MHz, DMSO-d6): δ 150.94, 142.23, 139.12, 134.36, 132.32, 131.78, 130.11, 128.83, 128.70, 126.63, 125.30, 123.83, 119.38, 106.56; HRMS [M+H]$^+$ calcd. = 279.0592 found = 279.0590; FTIR ν = 3325, 3061, 2201, 1583, 1546, 1487, 1445, 1363, 1308, 1286, 1261, 1211, 1166, 988, 892, 766 cm^{-1}.
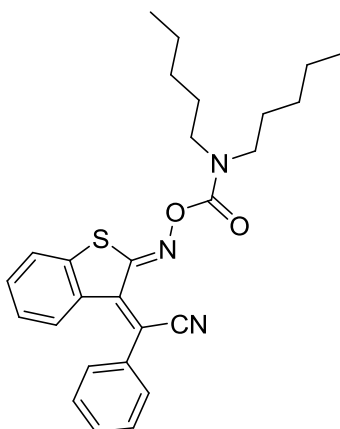
Synthesis of (Z)-2-((Z)-2-(dipentylcarbamoyloxyimino)benzo[b]thiophen-3(2H)-ylidene)-2-phenylacetonitrile (3.7). To a 5 mL round-bottom flask added **3.6** (0.109 g, 0.392 mmol), dry THF (3 mL) and dipentylcarbamyl chloride (0.315 g, 1.43 mmol). This solution was cooled to -78 °C and NaH (0.037 g, 60% mineral oil dispersion—0.925 mmol) was added in one portion. The reaction was then shielded from light and warmed to room temperature. Stirring was continued for 3 hours, at which point all starting material was consumed, as determined by TLC. The reaction was then quenched with water and diluted with ethyl acetate (50 mL). This was washed three times with water and once with brine, dried over $MgSO_4$, filtered and concentrated to obtain 0.286 grams of crude material. Crystallization from hexanes yielded **3.7** as a yellow solid (0.077 g, 43%). MP: 106-108 °C (dec; pronounced outgassing from the melt was observed, suggesting carbamate thermolysis); ^{1}H NMR (400 MHz, CD_3CN): δ 7.66 – 7.46 (m, 5H), 7.42 (d, J = 7.9 Hz, 1H), 7.34 (t, J = 7.6 Hz, 1H), 6.88 (dd, J = 8.2, 7.3 Hz, 1H), 6.50 (d, J = 8.3 Hz, 1H), 3.33 (t, J = 7.1 Hz, 4H), 1.65 (d, J = 27.1 Hz, 4H), 1.38 (s, 8H), 0.94 (s, 6H); ^{13}C NMR (101 MHz, CD_3CN): δ 159.54, 153.20, 142.84, 139.16, 135.45, 133.43, 132.76, 131.27, 131.09, 129.41, 128.13, 126.77, 124.30, 119.46, 111.93, 49.10, 48.58, 29.84, 29.64, 29.28, 28.30, 23.16, 14.36; HRMS [M+Na]$^+$ calcd. = 484.2029 found =

484.2039; FTIR ν = 2956, 2927, 2858, 2199, 1739, 1584, 1538, 1489, 1460, 1440, 1414, 1312, 1272, 1232, 1204, 1139, 1010, 972, 859, 757 cm^{-1}.

Photobleaching

UV/Visible spectra were collected using a Cary 1E spectrophotometer (Varian). A 9E-5 M stock solution of **3.7** was prepared in acetonitrile. Solutions were *not* degassed prior to exposure. Samples were irradiated in a quartz cell using a Novacure 2100 spot curing system (Lumen Dynamics) at a 5 inch distance. The source was filtered using a 405 nm bandpass filter (A_{405}: 1.571; 20 nm FWHM). The resulting intensity was 0.55 mW/cm^2, as measured using a PowerMax PM3 thermopile (Coherent) connected to a Field Max II power meter (Coherent).

NMR Photolysis

^{1}H NMR spectra were collected using a Varian Unity Plus 400 MHz instrument. Photobases were dissolved in CD$_3$CN to a concentration of 7 mM. The solutions were *not* degassed prior to exposure. Samples were irradiated using a Novacure 2100 spot curing system (Lumen Dynamics) at a 5 inch distance. The source was filtered using a 405 nm bandpass filter (A_{405}: 1.571; 20 nm FWHM). The resulting intensity was 0.46 mW/cm^2, as measured using a PowerMax PM3 thermopile (Coherent) connected to a Field Max II power meter (Coherent).

Chapter 4: Directly-Patternable Polyimide Dielectrics

INTEGRATED CIRCUIT PACKAGING

Photolithography and the pattern transfer processes described in Chapter 1 take place at the wafer level. In the final stages of semiconductor device fabrication, the painstakingly processed silicon wafer is diced into many individual chips (Figure 4.1). Each chip (commonly "die") is then encapsulated within a robust housing. Colloquially referred to as the "package," this enclosure isolates and supports the fragile die, protecting it from potential sources of damage. While an exposed integrated circuit will fail rapidly outside of a well-controlled laboratory or manufacturing environment, a packaged device can be handled by the end user with minimal precaution. Depending on the intended application, the package may be designed to withstand particularly harsh environments (high temperature, humidity, radiation flux, etc.).
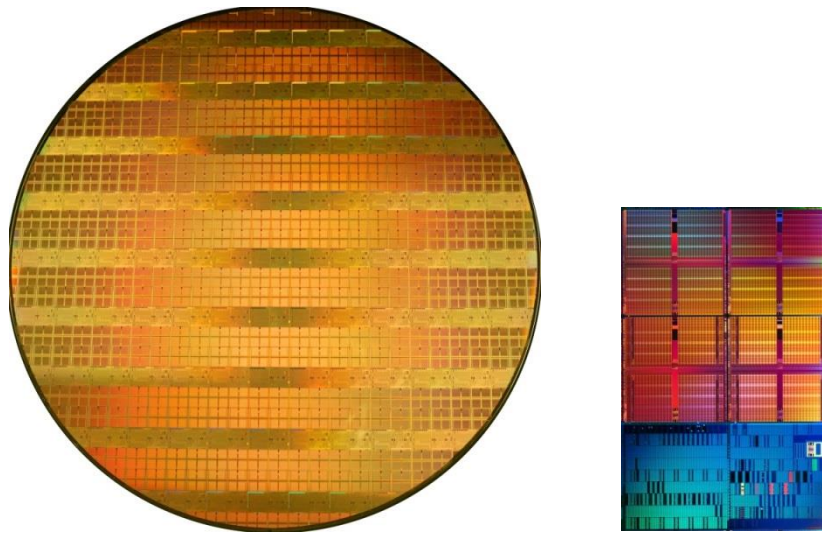
Figure 4.1: Patterned 300mm wafer (left) and an individual die (right).[167] *Copyright 2006, Intel Corporation.* Used with permission.

In addition to isolating the die from the environment, the package must provide electrical and thermal connectivity to the rest of the system. Particularly for high-performance applications such as microprocessors, it is desirable to increase the density of input/output (I/O) connections, thereby maximizing bandwidth between the chip and system board. Further considerations include power consumption and the field-serviceability of the connection (e.g. using a CPU socket instead of permanent solder joints), which is critical for high-value devices. Thermal conductivity is important in high-power applications, where peak temperatures may approach 100 °C. Moreover, the move towards 3-D integrated circuits (chip stacking) poses new challenges regarding heat-dissipation. Considering all of this, the package has a significant impact on the performance, reliability, and cost of a device.

The earliest IC packages were ceramic flatpacks. These were used in military and aerospace applications because of their excellent reliability. However, the dual in-line package (DIP) was the first scheme to attain widespread commercial success. Developed in 1965 at Fairchild Semiconductor, the DIP is exemplified by Intel's first microprocessor, the 4004 (Figure 4.2).[88] In this particular device there are a total of 16 pins, each connected to a different electrical contact on the die by a fine wire bonds. These 16 contacts provided connectivity for the 2,300 transistors manufactured using then-revolutionary 10 micron photolithography.[89] Like flatpacks, the packaging material was initially ceramic. While tough and hermetic, the package was relatively expensive to manufacture, owing to the co-firing processes required when forming ceramics. Later models were instead encased in a thermosetting plastic, which proved more amenable to mass production.
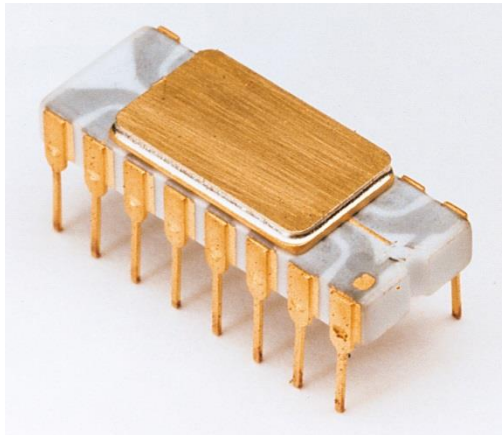
Figure 4.2: An Intel 4004 with ceramic packaging. The silicon die occupies a small region beneath the top metal plate.[168]

Though the 4004 was soon outdated, the dual in-line package architecture remained common for microprocessors throughout the 1970s. The steady increase in transistor count observed by Moore required a similar increase in the number of connections between the package and circuit board. The 8080, Intel's second 8-bit microprocessor, contained approximately 6,000 transistors in a 40-pin package. Industry standards fixed the pin spacing at 0.1 inches, so higher pin counts were only realized by increasing the total package length. In addition to the obvious drawbacks of increased bulk, this greatly extended the signal path length and increased propagation time. Ultimately dual in-line packages were limited to 64 leads.[169]

Wire-bonding remains the most versatile method of connecting a semiconductor die to its package. While universal in early microprocessors, modern devices only use wire-bonding when I/O density is a secondary concern. The continual growth of transistor density requires a concomitant growth in the number of interconnects, both from the die to the package, and the package to the board. Wire-bonding is limited to the die periphery (e.g. Figure 4.3), so a fundamentally different approach is required in order to achieve the required density. Flip-chip interconnection was developed by IBM for use

in mainframe applications.[170]   In this scheme, bonding pads are placed over the entire die surface, rather than just along the periphery.   The die is inverted and the pads are joined directly to the underlying package with solder, allowing for die-to-package connections which are shorter and more numerous.   Additionally, the solder joints conduct heat more effectively than wire bonds.
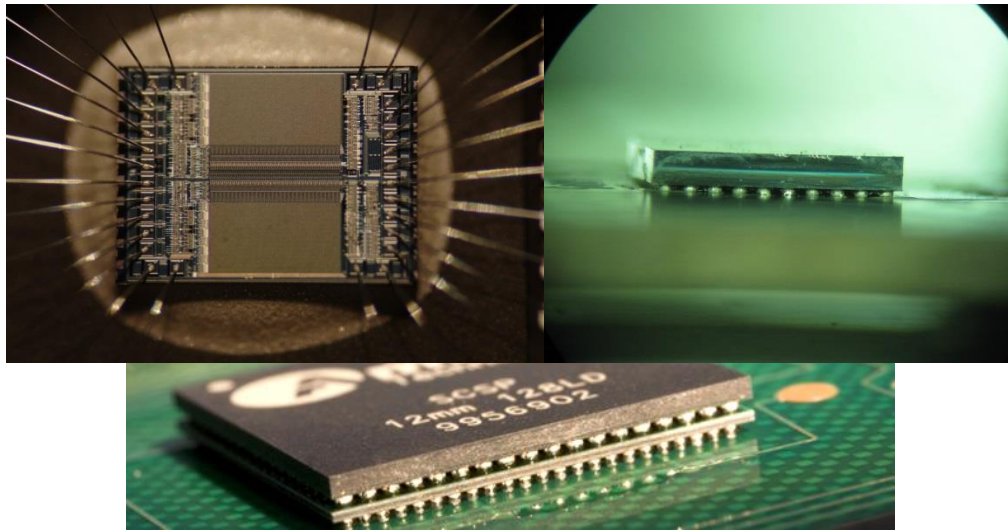
Figure 4.3: Peripherally wire-bonded die (top left) and flip-chip connections (top right, bottom). Image sources: top left – *adapted from Wheeler;* top right – *Copyright 2014, Advotec Company*; bottom – *Copyright 2014, Henkel AG & Co. KGaA*. All rights reserved.[171-173]

Outside of IBM, the first high-volume application of flip-chip mounting was the Pentium II microprocessor.[174] The package was given the designation Organic Land Grid Array (OLGA), differentiating it from the earlier Plastic Land Grid Array (PLGA), which employed wire bonds.   Both packages are constructed from epoxy thermosets.   The "Land Grid Array" designation describes how the package connects to the printed circuit board.   The underside of the package (opposite the die) is covered with an array of flat electrical contacts (Figure 4.4) which are held against a complementary array of pins

protruding from the system board. The opposite scheme is dubbed "Pin Grid Array," where the pins are instead mounted on the package.

Figure 4.4: The Intel Core i7-4770K, a modern microprocessor housed in a flip-chip LGA package. The die is concealed by the large metal heat spreader.[175]

Modern flip-chip packages are constructed through a process known as sequential build-up (SBU), a technology pioneered by IBM and later popularized by Intel.[170] It begins with a sheet of fiberglass-reinforced thermosetting resin—generally a blend of bismaleimide-triazine (BT) and bisphenol A diglycidyl ether. This layer is referred to as the "core." Both surfaces of the core are covered with copper foil which is subtractively patterned to generate the appropriate circuitry. These circuits are then interconnected by mechanically drilling through the core and electroplating copper inside the holes. Complex cores may contain multiple layers of resin and copper (as in Figure 4.5; the resin is the light blue material).

This core provides a rigid substrate upon which to place the many electrical connections to the chip. The "build-up" layers of an SBU substrate comprise much

116

smaller (~5-20 micron) features, which are constructed on both sides of the core. These are fabricated layer-by-layer, hence the "sequential" build-up. These layers also consist of copper conductor and an epoxy insulator (without fiberglass reinforcement). However, the smaller features of the build-up layers require photo-patterning, either through conventional photolithography/etch processes or laser drilling. Both methods suffer significant limitations. Photoprocessing requires use of a separate photoresist, and thus requires many steps to pattern a single layer (recall Figure 1.5). Laser drilling, though a direct patterning process, consumes a great deal of power and yields features of lower quality.[176] Ideally, a photosensitive dielectric material would be used in the build-up layers, eliminating the need for additional process steps. It is the goal of this project to develop a directly patternable dielectric material for use in the build-up layers.
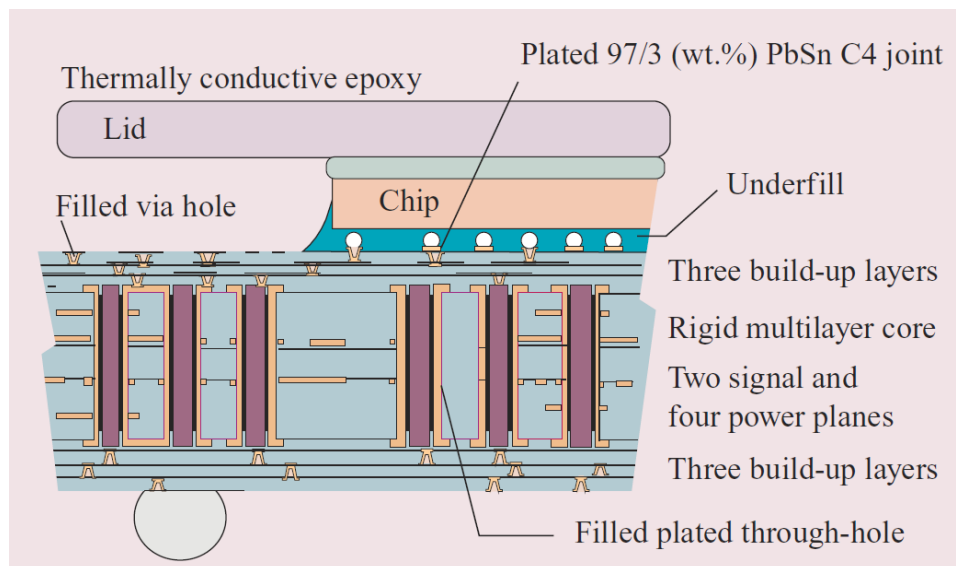
Figure 4.5: Cross section of a Flip-Chip Ball Grid Array (FCBGA) package, common in mobile applications. *Copyright 2014, IEEE.*[170]

Dielectric Properties

Foremost among the material requirements for a photopatternable build-up layer is the dielectric constant (ε_r). ε_r describes a material's polarization in response to an applied electric field. It is defined as the ratio of the capacitance in a structure containing the dielectric of interest to that measured for a similar capacitor with a vacuum dielectric. In this context, ε_r is a metric for how well a material is able to shield adjacent electrical pathways from one another. As wiring density is steadily increasing, in both the chip and package, the amount of dielectric material separating the paths must decrease. To compensate for this, the dielectric constant of the insulator must be reduced in order to maintain interline capacitance at an acceptably low level.

While incompatible with SBU laminate technology, silicon dioxide is a useful point of reference since it is used extensively in on-chip applications. As discussed in Chapter 1, bulk SiO_2 has been supplanted by dielectrics of much lower relative permittivity. Indeed, this is one key advantage of polymers, as many possess dielectric constants well below that of SiO_2 (ε_r=3.9). Current packaging dielectrics range from 2.6-3.2, so a value below 3.0 represents a reasonable target for a photodefinable material.[170, 177-181]

In designing for a low dielectric constant, it is useful to consider the structural components which contribute to permittivity, as described by the Debye equation:

$$\frac{\varepsilon_r-1}{\varepsilon_r+2} = \frac{N}{\varepsilon_0}\left(\alpha_e + \alpha_d + \frac{\mu^2}{3k_bT}\right) \qquad (4.1)$$

Where ε_0 is the vacuum permittivity, N is the number density of dipoles, α_e is the electronic polarizability and α_d is the distortion polarizability.[182] The final term,

$\mu^2/3k_bT$, denotes the orientation polarizability, where μ is the dipole moment, k_b is the Boltzmann constant, and T is temperature in Kelvins. As such, it is desirable to reduce the dipole density or lower the polarizability, or both. While porous materials have been used successfully in interlayer applications, where dielectric targets are more aggressive, this approach is impractical in packaging.[47, 48] However, structural motifs which introduce free volume to the material will tend to reduce the dielectric constant. This is a particularly convenient in polymers, where bulky substituents or bent backbones can be employed to disrupt chain packing and lower the density and, ultimately, ε_r.[183-185]

The effect of polarizability depends on the frequency at which the dielectric constant is measured. Therefore, one must keep in mind the frequency at which a device will operate. As an example, at optical frequencies (ca. 10^{14} Hz), only low-mass species such as electrons are able to reorient quickly enough to be affected by the electric field, and only electronic polarization term (α_e) contributes significantly. As frequency decreases, additional terms become important. Modern device frequencies are typically between 1-10 GHz, a regime where all three components are significant. From a structural perspective this means minimizing conjugated pi systems and nonbonding electrons (α_e), reducing bond polarizability (α_d) and eliminating large permanent dipoles ($\mu^2/3k_bT$).

While the dielectric constant describes how well a material stores electromagnetic energy though polarization, dielectric loss describes how efficiently a material dissipates it. Together these parameters comprise a material's complex permittivity, where ε' is the real component (dielectric constant) and ε'' is the imaginary component (dissipation factor, DF). Dielectric loss is generally described as the loss tangent (tan δ), which is the ratio of the two ($\varepsilon''/\varepsilon'$). Polar and ionic species are the primary structural culprits for

119

high dielectric loss and should be minimized. In packaging materials, values of 0.005-0.01 are typical, provided additives and impurities are kept to a minimum.[177-181, 186]

Coefficient of Thermal Expansion

While universally superior to *nonporous* inorganic dielectrics in terms of both permittivity and processability, organic materials suffer some serious drawbacks. Device integration involves combining many disparate materials into a single structure. Therefore it is crucial to match certain material properties such as the coefficient of thermal expansion (CTE). The negative effects of CTE mismatch are illustrated in Figure 4.6. The silicon die (CTE: 3 ppm/K) is attached to the package substrate (CTE: 10-20 ppm/K) through a reflow soldering process. A key advantage of reflow soldering is that the thousands of electrical connections from the die to substrate are formed simultaneously. However, the entire package is subjected to the high temperatures needed to melt the solder, causing appreciable thermal expansion in each component. As assembly is completed at the reflow temperature, this mismatch becomes apparent when returning the package to ambient conditions. With a higher CTE, the substrate will tend to shrink more than the die, causing tensile stress. The package experiences many temperature excursions, during both manufacturing and device operation. If severe enough, this stress can result in warpage (shown), delamination, solder joint failure, or even cracking of the die.

120
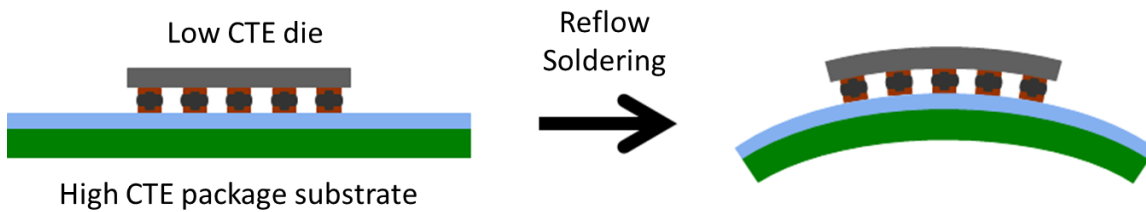
Figure 4.6: Exaggerated effect of CTE mismatch during flip-chip package assembly.

The many materials comprising the packaging substrate must be similarly matched. This includes the BT resin/fiberglass core (~8 ppm/K), the copper metallization (17 ppm/K), and the build-up dielectric.[181] Since the core and metallization properties are largely fixed, the dielectric must be made to match them. Practically, this means achieving a CTE below ~20-30 ppm/K.[181] Historically, polymers have been severely limited by this requirement. For example, Teflon and its amorphous derivatives have demonstrated dielectric constants ranging from 1.9-2.1—values unmatched for a bulk solid.[48, 187] Such materials would be competitive interlayer dielectrics if they also met integration requirements. However, the thermal expansion of PTFE is unacceptably high, with a CTE around 130 ppm/K.[48]

Lithographic Requirements

In packaging applications, patterning resolution requirements are relaxed in comparison to wafer-level photolithography. Build-up layer features (e.g. copper wires and vias) are typically no smaller than 5-10 microns.[135, 136, 181] However, a layer might be 15 microns thick, constituting an aspect ratio (height/width) of 3.[136] Therefore, it is the goal of this project to demonstrate a directly-patternable dielectric with a 5 micron resolution in a 15 micron thick film. Seeking to build on the combined work of DuPont and IBM, we selected polyimide due to its promising material properties and the imaging chemistry discussed in Chapter 3.

121

As a proof of concept, deep-ultraviolet patterning of the poly(amic ethyl ester) precursor of poly(pyromellitic dianhydride-co-4,4'-oxydianiline) (PMDA-ODA, Figure 4.7) was attempted in a manner analogous to the IBM process.[143] The precursor polymer, poly(para-diethyl pyromellitate-*co*-4,4'-oxydianiline) (PAETE, Figure 4.7), was formulated with 15 wt% of an ortho-nitrobenzyl carbamate photobase (ONB PBG, Figure 4.7). Thin (~0.7 μm) films were deposited by spin-coating and exposed to broadband UV light. Irradiation results in carbamate photolysis, releasing piperidine in the film (recall Figure 3.6). Following this, a post-exposure bake (PEB) at 150 °C for 10 minutes causes partial imidization in the exposed regions.

PAETE   **ONB PBG**
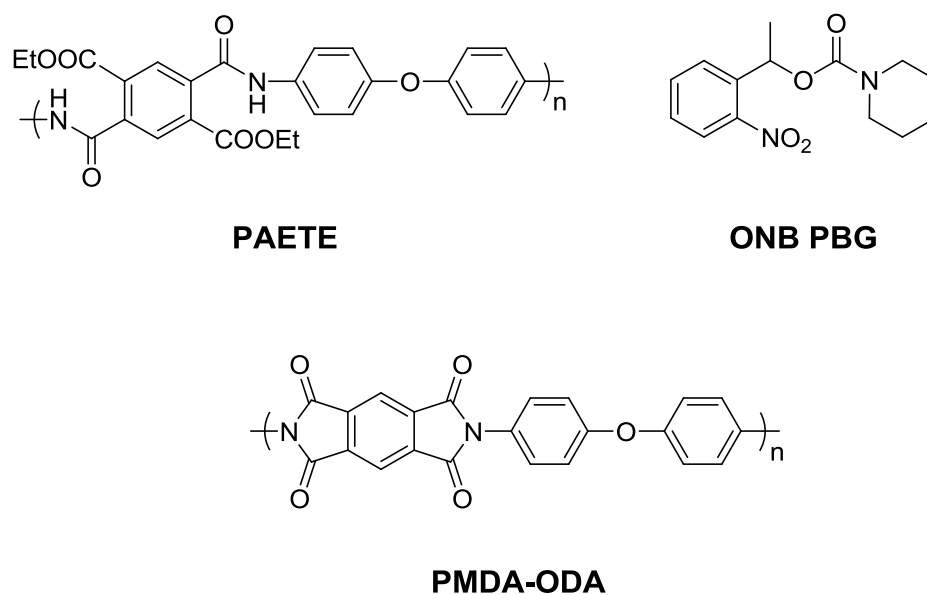
PMDA-ODA

Figure 4.7: Precursor polymer (PAETE), photobase generator (ONB PBG) and final polyimide (PMDA-ODA).

Following PEB, films were immersed in an organic developer to dissolve the unexposed regions. For this material, a mixture of N-methylpyrrolidone (10%) in diglyme proved optimal. By varying the exposure dose and measuring the film thickness

122

after development, the minimum dose (D_{100}) and contrast ($ɣ$) can be determined (Figure 4.8). A very high dose (920 mJ/cm^2 broadband UV) was required for complete film retention, owing to the optical density of PAETE at the relevant exposure wavelengths (deep ultraviolet). The contrast was relatively low at 1.7. However, this constitutes a successful demonstration of the patterning methodology. Similar exposure through a photomask yielded line/space patterns as small as 5 μm half-pitch (Figure 4.9), the ultimate resolution target.
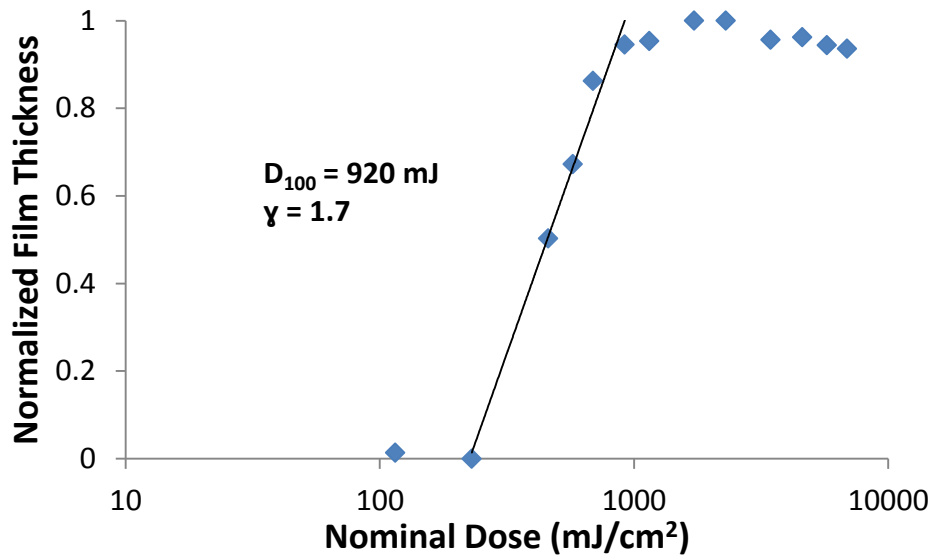
Figure 4.8: Contrast curve of PAETE/PBG illustrating negative-tone behavior. The film was developed with 10% NMP in diglyme for 60 seconds.
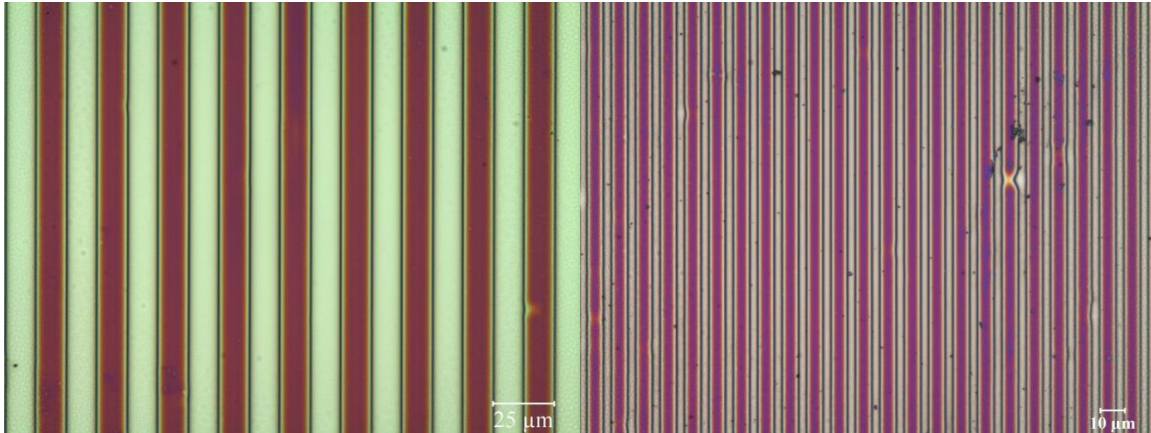
Figure 4.9: Optical micrographs (50x) of line/space patterns printed in PMDA-ODA at 12.5 µm half-pitch (left) and 5 µm half-pitch (right). Patterns were cured at 350 °C for one hour following development.

LOW-κ MATERIALS

PMDA-ODA is an effective model system with which to demonstrate the imaging chemistry. However, its material properties are inadequate for the ultimate application. Table 4.1 lists key properties and the project objectives; literature values for PMDA-ODA, as well as the initial lithographic results, are given for comparison. As seen, the dielectric constant (ε_r) and water absorption are well outside of specification. Additionally, feature heights beyond 5 microns are impractical due to the optical density of PAETE.[143]

Property	Target	PMDA-ODA	PMDA-TFMB
ε_r	<3.0	3.3-3.5	2.6
DF	<0.01	<0.005	-
CTE	<30 ppm/K	20-40 ppm/K	-3 ppm/K
H$_2$O abs.	<1%	4-5%	2%
Feature width	5 µm	5 µm	-
Feature height	15 µm	4 µm[143]	-

Table 4.1: Key material specifications and the reported properties of two aromatic polyimides.[181, 184, 188-190]

124

In the 1990s there was a concerted effort to develop polymer-based low-k interlayer dielectrics to replace SiO_2.[48, 187] While photo-patternability was not a requirement, many of the desired material properties are comparable to current packaging targets. Though few of these low-k polymers were integrated with silicon, many eventually found commercial success in IC packaging.[177, 178, 180] Several promising candidates emerged at DuPont, where researchers were focused on fluorinated polyimides such as poly(pyromellitic dianhydride-co-2,2'-bis(trifluoromethyl)benzidine) (PMDA-TFMB, Figure 4.10). As seen in Table 4.1, PMDA-TMFB demonstrates significant improvements over PMDA-ODA in dielectric constant, CTE and water absorption.
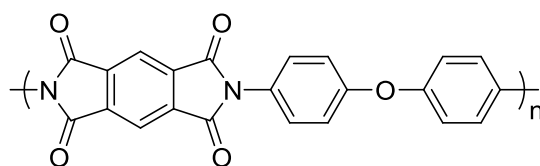
PMDA-ODA
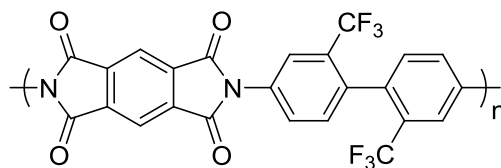
PMDA-TFMB

Figure 4.10: Structural comparison of PMDA-ODA and PMDA-TFMB.

The incorporation of fluorine has been a popular approach to reducing dielectric constant, as evidenced by the adoption of fluorosilicate glass (F-SiO_2) as the first low-k dielectric in 2000.[47] Furthermore, fluorination has the added benefit of reducing water

absorption, a significant problem for most polyimides.[47] PMDA-TFMB exceeds the target of <1% water absorption and there are several derivatives which meet this requirement.[188, 191] However, due to the improved transparency of the PMDA-TFMB precursor and otherwise excellent balance of material properties, it was decided to initially focus on this material.

PATTERNING

For successful thick-film patterning, the optical density of the precursor must be low. Fortuitously, the many modifications used to lower the dielectric constant of polyimides also tend to blue-shift absorbance. The primary cause of near-UV/visible absorbance in both polyimide and precursors such as PAETE is charge transfer between the electron-deficient dianhydride and electron-rich diamine.[192] Electronically and sterically, this effect is limited in both PMDA-TFMB and the poly(amic ester) precursor: poly(para-diethyl pyromellitate-co-2,2'-bis(trifluoromethyl)benzidine) (*p*-PMDA-EE-TFMB, Figure 4.12). 2,2'-bis(trifluoromethyl)benzidine is a much weaker electron donor than oxydianiline, and the twisted nature of the benzidine structure is expected to hinder complexation with PMDA. A comparison of the UV/Vis spectra of PAETE and *p*-PMDA-EE-TFMB films is shown in Figure 4.11. PAETE is effectively opaque at 365 nm (i-line), the intended patterning wavelength, with an absorbance per micron of 0.30. i-line absorbance in *p*-PMDA-EE-TFMB decreases nearly an order of magnitude to 0.051 μm^{-1}.
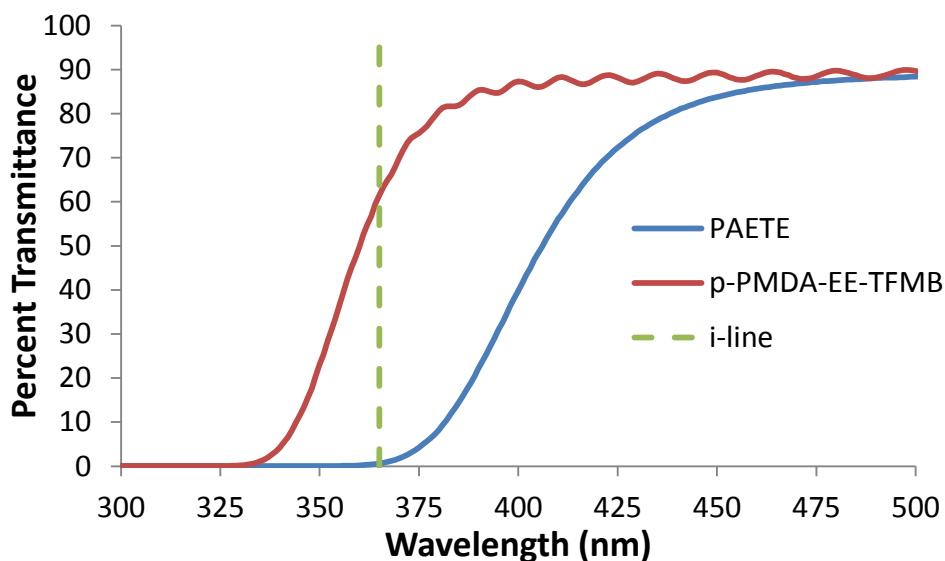
Figure 4.11: UV/Vis transmittance of PAETE and *p*-PMDA-EE-TFMB precursor films. 365 nm (Hg i-line) is highlighted in green.

Initial patterning efforts focused on the TFMB analog of PAETE (*p*-PMDA-EE-TFMB) with an ortho-nitroveratryl carbamate photobase (NVOC PBG, Figure 4.12). This PBG has been used successfully for i-line patterning of other transparent polyimides.[144, 145, 148] Films were exposed through a photomask to a dose of 1.7 J (broadband UV), baked for 10 minutes at 170 °C and then developed with a mixture of 10% N,N-dimethylacetamide (DMAC) in propylene glycol monomethyl ether acetate (PGMEA) for 60 seconds. This allowed resolution of 12.5 μm half-pitch lines (Figure 4.13). However, the resulting patterns exhibited significant roughness, both along the line edges and at the surface. It was also noted that films of the *p*-PMDA-EE-TFMB exhibited this granular texture, with or without the photobase (Figure 4.13).
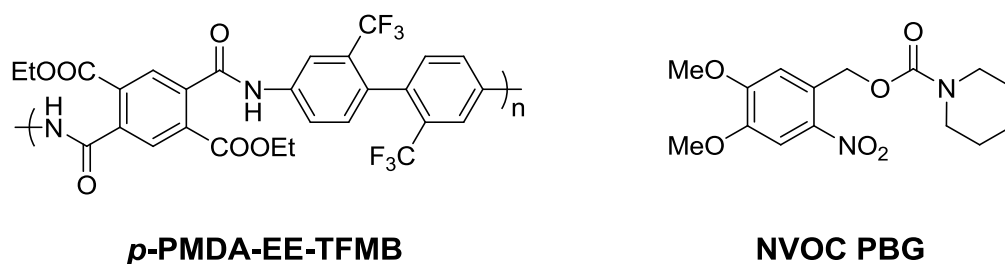
Figure 4.12: PMDA-TMFB precursor (left) and i-line sensitive photobase (right).
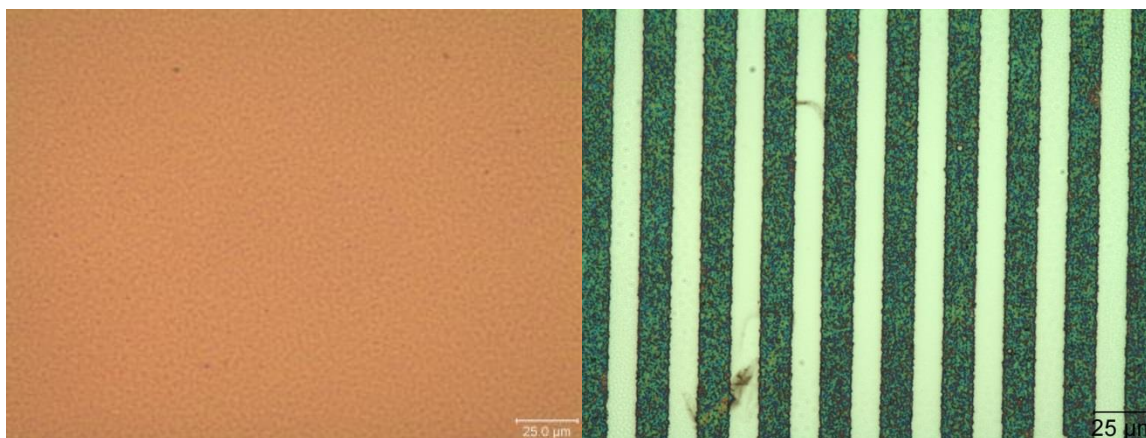
Figure 4.13: Optical micrographs of a *p*-PMDA-EE-TFMB film following post-apply bake (left) and a 12.5 µm half-pitch line/space pattern in fully-cured PMDA-TFMB (right). The characteristic roughness is visible in both images.

This behavior was presumed to result from the rigid linear backbone of the polymer, as it was not observed with flexible poly(amic ethyl esters) like PAETE. Additionally, the poly(amic acid) precursor of PMDA-TFMB, a mixture para and meta isomers, produced smooth films. It was anticipated that use of the meta isomer (Figure 4.14) would eliminate this behavior.[193]
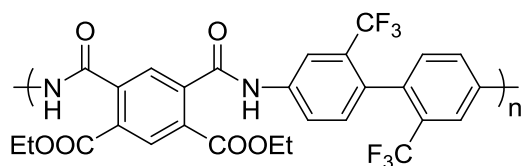
***m*-PMDA-EE-TFMB**

Figure 4.14: meta-PMDA-TMFB precursor.

The meta isomer produced smooth films and exhibited improved solubility. NMP solutions of up to ~30 wt% percent could be prepared (versus ~15 wt% for the para isomer). Patterning was performed using 5 wt% loading of NVOC PBG and a 160 °C post-exposure bake for 10 minutes; lower PEB temperatures led to catastrophic feature swelling, regardless of exposure dose. For these conditions, the optimal developer is a mixture of NMP in methanol (typically 25-35 wt% NMP). Following development, samples were fully cured at 350 °C for one hour.

Hard contact photolithography yielded features as small as 2.5 μm half-pitch in a 1.5 μm thick film (Figures 4.15, 4.16). In this case, the sample was exposed to a dose of 1500 mJ/cm^2 i-line radiation through a gradient density photomask. It is interesting to note the dramatic difference between the 2.5 μm and 2 μm features, with the latter exhibiting catastrophic failure. As the latent image appeared normal at 2 μm half-pitch, this suggests a problem with the development step. Regardless, this demonstration exceeds the resolution target of 5 μm.
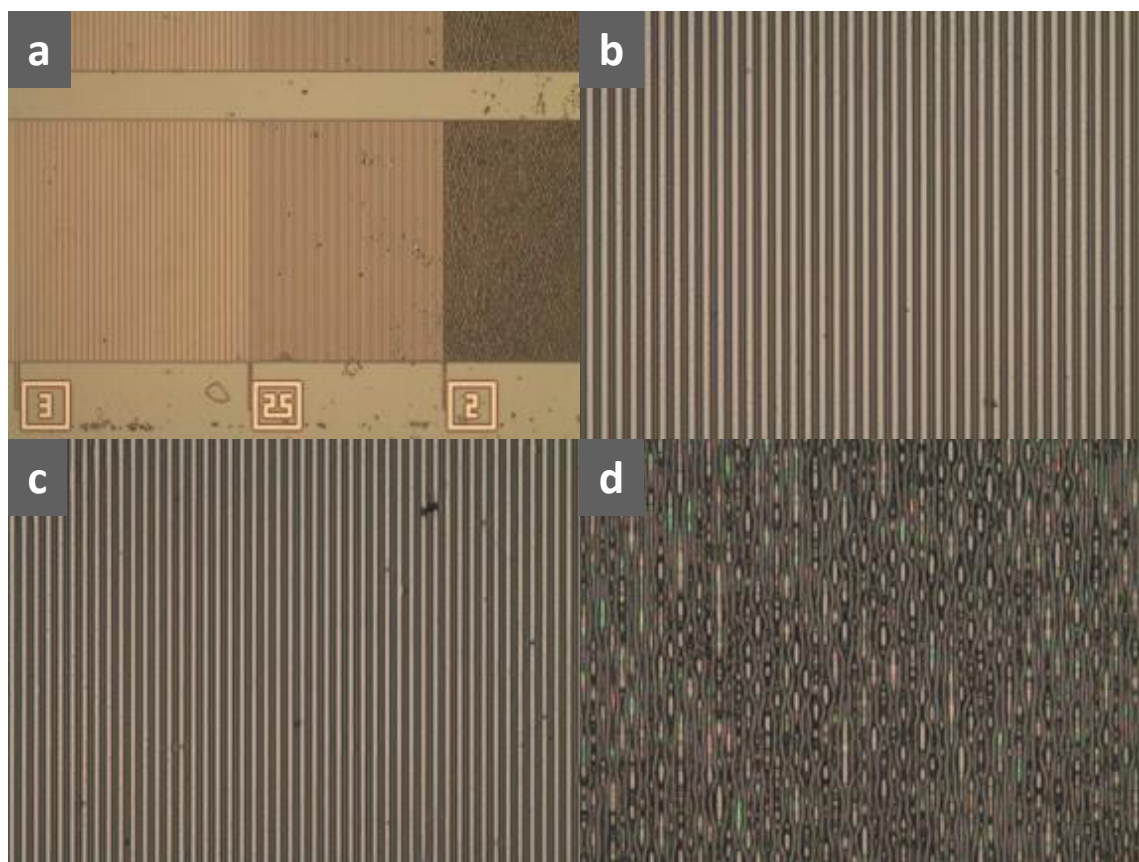
Figure 4.15: Optical micrographs of line/space patterns printed in a 1.5 µm thick film of fully-cured PMDA -TFMB: (a) gradient density: 3 µm, 2.5 µm and 2 µm half-pitch at 10X magnification, (b) 3 µm half-pitch at 50X magnification, (c) 2.5 µm half-pitch at 50X magnification, (d): 2 µm at 50X magnification.
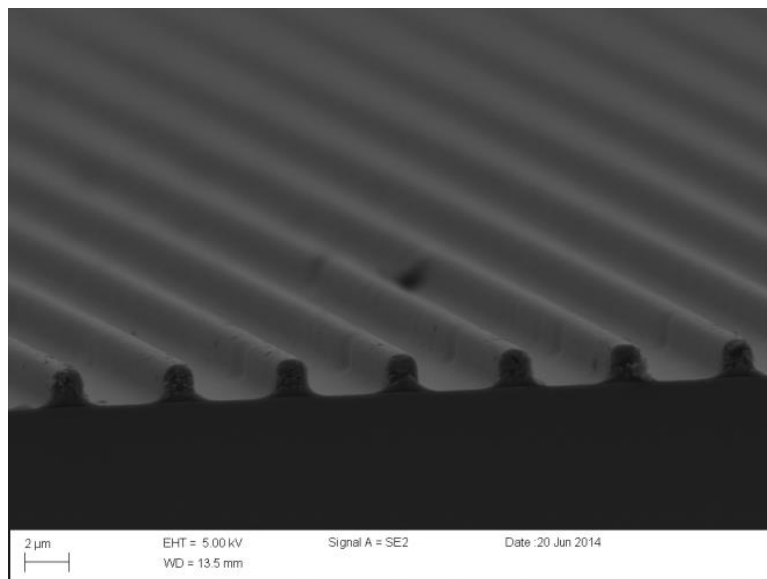
Figure 4.16: Cross-section scanning electron micrograph of a 2.5 µm half-pitch line/space pattern in a 1.5 µm thick film of PMDA-TFMB.

Thick films were successfully patterned in the same manner, with a concomitant increase in dose. 16 µm films were deposited by spin-coating and exposed under hard contact to a dose of 2100 mJ/cm^2. At this thickness, features as small as 7.5 µm half-pitch have been resolved (Figure 4.17). However, these higher aspect ratio patterns are susceptible to adhesive failure and collapse (as evidenced by Figure 4.17c). Though further optimization is needed to meet the project objectives, a key advantage of this method is apparent from these pattern profiles. While many photosensitive polyimides exhibit severe sidewall sloping when cured, the sidewalls shown in Figure 4.17 are nearly vertical.
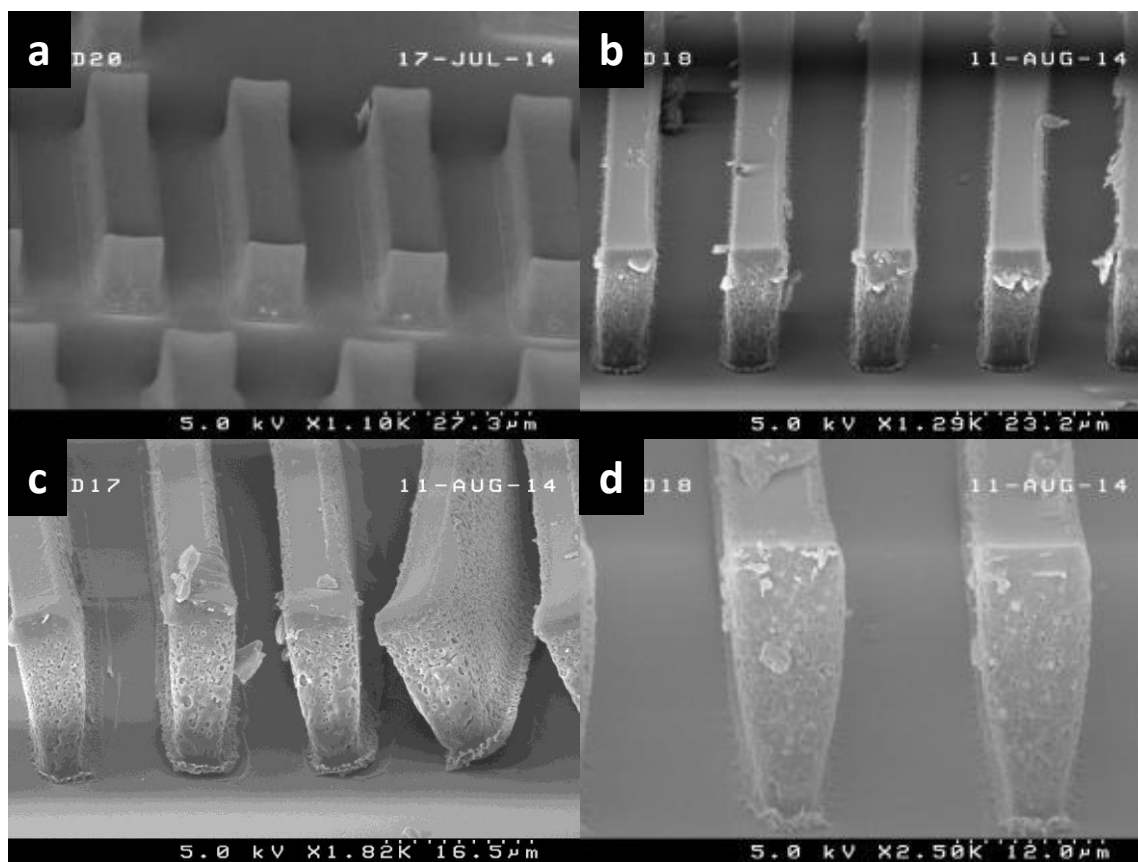
Figure 4.17: Scanning electron micrographs of fully-cured PMDA-TFMB pattern: (a) 12.5 µm half-pitch at 12 µm thickness, (b) 10 µm half-pitch at 14.5 µm thickness, (c) 7.5 µm half-pitch at 14.5 µm thickness—delaminated, (d) 10 µm half-pitch at 14.5 µm thickness with clear undercutting.

The tapered profile in Figure 4.17d is classical behavior for a negative-tone photoresist with significant absorbance at the exposure wavelength. While *m*-PMDA-EE-TFMB is relatively transparent at 365 nm, the photobase generator also contributes significantly to the optical density. At i-line, a 14 µm film of *m*-PMDA-EE-TFMB containing 5% NVOC PBG is effectively opaque, with an absorbance of 2 (Figure 4.18). Moreover, the formulation does not photobleach, but instead photodarkens both due to formation of 4,5-dimethoxy-2-nitrosobenzaldehyde and partial imidization of the resin.

To improve the photospeed and eliminate resist undercutting, NVOC PBG must be replaced with a more effective i-line photobase generator.
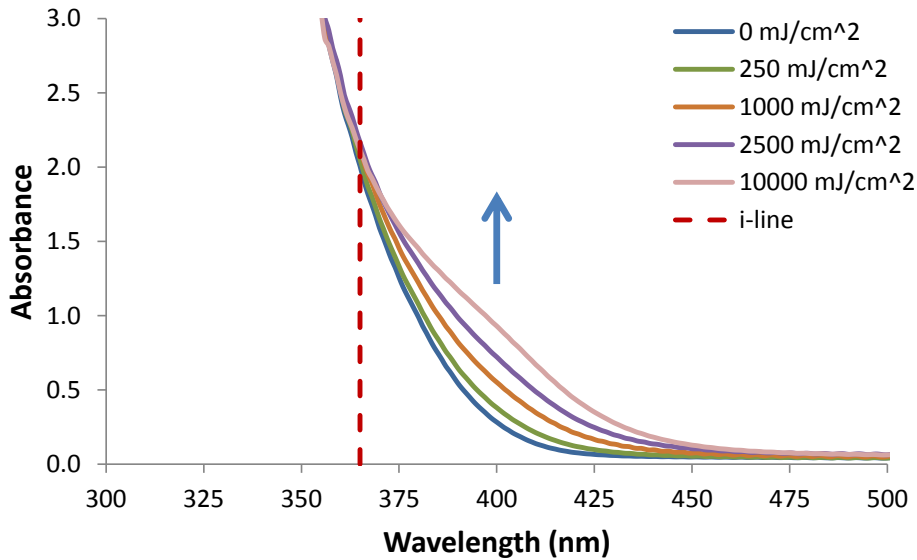
Figure 4.18: UV/Vis spectra of a 14 μm film of *m*-PMDA-EE-TFMB containing 5% NVOC PBG showing photodarkening. The exposure wavelength is indicated in red.

DIELECTRIC CHARACTERIZATION

The dielectric properties of PMDA-TFMB were first evaluated using spectroscopic ellipsometry in reflectance mode. For the case where a material is transparent, the dielectric constant is simply:

$$\epsilon_r = n_{ref}^2 \tag{4.2}$$

In this frequency regime (THz), electronic polarization is the only significant component of the dielectric constant.[182] As such, optical measurements tend to give lower results than those obtained at device frequencies (MHz to GHz). However, it has been shown in several fluorinated polyimides that the optical and microwave (GHz) dielectric constants

are very similar.[185]   Figure 4.19 shows a plot of n^2 and k versus wavelength for a film of PMDA-TFMB.   Immediately evident is the dielectric anisotropy, with a difference of more than 0.4 between in-plane and out-of-plane permittivities.   This amount of birefringence is relatively common in aromatic polyimides, where Δn may range from 0.075 to 0.23.[189]   At 633 nm, the in-plane and out-of-plane dielectric constants are 2.82 and 2.37, respectively.   Despite this extreme anisotropy, the in-plane value remains in specification.   As expected, the through-plane results are somewhat lower than the literature value of 2.6, which was determined using a parallel plate capacitor structure at a much lower frequency (1 MHz).[184, 188]
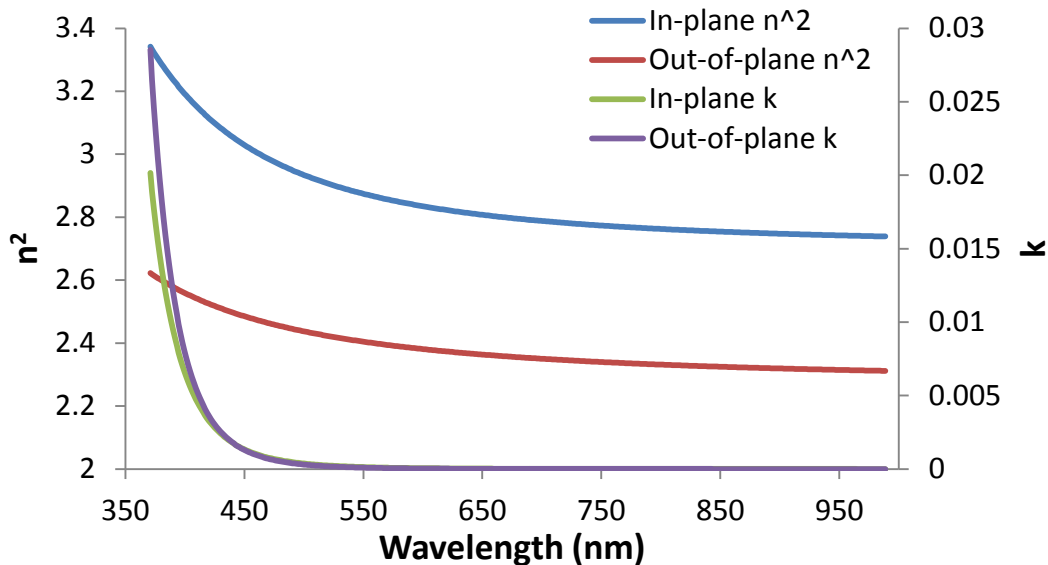
Figure 4.19: Dielectric constant of PMDA-TFMB as determined by spectroscopic ellipsometry.

Direct measurement of the dielectric constant and dissipation factor is beyond the present capabilities of our laboratory.   Parallel-plate capacitance measurements were performed by Mr. Brennen Mueller at the Georgia Institute of Technology at a frequency

of 200 kHz, yielding a dielectric constant of 2.89 and a dissipation factor of 0.011. This ε_r is significantly higher than that reported by Feiring *et al*. for a similar frequency range (2.6).[184] This discrepancy is likely due to residual water, as samples were dried for a shorter period (2 hours) and measurements were performed under ambient conditions. Feiring *et al*. conducted measurements at 0% relative humidity after drying for 48 hours.[184] Mr. Mueller reported a rapid increase in ε_r and DF once samples were exposed to air; without a dehydration bake, ε_r and DF were 3.16 and 0.016, respectively. High-frequency measurements were performed by Mr. David Zhang of the Intel Corporation using the split-post dielectric resonator technique.[194, 195] Unlike parallel-plate capacitance, this method provides the in-plane dielectric constant. In this case, films were not subjected to a dehydration bake prior to measurement. The results of both experiments are plotted against frequency in Figure 4.20.
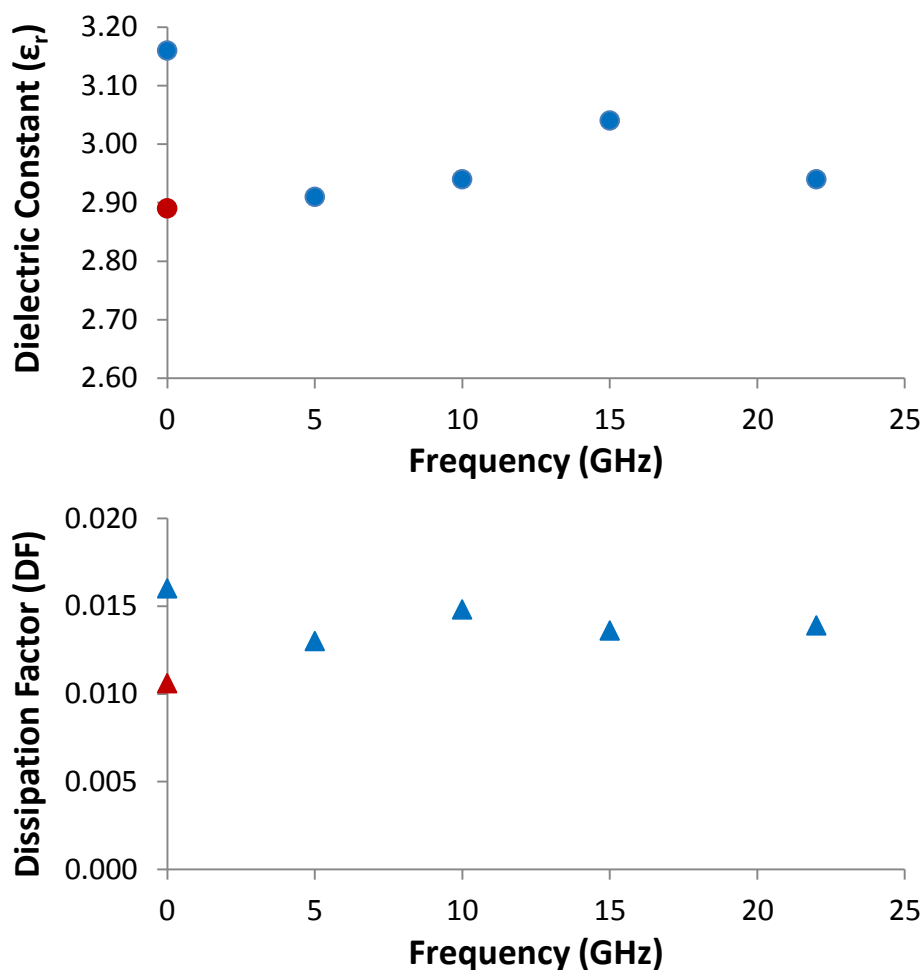
Figure 4.20: PMDA-TFMB dielectric constant (top) and dissipation factor (bottom) measured at 200 kHz (through-plane) and 5-22 GHz (in-plane). For the red data points, samples were subjected to a dehydration bake prior to measurement.

As a whole, these data are very encouraging. The microwave dielectric constant of PMDA-TFMB is approximately 3.0 in the plane of the film. The residual water presumably accounts for the difference between the optical and microwave results. The dissipation factor is somewhat high, but again this is attributed to moisture content— water exhibits extremely high dielectric loss in this frequency range.[196] However since the package will not be hermetic, this effect cannot be completely ignored. To address

this, focus is anticipated to gradually shift to poly(pyromellitic dianhydride-co-2,2'-bis(trifluoromethoxy)benzidine) (PMDA-TFMOB, Figure 4.21) and poly(cyclobutane-1,2,3,4-tetracarboxylic dianhydride-*co*-2,2'-bis(trifluoromethyl)benzidine) (CBDA-TFMB, Figure 4.21), which are reported to have water absorption below 1%.[184, 188, 197]

PMDA-TFMOB   **CBDA-TFMB**
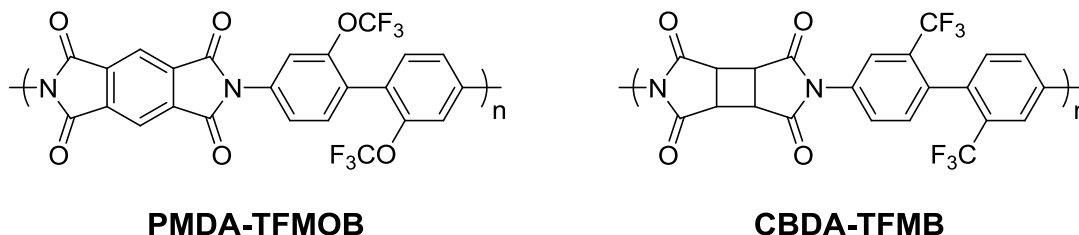
Figure 4.21: PMDA-TFMOB and CBDA-TFMB, fluorinated polyimides with reduced water absorption.

COEFFICIENT OF THERMAL EXPANSION

The coefficient of thermal expansion (CTE) is commonly determined using thermomechanical analysis (TMA). In this technique, a free-standing film is held under constant tension while the temperature is cycled over a predetermined range. The dimensional change of the sample is related to linear in-plane CTE (α_{xy}) by:

$$\alpha_{xy} = \frac{1}{L}\frac{dL}{dT} \tag{4.3}$$

Where *L* is the initial sample length and *T* is temperature. TMA was performed by Dr. Brandon Rawlings of the Intel Corporation, and the results from 0 to 150 °C are shown in Figure 4.22. PMDA-TFMB exhibits extremely low thermal expansion over this temperature range, with an average CTE of 6 ppm/°C. This is well below our target of 30, as well as the ITRS value of 12 ppm/°C in the film plane.[181]
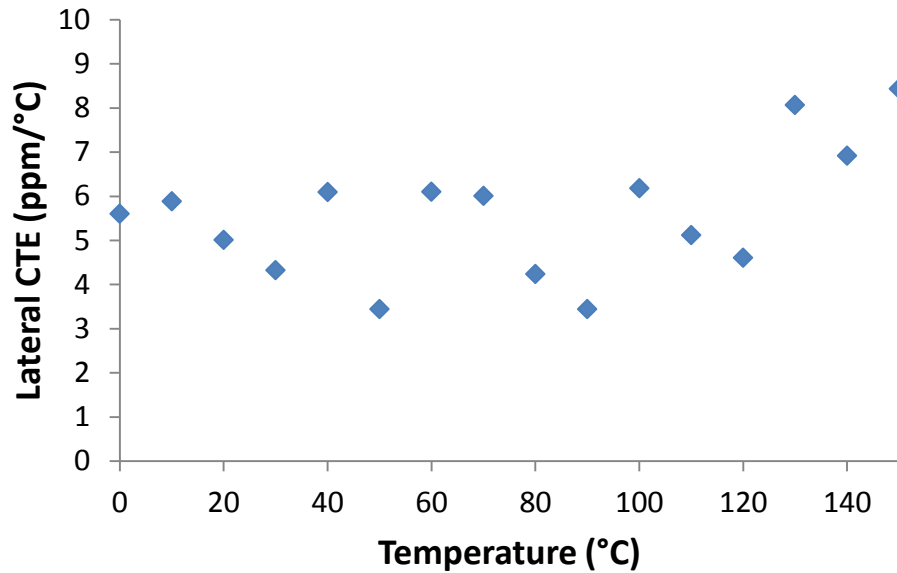
Figure 4.22: Linear CTE of a PMDA-TFMB film as measured by thermomechanical analysis. The temperature ramp rate is 5 °C/min.

Recall the birefringence exhibited by this material (Figure 4.19). It is well known that polyimides orient preferentially in the substrate plane when cast and cured, giving rise to uniaxial anisotropy.[198-200] This ordering tends to increase with decreasing backbone flexibility, with the rod-like PMDA-TFMB and poly (3,3′,4,4′-biphenyltetracarboxylic dianhydride-*co-p*-phenylenediamine) (BPDA-PPD, Figure 4.23) being particularly extreme examples.[189, 197] So-called low-stress (low-CTE) polyimides exploit this very phenomenon. As expansion along individual bonds, and thus polymer backbone, is relatively limited, a high degree of in-plane orientation results in a low in-plane CTE.[189, 201, 202] Figure 4.6 illustrated the effect of an in-plane CTE mismatch between materials. However, the through-plane CTE is equally important, as there are many vertical interconnects (vias) joining each wiring layer. If the vertical (z-axis) CTE of the build-up dielectric is significantly higher than that of copper, via delamination can

occur. Current targets are less aggressive than the in-plane CTE, with ITRS specifying a value of 40 ppm/°C.[181]
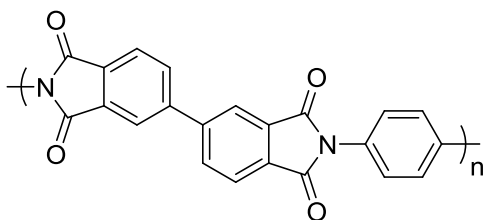
BPDA-PPD

Figure 4.23: BPDA-PPD, a common rod-like polyimide.

Out-of-plane thermal expansion was characterized using heated-stage ellipsometry.[203, 204] In this technique, the thickness and optical properties of a film are monitored as a function of temperature. Samples were cast on silicon and cured in the normal fashion (350 °C, 1 hour). Cured films were annealed at 188 °C for 15 minutes and then cooled at 5 °C/minute to 20 °C while measurements were performed. Note that the optical properties of the silicon substrate vary significantly over this temperature range and *must* be accounted for in the model.[204] If substrate temperature is neglected, the calculated thickness change (and resulting CTE) will be much higher.

Figure 4.24 shows results for a ~650 nm (at ambient) film of PMDA-TFMB. Data below 50 °C were discarded due to the effect of moisture uptake, which resulted in an apparent thickness increase below this temperature. Approximating the CTE as constant over this range, α_z is simply:

$$\alpha_z = \frac{1}{h}\frac{dh}{dT} \approx \frac{1}{h}\frac{\Delta h}{\Delta T} \qquad (4.4)$$

Where h is the film thickness. From Figure 4.24 it is apparent that the CTE is not constant (i.e. film thickness does not increase linearly). However, for comparative

purposes, it is common (and convenient) to report the average CTE for a specific temperature range.[184, 189, 191, 203]
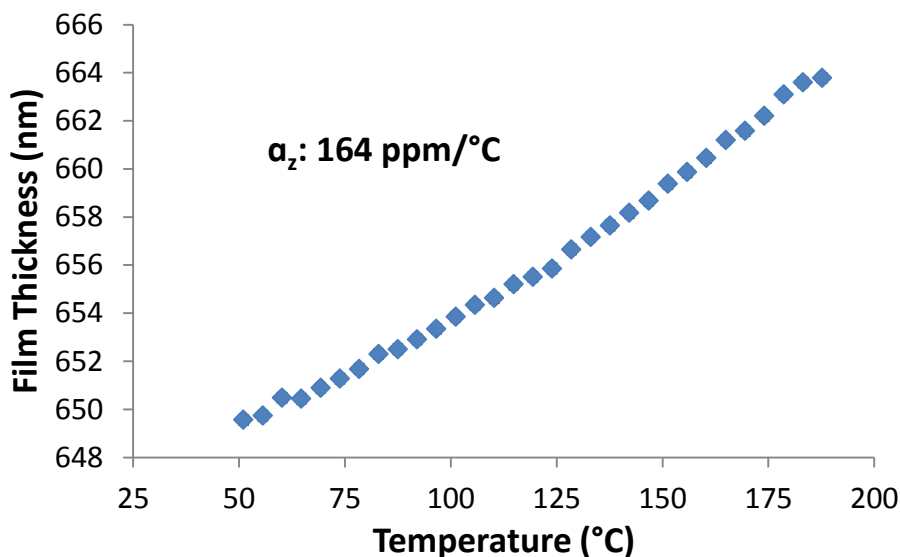
Figure 4.24: Heated-stage ellipsometry data for PMDA-TFMB. The temperature ramp rate is 5 °C/min (cooling from 188 °C).

Whereas TMA measures freestanding films, samples in heated-stage ellipsometry are confined by a rigid substrate. Stress from the in-plane CTE mismatch may contribute significantly to the observed thickness change. To determine the free-standing z-axis CTE, this effect must be corrected for. In a material with uniaxial anisotropy along the z-axis, this can be calculated from:

$$\alpha_{z\;corrected} = \alpha_z - \frac{2\nu}{(1-\nu)}(\alpha_{xy} - \alpha_{substrate}) \qquad (4.5)$$

Where ν is Poisson's ratio and $\alpha_{substrate}$ is the substrate CTE (3 ppm/°C for silcon).[189, 204] α_{xy} is determined by TMA. In addition to PMDA-TFMB, several other polyimides were evaluated by this method (Table 4.2). With flexible polymers (e.g. PMDA-ODA), a

140

Poisson's ratio of 0.35 was assumed.[189] For rigid materials, a value of 0.1 was instead used.[189, 202] However with low-α_{xy} polyimides (<10 ppm/°C), ν has a very limited effect on this calculation.

Polyimide	Δn	ν	α_{xy}	α_z measured	α_z corrected
PMDA-TFMB	0.130	0.1	6	164	163
PMDA-ODA	0.087	0.35	20[189]	151	133
BPDA-PPD	0.199	0.1	5[202]	143	143
CBDA-TFMB	0.048	0.35	33	121	89

Table 4.2: CTE results for several polyimides.

As seen from the table, these polyimides all exhibit very high z-axis coefficients of thermal expansion. This is generally in agreement with literature data for PMDA-ODA and BPDA-PPD, where values range from ~100-150 ppm/°C[189, 202, 205] These measurements were conducted with thicker films (>10 µm), so care must be taken when comparing these results, as ellipsometry is limited to thinner films (<2 µm). A limited thickness dependence of thermal expansion behavior has been reported.[189] However, it is clear that z-axis CTE of PMDA-TFMB is well above our target, and further effort must be made to reduce it. Most packaging dielectrics employ a silica nanoparticle filler to reduce CTE, due to the very low thermal expansion of SiO_2 (0.3 ppm/°C).[170] Other candidate fillers include zirconium tungstate, which exhibits negative thermal expansion over a wide temperature range.[206] This material has been demonstrated to dramatically reduce the CTE of both epoxy and polyimide dielectrics.[207-209] A final promising strategy involves the use of boron nitride nanotubes to simultaneously lower CTE and improve

thermal conductivity of the dielectric.[210] In the near-term, efforts will focus on silica nanoparticles and their compatibility with our patterning methodology.

CURE TEMPERATURE

A traditional limitation of polyimides is the high temperature (300-350 °C) required for curing. Typically, the highest temperature process in package assembly is solder reflow, which peaks around 200-250 °C for no more than a few minutes.[211] In addition to drawbacks relating to power consumption and infrastructural limitations, other materials in the package may not survive the high temperatures require to cure polyimide. This is particularly true of the epoxy resins used in the substrate and underfill materials.[170] Indeed, this drawback of polyimides has contributed to the popularity of lower cure temperature dielectrics such as Cyclotene (benzocyclobutene cure chemistry: 200-250 °C).[177, 178]

As such, we sought to apply amine catalysis in an attempt to reduce the final cure temperature, with the goal of fully curing the material within one hour at 200 °C. This has been demonstrated in poly(amic acids) using both thermal and photobase generators.[144-146, 212, 213] However, attempts to similarly cure poly(amic alkyl esters) were unsuccessful. Secondary amines such as piperidine yielded only partial (~50-70%) imidization when curing at 200 °C, and it was reasoned that a stronger base was required. Based on the original report by Volksen *et al.*, which describes the enhanced effect of amidine bases, 1,8-diazabicyclo[5.4.0]undec-7-ene (DBU, Figure 4.26) was tested.[128]

Addition of DBU to poly(amic alkyl ester) solutions leads to immediate gelation at room temperature. Therefore, films were cast from very dilute (1 wt% total solids) NMP solutions of *m*-PMDA-EE-TFMB containing DBU (1 wt% relative to polymer). Higher concentrations resulted in gelation, making spin-coating impossible. Once cast,

the relative imidization of films was determined by transmission FTIR; useful peaks in polyimides are the C=O (~1780 cm^{-1}) and C-N (~1370 cm^{-1}) stretches.[128, 212] Figure 4.25 shows a series of spectra for a film of *m*-PMDA-EE-TFMB containing 1 wt% DBU. The as-cast material (bottom) exhibits very slight imidization as evidenced by the faint carbonyl peak at 1784 cm^{-1}. Heating this film to 200 °C for 1 hour causes a major growth of the imide peaks (middle). Using the C=C stretch (1490 cm^{-1}) as an internal standard, the relative imidization is calculated from the C=O peak area of each spectrum, assuming full imidization for the 350 °C cure (top spectrum). For the middle spectrum in Figure 4.25, this yields a value of 100% imidization, which is unsurprising given how well the spectra match. Without DBU, very little imidization is observed at 200 °C (*vide infra*).
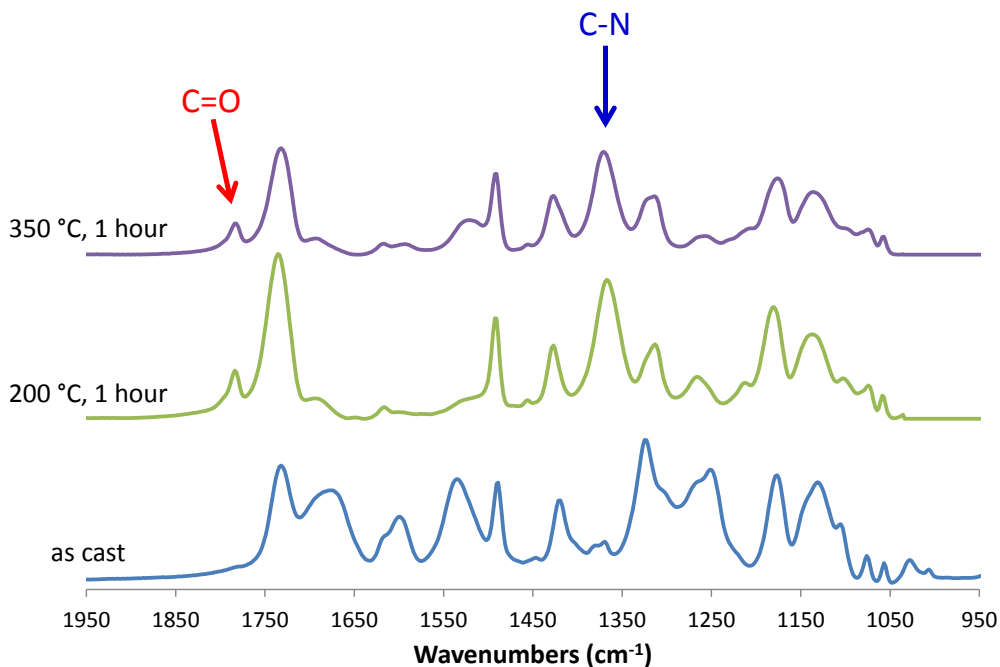
Figure 4.25: FTIR spectra of *m*-PMDA-EE-TFMB films containing 1 wt% DBU after casting on silicon (bottom), curing at 200 °C for 1 hour (middle), and curing at 350 °C for 1 hour (top). The characteristic imide peaks are highlighted.

Application of this approach requires a latent form of DBU. Initial effort focused on inactivating the base either by protonation or quaternization, as several amidine photobases have been reported based on these methods.[214-216] However, carboxylate salts such as DBU benzoate (Figure 4.26) were equally active. Solutions rapidly gelled and the cure behavior is similar to that with free DBU. Conversely, alkylation of the sp^2 nitrogen did inactivate the catalyst, and formulations containing quaternary DBU salts such as benzyl-DBU bromide (Figure 4.26) had adequate storage stability. In *m*-PMDA-EE-TFMB films containing up to 5 wt% benzyl-DBU bromide, very little imidization was observed up to 150 °C. Higher temperatures led to significant curing, reaching 94% after 15 minutes at 200 °C (Figure 4.27). Without this salt, the extent of imidization is only ~5% after 15 minutes at 200 °C. Used in combination with the NVOC PBG, this DBU salt should allow for the rapid curing of a photo-patterned *m*-PMDA-EE-TFMB film at 200 °C.

DBU   **DBU Benzoate**   **Benzyl-DBU Bromide**
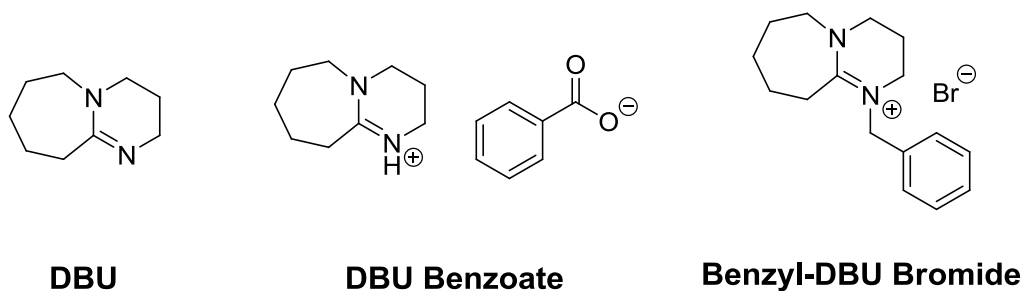
Figure 4.26: Several imidization catalysts tested in this study.
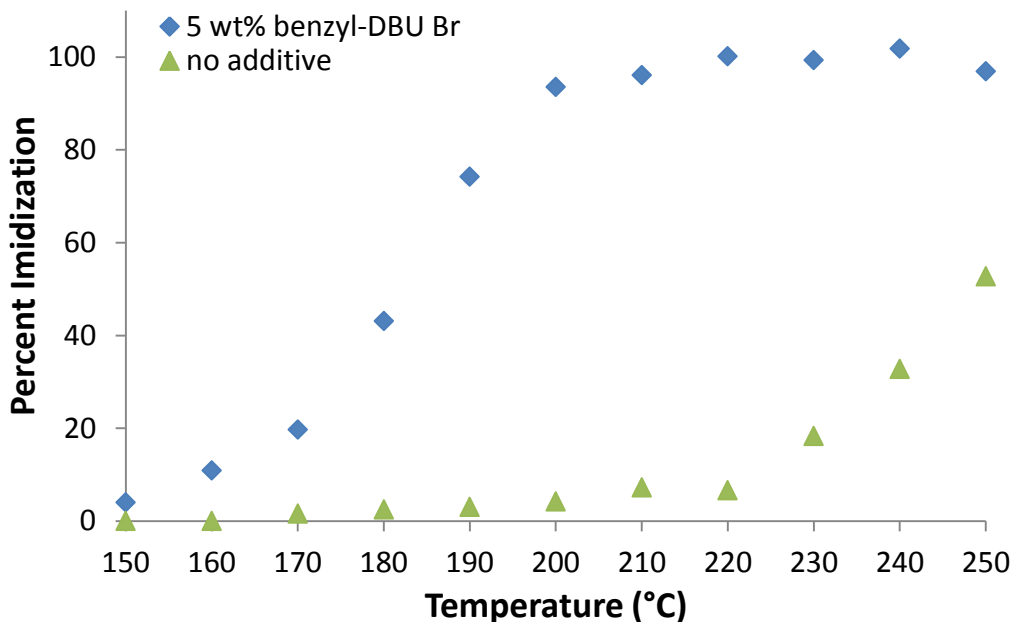
Figure 4.27: Percent imidization of *m*-PMDA-EE-TFMB films after curing for 15 minutes at various temperatures.

CONCLUSIONS

Directly-patternable low-k polyimides are under study for application as integrated circuit packaging dielectrics. By incorporating a small amount of photobase generator into films of the poly(amic ethyl ester) precursors, chemically-amplified negative-tone lithographic behavior has been demonstrated. With the PMDA-ODA precursor (PAETE), 5 μm features have been resolved. Applying this methodology to PMDA-TFMB has yielded patterns as small as 2.5 μm in thin (<2 μm) films. For thicker films, the resolution is somewhat lower due to difficulty developing high aspect ratio features. At present, an aspect ratio of 2 has been achieved at 14.5 μm thickness. However, it is anticipated that with additional optimization, the ultimate lithographic objectives will be realized.

145

The relevant material properties of PMDA-TFMB have been characterized by a range of techniques and are summarized in Table 4.3. The complex dielectric constant (ε_r and DF) is largely within specification for the target frequency range (1-20 GHz). These values are influenced significantly by water absorption, which has been reported at around 2% in PMDA-TFMB.[188] Structural modifications which reduce moisture uptake will simultaneous reduce ε_r and DF. Polymers such as PMDA-TFMOB and CBDA-TFMB are anticipated to exhibit adequate dielectric loss and water absorption.[197]

Property	Target	PMDA-TFMB
ε_r	3.0	3.0
DF	<0.01	0.015
H_2O abs.	<1%	2%
CTE (xy)	30 ppm/°C	6 ppm/°C
CTE (z)	30 ppm/°C	163 ppm/°C
Resolution	5 μm	2.5 μm
Aspect Ratio	3	1.5-2
Cure Temp.	200 °C	200 °C

Table 4.3: Summary of project objectives and current data for PMDA-TFMB. Green indicates that the target has been met. Yellow denotes results are near the target values and are anticipated to improve with continued material and process optimization. Red indicates a major shortcoming which may require significant design changes.

Thermal expansion was characterized through a combination of thermomechanical analysis and heated-stage ellipsometry to obtain both the in-plane (xy) and through-plane (z) CTE, respectively. PMDA-TFMB demonstrated an exceptionally low in-plane CTE, with an average value of 6 ppm/°C from 0-150 °C. Conversely, the

through-plane CTE was measured as 163 ppm/°C from 51-188 °C. This is the primary limitation of this material and the only issue with an as-yet unclear solution. Future studies will focus on polymer-nanoparticle composites with the aim of reducing z-axis thermal expansion to acceptable levels. Further, introduction of some flexibility to the polymer backbone (e.g. CBDA-TFMB) should further reduce the z-axis CTE, while maintaining an acceptable in-plane value.[188, 197]

Building on the patterning methodology, complete curing of PMDA-TFMB at 200 °C can be achieved by addition of small amounts of amidine or guanidine bases. It was found that adequate control and shelf-life could be achieved by instead using a quaternary salt of DBU. At temperatures below 150 °C, the catalytic effect of the base is suppressed. However, upon heating to 200 °C, imidization is effectively complete after 15 minutes. Further investigation of this effect is underway, with the goal of integration into the patterning process.

EXPERIMENTAL

General Methods

PAETE and *p*-PMDA-EE-TFMB were prepared by the diester diacid chloride method, while BPDA-PPD was prepared from the poly(amic acid).[128, 143] *m*-PMDA-EE-TFMB, CBDA-TFMB and the photobase generators were prepared by Mr. Andrew Dick. N-methylpyrrolidone was distilled from phosphoric anhydride to eliminate amine impurities. Solutions were prepared by dissolving the poly(amic ethyl ester) and appropriate additives in N-methylpyrrolidone. Concentrations typically ranged from 10-20 wt%, depending on the desired film thickness. Films were prepared by spin-coating onto silicon wafers. Spin speed varied depending on the target thickness, but spin time was 60 seconds. Wafers were treated with (3-aminopropyl)triethoxysilane prior to

polymer deposition. After spin-coating, films were baked at 100 °C (80 °C with free-base additives). Thin films were soft-baked for 2 minutes, while thick (>5 μm) films were baked for a minimum of 10 minutes. Thickness was measured with a Dektak 6M stylus profilometer (Veeco). Films were cured by heating at 350 °C for a minimum of 1 hour using a convection oven.

Patterning

Flood exposures were performed using a Novacure 2100 spot curing system (Lumen Dynamics) at a 1.5 inch distance. The source was filtered using a 365 nm bandpass filter (A_{365}: 0.050; 20 nm FWHM). The resulting intensity was 30 mW/cm^2 (150 mW/cm^2 for broadband), as measured using a PowerMax PM3 thermopile (Coherent) connected to a Field Max II power meter (Coherent). Contact photolithography was performed using a Karl Suss MA6 mask aligner operating in hard contact mode. No improvement in resolution was observed when using vacuum contact. The intensity at 365 nm was 7.0 mW/cm^2.

Photomasks used were 12.5 μm and 5 μm half-pitch Ronchi rulings (Edmund Optics) and gradient density photomasks (Opto Line, Inc. and Photronics, Inc.). Following exposure, films were baked (150 °C for PAETE, 160 °C for *m*-PMDA-EE-TFMB) for 10 minutes to partially imidize the irradiated regions. Development was performed by immersing films in the appropriate solvent/nonsolvent mixture (10% NMP in diglyme for PAETE, 25-35% NMP in methanol for *m*-PMDA-EE-TFMB). Development time ranged from 30 seconds to 6 minutes, depending on film thickness. Thick films were agitated during development. Films were cured by heating at 350 °C for a minimum of 1 hour using a convection oven.

Ellipsometry

Measurements were performed with a J.A. Woollam M-2000D ellipsometer in reflection geometry at a 60.00° angle of incidence. Full spectral range was 191.5 nm to 988.8 nm, but wavelengths below 350 nm were ignored due to absorbance effects. Films were modeled as a uniaxial anisotropic layer with Cauchy dispersion for both the ordinary (in-plane) and extraordinary (out-of-plane) optical constants (CompleteEASE software, J.A. Woollam). This uniaxial material was modeled on top of a silicon substrate with a 1.5 nm native oxide layer. Heated-stage ellipsometry experiments used a silicon substrate model with temperature-dependent optical properties. Film temperature was adjusted using an Instec mK1000 series temperature controller with an HCS 402 hot stage connected to an LN2-P liquid nitrogen cooling system. Films were annealed at to 188 °C for 10 minutes and then cooled to 20 °C at 5 °C/minute.

Imidization IR

IR measurements were taken using a Nicolet 6700 FTIR (Thermo Scientific) operating in transmission mode. High resistivity silicon wafers (P-type, 20-25 Ω·cm; Addison Engineering) were used to ensure maximum IR transmittance. Relative imidization was determined from the imide C=O peak area (ca. 1780 cm^{-1}), normalized to fully-cured samples. The aromatic C=C stretch (ca. 1500 cm^{-1}) was used as an internal standard. Partial/low temperature curing was performed using a hot plate at temperatures ranging from 150 to 250 °C. Films were fully cured by heating at 350 °C for 1 hour in a convection oven.

Appendix A: Thianaphthene Oxime Crystallography Data
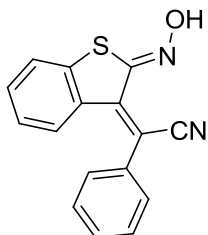
Figure A.1: View of **3.6** showing the atom labeling scheme. Displacement ellipsoids are scaled to the 50% probability level.
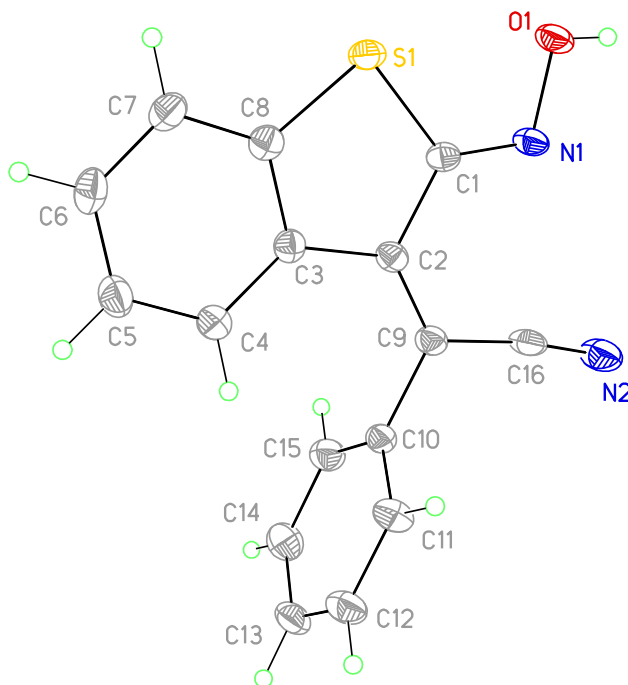
X-ray Experimental for C$_{16}$H$_{10}$N$_2$OS: Crystals grew as large, yellow prisms by slow evaporation from toluene. The data crystal was cut from a larger crystal and had approximate dimensions; 0.41 x 0.35 x 0.28 mm. The data were collected on a Rigaku

150

SCX-Mini diffractometer with a Mercury CCD using a graphite monochromator with MoKα radiation ($\lambda = 0.71075$Å). A total of 422 frames of data were collected using ω-scans with a scan range of 1° and a counting time of 12 seconds per frame. The data were collected at 153 K using a Rigaku XStream low temperature device. Details of crystal data, data collection and structure refinement are listed in Table 1. Data reduction were performed using the Rigaku Americas Corporation's Crystal Clear version 1.40.[1] The structure was solved by direct methods using SIR97[2] and refined by full-matrix least-squares on F^2 with anisotropic displacement parameters for the non-H atoms using SHELXL-97.[3] Structure analysis was aided by use of the programs PLATON98[4] and WinGX.[5] The hydrogen atoms on carbon were calculated in ideal positions with isotropic displacement parameters set to 1.2xUeq of the attached atom (1.5xUeq for methyl hydrogen atoms). The hydrogen atom bound to O1 was observed in a ΔF map and refined with an isotropic displacement parameter. The function, $\Sigma w(|F_o|^2 - |F_c|^2)^2$, was minimized, where $w = 1/[(\sigma(F_o))^2 + (0.0581*P)^2]$ and $P = (|F_o|^2 + 2|F_c|^2)/3$. $R_w(F^2)$ refined to 0.126, with R(F) equal to 0.0488 and a goodness of fit, S, = 1.03. Definitions used for calculating R(F), $R_w(F^2)$ and the goodness of fit, S, are given below.[6] The data were checked for secondary extinction effects but no correction was necessary. Neutral atom scattering factors and values used to calculate the linear absorption coefficient are from the International Tables for X-ray Crystallography (1992).[7] All figures were generated using SHELXTL/PC.[8] Tables of positional and thermal parameters, bond lengths and angles, torsion angles and figures are found elsewhere.

Table A.1: Crystal data and structure refinement for 3.6.

Empirical formula	C16 H10 N2 O S
Formula weight	278.32
Temperature	153(2) K
Wavelength	0.71075 Å
Crystal system	Triclinic
Space group	P-1
Unit cell dimensions	a = 6.857(4) Å α= 99.571(14)°.
	b = 8.647(5) Å β= 92.484(12)°.
	c = 11.426(7) Å γ = 91.042(15)°.
Volume	667.2(7) Å^3
Z	2
Density (calculated)	1.385 Mg/m^3
Absorption coefficient	0.238 mm^{-1}
F(000)	288
Crystal size	0.41 x 0.35 x 0.28 mm
Theta range for data collection	2.39 to 27.50°.
Index ranges	-8<=h<=8, -7<=k<=11, -14<=l<=14
Reflections collected	5436
Independent reflections	2984 [R(int) = 0.0493]
Completeness to theta = 27.50°	97.7 %
Absorption correction	Semi-empirical from equivalents
Max. and min. transmission	1.00 and 0.691
Refinement method	Full-matrix least-squares on F^2
Data / restraints / parameters	2984 / 0 / 185
Goodness-of-fit on F^2	1.033
Final R indices [I>2sigma(I)]	R1 = 0.0488, wR2 = 0.1239
R indices (all data)	R1 = 0.0530, wR2 = 0.1265
Largest diff. peak and hole	0.321 and -0.382 e.Å^{-3}

Table A.2: Atomic coordinates (x 10^4) and equivalent isotropic displacement parameters ($Å^2$x 10^3) for 3.6. U(eq) is defined as one third of the trace of the orthogonalized U^{ij} tensor.

	x	y	z	U(eq)
C1	6350(2)	4019(2)	887(1)	18(1)
C2	5204(2)	4900(2)	1846(1)	18(1)
C3	3455(2)	3948(2)	2018(1)	18(1)
C4	1927(2)	4329(2)	2790(2)	24(1)
C5	401(2)	3253(2)	2810(2)	27(1)
C6	349(2)	1800(2)	2067(2)	27(1)
C7	1833(2)	1398(2)	1285(2)	25(1)
C8	3362(2)	2481(2)	1272(1)	20(1)
C9	5744(2)	6338(2)	2462(1)	19(1)
C10	4700(2)	7231(2)	3484(1)	19(1)
C11	3277(2)	8296(2)	3281(1)	25(1)
C12	2348(2)	9128(2)	4237(2)	28(1)
C13	2844(2)	8931(2)	5389(1)	28(1)
C14	4268(3)	7877(2)	5591(1)	30(1)
C15	5198(2)	7028(2)	4639(1)	25(1)
C16	7437(2)	7205(2)	2186(1)	24(1)
N1	7935(2)	4530(2)	498(1)	20(1)
N2	8712(2)	8041(2)	2059(1)	35(1)
O1	8618(2)	3376(2)	-394(1)	26(1)
S1	5341(1)	2138(1)	329(1)	23(1)

References

1) DENZO-SMN. (1997). Z. Otwinowski and W. Minor, Methods in Enzymology, **276**: Macromolecular Crystallography, part A, 307 – 326, C. W. Carter, Jr. and R. M. Sweets, Editors, Academic Press.

2) SIR97. (1999). A program for crystal structure solution. Altomare, A., Burla, M. C., Camalli, M., Cascarano, G. L., Giacovazzo, C., Guagliardi, A., Moliterni, A. G. G., Polidori, G. and Spagna, R. J. Appl. Cryst. 32, 115-119.

3) Sheldrick, G. M. (2008). SHELXL97. Program for the Refinement of Crystal Structures. Acta Cryst., A64, 112-122.

4) Spek, A. L. (1998). PLATON, A Multipurpose Crystallographic Tool. Utrecht University, The Netherlands.

5) WinGX 1.64. (1999). An Integrated System of Windows Programs for the Solution, Refinement and Analysis of Single Crystal X-ray Diffraction Data. Farrugia, L. J. J. Appl. Cryst. 32. 837-838.

6) $R_W(F^2) = \{\Sigma w(|F_O|^2 - |F_C|^2)^2/\Sigma w(|F_O|)^4\}^{1/2}$ where w is the weight given each reflection.

   $R(F) = \Sigma(|F_O| - |F_C|)/\Sigma|F_O|\}$ for reflections with $F_O > 4(\sigma(F_O))$.

   $S = [\Sigma w(|F_O|^2 - |F_C|^2)^2/(n - p)]^{1/2}$, where n is the number of reflections and p is the number of refined parameters.

7) International Tables for X-ray Crystallography (1992). Vol. C, Tables 4.2.6.8 and 6.1.1.4, A. J. C. Wilson, editor, Boston: Kluwer Academic Press.

8) Sheldrick, G. M. (1994). SHELXTL/PC (Version 5.03). Siemens Analytical X-ray Instruments, Inc., Madison, Wisconsin, USA.

Appendix B: NMR Photolysis of 3.7
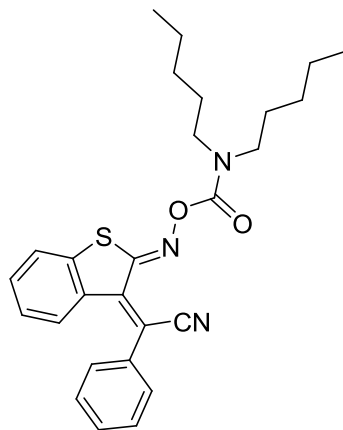
^{1}H NMR spectra were collected using a Varian Unity Plus 400 MHz instrument. Photobase **3.7** was dissolved in CD$_3$CN to a concentration of 7 mM. The solution was *not* degassed prior to exposure. The sample was irradiated using a Novacure 2100 spot curing system (Lumen Dynamics) at a 5 inch distance. The source was filtered using a 405 nm bandpass filter (A$_{405}$: 1.571; 20 nm FWHM). The resulting intensity was 0.46 mW/cm^2, as measured using a PowerMax PM3 thermopile (Coherent) connected to a Field Max II power meter (Coherent). Spectra are shown below from 6.0-9.5 and 0.0-4.0 ppm for each dose. No resonances were observed outside of these regions.

NMR File: WBVI-155_E0_s2pul_H1

Dose: 0 mJ/cm^2
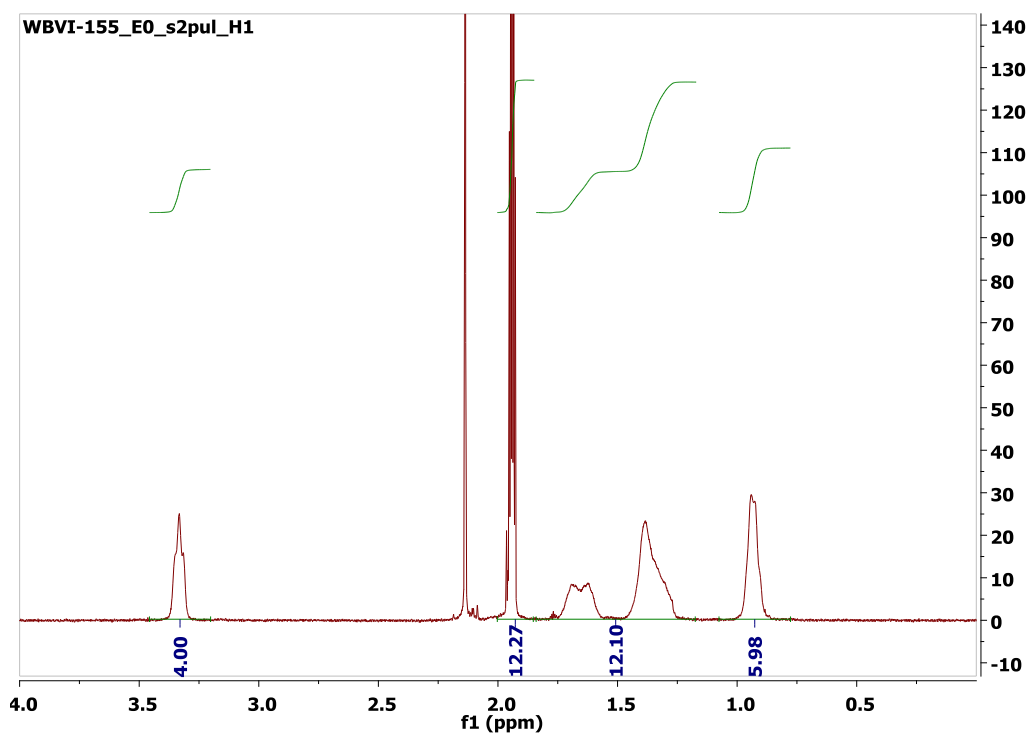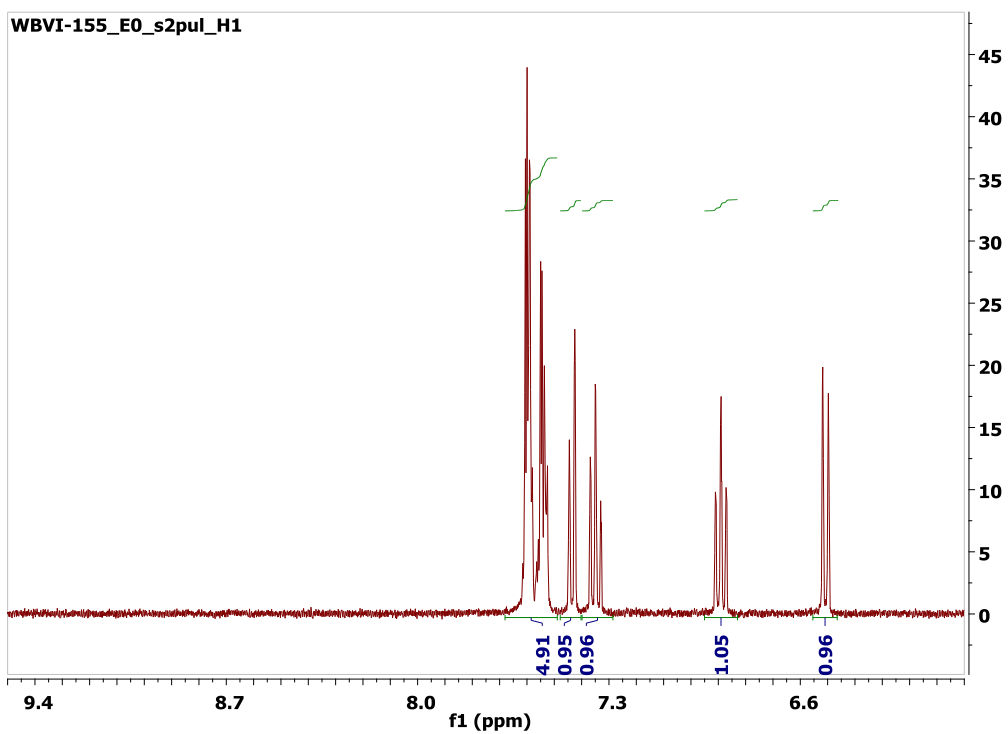
NMR File: WBVI-155_E1_s2pul_H1

Dose: 100 mJ/cm^2

WBVI-155_E1_s2pul_H1

WBVI-155_E1_s2pul_H1

157
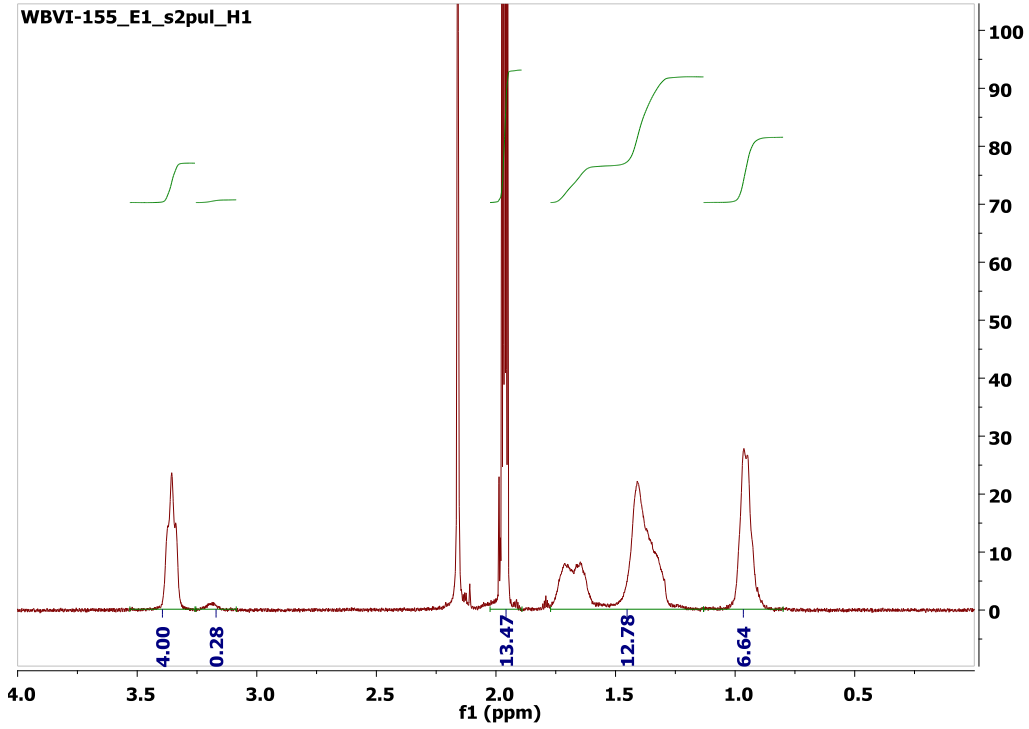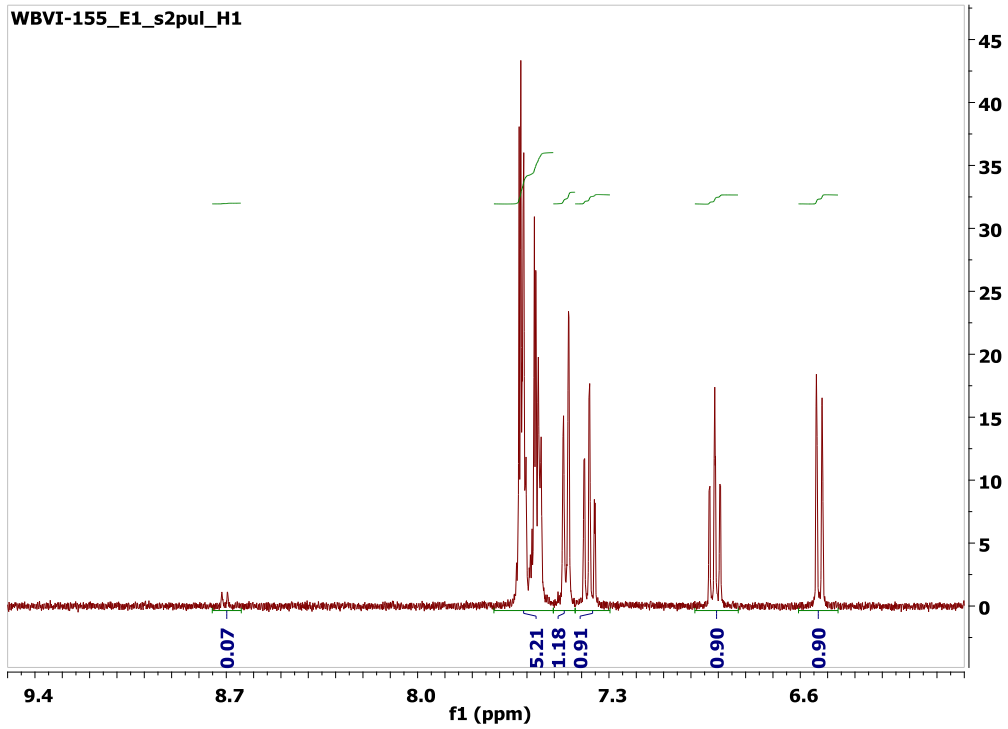
NMR File: WBVI-155_E2_s2pul_H1

Dose: 200 mJ/cm^2

WBVI_155_E2_s2pul_H1

0.07   5.50   1.45   0.97   0.94   1.03

WBVI_155_E2_s2pul_H1

4.00   0.59   0.10   14.56   14.30   7.06

f1 (ppm)
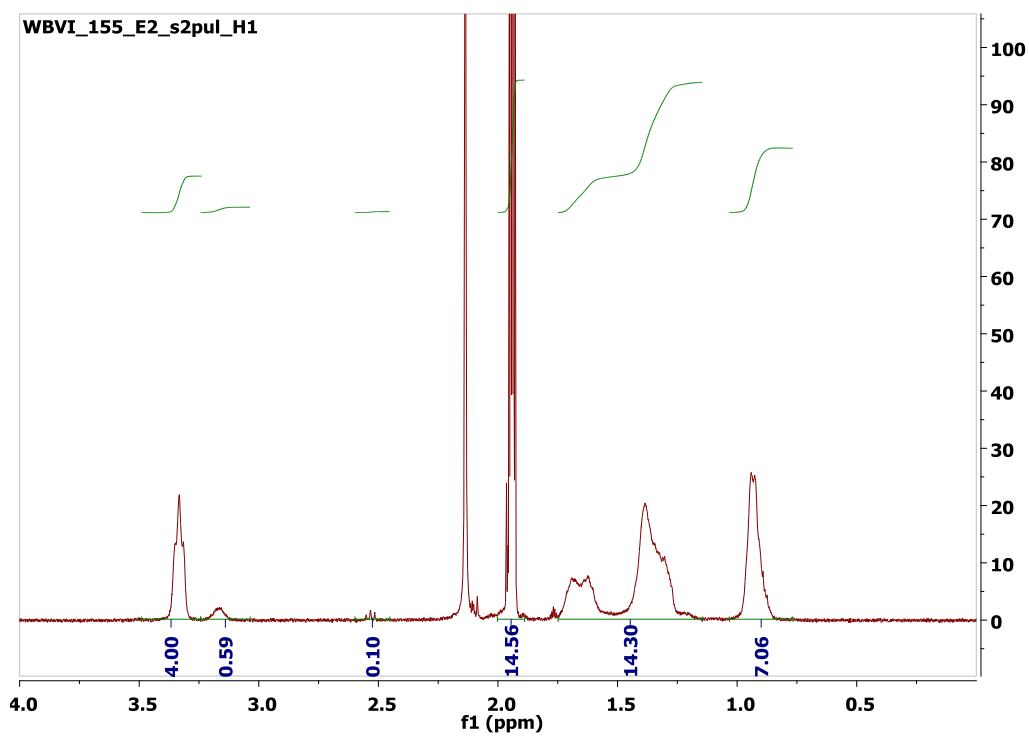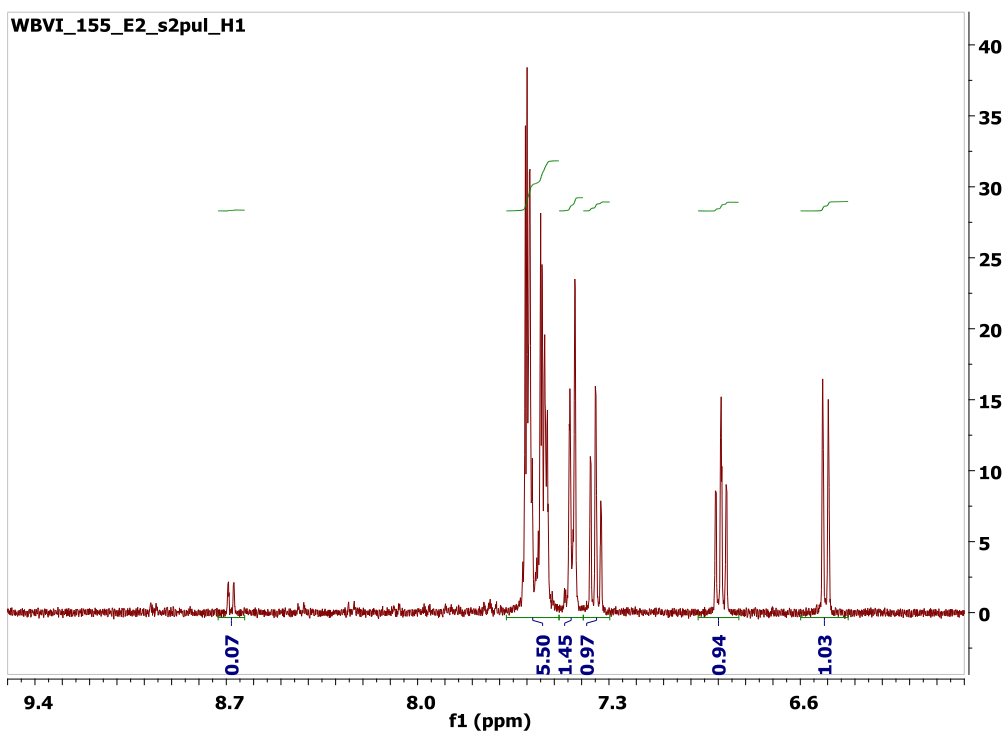
NMR File: WBVI-155_E3_s2pul_H1

Dose: 300 mJ/cm^2
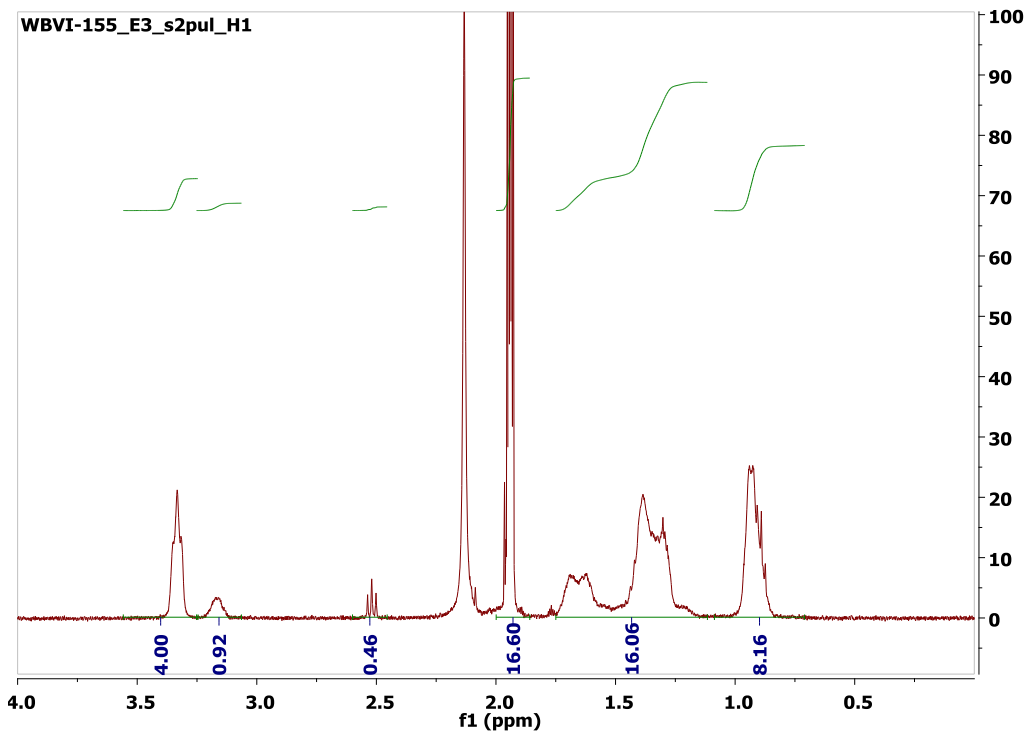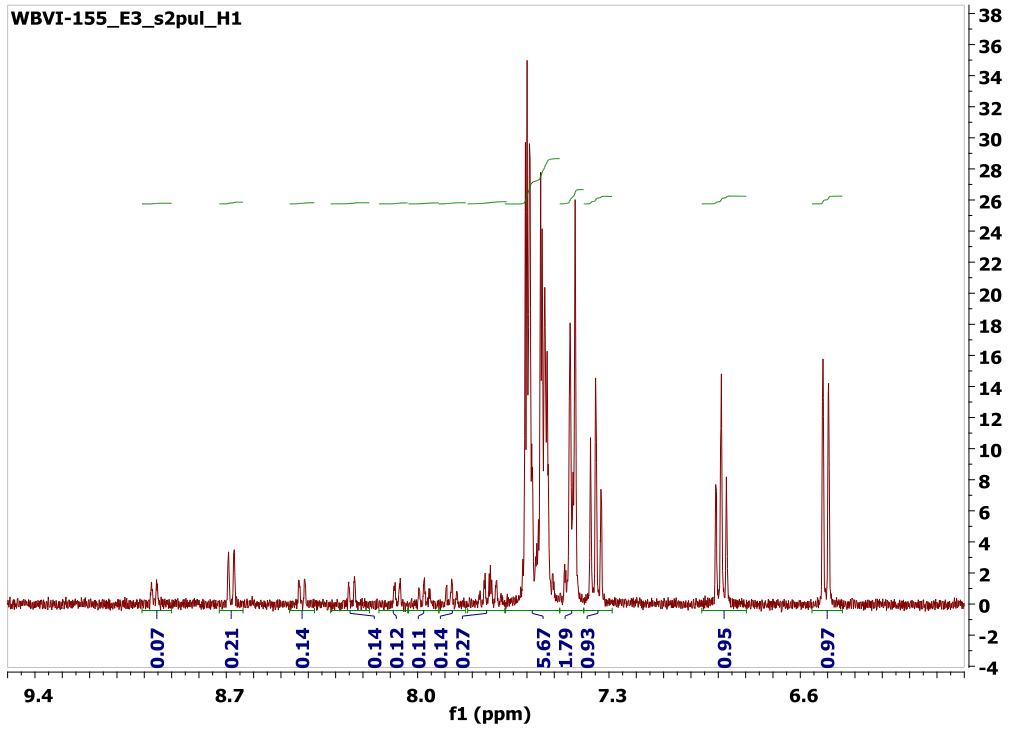
NMR File: WBVI-155_E4_s2pul_H1
Dose: 400 mJ/cm^2

WBVI-155_E4_s2pul_H1
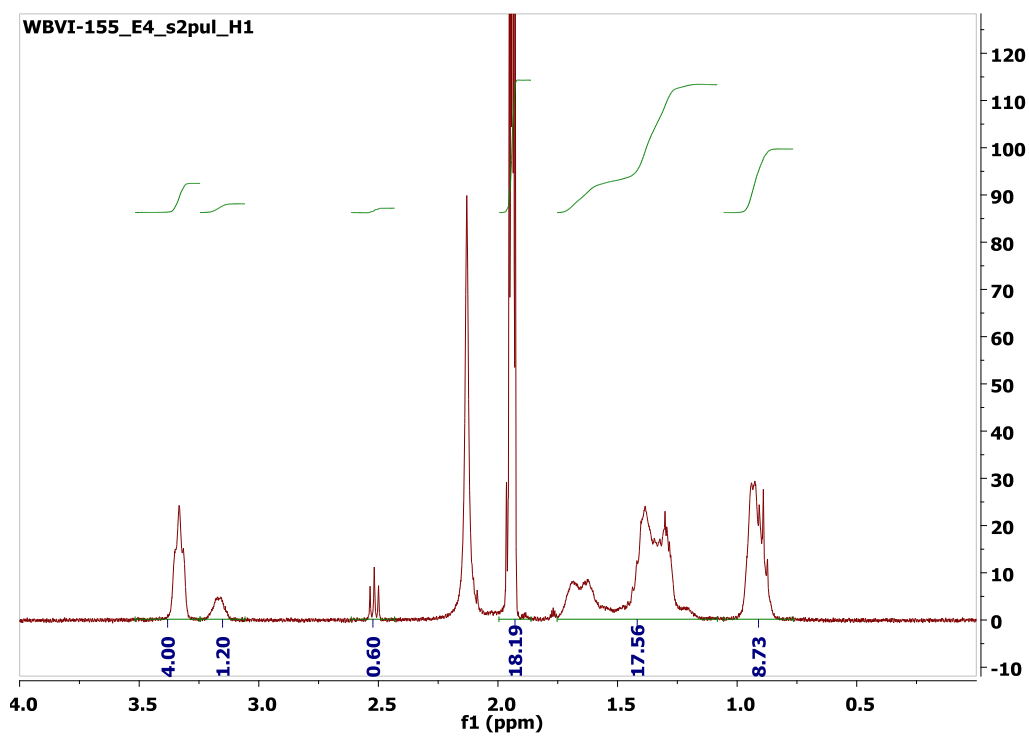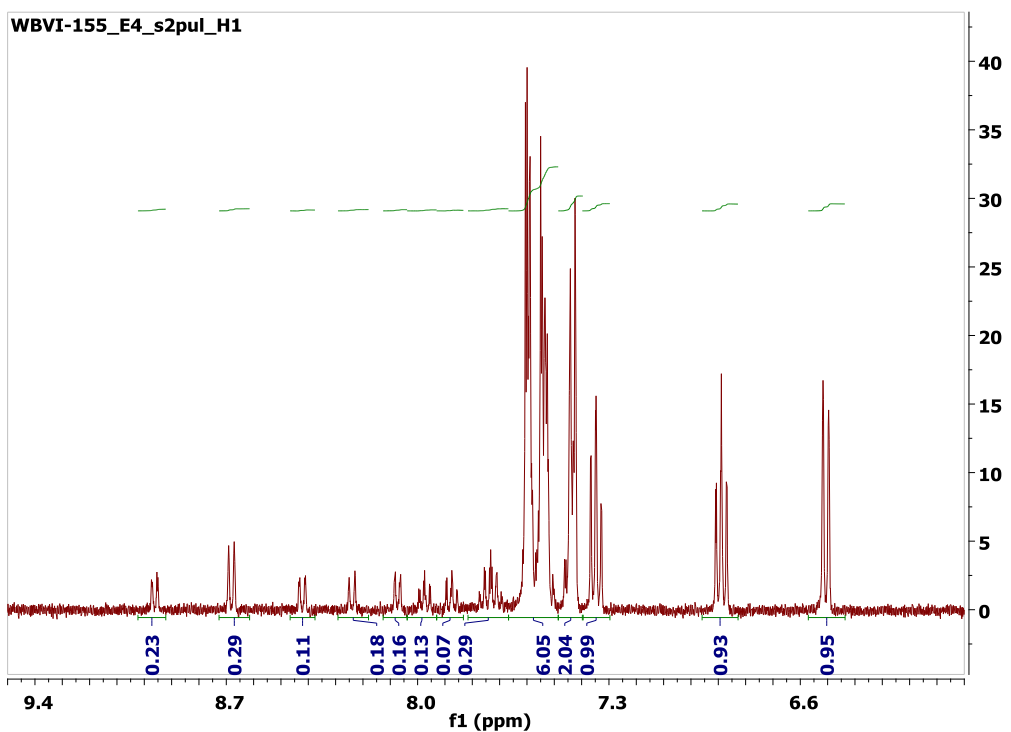
WBVI-155_E4_s2pul_H1

NMR File: WBVI-155_E5_s2pul_H1
Dose: 600 mJ/cm^2

WBVI-155_E5_s2pul_H1

0.31 0.45 0.25 0.25 0.24 0.33 0.20 0.45 6.72 2.41 0.98 1.07 1.19

f1 (ppm)

WBVI-155_E5_s2pul_H1

4.00 1.51 1.14 21.57 21.23 10.42

f1 (ppm)
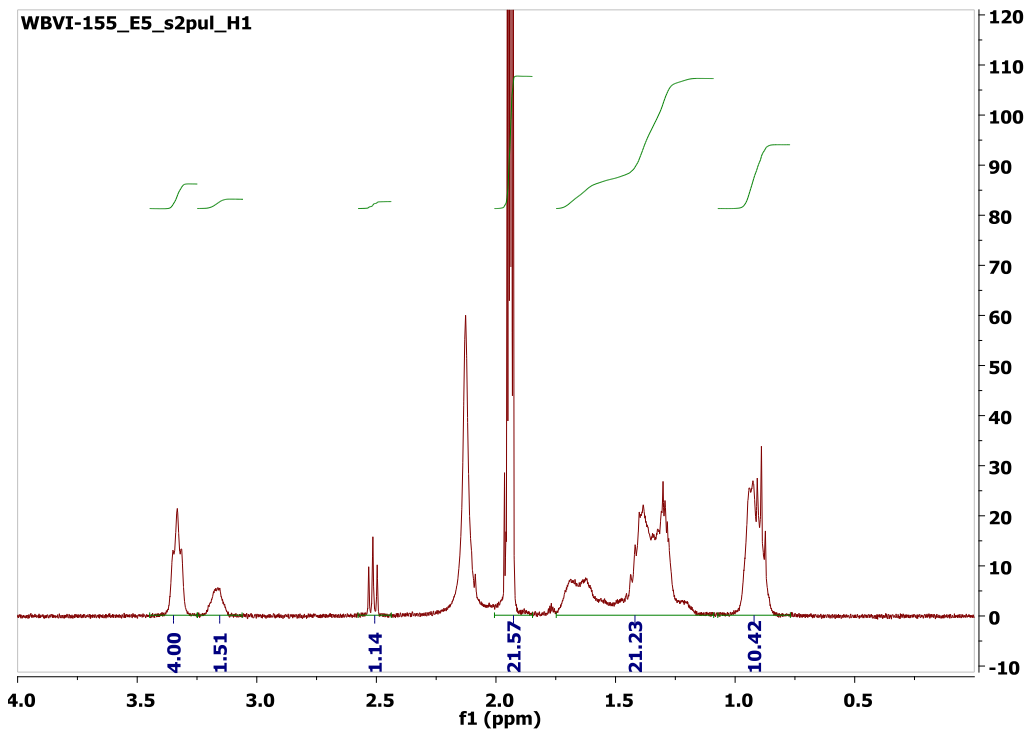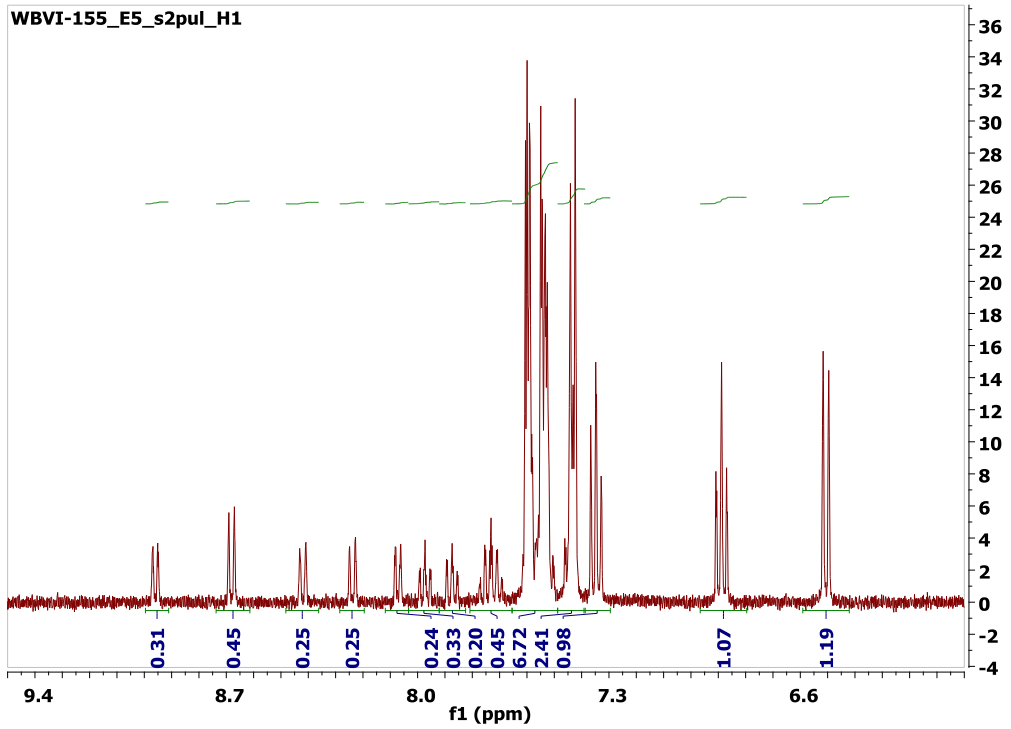
NMR File: WBVI-155_E6_s2pul_H1

Dose: 800 mJ/cm^2
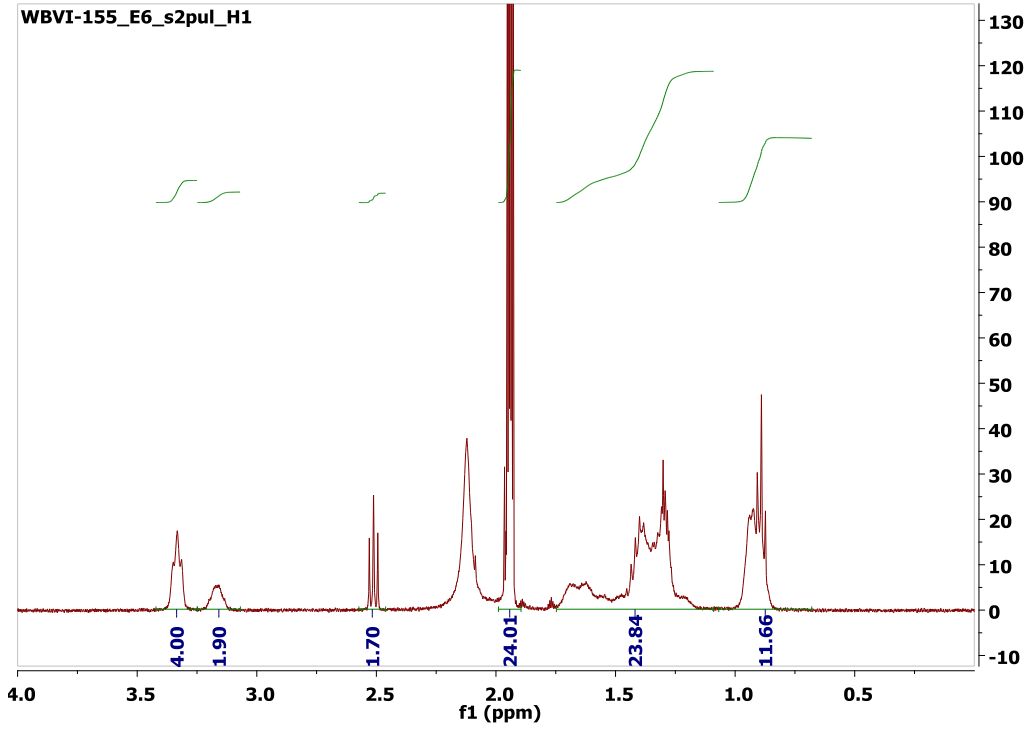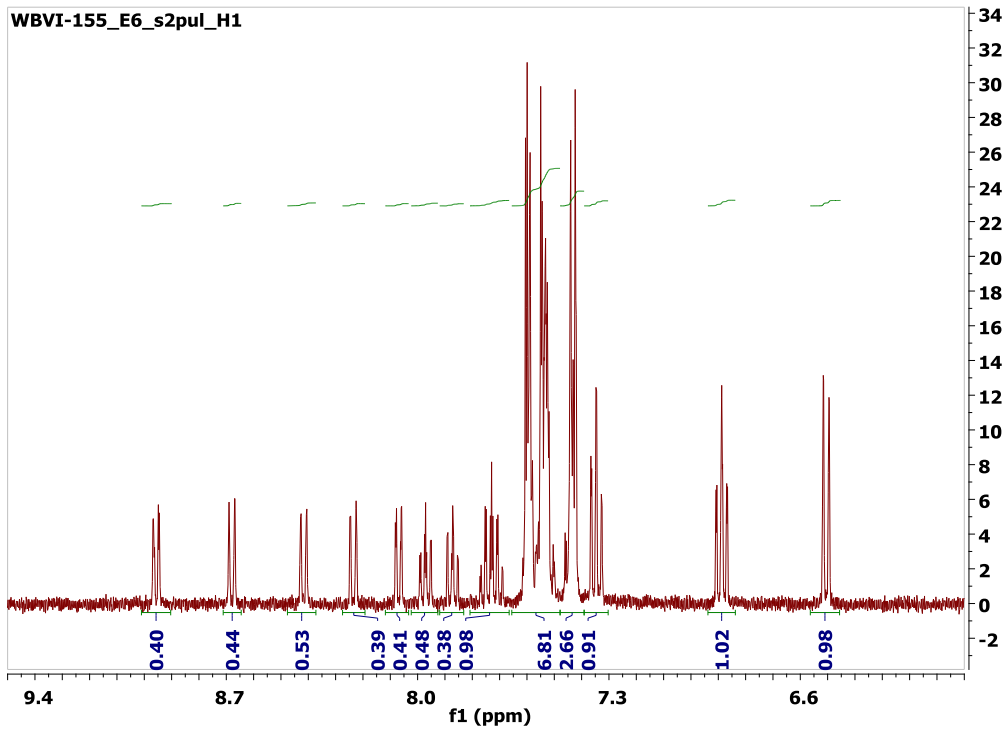
NMR File: WBVI-155_E7_s2pul_H1

Dose: 1000 mJ/cm^2
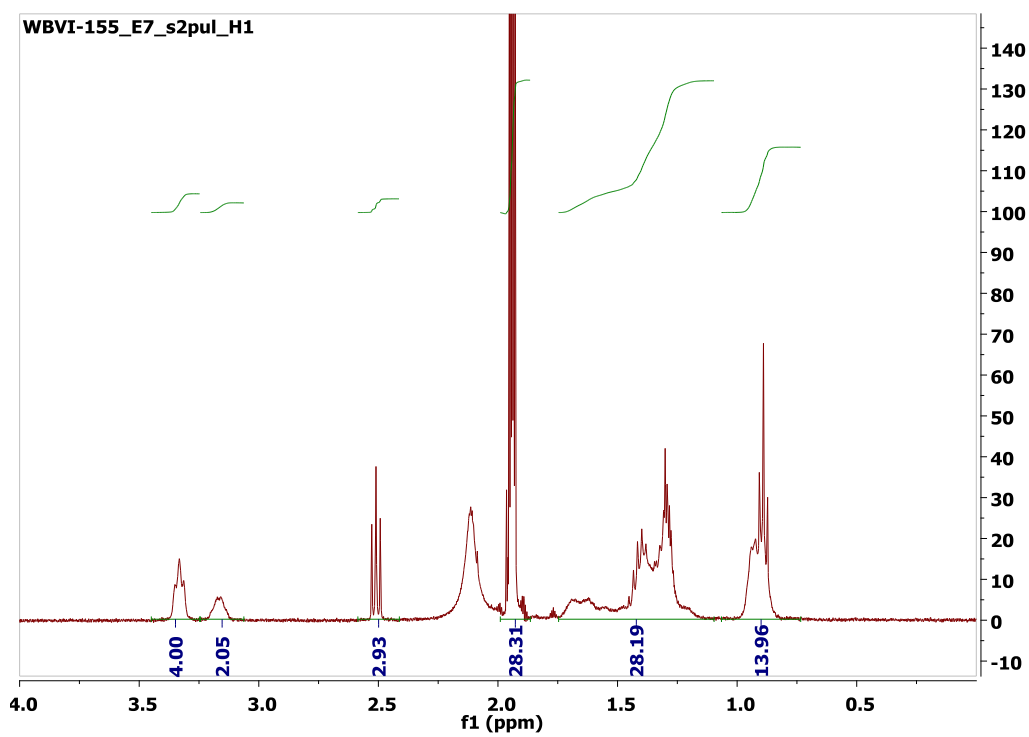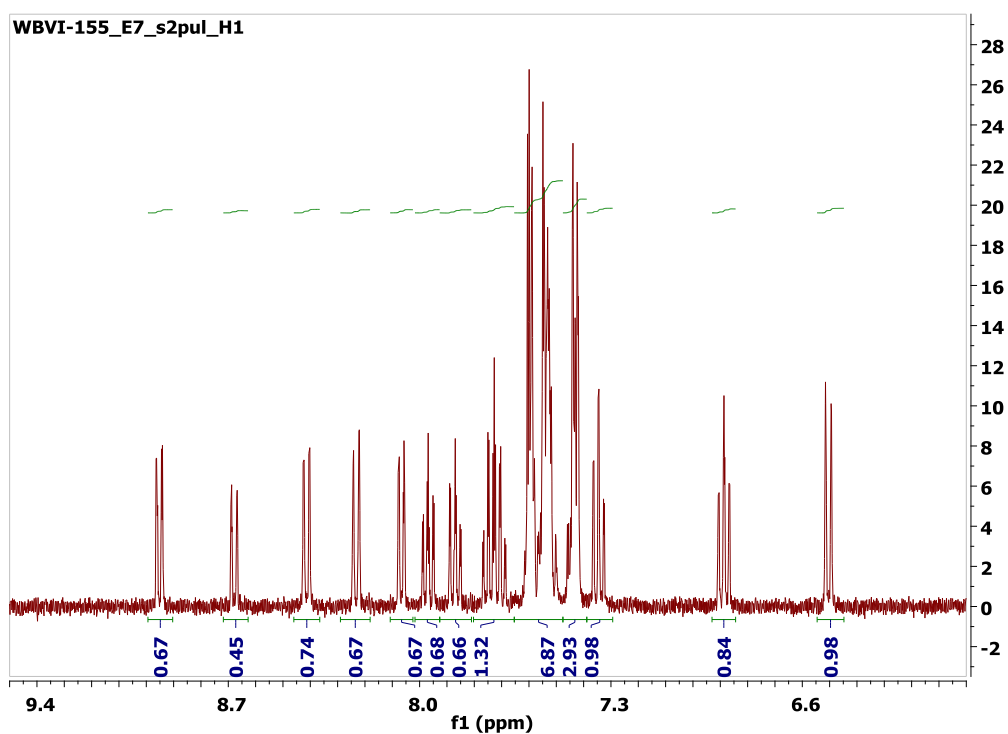
NMR File: WBVI-155_E8_s2pul_H1

Dose: 1200 mJ/cm^2
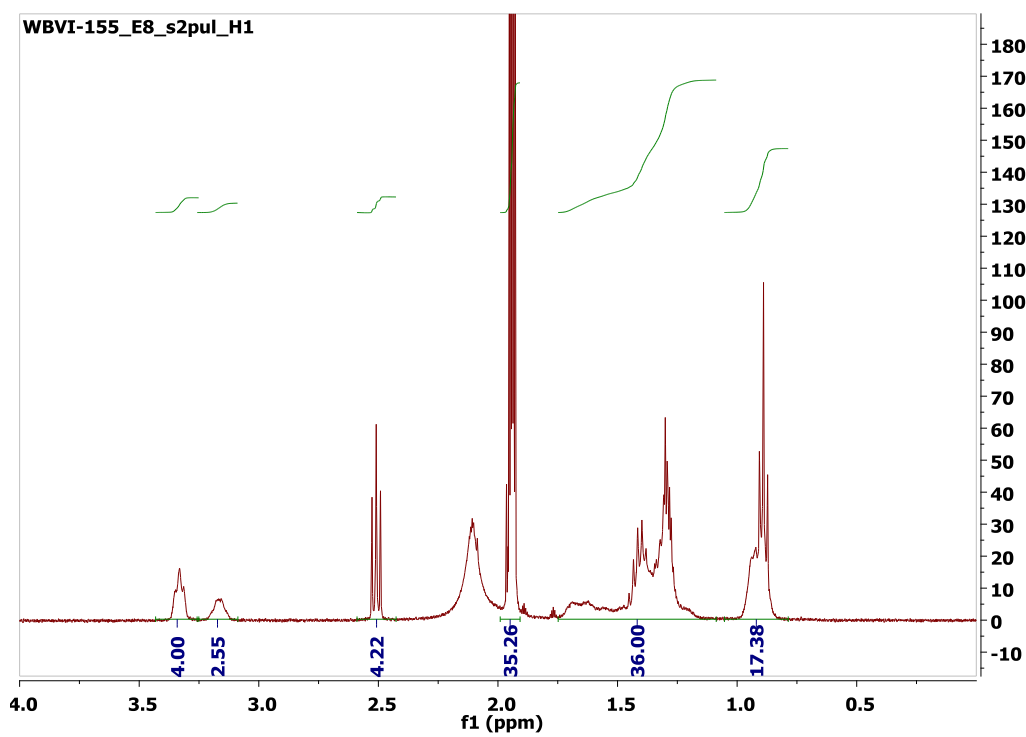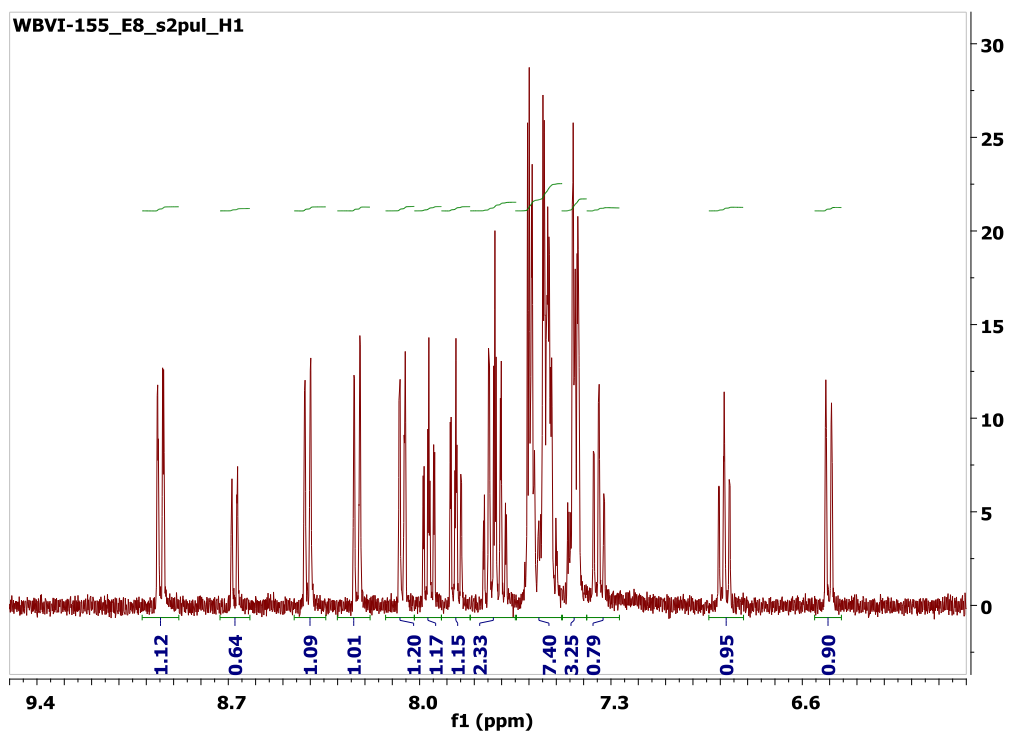
NMR File: WBVI-155_E9_s2pul_H1

Dose: 1600 mJ/cm^2
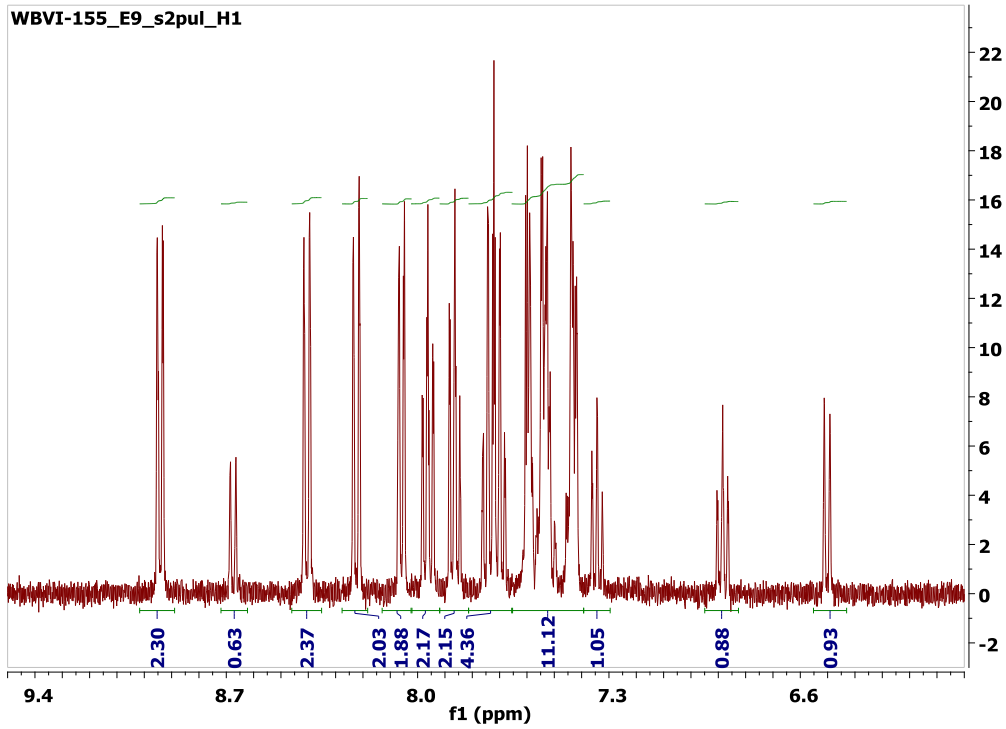
NMR File: WBVI-155_E10_s2pul_H1
Dose: 2000 mJ/cm^2
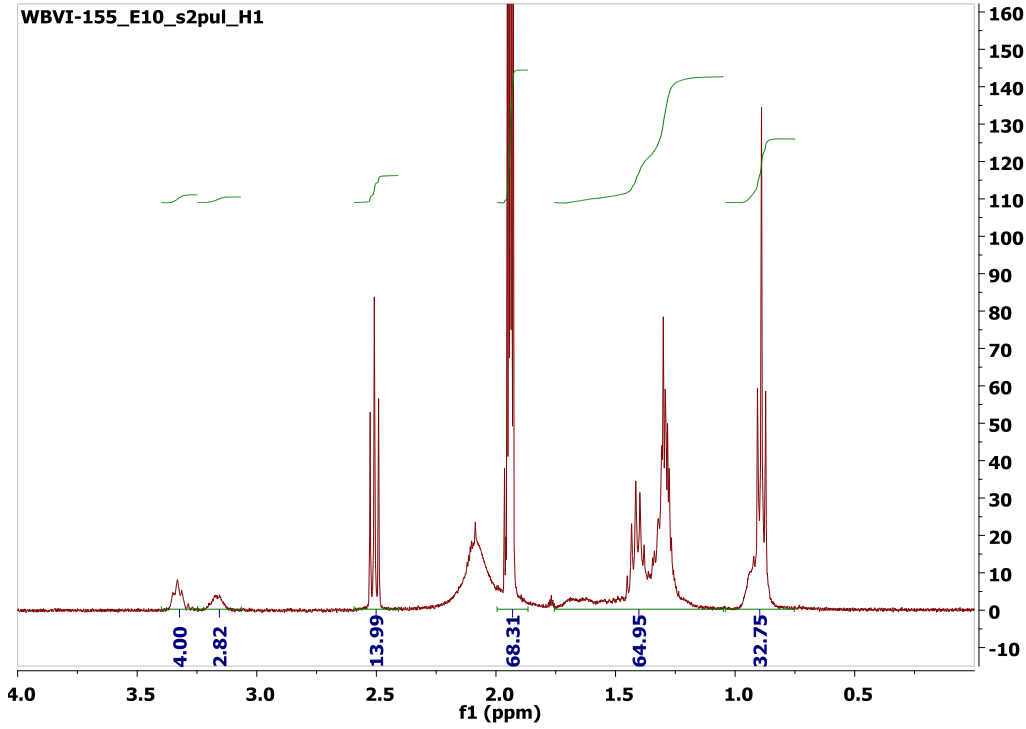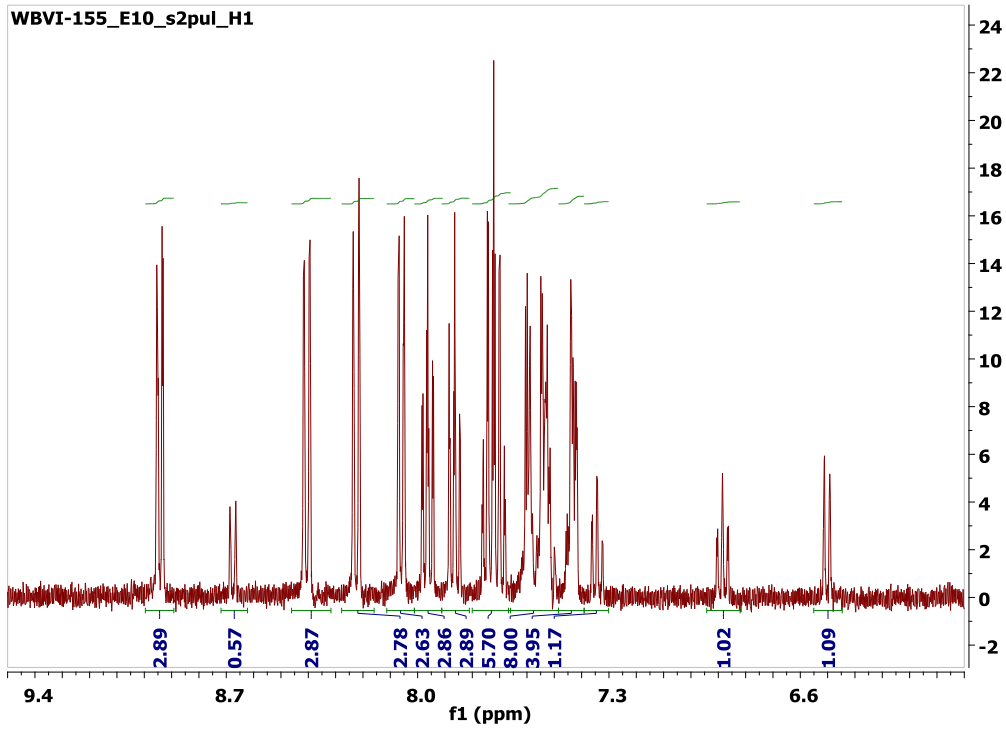
NMR File: WBVI-155_E11_s2pul_H1
Dose: 2400 mJ/cm^2
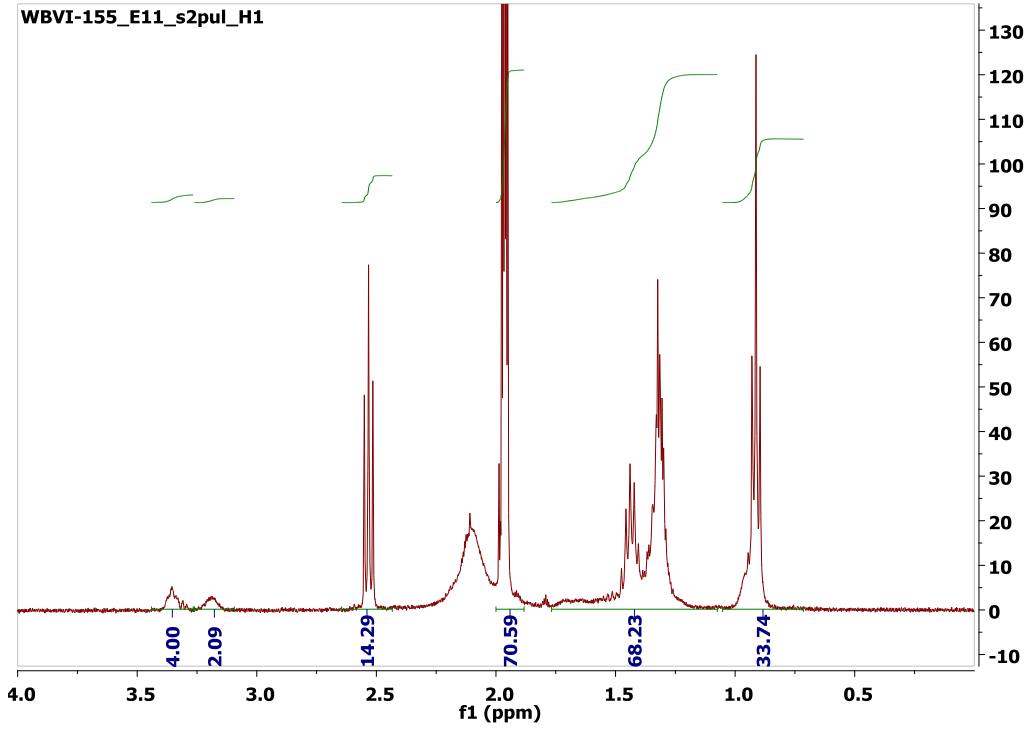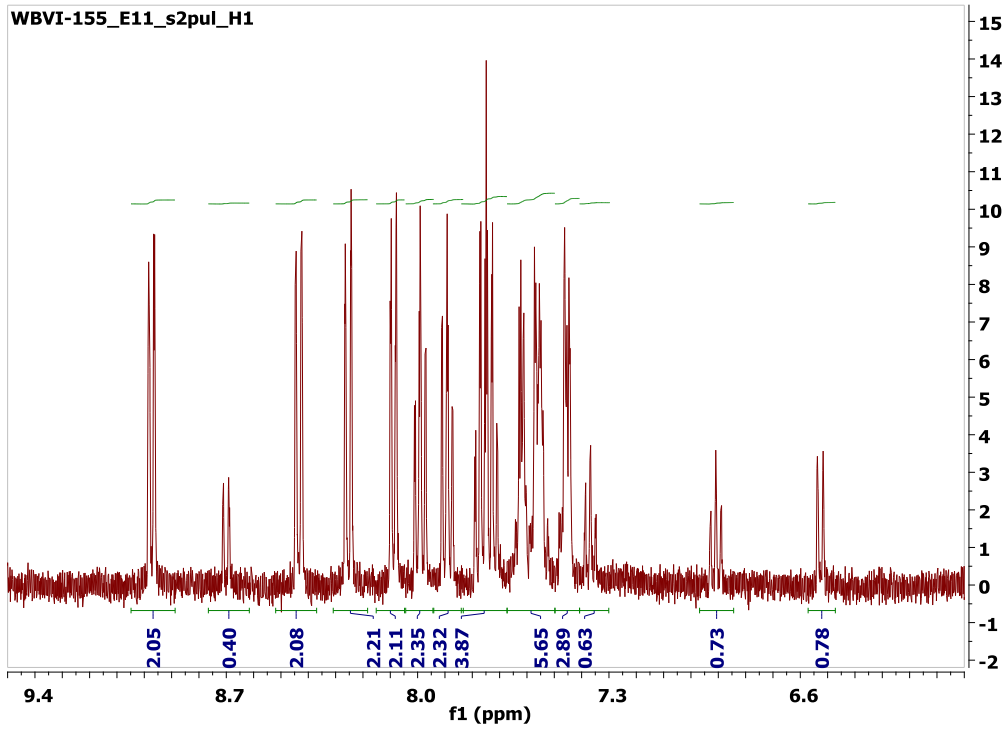
NMR File: WBVI-155_E12_s2pul_H1
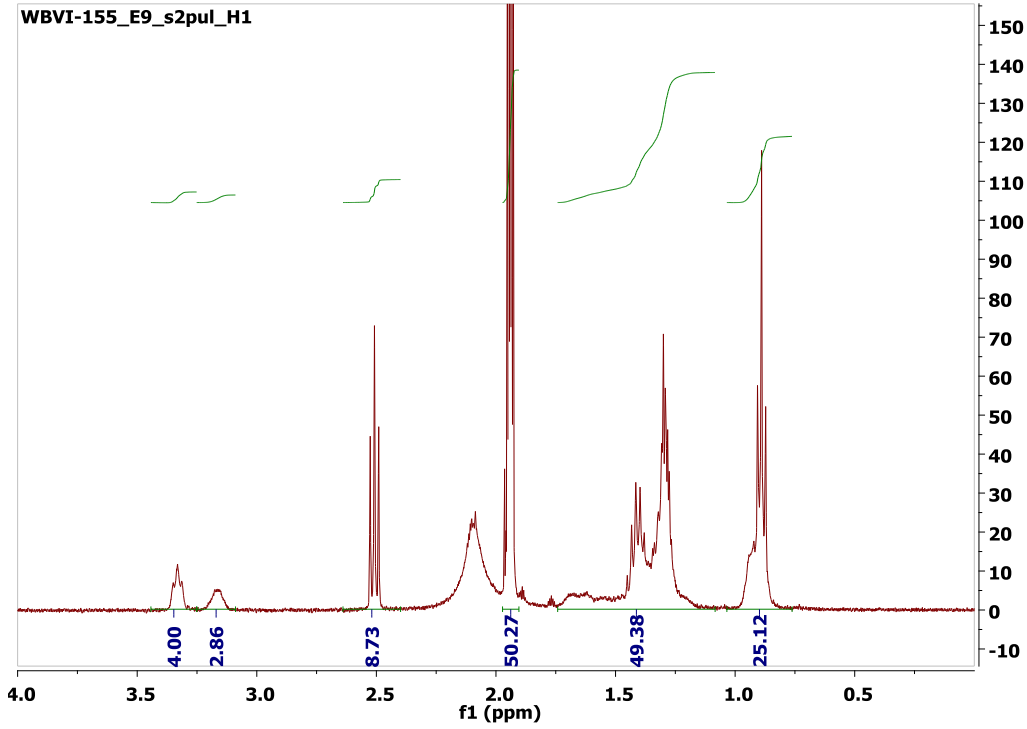**Dose:** 2800 mJ/cm^2
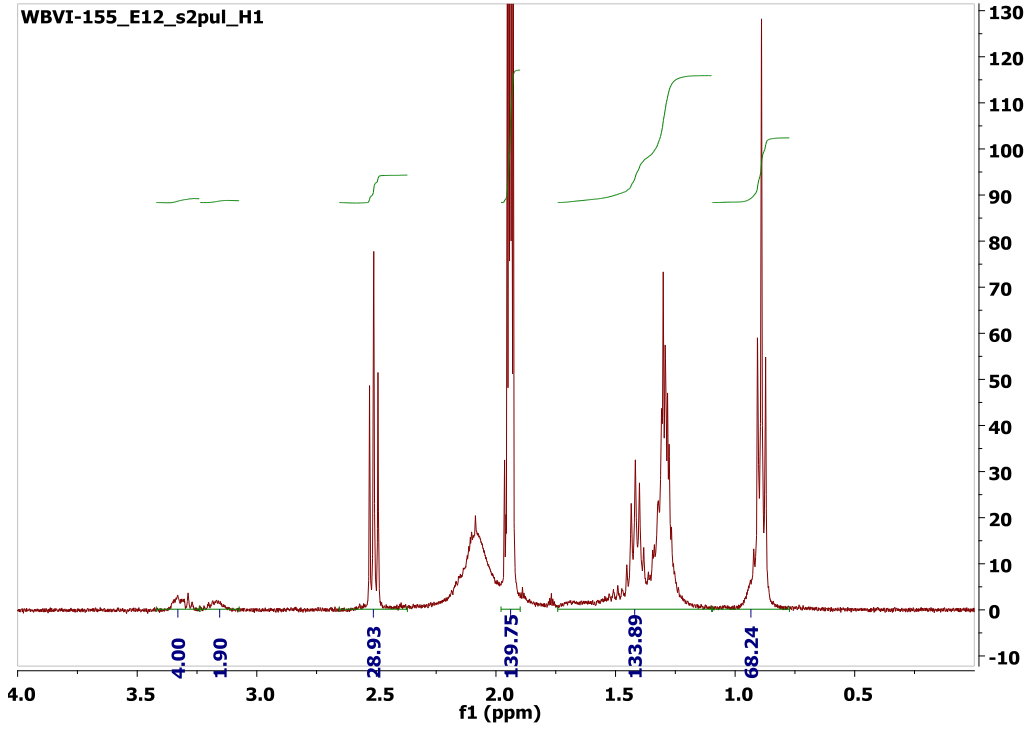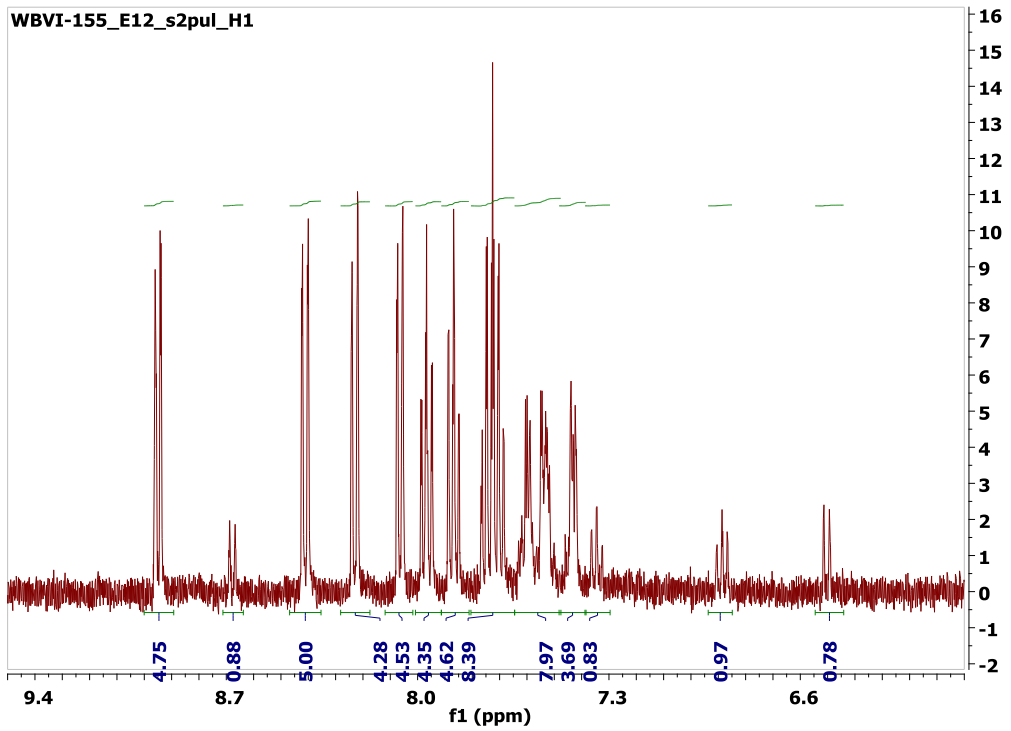
NMR File: WBVI-155_E13_s2pul_H1
Dose: 3600 mJ/cm^2
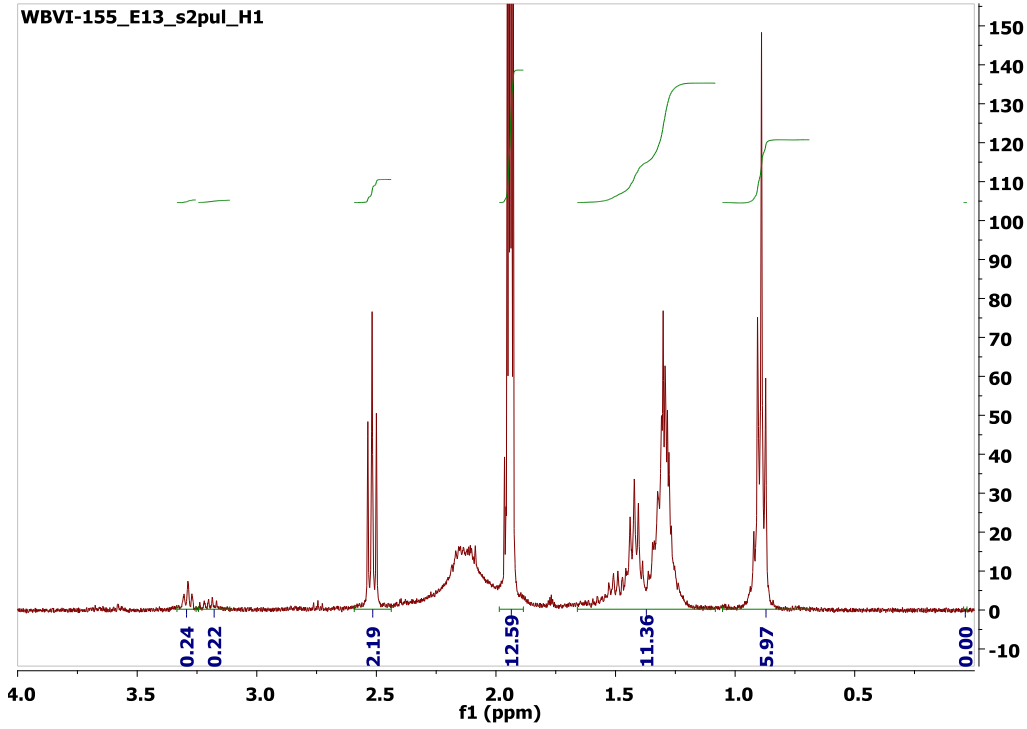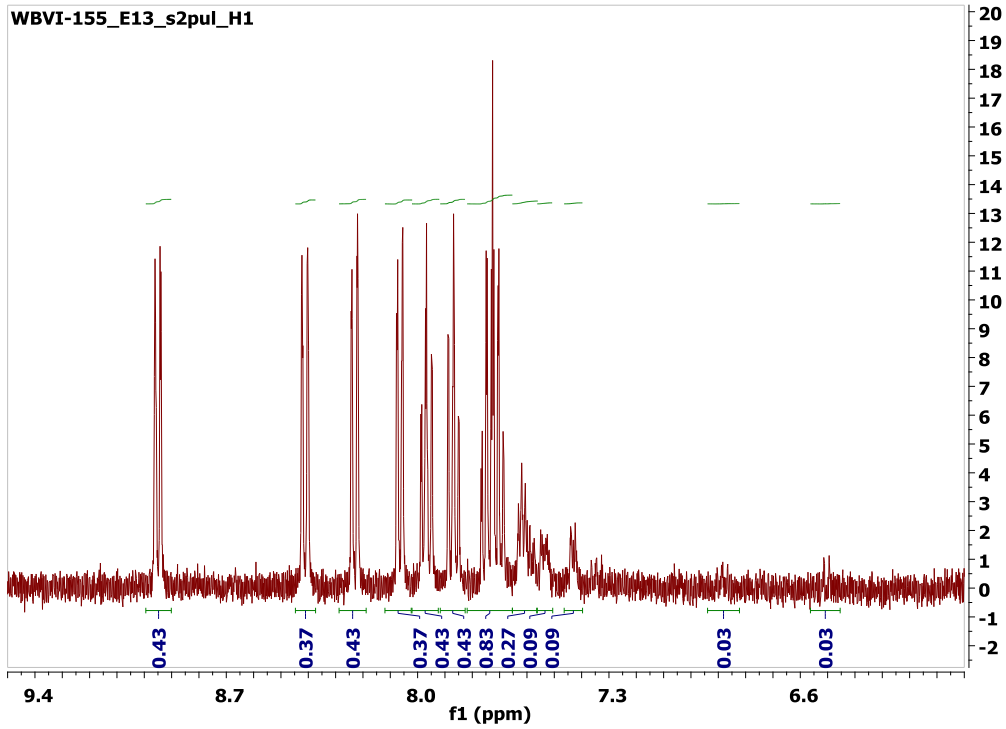
Bibliography

1. W. T. Moye, ENIAC: The Army-Sponsored Revolution, http://ftp.arl.mil/~mike/comphist/96summary/index.html, 2014.
2. M. H. Weik, The ENIAC Story, http://ftp.arl.mil/~mike/comphist/eniac-story.html, 2014.
3. F. H. Harlow and N. Metropolis, *Los Alamos Science*, 1983, 133.
4. W. B. Fritz, *Annals of the History of Computing, IEEE*, 1994, **16**, 25-45.
5. M. H. Weik, *Ballistic Research Laboratories Report № 971 – A Survey of Domestic Electronic Digital Computing Systems*, US Department of Commerce, 1955.
6. I. A. Young, E. Mohammed, J. T. S. Liao, A. M. Kern, S. Palermo, B. A. Block, M. R. Reshotko and P. L. D. Chang, *Solid-State Circuits, IEEE Journal of*, 2010, **45**, 235-248.
7. B. A. Block, T. R. Younkin, P. S. Davids, M. R. Reshotko, P. Chang, B. M. Polishak, S. Huang, J. Luo and A. K. Y. Jen, *Opt. Express*, 2008, **16**, 18326-18333.
8. J. Bardeen and W. H. Brattain, *Physical Review*, 1948, **74**, 230-231.
9. W. H. Brattain and J. Bardeen, *Physical Review*, 1948, **74**, 231-232.
10. W. Shockley and G. L. Pearson, *Physical Review*, 1948, **74**, 232-233.
11. K. Suyama and M. Shirai, *Progress in Polymer Science*, 2009, **34**, 194-209.
12. http://www.chipsetc.com/the-transistor.html.
13. J. S. Kilby, *Electron Devices, IEEE Transactions on*, 1976, **23**, 648-654.
14. Z. Shi, W. Liang, J. Luo, S. Huang, B. M. Polishak, X. Li, T. R. Younkin, B. A. Block and A. K. Y. Jen, *Chemistry of Materials*, 2010, **22**, 5601-5608.
15. J. A. Hoerni, Planar silicon diodes and transistors, 1960.
16. R. Norman, J. Last and I. Haas, Solid-state micrologic elements, 1960.
17. J. W. Stansbury, *Journal of Esthetic and Restorative Dentistry*, 2000, **12**, 300-308.
18. J. W. Stansbury and S. H. Dickens, *Dental Materials*, 2001, **17**, 71-79.
19. G. E. Moore, *Proceedings of the IEEE*, 1998, **86**, 82-85.
20. G. E. Moore, Progress in digital integrated electronics, 1975.
21. N. B. Cramer and C. N. Bowman, *Journal of Polymer Science Part A: Polymer Chemistry*, 2001, **39**, 3311-3319.
22. C. Mack, *Fundamental Principles of Optical Lithography*, John Wiley & Sons, Ltd., Chichester, West Sussex, 2007.
23. T. Y. Lee, T. M. Roper, E. S. Jonsson, I. Kudyakov, K. Viswanathan, C. Nason, C. A. Guymon and C. E. Hoyle, *Polymer*, 2003, **44**, 2859-2865.
24. R. H. French and H. V. Tran, *Annual Review of Materials Research*, 2009, **39**, 93-126.
25. C. G. Willson, in *Introduction to Microlithography*, AMERICAN CHEMICAL SOCIETY, 1983, vol. 219, ch. 3, pp. 87-159.

26.   *United Kingdom Pat.,* 762,985, 1954.

27.   J. M. J. Fréchet, E. Eichler, H. Ito and C. G. Willson, *Polymer*, 1983, **24**, 995-1000.

28.   J. V. Crivello, *Journal of Polymer Science Part A: Polymer Chemistry*, 1999, **37**, 4241-4254.

29.   C. G. Willson, H. Ito, J. M. J. Fréchet, T. G. Tessier and F. M. Houlihan, *Journal of The Electrochemical Society*, 1986, **133**, 181-187.

30.   E. Reichmanis and L. F. Thompson, *Chemical Reviews*, 1989, **89**, 1273-1289.

31.   C. P. Umbach, A. N. Broers, R. H. Koch, C. G. Willson and R. B. Laibowitz, *IBM Journal of Research and Development*, 1988, **32**, 454-461.

32.   S. A. MacDonald, W. D. Hinsberg, H. R. Wendt, N. J. Clecak, C. G. Willson and C. D. Snyder, *Chemistry of Materials*, 1993, **5**, 348-356.

33.   W. D. Hinsberg, S. A. MacDonald, N. J. Clecak, C. D. Snyder and H. Ito, Influence of polymer properties on airborne chemical contamination of chemically amplified resists, 1993.

34.   J. G. Maltabes, S. J. Holmes, J. R. Morrow, R. L. Barr, M. C. Hakey, G. Reynolds, W. R. Brunsvold, C. G. Willson, N. J. Clecak, S. A. MacDonald and H. Ito, 1X deep-UV lithography with chemical amplification for 1-micron DRAM production, 1990.

35.   Y. Kaimoto, K. Nozaki, S. Takechi and N. Abe, Alicyclic polymer for ArF and KrF excimer resist based on chemical amplification, 1992.

36.   R. R. Kunz, S. C. Palmateer, A. R. Forte, R. D. Allen, G. M. Wallraff, R. A. Di Pietro and D. C. Hofer, Limits to etch resistance for 193-nm single-layer resists, 1996.

37.   R. D. Allen, R. Sooriyakumaran, J. Opitz, G. M. Wallraff, G. Breyta, R. A. Dipietro, D. C. Hofer, R. R. Kunz, U. Okoroanyanwu and C. G. Willson, *Journal of Photopolymer Science and Technology*, 1996, **9**, 465-474.

38.   T. I. Wallow, F. M. Houlihan, O. Nalamasu, E. A. Chandross, T. X. Neenan and E. Reichmanis, Evaluation of cycloolefin-maleic anhydride alternating copolymers as single-layer photoresists for 193-nm photolithography, 1996.

39.   M. Rothschild, T. M. Bloomstein, T. H. Fedynyshyn, R. R. Kunz, V. Liberman, M. Switkes, N. N. Efremow, S. T. Palmacci, J. H. Sedlacek and D. E. Hardy, *Lincoln Laboratory Journal*, 2003, **14**, 221-236.

40.   J. Mick, in *Daily Tech*, 2014.

41.   A. K. Bates, M. Rothschild, T. M. Bloomstein, T. H. Fedynyshyn, R. R. Kunz, V. Liberman and M. Switkes, *IBM Journal of Research and Development*, 2001, **45**, 605-614.

42.   K. Ronse, P. De Bisschop, A. M. Goethals, J. Hermans, R. Jonckheere, S. Light, U. Okoroanyanwu, R. Watso, D. McAfferty, J. Ivaldi, T. Oneil and H. Sewell, *Microelectronic Engineering*, 2004, **73–74**, 5-10.

43.   F. L. Palmieri, University of Texas, 2008.

44.   J. R. Strahan, University of Texas, 2010.

45.   B. M. Jacobsson, University of Texas, 2011.

46. S.-P. Jeng, R. H. Havemann and M.-C. Chang, *MRS Online Proceedings Library*, 1994, **337**, 25-31.
47. W. Volksen, R. D. Miller and G. Dubois, *Chemical Reviews*, 2010, **110**, 56-110.
48. M. Morgen, E. T. Ryan, J.-H. Zhao, C. Hu, T. Cho and P. S. Ho, *Annual Review of Materials Science*, 2000, **30**, 645-680.
49. L. Zhang, Z. Cai, Q. Yu and Z. Liang, *Journal of Applied Polymer Science*, 1999, **71**, 1081-1087.
50. P. N. W. Prasad, David J., *Introduction To Nonlinear Optical Effects In Molecules And Polymers*, Wiley, New York, 1991.
51. P. A. Franken, A. E. Hill, C. W. Peters and G. Weinreich, *Physical Review Letters*, 1961, **7**, 118-119.
52. S. Haroche, *Physical Review Letters*, 2008, **101**, 160001.
53. KTP Properties, http://www.unitedcrystals.com/KTPProp.html.
54. I. A. Young, B. Block, M. Reshotko and P. Chang, Integration of nano-photonic devices for CMOS chip-to-chip optical I/O, 2010.
55. R. S. Weis and T. K. Gaylord, *Appl. Phys. A*, 1985, **37**, 191-203.
56. E. L. Wooten, K. M. Kissa, A. Yi-Yan, E. J. Murphy, D. A. Lafaw, P. F. Hallemeier, D. Maack, D. V. Attanasio, D. J. Fritz, G. J. McBrien and D. E. Bossi, *Selected Topics in Quantum Electronics, IEEE Journal of*, 2000, **6**, 69-82.
57. A. Hellwig, http://upload.wikimedia.org/wikipedia/commons/f/f5/Linbo3_Unit_Cell.png.
58. H. Ma, A. K. Y. Jen and L. R. Dalton, *Advanced Materials*, 2002, **14**, 1339-1365.
59. D. Chen, H. R. Fetterman, A. Chen, W. H. Steier, L. R. Dalton, W. Wang and Y. Shi, *Applied Physics Letters*, 1997, **70**, 3335-3337.
60. J. Chen, A. Chen, H. R. Fetterman, V. Chuyanov, F. Wang, J. Zhu, H. Zhang, S. Garner, M. He, Y. Ra, S.-S. Lee, W. H. Steier, S. S. H. Mao, A. W. Harper and L. R. Dalton, *OPTICE*, 1999, **38**, 2000-2008.
61. O. Hyun-Ho, S.-W. Ahn and S. Sang-Yung, *Electronics Letters*, 2000, **36**, 969-970.
62. C. Zhang, L. R. Dalton, M.-C. Oh, H. Zhang and W. H. Steier, *Chemistry of Materials*, 2001, **13**, 3043-3050.
63. M. Sprave, R. Blum and M. Eich, *Applied Physics Letters*, 1996, **69**, 2962-2964.
64. R. A. Hill, A. Knoesen and M. A. Mortazavi, *Applied Physics Letters*, 1994, **65**, 1733-1735.
65. M. A. Pauley and C. H. Wang, *Chemical Physics Letters*, 1997, **280**, 544-550.
66. J. A. Davies, A. Elangovan, P. A. Sullivan, B. C. Olbricht, D. H. Bale, T. R. Ewy, C. M. Isborn, B. E. Eichinger, B. H. Robinson, P. J. Reid, X. Li and L. R. Dalton, *Journal of the American Chemical Society*, 2008, **130**, 10565-10575.
67. B. M. Polishak, S. Huang, J. Luo, Z. Shi, X.-H. Zhou, A. Hsu and A. K. Y. Jen, *Macromolecules*, 2010, **44**, 1261-1265.
68. Y. Takimoto, C. M. Isborn, B. E. Eichinger, J. J. Rehr and B. H. Robinson, *The Journal of Physical Chemistry C*, 2008, **112**, 8016-8021.
69. L. R. Dalton, P. A. Sullivan and D. H. Bale, *Chemical Reviews*, 2010, **110**, 25-55.

70. L. R. S. Dalton, P.; Jen, A. K. Y., in *The Handbook of Photonics*, CRC Press, Boca Raton, FL, Second Edition edn., 2007, ch. Second and Third-Order Nonlinear Optical Materials.

71. D. R. Kanis, M. A. Ratner and T. J. Marks, *Chemical Reviews*, 1994, **94**, 195-242.

72. S. R. Marder, C. B. Gorman, B. G. Tiemann and L. T. Cheng, *Journal of the American Chemical Society*, 1993, **115**, 3006-3007.

73. L. T. Cheng, W. Tam, S. R. Marder, A. E. Stiegman, G. Rikken and C. W. Spangler, *The Journal of Physical Chemistry*, 1991, **95**, 10643-10652.

74. A. Dulcic, C. Flytzanis, C. L. Tang, D. Pépin, M. Fétizon and Y. Hoppilliard, *The Journal of Chemical Physics*, 1981, **74**, 1559-1563.

75. B. H. Robinson, L. R. Dalton, A. W. Harper, A. Ren, F. Wang, C. Zhang, G. Todorova, M. Lee, R. Aniszfeld, S. Garner, A. Chen, W. H. Steier, S. Houbrecht, A. Persoons, I. Ledoux, J. Zyss and A. K. Y. Jen, *Chemical Physics*, 1999, **245**, 35-50.

76. M. He, T. M. Leslie and J. A. Sinicropi, *Chemistry of Materials*, 2002, **14**, 4662-4668.

77. H. Ma, S. Liu, J. Luo, S. Suresh, L. Liu, S. H. Kang, M. Haller, T. Sassa, L. R. Dalton and A. K. Y. Jen, *Advanced Functional Materials*, 2002, **12**, 565-574.

78. J. Luo, S. Huang, Y.-J. Cheng, T.-D. Kim, Z. Shi, X.-H. Zhou and A. K. Y. Jen, *Organic Letters*, 2007, **9**, 4471-4474.

79. Y.-J. Cheng, J. Luo, S. Huang, X. Zhou, Z. Shi, T.-D. Kim, D. H. Bale, S. Takahashi, A. Yick, B. M. Polishak, S.-H. Jang, L. R. Dalton, P. J. Reid, W. H. Steier and A. K. Y. Jen, *Chemistry of Materials*, 2008, **20**, 5047-5054.

80. M. E. DeRosa, M. He, J. S. Cites, S. M. Garner and Y. R. Tang, *The Journal of Physical Chemistry B*, 2004, **108**, 8725-8730.

81. M. J. Cho, D. H. Choi, P. A. Sullivan, A. J. P. Akelaitis and L. R. Dalton, *Progress in Polymer Science*, 2008, **33**, 1013-1058.

82. S. R. Marder and J. W. Perry, *Science*, 1994, **263**, 1706-1707.

83. S.-H. Jang, J. Luo, N. M. Tucker, A. Leclercq, E. Zojer, M. A. Haller, T.-D. Kim, J.-W. Kang, K. Firestone, D. Bale, D. Lao, J. B. Benedict, D. Cohen, W. Kaminsky, B. Kahr, J.-L. Brédas, P. Reid, L. R. Dalton and A. K. Y. Jen, *Chemistry of Materials*, 2006, **18**, 2982-2988.

84. G. Melikian, F. P. Rouessac and C. Alexandre, *Synthetic Communications*, 1995, **25**, 3045-3051.

85. M. He, T. M. Leslie and J. A. Sinicropi, *Chemistry of Materials*, 2002, **14**, 2393-2400.

86. Y. Liao, B. E. Eichinger, K. A. Firestone, M. Haller, J. Luo, W. Kaminsky, J. B. Benedict, P. J. Reid, A. K. Y. Jen, L. R. Dalton and B. H. Robinson, *Journal of the American Chemical Society*, 2005, **127**, 2758-2766.

87. T.-D. Kim, J.-W. Kang, J. Luo, S.-H. Jang, J.-W. Ka, N. Tucker, J. B. Benedict, L. R. Dalton, T. Gray, R. M. Overney, D. H. Park, W. N. Herman and A. K. Y. Jen, *Journal of the American Chemical Society*, 2007, **129**, 488-489.

88. S. Liu, M. A. Haller, H. Ma, L. R. Dalton, S. H. Jang and A. K. Y. Jen, *Advanced Materials*, 2003, **15**, 603-607.

89. G. R. Meredith, J. VanDusen and D. J. Williams, *Macromolecules*, 1982, **15**, 1385-1389.

90. L. R. Dalton, A. W. Harper, B. Wu, R. Ghosn, J. Laquindanum, Z. Liang, A. Hubbel and C. Xu, *Advanced Materials*, 1995, **7**, 519-540.

91. L. Dalton, ed. K.-S. Lee, Springer Berlin / Heidelberg, 2002, vol. 158, pp. 1-86.

92. J. R. R. Barto, C. W. Frank, P. V. Bedworth, S. Ermer and R. E. Taylor, *The Journal of Chemical Physics*, 2005, **122**, 234907-234914.

93. D. Jin, H. Chen, A. Barklund, J. Mallari, G. Yu, E. Miller and R. Dinu, EO polymer modulators reliability study, San Francisco, California, USA, 2010.

94. Z. Shi, J. Luo, S. Huang, B. M. Polishak, X.-H. Zhou, S. Liff, T. R. Younkin, B. A. Block and A. K. Y. Jen, *Journal of Materials Chemistry*, 2012, **22**, 951-959.

95. K. D. Singer, M. G. Kuzyk, W. R. Holland, J. E. Sohn, S. J. Lalama, R. B. Comizzoli, H. E. Katz and M. L. Schilling, *Applied Physics Letters*, 1988, **53**, 1800-1802.

96. Z. Shi, J. Luo, S. Huang, Y.-J. Cheng, T.-D. Kim, B. M. Polishak, X.-H. Zhou, Y. Tian, S.-H. Jang, J. D. B. Knorr, R. M. Overney, T. R. Younkin and A. K. Y. Jen, *Macromolecules*, 2009, **42**, 2438-2445.

97. M. Mitchell, J. Mulvaney, H. K. Hall, Jr., C. Willand, H. Hampsch and D. Williams, *Polymer Bulletin*, 1992, **28**, 381-388.

98. H.-C. Tsai, W.-J. Kuo and G.-H. Hsiue, *Macromolecular Rapid Communications*, 2005, **26**, 986-991.

99. C. Xu, B. Wu, L. R. Dalton, P. M. Ranon, Y. Shi and W. H. Steier, *Macromolecules*, 1992, **25**, 6716-6718.

100. R. D. Miller, D. M. Burland, M. Jurich, V. Y. Lee, C. R. Moylan, J. I. Thackara, R. J. Twieg, T. Verbiest and W. Volksen, *Macromolecules*, 1995, **28**, 4970-4974.

101. T. Verbiest, D. M. Burland, M. C. Jurich, V. Y. Lee, R. D. Miller and W. Volksen, *Science*, 1995, **268**, 1604-1606.

102. M. Eich, G. C. Bjorklund and D. Y. Yoon, *Polymers for Advanced Technologies*, 1990, **1**, 189-198.

103. M. A. Hubbard, T. J. Marks, J. Yang and G. K. Wong, *Chemistry of Materials*, 1989, **1**, 167-169.

104. M. Eich, B. Reck, D. Y. Yoon, C. G. Willson and G. C. Bjorklund, *Journal of Applied Physics*, 1989, **66**, 3241-3247.

105. D. Jungbauer, I. Teraoka, D. Y. Yoon, B. Reck, J. D. Swalen, R. Twieg and C. G. Willson, *Journal of Applied Physics*, 1991, **69**, 8011-8017.

106. X. Wang, J.-I. Chen, S. Marturunkakul, L. Li, J. Kumar and S. K. Tripathy, *Chemistry of Materials*, 1997, **9**, 45-50.

107. S. S. H. Mao, Y. Ra, L. Guo, C. Zhang, L. R. Dalton, A. Chen, S. Garner and W. H. Steier, *Chemistry of Materials*, 1998, **10**, 146-155.

108. M. Chen, L. R. Dalton, L. P. Yu, Y. Q. Shi and W. H. Steier, *Macromolecules*, 1992, **25**, 4032-4035.

109. Y. Shi, W. H. Steier, M. Chen, L. Yu and L. R. Dalton, *Applied Physics Letters*, 1992, **60**, 2577-2579.
110. C. Cabanetos, E. Blart, Y. Pellegrin, V. Montembault, L. Fontaine, F. Adamietz, V. Rodriguez and F. Odobel, *European Polymer Journal*, 2011, **48**, 116-126.
111. B. K. Spraul, S. Suresh, J. Jin and D. W. Smith, *Journal of the American Chemical Society*, 2006, **128**, 7055-7064.
112. C. Zhang, H. Zhang, M.-C. Oh, L. R. Dalton and W. H. Steier, What the ultimate polymeric electro-optic materials will be: guest-host, crosslinked, or side-chain?, 2003.
113. J. Luo, M. Haller, H. Li, T. D. Kim and A. K. Y. Jen, *Advanced Materials*, 2003, **15**, 1635-1638.
114. M. Haller, J. Luo, H. Li, T.-D. Kim, Y. Liao, B. H. Robinson, L. R. Dalton and A. K. Y. Jen, *Macromolecules*, 2004, **37**, 688-690.
115. A. Hayashi, Y. Goto, M. Nakayama, H. Sato, T. Watanabe and S. Miyata, *Macromolecules*, 1992, **25**, 5094-5098.
116. X. Zhang, M. Li, Z. Shi, R. Jin, X. Wang, Y. Yan, M. Yi, D. Zhang and Z. Cui, *Journal of Materials Science*, 2011, **46**, 4458-4464.
117. A. Godt, J. M. J. Fréchet, J. E. Beecher and C. S. Willand, *Macromolecular Chemistry and Physics*, 1995, **196**, 133-147.
118. S. Muller, P. Le Barny, E. Chastaing and P. Robin, *Molecular Engineering*, 1992, **2**, 251-272.
119. S. K. Lee, M. J. Cho, J.-I. Jin and D. H. Choi, *Journal of Polymer Science Part A: Polymer Chemistry*, 2007, **45**, 531-542.
120. T.-D. Kim, J. Luo, Y. Tian, J.-W. Ka, N. M. Tucker, M. Haller, J.-W. Kang and A. K. Y. Jen, *Macromolecules*, 2006, **39**, 1676-1680.
121. Y. H. Kuo, L. Jingdong, W. H. Steier and A. K. Y. Jen, *Photonics Technology Letters, IEEE*, 2006, **18**, 175-177.
122. K. E. Betterton, M.; Haeussling, L.; Lux, M. G.; Twieg, R. J.; Willson, C. G.; Yoon, D.; Burns, E. G.; Grubbs, R., *Polymeric Materials Science and Engineering*, 1992, **66**, 12-13.
123. J. Luo, S. Liu, M. Haller, L. Liu, H. Ma and A. K. Y. Jen, *Advanced Materials*, 2002, **14**, 1763-1768.
124. B. K. Long, Ph.D. Dissertation, University of Texas, 2009.
125. C. Decker, *Macromolecular Rapid Communications*, 2002, **23**, 1067-1093.
126. BASF, Photoacid Generator Selection Guide, http://www.basf.com/group/corporate/us/en/literature-document:/Brand+Irgacure-Brochure--Photoacid+Generator+Selection+Guide-English.pdf, 2014.
127. BASF, High lights! Radiation curing with resins and photoinitiators for industrial coatings and graphic arts: Laromer® and Irgacure®, http://www.dispersions-pigments.basf.com/portal/load/fid790950/Radiation%20Curing.pdf, 2014.
128. W. Volksen, T. Pascal, J. W. Labadie and M. I. Sanchez, in *Polymers for Microelectronics*, American Chemical Society, 1993, vol. 537, ch. 27, pp. 403-416.

129. D. R. McKean, G. M. Wallraff, W. Volksen, N. P. Hacker, M. I. Sanchez and J. W. Labadie, in *Polymers for Microelectronics*, American Chemical Society, 1993, vol. 537, ch. 28, pp. 417-427.

130. J. M. J. Fréchet, J. F. Cameron, C. M. Chung, S. A. Haque and C. G. Willson, *Polymer Bulletin*, 1993, **30**, 369-375.

131. K.-i. U. Fukukawa, Mitsuru, *Polymer Journal*, 2008, **40**, 281-296.

132. R. Rubner, H. Ahne, E. Kuehn and G. Kolodziej, *Photogr. Sci. Eng.*, 1979, **23**, 303-309.

133. N. Yoda and H. Hiramoto, *Journal of Macromolecular Science: Part A - Chemistry*, 1984, **21**, 1641-1663.

134. M. Ree, T. L. Nunes and K. J. R. Chen, *Journal of Polymer Science Part B: Polymer Physics*, 1995, **33**, 453-465.

135. W. W. Flack, G. E. Flores, L. D. Christensen and G. Newman, Investigation of the properties of photosensitive polyimide films, 1996.

136. P. Cheang, L. Christensen and C. Reynaga, Optimization of Photosensitive Polyimide Process for Cost Effective Packaging, 1996.

137. M. Oba and Y. Kawamonzen, *Journal of Applied Polymer Science*, 1995, **58**, 1535-1542.

138. H. Seino, A. Mochizuki, O. Haba and M. Ueda, *Journal of Polymer Science Part A: Polymer Chemistry*, 1998, **36**, 2261-2267.

139. S. L.-C. Hsu, P.-I. Lee, J.-S. King and J.-L. Jeng, *Journal of Applied Polymer Science*, 2003, **90**, 2293-2300.

140. X. Z. Jin and H. Ishii, *Journal of Applied Polymer Science*, 2005, **98**, 15-21.

141. S. Lien-Chung Hsu, H.-T. Chen and S.-J. Tsai, *Journal of Polymer Science Part A: Polymer Chemistry*, 2004, **42**, 5990-5998.

142. M.-k. Leung and J. M. J. Frechet, *Journal of the Chemical Society, Perkin Transactions 2*, 1993, 2329-2335.

143. D. R. McKean, G. M. Wallraff, W. Volksen, N. P. Hacker, M. I. Sanchez and J. W. Labadie, Base-catalyzed photosensitive polyimide, 1993.

144. K.-i. Fukukawa, Y. Shibasaki and M. Ueda, *Polymers for Advanced Technologies*, 2006, **17**, 131-136.

145. K. Mizoguchi, Y. Shibasaki and M. Ueda, *Journal of Photopolymer Science and Technology*, 2007, **20**, 181-186.

146. T. Ogura, K. Mizoguchi and M. Ueda, *Journal of Photopolymer Science and Technology*, 2008, **21**, 125-130.

147. S. Fukuda, M. Katayama and K. Sakayori, *Journal of Photopolymer Science and Technology*, 2009, **22**, 391-392.

148. T. Ogura, T. Higashihara and M. Ueda, *Journal of Polymer Science Part A: Polymer Chemistry*, 2010, **48**, 1317-1323.

149. S. Fukuda, K. Amagai, S. Kanke and K. Sakayori, *Journal of Photopolymer Science and Technology*, 2011, **24**, 267-268.

150. F. M. Houlihan, A. Shugard, R. Gooden and E. Reichmanis, *Macromolecules*, 1988, **21**, 2001-2006.

176

151. T. Asakura, H. Yamato and M. Ohwa, *Journal of Photopolymer Science and Technology*, 2000, **13**, 223-230.
152. G. Bucher, J. C. Scaiano, R. Sinta, G. Barclay and J. Cameron, *Journal of the American Chemical Society*, 1995, **117**, 3848-3855.
153. K.-H. Song, M. Tsunooka and M. Tanaka, *Journal of Photochemistry and Photobiology A: Chemistry*, 1988, **44**, 197-208.
154. K. H. Chae, *Macromolecular Rapid Communications*, 1998, **19**, 1-4.
155. S. Kanji, N. Satoshi and S. Masamitsu, *Journal of Photopolymer Science and Technology*, 2005, **18**, 141-148.
156. *United States Pat.,* 6,004,724, 1999.
157. R. B. Davis, L. C. Pizzini and J. D. Benigni, *Journal of the American Chemical Society*, 1960, **82**, 2913-2915.
158. R. B. Davis, L. C. Pizzini and E. J. Bara, *The Journal of Organic Chemistry*, 1961, **26**, 4270-4274.
159. R. B. Davis and L. C. Pizzini, *The Journal of Organic Chemistry*, 1960, **25**, 1884-1888.
160. W. H. Heath, University of Texas, 2006.
161. P. Fournari and T. Marey, *Bull. Soc. Chim. Fr.*, 1968, 3223-3233.
162. G. V. Zyl, C. J. Bredeweg, R. H. Rynbrandt and D. C. Neckers, *Canadian Journal of Chemistry*, 1966, **44**, 2283-2289.
163. J. Youn, M.-C. Chen, Y.-j. Liang, H. Huang, R. P. Ortiz, C. Kim, C. Stern, T.-S. Hu, L.-H. Chen, J.-Y. Yan, A. Facchetti and T. J. Marks, *Chemistry of Materials*, 2010, **22**, 5031-5041.
164. W. T. Smith, *Journal of the American Chemical Society*, 1949, **71**, 2855-2856.
165. W. T. Smith and L. Campanaro, *Journal of the American Chemical Society*, 1953, **75**, 3602-3603.
166. D. E. Boswell, J. A. Brennan, P. S. Landis and P. G. Rodewald, *Journal of Heterocyclic Chemistry*, 1968, **5**, 69-75.
167. Intel First to Demonstrate Working 45nm Chips, http://www.intel.com/pressroom/archive/releases/2006/20060125comp.htm, 2014.
168. R. Myslewski, Happy 40th birthday, Intel 4004!, http://www.theregister.co.uk/2011/11/15/the_first_forty_years_of_intel_micropro cessors/, 2014.
169. M. Pecht, *Integrated Circuit, Hybrid, and Multichip Module Package Design Guidelines: A Focus on Reliability*, Wiley, 1994.
170. E. D. Blackshear, M. Cases, E. Klink, S. R. Engle, R. S. Malfatt, D. N. De Araujo, S. Oggioni, L. D. LaCroix, J. A. Wakil, N. H. Pham, G. G. Hougham and D. J. Russell, *IBM Journal of Research and Development*, 2005, **49**, 641-661.
171. Advotech, http://www.advotech.com/uimages/services/die-attach/die-attach-flip-chip.jpg, 2014.
172. Henkel, http://www.henkel.com/com/content_images/SolderMaterials_197203_web_606 W.jpg, 2014.

173. R. Wheeler, http://upload.wikimedia.org/wikipedia/commons/e/ee/EPROM_Microchip_Super Macro.jpg, 2014.

174. R. Shukla, V. Murali and A. Bhansali, Flip chip CPU package technology at Intel: a technology and manufacturing overview, 1999.

175. Y.-J. Cheng, J. Luo, S. Hau, D. H. Bale, T.-D. Kim, Z. Shi, D. B. Lao, N. M. Tucker, Y. Tian, L. R. Dalton, P. J. Reid and A. K. Y. Jen, *Chemistry of Materials*, 2007, **19**, 1154-1163.

176. T. Antesberger, Laser Drilling For Electrical Interconnection in Advanced Flexible Electronics Applications, http://people.ccmr.cornell.edu/~cober/MSE5420/page2/files/LaserProcessing.pdf, 2014.

177. CYCLOTENE 3000 Series Advanced Electronics Resins, http://msdssearch.dow.com/PublishedLiteratureDOWCOM/dh_08b4/0901b80380 8b4ed7.pdf?filepath=cyclotene/pdfs/noreg/888-00006.pdf&fromPage=GetDoc.

178. CYCLOTENE 4000 Series Advanced Electronic Resins, http://www.dow.com/cyclotene/docs/cyclotene_4000_immersion_dev.pdf.

179. PI-2600 Series, http://hdmicrosystems.com/HDMicroSystems/en_US/pdf/PI-2600_ProcessGuide.pdf.

180. HD-8820 Aqueous Positive Polyimide, http://hdmicrosystems.com/HDMicroSystems/en_US/pdf/HD-8820_ProcessGuide.pdf.

181. ITRS, Package Substrates: Cost Performance, http://www.itrs.net/Links/2012ITRS/2012Tables/AssemblyPkg_2012Tables.xlsx, 2014.

182. K. Maex, M. R. Baklanov, D. Shamiryan, F. Iacopi, S. H. Brongersma and Z. S. Yanovitskaya, *Journal of Applied Physics*, 2003, **93**, 8793-8841.

183. V. V. Korshak, S. V. Vinogradova and Y. S. Vygodskii, *Journal of Macromolecular Science, Part C*, 1974, **11**, 45-142.

184. A. E. Feiring, B. C. Auman and E. R. Wonchoba, *Macromolecules*, 1993, **26**, 2779-2784.

185. J. O. Simpson and A. K. St.Clair, *Thin Solid Films*, 1997, **308–309**, 480-485.

186. S. Ying-Hung So Ying-Hung, E. Stark, L. Yongfu Li Yongfu, T. Stokich, K. Ober, A. Achen, D. Scheck, S. Kisting, J. Hetzner, K. Baranek, J. Curphy, S. Thurston, E. Beach, J. Folkenroth, T. Richardson and S. Rozeveld, *Electronic Components & Technology Conference. Proceedings*, 2005, 1228-1233.

187. G. Maier, *Progress in Polymer Science*, 2001, **26**, 3-65.

188. B. C. Auman, *MRS Online Proceedings Library*, 1995, **381**, null-null.

189. H.-C. Liou, P. S. Ho and R. Stierman, *Thin Solid Films*, 1999, **339**, 68-73.

190. Kapton® polyimide film, http://www2.dupont.com/Kapton/en_US/assets/downloads/pdf/summaryofprop.pdf, 2014.

191. J. Pellerin, R. Fox and H.-M. Ho, *MRS Online Proceedings Library*, 1997, **476**, null-null.
192. B. V. Kotov, T. A. Gordina, V. S. Voishchev, O. V. Kolninov and A. N. Pravednikov, *Polymer Science U.S.S.R.*, 1977, **19**, 711-716.
193. W. Volksen, personal communication.
194. J. Krupka, R. G. Geyer, J. Baker-Jarvis and J. Ceremuga, Measurements of the complex permittivity of microwave circuit board substrates using split dielectric resonator and reentrant cavity techniques, 1996.
195. C. Fang, M. Sheng, W. Xiaohui, E. Semouchkina and M. Lanagan, Effects of cavity dimensions in split-post dielectric resonator technique for complex permittivity measurements, 2012.
196. U. Kaatze, *Journal of Chemical & Engineering Data*, 1989, **34**, 371-374.
197. M. Hasegawa, M. Horiuchi, K. Kumakura and J. Koyama, *Polymer International*, 2013, n/a-n/a.
198. T. P. Russell, H. Gugger and J. D. Swalen, *Journal of Polymer Science: Polymer Physics Edition*, 1983, **21**, 1745-1756.
199. N. Takahashi, D. Y. Yoon and W. Parrish, *Macromolecules*, 1984, **17**, 2583-2588.
200. D. Boese, H. Lee, D. Y. Yoon, J. D. Swalen and J. F. Rabolt, *Journal of Polymer Science Part B: Polymer Physics*, 1992, **30**, 1321-1327.
201. R. F. Saraf, H.-M. Tong, T. W. Poon, B. D. Silverman, P. S. Ho and A. R. Rossi, *Journal of Applied Polymer Science*, 1992, **46**, 1329-1337.
202. S. T. Chen and H. H. Wagner, *JEM*, 1993, **22**, 797-799.
203. G. Beaucage, R. Composto and R. S. Stein, *Journal of Polymer Science Part B: Polymer Physics*, 1993, **31**, 319-326.
204. J. E. Pye and C. B. Roth, *Macromolecules*, 2013, **46**, 9455-9463.
205. T. Pottiger Michael and C. Coburn John, in *Polymers for Microelectronics*, American Chemical Society, 1993, vol. 537, ch. 18, pp. 282-292.
206. T. A. Mary, J. S. O. Evans, T. Vogt and A. W. Sleight, *Science*, 1996, **272**, 90-92.
207. L. M. Sullivan and C. M. Lukehart, *Chemistry of Materials*, 2005, **17**, 2136-2141.
208. N. Yamashina, T. Isobe and S. Ando, *Journal of Photopolymer Science and Technology*, 2012, **25**, 385-388.
209. H. Wu, M. Rogalski and M. R. Kessler, *ACS Applied Materials & Interfaces*, 2013, **5**, 9478-9487.
210. C. Zhi, Y. Bando, T. Terao, C. Tang, H. Kuwahara and D. Golberg, *Advanced Functional Materials*, 2009, **19**, 1857-1862.
211. Intel, 2000.
212. K.-i. Fukukawa, Y. Shibasaki and M. Ueda, *Chemistry Letters*, 2004, **33**, 1156-1157.
213. K.-i. Fukukawa, T. Ogura, Y. Shibasaki and M. Ueda, *Chemistry Letters*, 2005, **34**, 1372-1373.
214. K. Arimitsu and R. Endo, *Chemistry of Materials*, 2013, **25**, 4461-4463.
215. K. Suyama, H. Araki and M. Shirai, *Journal of Photopolymer Science and Technology*, 2006, **19**, 81-84.

216.   X. Sun, J. P. Gao and Z. Y. Wang, *Journal of the American Chemical Society*, 2008, **130**, 8130-8131.